TEMPLATE-FREE ELECTROSYNTHESIS OF METAL NANOPARTICLES

By

SAURAV K. GUIN

CHEM01200904005

Bhabha Atomic Research Centre, Mumbai, INDIA

A thesis submitted to the

Board of Studies in Chemical Sciences

In partial fulfillment of requirements

for the Degree of

DOCTOR OF PHILOSOPHY

of

HOMI BHABHA NATIONAL INSTITUTE

March, 2015

Homi Bhabha National Institute

Recommendations of the Viva Voce Committee

As members of the Viva Voce Committee, we certify that we have read the dissertation prepared by Mr. Saurav K. Guin entitled "*Template-free Electrosynthesis of Metal Nanoparticles*" and recommend that it may be accepted as fulfilling the thesis requirement for the award of Degree of Doctor of Philosophy.

External Examiner – Prof. R.N. Goyal Date: 9.3.15

S.K. Aggar
Chairman - Prof. S.K. Aggarwal Date: 9.3.15

Guide / Convener - Prof. S. Kannan Date: 9.3.15

Goswami
Member 1 - Prof. A. Goswami Date: 9.3.15

N. Krishnamurthy
Member 2 - Prof. N. Krishnamurthy Date: 9.3.15

Final approval and acceptance of this thesis is contingent upon the candidate's submission of the final copies of the thesis to HBNI.

I hereby certify that I have read this thesis prepared under my direction and recommend that it may be accepted as fulfilling the thesis requirement.

Date: 09/03/2015

Place: MUMBAI

(S. Kannan)

STATEMENT BY AUTHOR

This dissertation has been submitted in partial fulfillment of requirements for an advanced degree at Homi Bhabha National Institute (HBNI) and is deposited in the Library to be made available to borrowers under rules of the HBNI.

Brief quotations from this dissertation are allowable without special permission, provided that accurate acknowledgement of source is made. Requests for permission for extended quotation from or reproduction of this manuscript in whole or in part may be granted by the Competent Authority of HBNI when in his or her judgment the proposed use of the material is in the interests of scholarship. In all other instances, however, permission must be obtained from the author.

(Saurav K. Guin)

List of Publications Arising from the Thesis

Journal

1. "A mechanistic study on the effect of surface protecting agent on electrocrystallization of silver nanoparticles", Saurav K. Guin, Rohan Phatak, Jisha S. Pillai, Arnab Sarkar, Suresh K. Aggarwal, *RSC Advances*, **2014**, DOI: 10.1039/C4RA12877J.

2. "Prospective use of the potentiostatic triple pulse strategy for the template-free electrosynthesis of metal nanoparticles", Saurav K. Guin, Suresh K. Aggarwal, *RSC Advances*, **2014**, 4, 55349-55353.

3. "Template-free electrosynthesis of gold nanoparticles of controlled size dispersion for the determination of lead at ultratrace levels", Saurav K. Guin, Jisha S. Pillai, Arvind S. Ambolikar, Abhijit Saha, Suresh K. Aggarwal; *RSC Advances*, **2013**, 3, 17977-17988.

4. "Electrosynthesis of lead nanoparticles on template free gold surface by potentiostatic triple pulse technique"; Saurav K. Guin, H.S. Sharma, Suresh K. Aggarwal; *Electrochimica Acta*, **2010**, 55, 1245-1257.

5. "An insight into the electrocatalysis of uranyl sulphate on gold nanoparticles modified glassy carbon electrode"; Saurav K. Guin, Parvathi K., Arvind S. Ambolikar, Jisha S. Pillai, D.K. Maity, S. Kannan, Suresh K. Aggarwal; *Electrochimica Acta,* **2015**, 154, 413-420.

Lecture Note

1. "Understanding electrochemical quartz crystal microbalance", Saurav K. Guin, Suresh K. Aggarwal, *Highlights in Electro-Analytical Techniques (HEAT)*; ISEAC Publications, **2013**, 2, 76-81.

Paper Presentations in International Conferences

1. "An insight into the electrocatalysis of U(VI) on gold nanoparticles (AuNPs)", Saurav K. Guin, Parvathi K., Arvind S. Ambolikar, Jisha S. Pillai, D.K. Maity, S. Kannan, Suresh K. Aggarwal; *ECHEMS -2014 : Electrochemistry in Molecular Understanding* held at Wells in United Kingdom during June 17-20, 2014 (Poster Presentation).

   [Awarded First Prize in Poster Presentation in this International Conference].

2. "A Mechanistic study on the effect of surface protecting agent on electrocrystallization of metal nanoparticles", Saurav K. Guin, Rohan Phatak, Jisha S. Pillai, Suresh K. Aggarwal, *ECHEMS -2014 : Electrochemistry in Molecular Understanding* held at Wells in United Kingdom during June 17-20, 2014 (Oral Presentation).

3. "Template-free electrosynthesis of monodispersed gold nanoparticles on glassy carbon electrode for the determination of Pb(II) at ultratrace levels", Saurav K. Guin, Jisha S. Pillai, Arvind S. Ambolikar, Suresh K. Aggarwal, *64th Annual Meeting of the International Society of Electrochemistry – Electrochemistry for a New Era* held at Santiago de Queretaro in Mexico during September 8-13, 2013 (Poster Presentation).

   [Received Best Poster Presentation Award in this International Conference].

4. “Electrosynthesis of nanoparticles on template free electrode : Influence of potentiostatic pulse strategy”, Saurav K. Guin, Suresh K. Aggarwal, *64th Annual Meeting of the International Society of Electrochemistry – Electrochemistry for a New Era* held at Santiago de Queretaro in Mexico during September 8-13, 2013 (Oral Presentation).

5. “Effect of stabilizing agent on electrocrystallization of silver : A mechanistic study”, Saurav K. Guin, Jisha S. Pillai, Rohan Phatak, Suresh K. Aggarwal, *4th ISEAC International Discussion Meet on Electrochemistry and its Applications* held at Thiruvananthapuram in India during February 7-10, 2011 (Poster Presentation).

   [Received Best Poster Presentation Award in this International Conference].

DEDICATIONS

This thesis is dedicated to

my best friend cum wife

Jhimli Paul Guin

&

to my beloved teachers

Dr. Sujoy Kumar Chakrabarty,
Dr. Chandan Kumar Pal,
Dr. Chandan Saha,
Dr. Rajsekhar Bhattacharyya

ACKNOWLEDGEMENTS

This thesis owes its existence to the help, support, and inspiration of many people. I would like to thank my supervisor, Prof. S. Kannan for his support and encouragement during my studies. I would also like to express my sincere appreciation and gratitude to Prof. S.K. Aggarwal for his patient guidance, encouragement and excellent advice for more than three years of this thesis's work. Deepest gratitude is also due to the members of the HBNI Doctoral Committee members Prof. A. Goswami and Prof. N. Krishnamurthy for their comments and suggestions to improve the shape of the study.

Special thanks to Dr. H.S. Sharma, Dr. Dilip K. Maity, Mr. Arvind S. Ambolikar, Smt. Jisha S. Pillai, Mr. Arnab Sarkar, Mr. Rohan Phatak, Dr. K. Krishnan, Kum. K. Parvathi, Mr. Abhijit Saha for extending their support at various stages to complete my work. I would also like to thank Dr. N.L. Misra, Mr. S. Sanjay Kumar, Mr. Santu Kaity and Dr. A.K. Debnath for helping me wherever needed. I also extend my appreciations to Mr. R. Shivaraman, Smt. Nilima Bhoir and Mr. Rawte for their assistance in various stages of my PhD program.

I express gratitude to Dr. (Smt.) J.V. Kamat, Shri N. Gopinath, Dr. Manoj K. Sharma, Dr. (Smt.) Ruma Gupta and all other colleagues in the Electrochemistry Section for their wholehearted support, encouragement and co-operation. I would also like to thank all of my friends and colleagues for their constant support.

……………………Saurav K. Guin

CONTENTS

Synopsis

Metal nanoparticles offer excellent chemistry compared to its bulk equivalent because of the large surface area-to-volume ratio, large surface energies, specific electronic structure, plasmon excitation, quantum confinement, short range ordering, and increased number of kinks and low-coordination sites such as corners & edges, having a large number of dangling bonds. There are two general approaches for synthesising metal nanoparticles. The first one is the "top down approach", which begins with a pattern generated on a larger macroscopic initial structure, and then it reduces to nanoscale. Ball millings, photolithography, embossing and moulding, micro-contact printing etc. are included in the top down approach. However, the applicability of this approach is limited by the high expenditure, broad particle size distribution and slow rate of production of metal nanoparticles. The other approach is the "bottom up approach", which starts with atoms or molecules and builds up to nanostructures. This approach is much less expensive comparative to top down approach. The bottom up approach consists of two popular routes viz. gas (or vapour) and solution phase synthesis. Inert gas condensation, pulsed laser ablation, spark discharge generation, ion sputtering, chemical vapour synthesis, spray pyrolysis etc. are the gas (or vapour) phase synthesis route of bottom up approach. On the other hand, co-precipitation or colloidal synthesis, sol-gel processing, micro-emulsion, hydrothermal/solvothermal synthesis, bioreduction, electrodeposition, polyol method etc. are the solution phase synthesis route of bottom up approach. Among these processes, electrosynthesis is one of the promising techniques for preparing supported metal nanoparticles of controlled size, shape and crystallographic orientation. During electrosynthesis, the metal nanoparticles are prepared on the electrode surface by an external source of electrons to its precursor ions present in the solution. This is generally a room temperature process and gives better purity of the particles due to the absence of a vast number of auxiliary chemicals.

Templating is one of the most important techniques for the controlled synthesis of nanostructured materials of well-defined size, shape and configuration. The general route for templated electrosynthesis of nanostructured materials includes the following steps: (1) template preparation, (2) directed electrosynthesis of target materials using the template, and (3) template removal. The bottle necks of the templated electrosynthesis are the first and the last steps. The preparation of templates of precise nanometer dimensions is itself a costly and delicate step. It requires sometimes sophisticated instruments. On the other hand, both physical methods such as dissolution and chemical methods including calcinations and etching are applied to remove the template after synthesis of the nanoparticles. Therefore, the property of metal nanoparticles may be altered due to the harsh conditions of using extensive corrosive acid or base in the template removal step.

Hence the prime aim of the present thesis was to develop the strategies for electrosynthesis of metal nanoparticles without using any physical or chemical templates. The difficulties in controlling the size as well as size dispersion of metal nanoparticles are also addressed in the thesis. The work described in this thesis is divided into six chapters followed by the bibliography.

Chapter 1: Introduction

This chapter gives a general introduction to the synthesis of metal nanoparticles. The fundamentals of electrodeposition of metals and electrochemical nucleation and growth are also discussed in this chapter. A brief discussion is presented on the development of the electrochemical nucleation and growth models for electrodeposition of metals at constant potential. Finally, the scope of the work is highlighted.

Chapter 2: Experimental

This chapter gives the brief descriptions of the electrochemical workstation (potentiostat/galvanostat), electrochemical techniques, electrochemical quartz crystal microbalance (EQCM), spectroelectrochemistry, electrochemical impedance spectroscopy (EIS), atomic force microscope (AFM), scanning electron microscope (SEM), X-ray photoelectron spectroscopy (XPS), X-ray diffraction (XRD) and inductively coupled plasma mass-spectroscopy (ICP-MS) employed at different stages of present work. It also consists of a brief description of the chemicals, methodologies and computer based programs employed at different stages of present work.

Chapter 3: Template-free Electrosynthesis of Lead Nanoparticles (PbNPs) by Potentiostatic Triple Pulse Strategy (PTPS)

There is an increasing interest to synthesize PbNPs for various applications. Electrochemical deposition is advantageous because of the least requirement of the additives and absence of any interfering products generated during the electrodeposition of lead metal. It is interesting to note that the deposition of PbNPs on a supported material has not been attempted electrochemically in spite of the reversible electrode behavior of Pb(II)/Pb couple. This is the first effort for the electrosynthesis of PbNPs (without any adlayer of Pb) on a template free substrate and this necessitated the optimization of different parameters to achieve the desired quality of the PbNPs. In this context, it is therefore of interest to develop a strategy for the electrochemical synthesis of PbNPs on a template free substrate, their characterization and study on the influence of the electrochemical parameters on size and size distribution of PbNPs.

An attempt was made for the electrosynthesis of PbNPs employing a potentiostatic triple pulse strategy (PTPS) where the first pulse employed is the perturbation pulse for the removal of the adsorbed Pb^{2+} ions from the electrode surface. The dual role of the first pulse is the restriction of pre-adsorption of Pb(II) on electrode surface and simultaneously providing the fresh surface for the nucleation and growth processes. The second and third pulses are responsible for the controlled nucleation and growth of PbNPs, respectively. This chapter is subdivided into two parts. The first part deals with the implementation of the PTPS for the electrosynthesis of PbNPs on gold surface, where gold facilitates the electrodeposition of Pb as the energy of Pb-Au interaction is much stronger for the first monolayer than that of the Pb-Pb interaction. The second part of this chapter deals with the implementation of the PTPS for the electrosynthesis of PbNPs on glassy carbon (GC) surface, where GC provides a low surface energy conductive substrate and exhibits weak metal-substrate interaction.

The pulse potentials were chosen from cyclic voltammetry (CV) and electrochemical quartz crystal microbalance (EQCM) studies of Pb(II)/Pb couple in 0.1 M $HClO_4$. The electrodeposited PbNPs were characterized ex situ independently by XRD, XPS and AFM. The results obtained suggested the presence of chemisorbed oxygen on the surface of PbNPs. The influence of pulse parameters (viz. nucleation pulse duration, growth pulse duration and growth pulse potential) was investigated on the size, particle density and monodispersity of the deposited PbNPs. Figure S1 shows the (a) surface topography and (b) particle size histograms of PbNPs synthesised by PTPS employing first pulse at +0.2 V (E_1) for 60 s (t_1) followed by a nucleation pulse at -0.53 V (E_2) for 0.06 s (t_2) and a growth pulse at -0.455 V (E_3) for 60 s (t_3). The surface height distribution of the bare gold surface is also shown in the figure for comparison purpose. The potentials mentioned here are with reference to the Ag/AgCl(Saturated KCl) electrode.

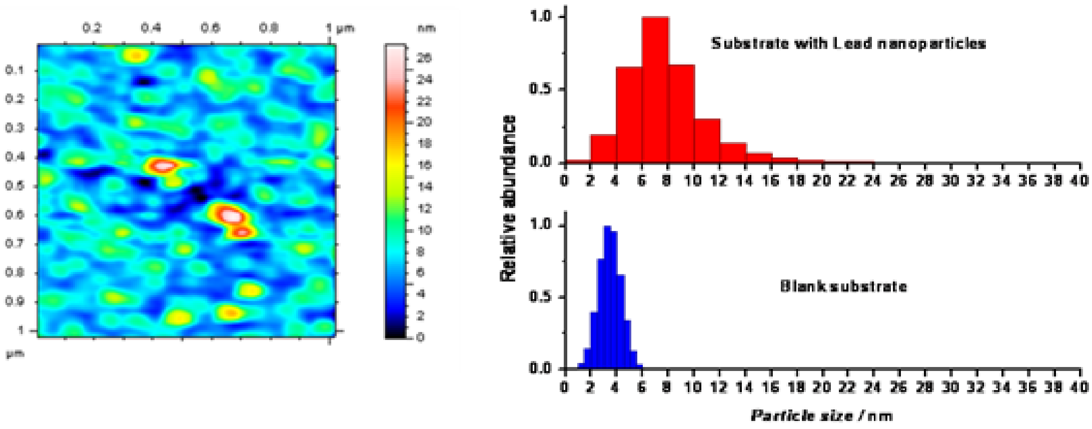

Figure S1 *The (a) surface topography and (b) particle size histograms of PbNPs synthesised by PTPS.* $E_1 = +0.2$ *V;* $t_1 = 60$ *s;* $E_2 = -0.53$ *V;* $t_2 = 0.06$ *s;* $E_3 = -0.455$ *V;* $t_3 = 60$ *s.*

The second part of this chapter deals with the implementation of the PTPS for the electrosynthesis of PbNPs on GC surface. GC does not provide any favorable interaction on Pb deposition i.e. Pb adatoms - adatoms interaction is stronger than the interaction of Pd adatoms with the GC surface. The PTPS was compared to the conventional potentiostatic double pulse strategy (PDPS). The final surface topography of the PbNPs/GC at the end of 70 s of the current transients is shown in Figure S2. The instantaneous nucleation and growth of PTPS resulted into discrete and monodispersed (average height 8±2 nm) tapped hemispherical PbNPs. However, the progressive nucleation and growth and prolonged induction time in PDPS resulted in small, overlapped and polydispersed (average height 5±5 nm) PbNPs. The optimized PTPS can electrochemically produce discrete and monodispersed capped hemispherical metal nanoparticles on a low surface energy conductive substrate.

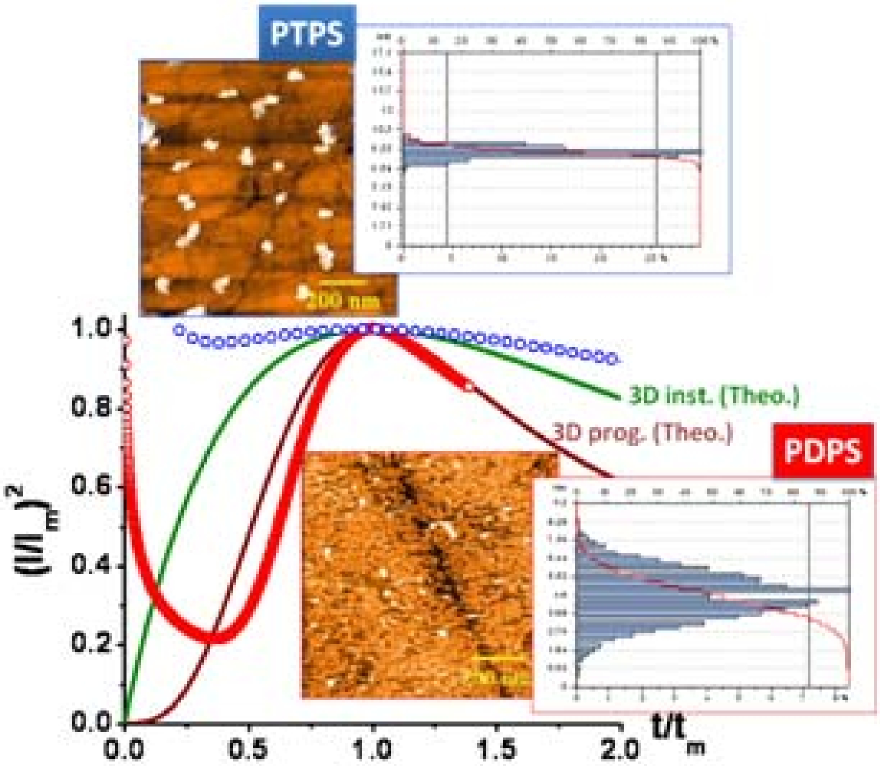

Figure S2 *The progressive (in PDPS) and instantaneous (in PTPS) types of nucleation and growth for the electrocrystallization on PbNPs during the last pulse. The surface topographies and particle size dispersions are shown along side. For PTPS,* $E_1 = 0.4$ *V,* $t_1 = 60$ *s,* $E_2 = -0.7$ *V,* $t_2 = 1$ *ms,* $E_3 = -0.49$ *V,* $t_3 = 70$ *s; for PDPS,* $E_1 = 0.4$ *V,* $t_1 = 60$ *s,* $E_2 = -0.49$ *V,* $t_2 = 70$ *s.*

Chapter 4: Template-free Electrosynthesis of Gold Nanoparticles (AuNPs)

Gold nanoparticles (AuNPs) are the most stable among all the metal nanoparticles and they also have fascinating material properties. Novel multiple potentiostatic pulse (MPP) and multiple galvanostatic pulse (MGP) strategies were developed for the template free electrosynthesis of AuNPs on a GC electrode with the objective of achieving better electroanalytical performance compared to that of the bulk metal electrode. The mechanism of electrocrystallization in the initial stages of metal deposition was studied by cyclic voltammetry, chronoamperomentry, chronopotentiometry and in situ spectroelectrochemistry. The key parameters controlling the size dispersion of the metal nanoparticles in the template-free electrosynthesis of AuNPs were evaluated.

In the MPP strategy, the tapped hemispherical gold nanoparticles (AuNPs(P)/GC) of average diameter of 250-300 nm and average height of 10-15 nm were deposited on a GC electrode covering about 61% of the effective surface area of the electrode. In the MGP strategy, the tapped hemispherical gold nanoparticles (AuNPs(G)/GC) of average diameter of 350-400 nm and average height of 25-30 nm were deposited on a GC electrode covering about 18% of the effective surface area of the electrode.

The synthesized AuNPs were utilized for different electrochemical applications which are subdivided into two sections. The first section represents the excellent sensitivity of AuNPs(P)/GC for the determination of Pb(II) by square wave anodic stripping voltammetry (SWASV) by virtue of the underpotential deposition of lead on the gold surface. The limits of detection of Pb(II) obtained with a bare GC, bare Au, AuNPs(G)/GC and AuNPs(P)/GC electrodes were calculated as 1.22 μg L^{-1} (5.86 nM), 122 ng L^{-1} (587 pM), 86.4 ng L^{-1} (416 pM) and 57 ng L^{-1} (274 pM), respectively, at $S/N = 3$. The analytical response of the AuNPs(P)/GC electrode was found to be the best among the four electrodes. The concentrations of Pb(II) in some of the environmental samples were determined by SWASV at AuNPs(P)/GC electrode. The results showed a good agreement with the ICP-MS data for the same samples.

The second section represents the electrocatalytic reduction of U(VI) in 1 M H_2SO_4 at AuNPs(G)/GC. The supported gold nanoparticles (AuNPs) exhibited high electrocatalytic activity for CO oxidation and oxygen reduction. The oxygen reduction on AuNPs occurs in the potential range -0.5 to -0.15 V vs. Ag/AgCl (saturated KCl) reference electrode, which is similar range of reduction potential of the uranyl (UO_2^{2+}) complexes on mercury pool electrode. $U^{VI}O_2^{2+}$ is chemically robust due to the presence of trans-dioxo bonds around the uranium and it is highly oxidative in acidic solutions, exhibiting interesting and useful oxidation–reduction chemistry, which indeed requires more exploration. This is the first report on the electrocatalysis of $U^{VI}O_2^{2+}$ in 1 M H_2SO_4 at AuNPs supported on glassy carbon electrode (AuNPs(G)/GC) evidenced from the cyclic voltammetry (CV), differential pulse voltammetry and electrochemical impedance spectroscopy experiments. The molecular understanding of the electrocatalytic mechanism was evaluated by the relative stability of molecular orbitals of the most abundant U(VI) complex in sulphuric acid solution by quantum chemical calculations.

The rates of electron transfer reaction from the electrode to U(VI) were determined as 3.5×10^{-5}, 5.0×10^{-5} and 5.4×10^{-3} cm s^{-1} at GC, Au and AuNPs(G)/GC, respectively. This indicates that heterogeneous charge transfer rate of AuNPs(G)/GC is much faster compared to Au and GC. Moreover, the average charge transfer coefficients (α; symmetry factor of the transition state) were determined as 0.14, 0.47 and 0.83 at GC, Au and AuNPs(G)/GC, respectively, by cyclic voltammetric simulation, Tafel's slope and analytical equation for irreversible reaction. Therefore, it can be speculated that the rate as well as the symmetry of the potential energy barrier of the heterogeneous electron transfer reaction from metal to U(VI) improves in the order GC < Au <AuNPs(G)/GC.

For molecular level understanding of electrocatalysis of U(VI) at AuNPs, quantum chemical calculations were performed to optimise the geometry of the most probable U(VI) species in sulphuric acid solution. $[U^{VI}O_2(\eta^1\text{-}OSO_3)(\eta^2\text{-}O_2SO_2)$,

$2H_2O]^{2-}$ was found to be the predominant species under the conditions studied. The nonadiabatic electron affinity of $[U^{VI}O_2(\eta^1\text{-}OSO_3)(\eta^2\text{-}O_2SO_2), 2H_2O]^{2-}$ was calculated as -6.57 eV vs. vacuum in the aqueous phase without structural optimization of the reduced state using optimised structure of the oxidised form for the starting point of the electron/charge transfer. The energies of the highest occupied molecular orbital (HOMO) and the lowest unoccupied molecular orbital (LUMO) were calculated as -7.01 and -5.84 eV vs. vacuum, respectively. It is interesting to note that the HOMO is comprised mostly of O(p)-orbitals of monodentate sulphate ion, whereas the LUMO is comprised of U $5f_{z(x2-y2)}$ orbital. It shows that an interaction between filled p-orbital of oxygen atom of sulphate with that of vacant f orbital of uranium(VI) ion, indicating the f-orbital participation in bonding.

The heterogeneous electron transfer rates are dependent on the density of states (DOS) of the electrode material i.e. higher DOS means a higher probability of electrons of correct energy available for an electron transfer to a redox system. The DOS of the sp-band of GC depends on the energy range and it is very low ($\sim 2.2\times10^{-3}$ states/eV) i.e. below -0.1 V vs. Ag/AgCl. Therefore, the heterogeneous rate of electron transfer to U(VI) was found to be the lowest at GC. Moreover, the weak interaction of LUMO (made of U-5f orbital) of $[U^{VI}O_2(\eta^1\text{-}OSO_3)(\eta^2\text{-}O_2SO_2), 2H_2O]^{2-}$ with carbon sp-band creates a virtual state (VS-LUMO) at -4.372 eV vs. vacuum (calculated from the formula; $E_{VS\text{-}LUMO} = -e[E_c + 4.65]$ eV vs. vacuum; where E_c is the onset potential vs. Ag/AgCl in the CV) for the heterogeneous electron transfer reaction to take place. The weak absorption of $[U^{VI}O_2(\eta^1\text{-}OSO_3)(\eta^2\text{-}O_2SO_2), 2H_2O]^{2-}$ on GC surface leads to the lowest charge transfer coefficient of the reaction. On the other hand, Gold has a DOS of 0.28 states/eV and this value is relatively constant with energy. The metal 5d-band interacts comparatively strongly with the LUMO (U-5f orbital) of $[U^{VI}O_2(\eta^1\text{-}OSO_3)(\eta^2\text{-}$

O_2SO_2), $2H_2O]^{2-}$ creating VS-LUMO at -4.549 eV vs. vacuum. Moreover, the strong adsorption of $[U^{VI}O_2(\eta^1\text{-}OSO_3)(\eta^2\text{-}O_2SO_2), 2H_2O]^{2-}$ on Au improves the charge transfer coefficient of the cathodic reaction. In AuNPs(G)/GC, not only the DOS is expected to be increased, but also the 5d-band centre is to be lifted up towards the Fermi level. The highest observed value of the charge transfer coefficient and rate of electron transfer at AuNPs are attributed to the highest density of states of 5d-band of gold and its strong interaction with the LUMO contributed by U-$5f_{z(x2\text{-}y2)}$ orbital of $[U^{VI}O_2(\eta^1\text{-}OSO_3)(\eta^2\text{-}O_2SO_2), 2H_2O]^{2-}$, predominant stable species of $U^{VI}O_2^{2+}$ in 1 M H_2SO_4.

Chapter 5: The Effect of Surface Protecting Agent on Electrocrystallization of Silver Nanoparticles (AgNPs)

Silver nanoparticles (AgNPs) have received considerable attention in the field of catalysis, biological and chemical sensors and surface-enhanced Raman spectroscopy. The cationic surfactant, cetyltrimethylammonium bromide (CTAB), is most extensively used as a stabilizer to fabricate positively charged bi-layer shell on AgNPs. In our previous studies, the template-free electrosynthesis of metal nanoparticles was well established. However, from the application point of view, the chemical stability of the synthesised nanoparticles in the absence of any surface stabilizing or protecting agent is often questioned. In this chapter, the mechanisms of electrocrystallization of AgNPs from its aqueous solution at selected constant potentials both in the presence and absence of surface protecting agent tetrabutylammonium tetrafluoroborate ($TBABF_4$) are reported by cyclic voltammetry and chronoamperometry to understand the effect of the stabilizing agent on the formation and growth of AgNPs.

The electrocrystallization of metal basically involves nucleation of metal adatoms on the active sites of the electrodes followed by three dimensional diffusion controlled growth of the nuclei. Four popular electrocrystallization models viz. Scharifker and Hills (SH), Scharifker and Mostany (SM), Sluyters-Rehbach, Wijenberg, Bosco and Sluyters (SRWBS) and Heerman and Tarallo (HT) have been developed from the same nucleation rate law (of constant nucleation rate) and Avrami's theorem of projecting diffusion flux. The aim of the study was to understand the influence of TBA^+ ions on the electrocrystallization of AgNPs by evaluating the electrocrystallization parameters viz. initial current density (j_0), decay constant (τ), diffusion coefficient (D) of Ag(I), number of active sites (N_0) and nucleation rate (a). These were calculated by fitting the experimentally obtained current transients with the calculated current transients (from the models) using hybrid genetic algorithm (HGA). All the three models fitted well by HGA with each of the potentiostatic current transients with residual sum of squares ($\sim 4.6\times10^{-7}$) and reduced χ^2 ($\sim 1.2\times10^{-10}$); but with different values of electrocrystallization parameters.

Irrespective of the differences in the numerical values of the electrocrystallization parameters, each of the models independently revealed that the surface protecting agent would make the kinetics of electrocrystallization sluggish due to induction of activation overpotential at the electrode-electrolyte interface and subsequently the number of nuclei on the electrode surface decreased in presence of TBA^+ ions. However, the principal component analysis of the evaluated parameters (i.e. D, N_0) and derived parameter (i.e. aN_0) revealed that no correlation exists among the electrocrystallization parameters derived from the SH, SM, SRWBS and HT models; though they originated from the same nucleation law of electrocrystallization and Avrami's theorem. In connection to this result, some of the important observations/comments on the validity of the nucleation law (of constant nucleation rate), diffusion zones and Avrami's theory, which are the foundations of the SH, SM, SRWBS and HT models of electrocrystallization were addressed.

Chapter 6: Summary of Key Findings

The important conclusions of the work are as follows:

1. A novel potentiostatic triple pulse strategy (PTPS) was developed for the template-free electrosynthesis of lead nanoparticles. This is the first effort for the electrosynthesis of PbNPs (without any adlayer of Pb) on a template free substrate. The electrodeposited PbNPs were characterized *ex-situ* independently by the XRD, XPS and AFM. The results obtained suggested the presence of chemisorbed oxygen on the surface of PbNPs. The influence of pulse parameters (viz. nucleation pulse duration, growth pulse duration and growth pulse potential) was investigated on the size, particle density and monodispersity of the deposited PbNPs.

2. The systematic studies revealed, for the first time, the cause of improvement in the particle size and size dispersion in potentiostatic triple pulse strategy (PTPS) compared to conventional potentiostatic double pulse strategy (PDPS), and at the same time it also showed a prospect of PTPS for template-free electrosynthesis of metal nanoparticles. The instantaneous nucleation and growth of PTPS resulted into discrete and monodispersed (average height 8±2 nm) tapped hemispherical PbNPs. However, the progressive nucleation and growth and prolonged induction time in PDPS resulted in small, overlapped and polydispersed (average height 5±5 nm) PbNPs.

3. Novel multiple potentiostatic pulse (MPP) and multiple galvanostatic pulse (MGP) strategies were developed for the template free electrosynthesis of AuNPs on a GC electrode with the objective of achieving better electroanalytical performance

compared to that of the bulk metal electrode. Excellent control of the particle size dispersion was achieved in both the routes of synthesis.

4. The AuNPs(P)/GC showed excellent sensitivity and lowest limit (57 ng L^{-1} or 274 pM) of detection for the determination of Pb(II) at ultratrace levels by square wave anodic stripping voltammetry (SWASV) by virtue of the underpotential deposition of lead on the gold surface. The stability, repeatability, reproducibility and accuracy of the analytical response were found to be satisfactory for the analytical purposes.

5. The AuNPs(G)/GC showed excellent electrocatalytic reduction of U(VI) in 1 M H_2SO_4. This was the first report on the electrocatalysis of $U^{VI}O_2^{2+}$ in 1 M H_2SO_4 at AuNPs supported on glassy carbon electrode (AuNPs(G)/GC) evidenced from the cyclic voltammetry, differential pulse voltammetry and electrochemical impedance spectroscopy experiments. Molecular understanding of the electrocatalytic mechanism was evaluated by the relative stability of molecular orbital of the most abundant U(VI) complex in sulphuric acid solution by quantum chemical calculations. The highest observed value of the charge transfer coefficient and rate of electron transfer at AuNPs are attributed to the highest density of states of 5d-band of gold and its strong interaction with the LUMO contributed by U-$5f_{z(x2-y2)}$ orbital of $[U^{VI}O_2(\eta^1\text{-}OSO_3)(\eta^2\text{-}O_2SO_2),\ 2H_2O]^{2-}$, predominant stable species of $U^{VI}O_2^{2+}$ in 1 M H_2SO_4.

6. The surface protecting agent, viz. tetrabutylammonium tetrafluoroborate ($TBABF_4$) slowed down the kinetics of electrocrystallization of AgNPs because of the induction of activation overpotential at the electrode-electrolyte interface and subsequently the number of nuclei on the electrode surface decreased in presence of TBA^+ ions. This study also revealed that enough artifacts may exist in the optimized

values of the number of nuclei; nucleation rate etc. following SH, SM, SRWBS, and HT models and it may be far off from the reality. Therefore, enough need exists to validate the compatibility of the nucleation law (of constant nucleation rate), diffusion zones and Avrami's theory, which are the foundations of the SH, SM, SRWBS and HT models of electrocrystallization.

In conclusion, the work reported in this thesis has led to the development of several new strategies for electrochemical synthesis of metal nanoparticles without using any additional structure directing agents. These synthesis strategies have immense potentials for development of new catalytic and sensor materials for various applications.

List of Symbols

Symbol	Meaning
μ_{ad}	: Electrochemical potential of the adatoms
$\mu_{ad}{}^{0}$	: Standard chemical potential of M_{ad}
μ_{s}	: Electrochemical potential of M^{n+} in solution
$\mu_{s}{}^{0}$	: Standard chemical potential of M^{n+}
a	: Nucleation rate constant
A	: Area of the electrode
a_{ad}	: Activity of M_{ad} on electrode
a_{s}	: Activity of M^{n+}
A_{t}	: Planar area of a single diffusion zone at time t
Au	: Gold
C^{*}	: Bulk concentration of the metal ions
$C^{*}{}_{M}$	: Concentrations of the M_{ad} at E_{∞}
$C^{*}{}_{Mn+}$	: Concentrations of M^{n+} in the bulk
$C^{0}{}_{Mn+}$	: Concentrations of M^{n+} at the surface
C_{DL}	: Capacitance of the electrode-electrolyte interface
C_{f}	: Sensitivity Factor
C_{M}	: Concentrations of the M_{ad} at η
D	: Diffusion coefficient of the metal ions
e	: Charge of an electron
$E_{0}{}^{'}$	: Standard reduction potential
$E_{1/2}$	: Half wave potential
E_{∞}	: Equilibrium potential difference between the M_{ad} and M^{n+}
E_{c}	: Cathodic Onset Potential

Symbol	**Meaning**
E_p	Peak potential in voltammetry
E_p^a	Anodic peak potential in cyclic voltammetry
E_p^c	Cathodic peak potential in cyclic voltammetry
E_{SW}	Amplitude of the square wave pulse
E_{th}	Threshold Potential of Nucleation
$E_{VS\text{-}LUMO}$	Energy of the Virtual electronic State
F	Faraday’s Constant
f	Frequency of the sine wave for EIS
f_{SW}	Frequency of the square wave
G	Gain of OPAMP
i or I	Current
i_{Cell}	Cell current flowing between the counter and working electrodes
i_F	Faradaic current
i_m or I_m	Maximum current of a potentiostatic current transient
i_{NF}	Non-faradaic current
i_p	Peak current in voltammetry
j	Current density
j_0	Initial current density
k	Material constant for instantaneous nucleation
k’	Material constant for progressive nucleation
k”	lattice incorporation rate constant (mol cm^{-2} s^{-1})
k_s	Electrochemical rate constant
M	Molecular weight of the deposited phase
M_{ad}	Metal adatoms
M_{aq}^{n+}	Solvated metal ion of charge n+.

Symbol	**Meaning**
n	: Charge of the metal ion
N	: Number density of nuclei at time t
N'	: Number of adatoms in the nucleus
N_0	: Total number of active sites
N_c	: Critical nucleus
N_s	: Saturation number density of nuclei
Pb	: Lead
PC1	: Principal Component 1
PC2	: Principal Component 2
R	: Universal gas constant
R	: Resistance of an electrical circuit
R'	: Radius of curvature of the nucleus
r_c	: Radius of the critical nucleus
R_{CT}	: Charge transfer resistance across the electrode-electrolyte interface
R_f	: Feedback resistance
R_s	: Solution Resistance
R_u	: Uncompensated resistance
S	: Inert substrate
S_a	: Area Roughness Average
S_q	: Root Mean Square Roughness Average
T	: Temperature in absolute scale
t_m	: Time correspond to the maximum current of a potentiostatic current transient
u	: Age of the nucleus
V	: Volume of the deposited phase

Symbol	**Meaning**
$V_{Feedback}$	: Feedback potential to the input voltage for compensating the iR drop
V_{IN}	: Complex voltage waveform generated by the adder circuit of a potentiostat
V_{iR}	: iR drop
V_n	: Volume of the nucleus
V_{VF}	: Voltage of the voltage follower
Z	: Impedance of an electrical circuit
Z_{Im} or Z''	: Imaginary component of the impedance
Z_{Re} or Z'	: Real component of the impedance
Z_W	: Warburg impedance
$\Delta\mu$	: Change in the chemical potential of the cell during electrodeposition
Δf	: Frequency Change of EQCM
$\Delta G(N,\eta)$	: Nucleation work
ΔG_{Crit}	: Critical energy
Δm	: Change in mass on the EQCM
δ_t	: Radial velocity of the circular patches on the electrode
η	: Overpotential
η^1	: Monodentate Ligand
η^2	: Bidentate Ligand
η_a	: Activation polarization
η_c	: Concentration polarization
θ	: Actual fraction of area covered by diffusion zone assuming overlap
θ'	: Contact angle of the nucleus with the substrate
θ_{ex}	: Fraction of the area covered by diffusion zones assuming no overlap
ν	: Scan rate

Symbol	**Meaning**
ρ	: Density of the deposited phase
σ	: Specific surface energies of the nucleus
σ_i	: Specific surface energies of the nucleus-substrate interface
σ_s	: Specific surface energies of the substrate
τ	: Time constant or Decay time
τ'	: Transition time
φ	: Phase difference between the applied voltage and the response current
$\Phi(N)$	: Total excess energy in creating the new interfaces (nuclus-electrode and nucleus-solution interfaces) during nucleation
Φ_{ad}	: Electric potential of the adatoms on the inert electrode
Φ_s	: Electric potential of the metal ions in the bulk of the solution

List of Abbreviations

Abbreviation	Meaning
ADC	: Analog-to-Digital Converter
AFM	: Atomic Force Microscope
AgNPs	: Silver Nanoparticles
AuNPs	: Gold Nanoparticles
AuNPs(G)/GC	: The AuNPs deposited on the GC by MGPS
AuNPs(P)/GC	: The AuNPs deposited on the GC by MPPS
AuNPs/GC	: AuNPs supported on glassy carbon electrode
Au-QC	: Au coated EQCM crystal
CE	: Counter Electrode
CF	: Current Follower
CTAB	: Cetyltrimethylammonium Bromide
CV	: Cyclic Voltammetry
DAC	: Digital-to-Analog Converter
DPV	: Differential Pulse Voltammetry
EEC	: Electrical Equivalent Circuit/Components
EIS	: Electrochemical Impedance Spectroscopy
EQCM	: Electrochemical Quartz Crystal Microbalance
EWS	: Electrochemical Work-Station
GA	: Genetic Algorithm
GC	: Glassy Carbon
HGA	: Hybrid Genetic Algorithm
HT	: Heerman and Tarallo Model of electrochemical nucleation and growth

Abbreviation	**Meaning**
ICPMS	: Inductively Coupled Plasma Mass Spectrometry
IHP	: Inner Helmholtz Plane
LMA	: Levenberg-Marquardt algorithms
LOD	: Limit of Detection
MGPS	: Multiple Galvanostatic Pulse Strategy
MPPS	: Multiple Potentiostatic Pulse Strategy
NHE	: Normal Hydogen Electrode
NP	: Nanoparticles
OCP	: Open Circuit Potential
OHP	: Outer Helmholtz Plane
OPAMP	: Operational Amplifier
OPD	: Over-Potential Deposition
PbNPs	: Lead Nanoparticles
PCA	: Principal Component Analysis
PTPS	: Potentiostatic Triple Pulse Strategy
PZC	: Potential of Zero Charge
RE	: Reference Electrode
SE	: Supporting Electrolyte
SEM	: Scanning Electron Microscope
SERS	: Surface-Enhanced Raman Spectroscopy
SH	: Scharifker and Hills Model of electrochemical nucleation and growth
SM	: Scharifker and Mostany Model of electrochemical nucleation and growth

Abbreviation	**Meaning**
SRWBS	: Sluyters-Rehbach, Wijenberg, Bosco and Sluyters Model of electrochemical nucleation and growth
SWASV	: Square Wave Anodic Stripping Voltammetry
SWV	: Square Wave Voltammetry
UPD	: Uunder-Potential Deposition
VF	: Voltage Follower
WE	: Working Electrode
WHO	: World Health Organization
XPS	: X-ray Photoelectron Spectroscopy
XRD	: X-ray Diffraction

List of Figures

List of Tables

CHAPTER 1

Introduction

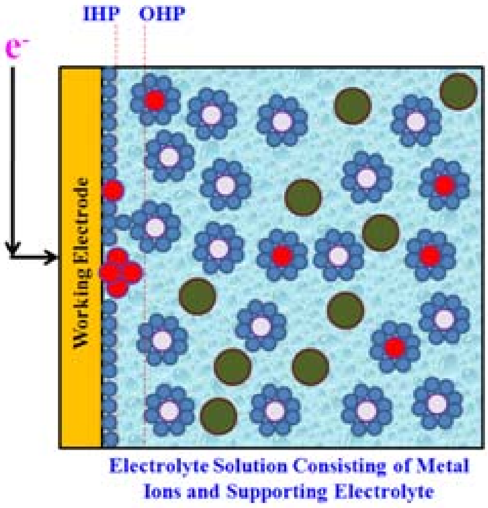

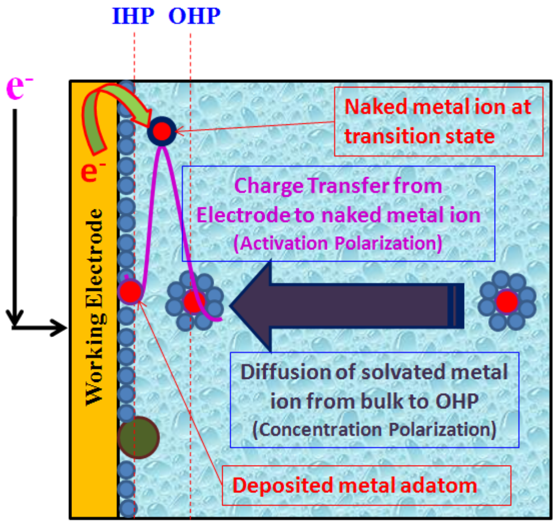

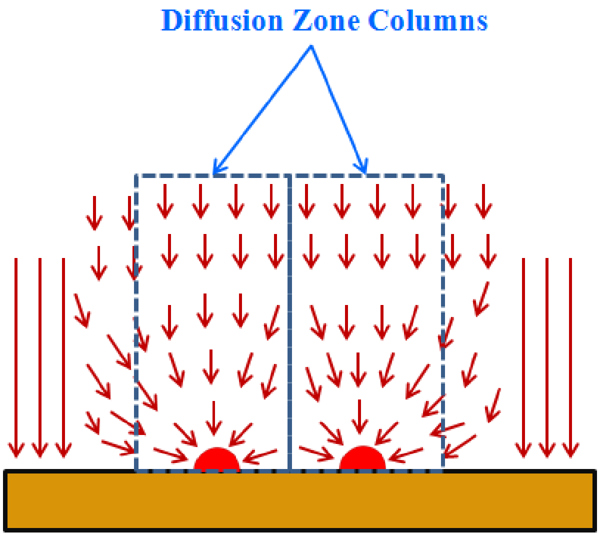

1.1. Synthesis of Metal Nanoparticles

The metals having one or more dimensions (length or width or thickness) in the nanometer size range (1-100 nm) are known as 'metal nanoparticles'. The prefix "nano" is believed to be derived from the Greek word "νάνος" or the Latin word "nannus", both meaning "dwarf". The phrase 'nano-' was officially adopted as a SI prefix (meaning 10^{-9} of SI base unit) in Resolution#12 at the Eleventh Conférence Générale des Poids et Mesures in 1960 *[1]*.

Metal nanoparticles are being investigated in an interdisciplinary area covering Physics, Chemistry, Materials Science and Engineering, because they offer excellent chemistry compared to the bulk metals. In the present era, engineering of metal nanoparticles has got increasing importance in a number of sectors, including biotechnology, electronics, energy, and industrial products *[2-23]*.

Dr. Richard P. Feynman delivered a famous lecture entitled "There's Plenty of Room at the Bottom" on December 26, 1959 in the Annual Meeting of the American Physical Society at California Institute of Technology. In that lecture, he demonstrated that there was chance that one could decrease the size of things in a practical way *[24]*. In 1995, Dr. Jean-Marie Lehn revealed that "There's even more Room at the Top", which proposed that atoms and molecules could be assembled into short range order at nanoscale *[25]*. These two novel thoughts led two basic approaches for synthesising metal nanoparticles *[26, 27]*. The 'top-down' approach is believed to be pioneered by Dr. Feynman, while the 'bottom-up' approach belongs to Dr. Lehn.

The electrosynthesis belongs to the solution based 'bottom-up' approach for preparing supported metal nanoparticles at room temperature *[28-36]*. This gives better purity for the particles due to the absence of a vast number of auxiliary chemicals in the synthesis step. Further, electrosynthesis can produce materials of variable size, shape, crystallographic orientation, density and composition by a judicial choice of electrochemical strategy, nature of the electrode surface and the composition of the electrodeposition solution. In electrosynthesis, the reduction potential can be carefully controlled by fixed, stepped or pulse potentials or current densities, or by sweeping the applied deposition potential. Therefore, it provides better control in the preparation of nanoparticles compared to chemical reducing agent, which provides only fixed reduction potential *[36]*.

Templating is one of the most important techniques for the controlled synthesis of nanostructured materials *[37]*. A template is a physical and chemical gauge, pattern or mold used as a guide to the form of a piece being made. It reveals as a powerful tool using pre-existing guide with desired nanoscale features to direct the formation of nanomaterials into forms that are otherwise difficult to obtain. Typically, nanomaterials synthesized by templating strategies have well-defined size, shape and configuration *[38-45]*. The general route for templated electrosynthesis of nanostructured materials includes the following steps: (1) template preparation, (2) directed electrosynthesis of target materials using the template, and (3) template removal. The bottle necks of the templated electrosynthesis are the first and the last steps. The preparation of templates of precise nanometer dimensions itself is a costly and delicate step. Sometimes, it requires sophisticated instruments. On the other hand, both physical methods such as dissolution and chemical methods including calcinations and etching are applied to remove the template after the synthesis of metal nanoparticles. Therefore, there is a possibility to alter the property of metal nanoparticles due to the harsh conditions of using extensive corrosive acid or base in the template removal step. Hence this thesis presents the studies on the development of various strategies for electrosynthesis of metal nanoparticles without using any physical or chemical templates.

1.2. Electrodeposition

Figure 1.1 shows the schematic representation of the working electrode and electrolyte interface at equilibrium (*Figure 1.1a*) and during the steps of electrodeposition (*Figure 1.1b,c*). The concentration of the solvated cations (white balls) and anions (green balls) of the supporting electrolyte (SE) is much higher compared to the solvated metal ions (M_{aq}^{n+}, red balls). The water molecules (blue balls) assemble at the electrode-electrolyte interface in the form of a layer, which is known as Inner Helmholtz Plane (IHP). The blue background is the continuous aqueous phase, where few water molecules are represented to show the IHP and hydrated ions.

The solvated metal ions can approach the working electrode only up to Outer Helmholtz Plane (OHP). The metal ions, at the interface, are transformed to metal adatoms (M_{ad}) by the supply of electrons from the working electrode, which is kept at the overpotential η (*Figure 1.1b*). The M_{ad}s, situated on the working electrode, form a cluster on metal atoms (*Figure 1.1c*) and this cluster of metal ions is known as the nucleus.

The electrochemical potential (μ_s) of M^{n+} can be represented by *Eq. 1.1*.

$$\mu_s = \mu_s^0 + RT \ln a_s + ne\varphi_s \qquad (1.1)$$

where, μ_s^0 and a_s are the standard chemical potential and activity of M^{n+}, respectively. R and T are the universal gas constant and temperature in absolute scale, respectively. n and e are the charge of the metal ion and charge of an electron, respectively. Φ_s is the electric potential of the metal ions in the bulk of the solution.

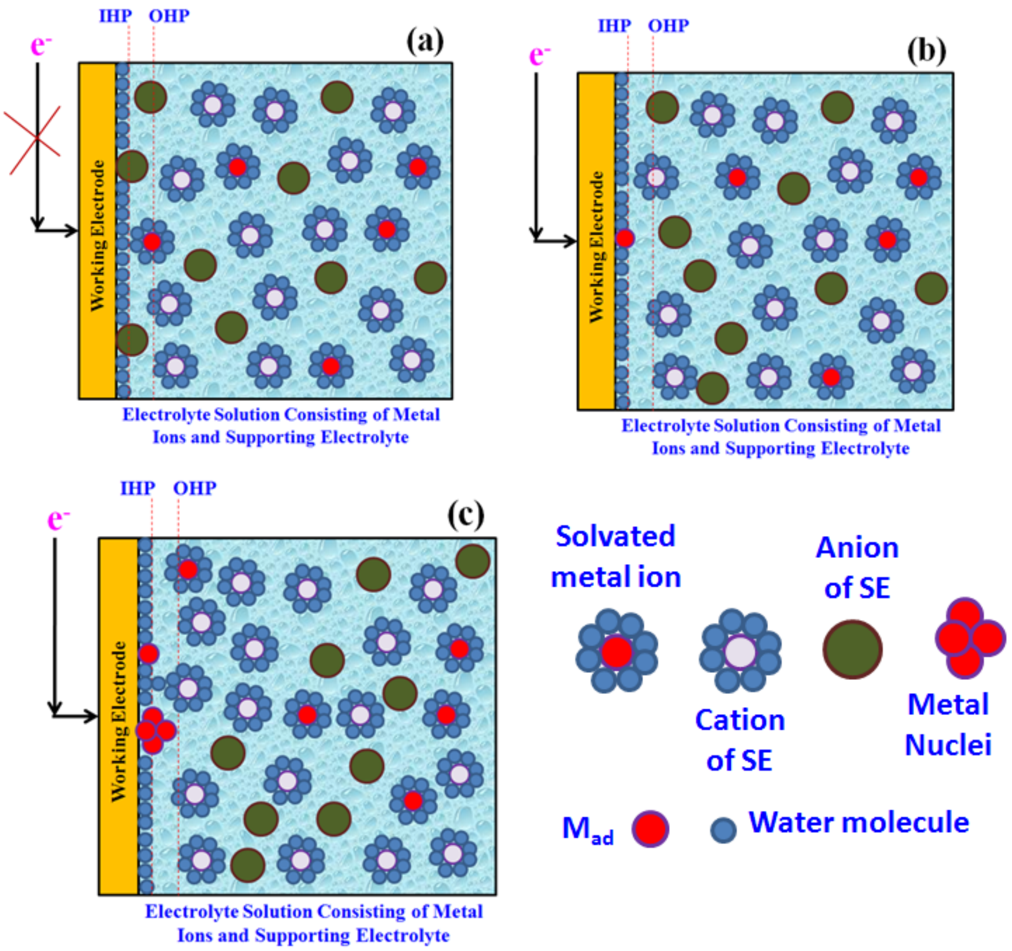

Figure 1.1 *The schematic representation of the working electrode electrolyte interface (a) at equilibrium, (b) at beginning of the birth of metal adatoms and during the nucleation (c). The blue background is the continuous aqueous phase, where a few water molecules are represented to show the IHP and hydrated ions.*

A three-electrode (i.e. working electrode, reference electrode and counter electrode) assembly is immersed into the solution to complete an electrochemical cell. If the electrochemical potential of the working electrode is changed without changing the activity of the metal ions in solution, then some metal ions get reduced to M_{ad} on the working electrode. The electrochemical potential (μ_{ad}) of the adatoms can be represented by *Eq. 1.2*.

$$\mu_{ad} = \mu_{ad}^{0} + RT\ln a_{ad} + ne\varphi_{ad} \tag{1.2}$$

where, μ_{ad}^{0} and a_{ad} are the standard chemical potential and activity of the adatoms, respectively. Φ_{ad} is the electric potential of the adatoms on the inert electrode. When the metal ions and the metal adatoms are in equilibrium, then $\mu_s = \mu_s^{\infty}$; $\mu_{ad} = \mu_{ad}^{\infty}$; $a_s = a_s^{\infty}$ and $a_{ad} = a_{ad}^{\infty}$. Therefore,

$$\mu_{s}^{\infty} = \mu_{ad}^{\infty} \tag{1.3}$$

and $$\varphi_{ad}^{\infty} - \varphi_{s}^{\infty} = \left[\frac{\mu_{s}^{0} - \mu_{ad}^{0}}{ne}\right] + \frac{RT}{nF}\ln\left[\frac{a_{s}^{\infty}}{a_{ad}^{\infty}}\right] \tag{1.4}$$

or $$E_{\infty} = E_{0}' + \frac{RT}{nF}\ln\left[\frac{a_{s}^{\infty}}{a_{ad}^{\infty}}\right] \tag{1.5}$$

where, E_{∞} represents the equilibrium potential difference between the M_{ad} and M^{n+}. E_{0}' represents the standard reduction potential of the metal. F is the Faraday's Constant.

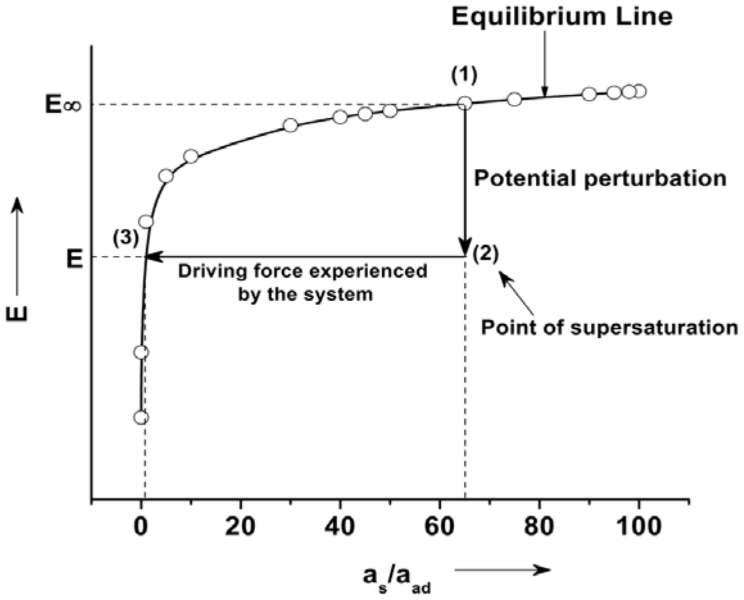

***Figure 1.2** Variation of the equilibrium potential of M^{n+} as a function of a_s/a_{ad} at constant T and P.*

The 'equilibrium line' of E_∞ vs. (a_s^∞/a_{ad}^∞) is shown in *Figure 1.2.* We assume that the equilibrium electrochemical cell, at the start of the experiment, is represented by position (1) in *Figure 1.2.* When the electrode potential is decreased to E ($E < E_\infty$) without changing the bulk concentration of M^{n+}; the system deviates from the 'equilibrium line' to a position (2), which is unstable at T. This situation is known as the 'supersaturation'. Therefore, to reach the 'equilibrium line', the system drives towards the position (3) by decreasing the a_s^∞ of M^{n+}. The driving force to decrease the activity of M^{n+} causes a first order phase transition at the working electrode, where the adequate amount of M^{n+} ions transform to M_{ad} by taking electrons from the working electrode (*Figure 1.1b*). This phenomenon is known as electrodeposition (*Eq. 1.6*)

$$M^{n+} + ne^- = M_{ad} \qquad (1.6)$$

The change in the chemical potential ($\Delta\mu$) of the cell during electrodeposition can be represented as *Eq. 1.7.*

$$\Delta\mu = nF(E_\infty - E) + RT\ln\left[\frac{a_{ad}^\infty}{a_{ad}}\right] \qquad (1.7)$$

Where, a_{ad} is the activity of M_{ad} at E. If we assume, for simplicity, that $a_{ad}^\infty = a_{ad} = 1$, then,

$$\Delta\mu = nF(E_\infty - E) \qquad (1.8)$$

$$\text{or} \quad \Delta\mu = -nF\eta \qquad (1.9)$$

where the overpotential (η) is defined as follows:

$$\eta = E - E_\infty \qquad (1.10)$$

Under this assumption, we can consider E_∞ as the open circuit potential (OCP) and it can be calculated by *Eq. 1.11*

$$OCP\ (E_\infty) = E'_0 + \frac{RT}{nF} \ln a_s \qquad (1.11)$$

Since, E < E_∞, thus electrodeposition occurs at the negative values of η. This type of electrodeposition is known as 'overpotential' deposition (OPD). Though, OPD is generally encountered for electrodeposition, but in some special cases, electrodeposition for at least monolayer or sub-monolayer level happens at potential E < E_∞. This type of electrodeposition is known as 'underpotential' deposition (UPD) as in this case electrodeposition occurs at the positive values of η. The electrodeposition of lead (Pb) on gold (Au) is an example of UPD *[46-63]*. The two criteria for UPD of Pb on Au are : (1) The binding energy for Pb-Au (-1.35 eV) is more negative than that for Pb-Pb (-0.897 eV) *[47]* and (2) The chloride ions (Cl^-) adsorb at the Au surface and they induce the adsorption of Pb(II) on Au through a ligand (Cl^-) bridge *[46,48]*. The general mechanism of UPD can be explained by *Eqs. 1.12-1.15.*

$$S + nCl^- = [S\text{-}nCl]^{n-} \qquad (1.12)$$

$$[S\text{-}nCl]^{n-} + M^{n+} = [S\text{-}nCl\text{-}M] \qquad (1.13)$$

$$[S\text{-}nCl\text{-}M] = [S\text{-}M\text{-}nCl] \qquad (1.14)$$

$$[S\text{-}M\text{-}nCl] + ne^- = S\text{-}M + nCl^- \qquad (1.15)$$

where, S represents the inert substrate and Cl^- acts as a bridging ligand.

The electrodeposition, in general, involves a couple of sequential processes (*Figure 1.3*): (1) transfer of hydrated metal ion from the bulk of the solution to the OHP near the working electrode by diffusion *[Note: The convection and migration modes of mass transfer are ignored in quiescent aqueous solution having excess (concentration more than 100 times compared to the metal ions) SE]*, (2) stripping off the water molecule from the hydrated metal ion to produce naked metal ion near the IHP, (3) transfer of electron from the working electrode to the naked metal ion forming metal adatom, and (4) attachment of the metal adatoms to form metal nuclei. The η for OPD is mainly contributed by the 'activation polarization' (η_a), which represents the height of the energy barrier of the electron transfer from the working electrode to the naked metal ion and 'concentration polarization' (η_c), which represents the limitation experienced for the electrochemical reduction because of the transport of ions from the bulk to the OHP.

Therefore, $\eta = \eta_a + \eta_c$ (1.16)

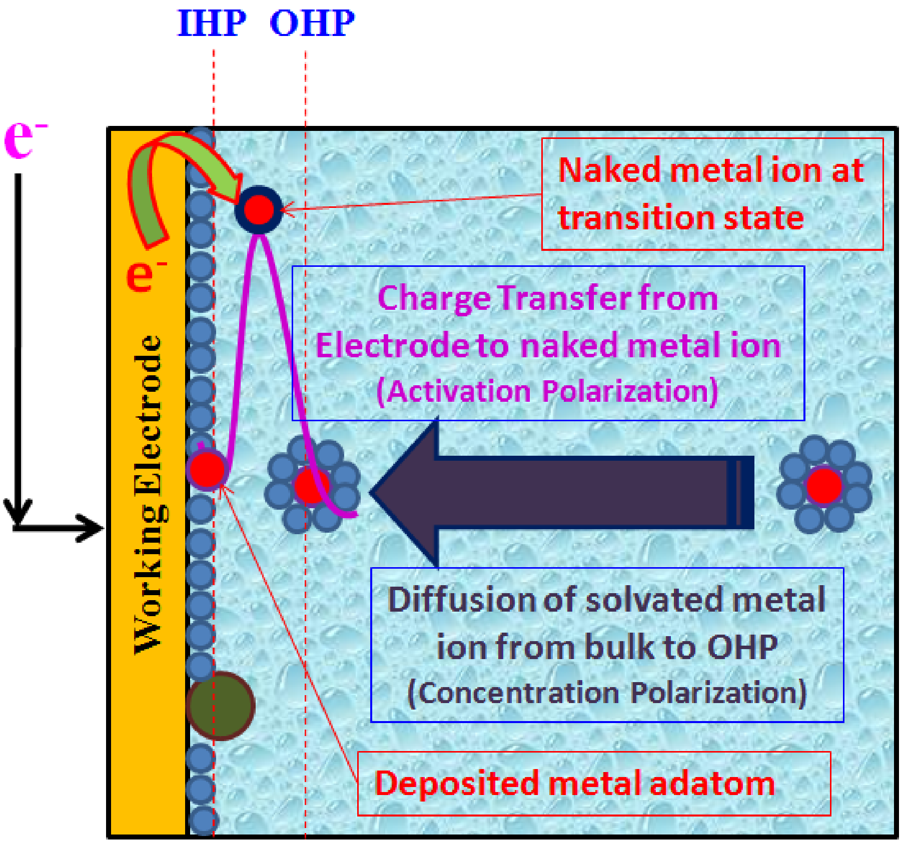

Figure 1.3 *The representation of the sequential processes of electrodeposition under the concentration and activation polarizations.*

1.3. Electrochemical Nucleation and Growth

The closely spaced metal adatoms join together on the electrode surface to form metal nuclei and this process is known as electrochemical nucleation. Once the nuclei are formed, they grow by the continuous attachment of the metal adatoms to the existing nuclei and this process is known as growth. The electrochemical nucleation and growth is the most important stage of electrosynthesis to control the size, shape, size distribution of the metal nanoparticles.

It was shown in the previous section that, for an overpotential η, a thermodynamic driving force exists for the transformation of $N^{'}M^{n+}$ ions to a metal nucleus of $N^{'}$ atoms. However, the nucleation is not a spontaneous process. A thermodynamic energy barrier, known as 'nucleation work' ($\Delta G(N^{'},\eta)$), guides the formation of new nucleus on the electrode surface (*Eq. 1.17&1.18*) *[64-70]*

$$\Delta G(N,\eta) = -N'\Delta\mu + \varphi(N) \qquad (1.17)$$

or $$\Delta G(N,\eta) = N'nF\eta + \varphi(N) \qquad (1.18)$$

The first term of *Eqs. 1.17 and 1.18* is negative, since it represents the energy gained by transforming N metal ions from higher electrochemical potential to $N^{'}$ adatoms at lower electrochemical potential. However, the second term of *Eqs. 1.17 and 1.18* is positive, because it represents the total excess energy in creating the new interfaces (nucleus-electrode and nucleus-solution interfaces) during nucleation.

The nuclei can have either two-dimensions (2D, i.e. disc like) or three-dimensions (3D, i.e. particle like). However, discussion will be restricted only to the 3D nuclei, because no 2D nuclei formation was encountered in the present study.

The variation of $\Delta G(N,\eta)$ with respect to $N^{'}$ and η can be described by (1) classical nucleation theory and (2) atomistic nucleation theory.

1.3.1. Classical Nucleation Theory

The classical theory assumes φ($N^{'}$) to be a continuous function of $N^{'}$. This assumption is macroscopically valid for the large cluster. Consider the formation of a 3D heterogeneous spherical cap nucleus of radius of curvature R' on the electrode (*Figure 1.4*). The contact angle of the nucleus with the substrate is $\theta^{'}$. The specific surface energies of the nucleus, substrate and nucleus-substrate interface are σ, σ_S and σ_i, respectively. Therefore, the actual volume (V_n) of the nucleus should be

$$V_n = \frac{1}{3}\pi R'^3[2 - 3\cos\theta' + cos^3\theta'] \tag{1.19}$$

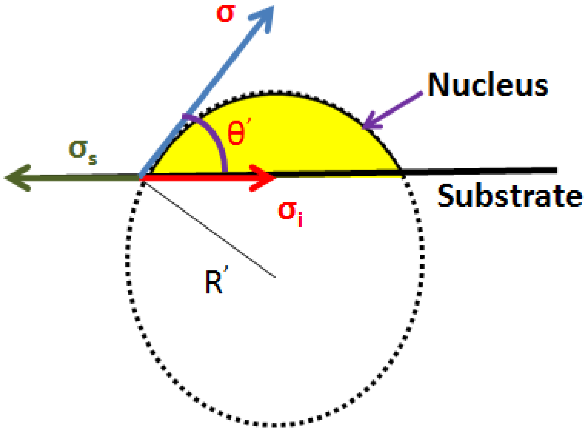

Figure 1.4 *3D heterogeneous spherical cap nucleus of radius of curvature R' formed on the electrode (Substrate).*

Figure 1.5a shows the continuous variations of (i) $N^{'}\Delta\mu$, (ii) φ($N^{'}$) and (iii) nucleation energy as a function of $N^{'}$ at constant overpotential η. Since ΔG($N^{'}$,η) is a continuous function of $N^{'}$, and, therefore, it is a differentiable function. The size of the nucleus having a maximum nucleation work is known as the critical nucleus ($N^{'}_c$) and the maximum nucleation work is known as critical energy (ΔG_{Crit}). Therefore, one can write that

$$\left[\frac{d(\Delta G(\eta,N\prime))}{dN}\right]_{\eta,N\prime=N\prime_c} = 0 \tag{1.20}$$

For 3D heterogeneous spherical cap critical nucleus, r = r_c and thus,

$$\Delta G_{Crit} = \frac{16\pi\sigma^3 M^2}{3n^2\rho^2F^2\eta^2}\mathrm{f}(\theta') \tag{1.21}$$

$$\text{where, } f(\theta) = \frac{1}{4}[2 - 3\cos\theta' + \cos^3\theta'] \tag{1.22}$$

$$r_c = \frac{2\sigma M}{\rho n F\eta} \tag{1.23}$$

$$\mathrm{N}'_c = \frac{32\pi\sigma^3 M^2}{3n^3\rho^3F^3\eta^3}\mathrm{f}(\theta') \tag{1.24}$$

Therefore, r_c is independent of the contact angle (*Eq. 1.23*). Further ΔG_{Crit}, N'_c and r_c decrease with increasing η (*Eqs. 1.21, 1.23, 1.24*). *Figure 1.5b* shows the nucleation work for three η, where $\eta_3 > \eta_2 > \eta_1$.

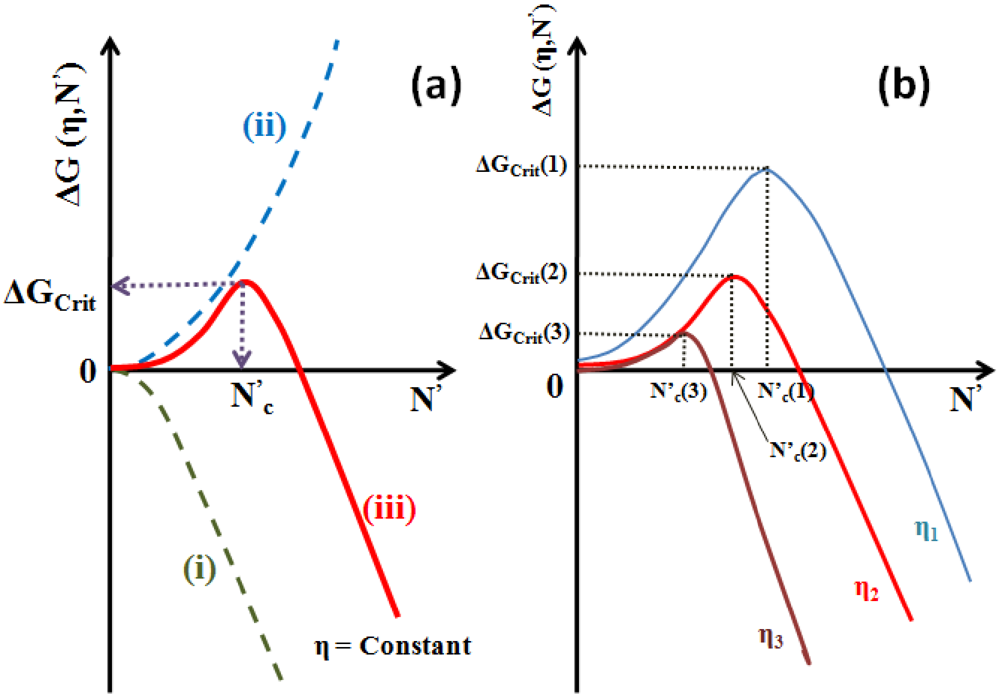

Figure 1.5 *(a) (i) NΔμ and (ii) φ(N) and (iii) nucleation energy as a function of N at constant overpotential η. (b) the nucleation energies at three different η, where $\eta_3 > \eta_2 > \eta_1$.*

1.3.2. Atomistic Nucleation Theory

This theory assumes that $\Delta G(N^{'},\eta)$ can not be a continuous function of $N^{'}$ for small size of nuclei. The $\Delta G(N^{'},\eta)$ versus $N^{'}$ relationship is not a fluent curve but displays minima and maxima, depending on the structure and energy state of the cluster (*Figure 1.6*). The highest maximum at a given supersaturation corresponds to the critical nucleus size.

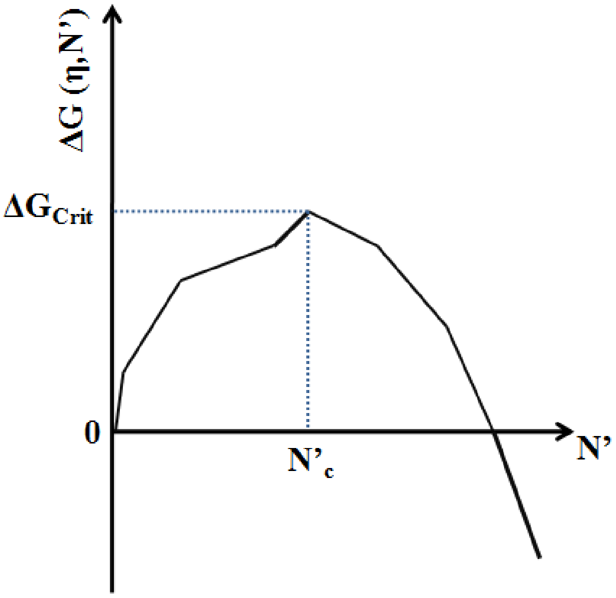

Figure 1.6 *The atomistic approach of the nucleation energy, $\Delta G(\eta,N)$ as a function of N at constant overpotential η.*

1.3.3. Kinetics of Nucleation

The nucleation work, ΔG_{Crit}, is a measure of the thermodynamic barrier, which has to be overcome in order to transform $N^{'}_{c}$ number of M^{n+} ions from the electrolyte solution into a nucleus of atoms $N^{'}_{c}$ on the electrode surface. Any nucleus of $N^{'} < N^{'}_{c}$, will be dissolved into the solution. The probability of the formation of nuclei can be expressed by *Eq. 1.25*:

$$a = A_j \exp\left(-\frac{\Delta G_{Crit}}{k_B T}\right) \qquad (1.25)$$

Where, 'a' is the rate of nucleation (number of nuclei cm^{-2} s^{-1}), A_J is the proportionality constant. Since, ΔG_{Crit} is inversely proportional to the square of η (Eq. 20), thus the rate of nucleation increases significantly with increasing η.

Therefore, we can derive the relation (*Eq. 1.26*) between 'a' and η for 3D heterogeneous nucleation by *Eqs. 1.21-1.25*.

$$\frac{d \ln a}{d|\eta|} = -\frac{nF}{RT} N_c \qquad (1.26)$$

1.3.4. Energy State of the Electrode Substrate

In all the above sections, it was assumed that the working electrode is inert and it provides isoenergic surface for the nucleation. However, in reality, the working electrodes provide active sites (may be crystal defect, dislocation, scratches etc.) at the atomic level on the electrode surface. The active sites are bonded to the nuclei in such a way that the free energy of bond formation leads to a pronounced decrease in ΔG_{Crit}, so that the 'a' at these sites is considerably higher than at the surrounding locations. The theoretical models of electrocrystallization are developed on the time-dependent variation of the active sites under the electrodeposition condition.

The total number of active sites (N_0, cm^{-2}) represents the theoretically possible maximum number density of nuclei on an electrode. The number of nuclei at time 't' is represented by N (cm^{-2}). Therefore, the nucleation rate law will be

$$\frac{dN}{dt} = a(N_0 - N) \qquad (1.27)$$

If we assume, N = 0 at t = 0 (i.e. at the start of the nuclei), then the integration leads to

$$N = N_0[1 - \exp(-at)] \tag{1.28}$$

The *Eq. 1.28* is the general rate law of the number density of nuclei on the electrode surface at any time t. The value of ‘a’ will have two limiting cases:

Case-I : Instantaneous Nucleation

If ‘at’ is very large for very high rate of nucleation (i.e. high ‘a’ value), then *Eq. 1.27* can be expressed by a delta function of ‘t’ i.e.,

$$\frac{dN}{dt} = N_0\delta(t) \tag{1.29}$$

where, $\delta(t) = 1$ at $t = 0$ and $\delta(t) = 0$ for $t > 0$.

Therefore, $N = N_0 \int_0^t \delta(t)dt$ (1.30)

and $N = N_0$ (at $t > 0$) (1.31)

Therefore, at very fast rate of nucleation, the maximum number of nuclei is formed virtually immediately after the start of the perturbation from the equilibrium. This type of nucleation is known as ‘instantaneous nucleation’ (*Figure 1.7a*).

Case-II : Progressive Nucleation

If ‘at’ is very small for very slow rate of nucleation (i.e. small ‘a’ value), then *Eq. 28* can be expressed by *Eq. 1.32.*

$$N = N_0at \tag{1.32}$$

As. $[\exp(-x) \approx (1 - x)]$; (for small value of x)

Therefore, $\frac{dN}{dt} = aN_0$ (1.33)

In this case, the number of nuclei grows with time and this type of nucleation is known as ‘progressive nucleation’ (*Figure 1.7b*).

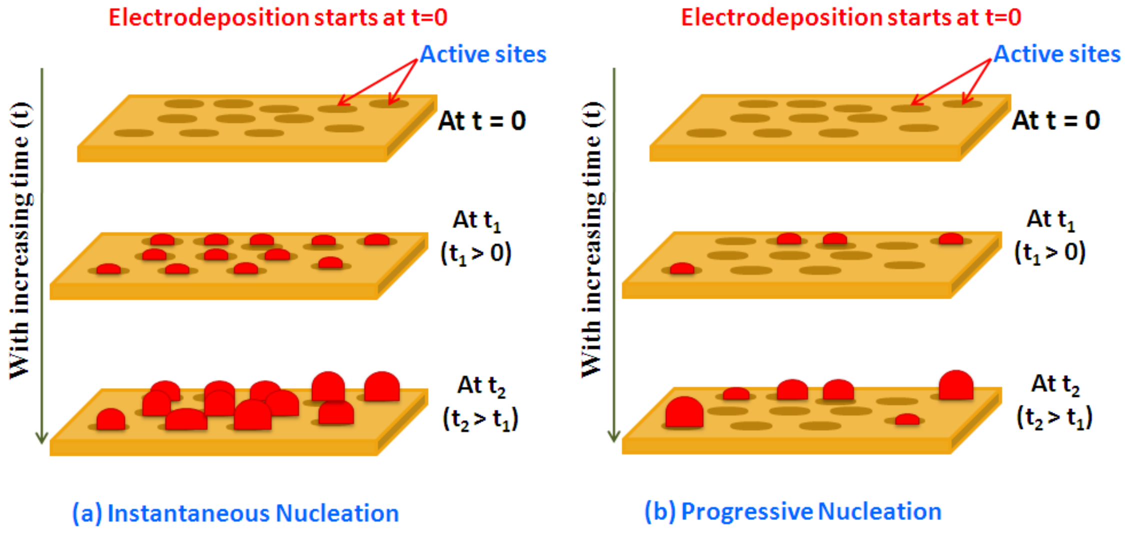

(a) Instantaneous Nucleation (b) Progressive Nucleation

Figure 1.7 *The schematic representation of (a) instantaneous and (b) progressive nucleations.*

1.4. Electrochemical Nucleation and Growth Models for Electrodeposition at Constant Potential

Let us assume that an isolated hemispherical nucleus of radius ‘r’ is growing under the linear diffusion flux of the metal ions M^{n+} (*Figure 1.8*). Then the current i can be expressed as:

$$i = nFk''A \tag{1.34}$$

Where, n is the charge transfer during the deposition, F is the Faraday’s constant (C mol^{-1}), k'' is the lattice incorporation rate constant (mol cm^{-2} s^{-1}), ‘A’ is the surface area of the hemispherical nucleus (cm^2). Here we assume that the coulombic efficiency of the electrodeposition is 100%, i.e. the charge transfer to the electrode is solely responsible for the deposition of new phase on the electrode. Then, current ‘i’ should be equal to the rate of growth of the nucleus. Therefore,

$$i = \frac{nF\rho}{M}\frac{dV}{dt} \qquad (1.35)$$

Where, ρ and V are the density and volume of the deposited phase, respectively, of molecular weight M. For hemispherical nucleus of radius r,

$$A = 2\pi r^2 \qquad (1.36)$$

and $V = \frac{2}{3}\pi r^3$ (1.37)

From *Eqs. 1.36 and 1.37*, we can get,

$$\frac{dV}{dt} = A\frac{dr}{dt} \qquad (1.38)$$

From *Eqs. 1.34, 1.35, 1.38* we can get,

$$\frac{dr}{dt} = \frac{Mk''}{\rho} \qquad (1.39)$$

If we assume that r = 0 at t = 0, then from *Eq. 1.39* we get

$$r = \frac{Mk''t}{\rho} \qquad (1.40)$$

From *Eqs. 1.34, 1.36, 1.40*, we get

$$i = \frac{2nF\pi M^2 k''^3}{\rho^2} t^2 \qquad (1.41)$$

Therefore, the current for growth of an isolated hemispherical nucleus is proportional to the square of the time from the birth of the nucleus *[71]*.

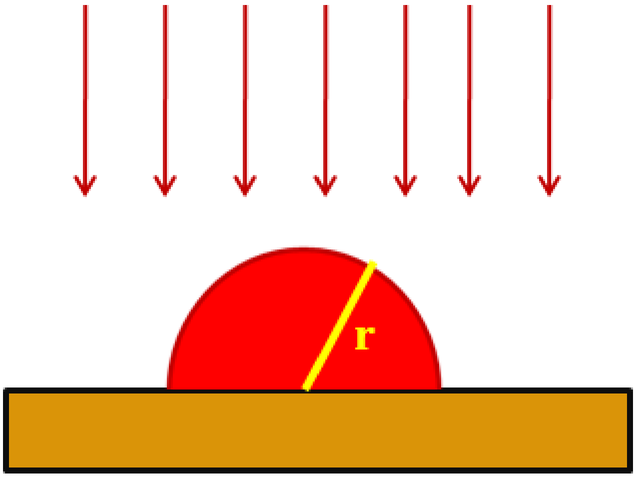

Figure 1.8 *The schematic representation of the growth of a hemispherical nucleus under the control of linear diffusion of metal ions from the bulk of the solution.*

The concentration of M^{n+} at the surface of the nucleus is governed by the Nernst equation (*Eq. 1.42*):

$$\frac{C_M}{C_M^*} exp\left[\frac{-(\alpha-1)nF\eta}{RT}\right] = \frac{C^0_{M^{n+}}}{C^*_{M^{n+}}} \exp\left[\frac{-\alpha nF\eta}{RT}\right] \qquad (1.42)$$

where, C_M and C^*_M are the concentrations of the M_{ad} at η and E_∞, respectively. C^0_{Mn+} and C^*_{Mn+} are the concentrations of M^{n+} at the surface and in the bulk, respectively. Therefore,

$$C^0_{M^{n+}} = C^*_{M^{n+}}\left[\frac{C_{Ag}}{C^*_{Ag}}\right] \exp\left[\frac{nF\eta}{RT}\right] \qquad (1.43)$$

For electrodeposition, η is negative. Therefore, the surface concentration of M^{n+} becomes effectively zero just after the application of η. Therefore, current ‘i’ is governed by the transport of M^{n+} by linear diffusion to the surface of the nucleus. Therefore,

$$i = nFAC^0_{M^{n+}}\sqrt{\frac{D}{\pi t}} \qquad (1.44)$$

Where, D is the diffusion coefficient of the metal ions. From *Eqs. 1.35, 1.38, 1.44*, we can get

$$r = \frac{2MC^0_{M^{n+}}}{\rho}\sqrt{\frac{Dt}{\pi}} \qquad (1.45)$$

From *Eqs. 1.34, 1.41 and 1.45* we get,

$$i = \frac{8nFM^2C^0_{M^{n+}}D^{\frac{3}{2}}}{\pi^{\frac{1}{2}}\rho^2}t^{\frac{1}{2}} \qquad (1.46)$$

Therefore, the current responsible for the growth of the single hemispherical nucleus under the linear diffusion flux of metal ions is proportional to the square-root of time *[72]*. Practically, many nuclei form on the electrode depending on the rate of nucleation (Section 1.3.4). Therefore, nucleation and growth occur simultaneously and the total current is given by *Eq. 1.47*.

$$i = \int_0^t i(u)\left[\frac{\partial N}{\partial t}\right]_{t-u} du \qquad (1.47)$$

Where, u is the age of the nucleus. Therefore, from *Eqs. 1.29, 1.33, 1.46 and 1.47*, we can get for 'instantaneous nucleation'

$$i = \frac{8nFM^2C^0_{M^{n+}}D^{\frac{3}{2}}N_0}{\pi^{\frac{1}{2}}\rho^2}t^{\frac{1}{2}} \qquad (1.48)$$

And for 'progressive nucleation'

$$i = \frac{16nFM^2C^0_{M^{n+}}D^{\frac{3}{2}}aN_0}{3\pi^{\frac{1}{2}}\rho^2}t^{\frac{3}{2}} \qquad (1.49)$$

The assumption of linear diffusion of metal ions was challenged by Hills et al. *[73]* and they modified the *Eq. 1.44 by Eq. 1.50* on the basis of spherical diffusion (*Figure 1.9*).

$$i = \frac{nFAC^{0}_{M^{n+}}D}{r} \tag{1.50}$$

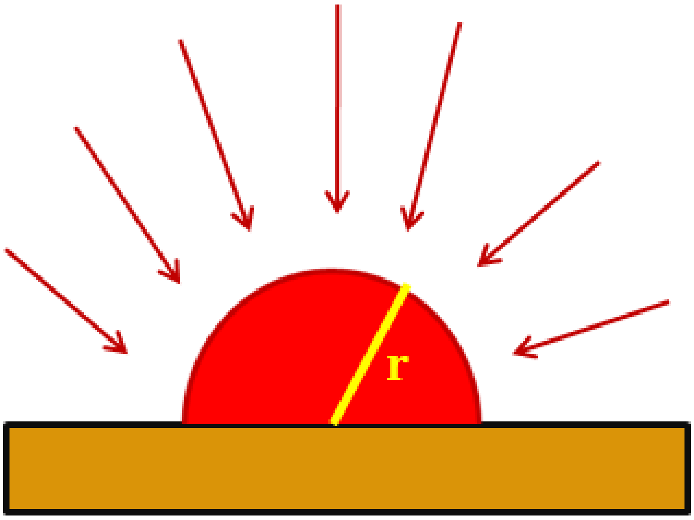

***Figure 1.9** The schematic representation of the growth of a hemispherical nucleus under the control of spherical diffusion of metal ions from the bulk of the solution.*

Performing treatment as similarly was done for *Eqs. 1.45 & 1.46*, we get

$$r = \sqrt{\frac{2DC^{0}_{M^{n+}}Mt}{\rho}} \tag{1.51}$$

and $$i = \frac{nF\pi\left(2DC^{0}_{M^{n+}}\right)^{\frac{3}{2}}M^{\frac{1}{2}}}{\rho^{\frac{1}{2}}}t^{\frac{1}{2}} \tag{1.52}$$

Therefore, the current for the nucleation and growth through hemispherical diffusion by ‘instantaneous nucleation’ is

$$i = \frac{nF\pi\left(2DC^{0}_{M^{n+}}\right)^{\frac{3}{2}}M^{\frac{1}{2}}N_{0}}{\rho^{\frac{1}{2}}}t^{\frac{1}{2}} \tag{1.53}$$

and for ‘progressive nucleation’ is

$$i = \frac{2nF\pi\left(2DC^0_{M^{n+}}\right)^{\frac{3}{2}} M^{\frac{1}{2}} aN_0}{3\rho^{\frac{1}{2}}} t^{\frac{3}{2}} \qquad (1.54)$$

Therefore, the initial (i.e., just after the application of pulse) current is proportional to $t^{1/2}$ and $t^{3/2}$ for instantaneous and progressive nucleations, respectively.

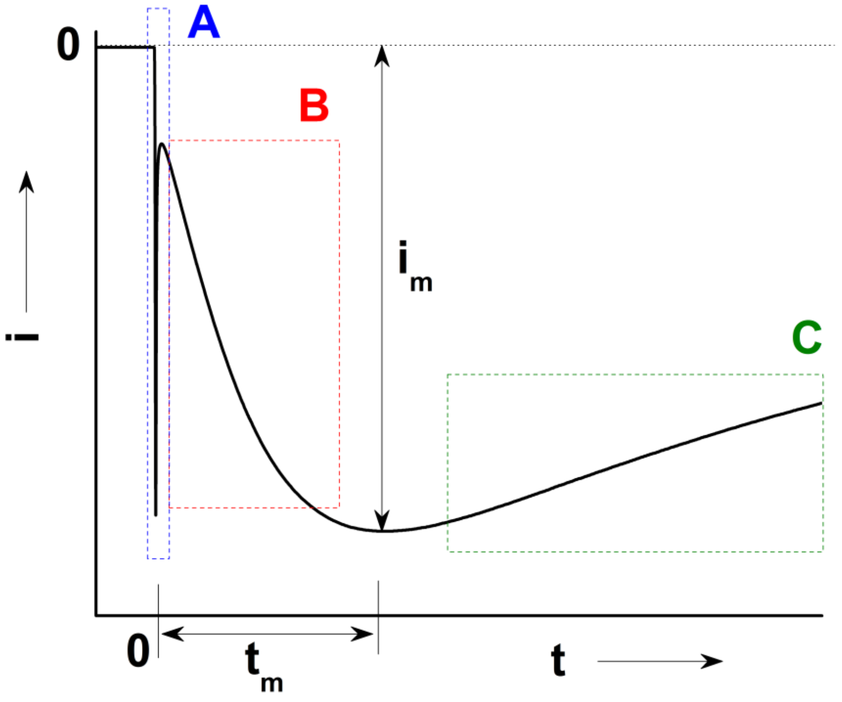

Figure 1.10 *The schematic representation of current transient for an electrodeposition after applying a constant overpotential pulse at t = 0. The cathodic current is negative.*

Figure 1.10 represents the current transient recorded for an electrodeposition experiment after applying a potentiostatic pulse at a fixed overpotential. The initial current decreases significantly at a time scales of 5-300 ms (Segment A), which is mainly attributed to the rearrangement of electrolyte species (ions/molecules) at the electrode-electrolyte interface. In the succeeding part of the transient, the current increases with time (Segment B) and passes through a maximum value followed by a steady decrease (Segment C). The subsequent rise in current corresponds to the increase in the overall electroactive area due to increase(s) in the number of nuclei and/or size of nuclei, as described by *Eq. 1.53 or 1.54 [74, 75]*. The spherical diffusion zone around each nucleus (*Figure 1.9*) grows with time. The overlap of neighboring diffusion zones (*Figure 1.11*) is responsible for the current maxima ($i = i_m$) at $t = t_m$ (*Figure 1.10*). At the time corresponding to the current maxima, the spherical diffusion zones overlap and mass transfer becomes linear (*Figure 1.11*). The change in diffusion regime leads to a decrease in the current with increasing time obeying Cottrell equation (Segment C in *Figure 1.10*).

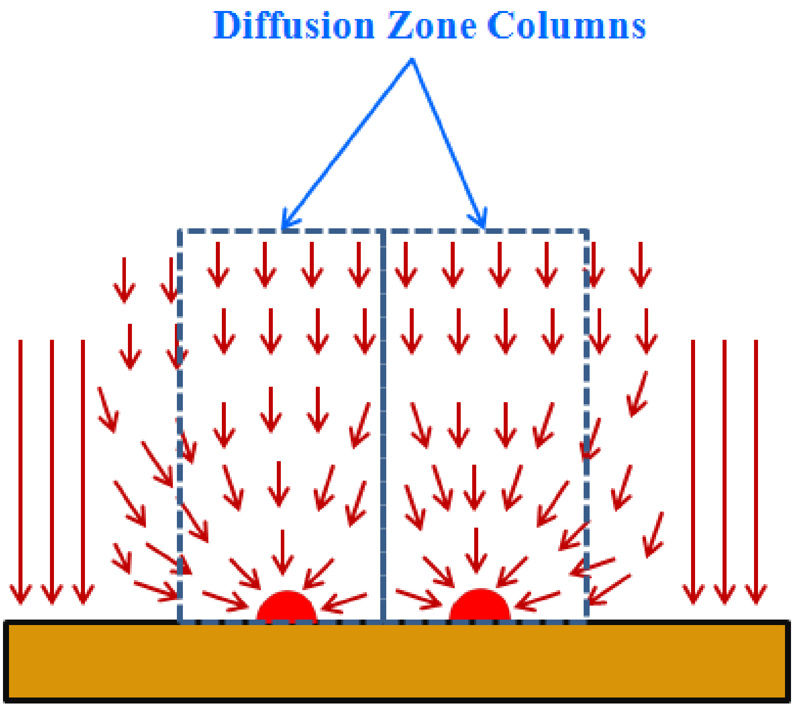

Figure 1.11 *The schematic representation of the growth of the diffusion flux and transformation from the radial to linear diffusion flux. The diffusion zone column represents the effective boundary between the adjacent columns.*

Scharifker and Hills (SH) simplified the above situation by (1) assuming that the overlap of neighboring diffusion zone columns is equivalent to the overlap of the circular patches on the electrode surface and (2) calculating the overall current by considering only the linear diffusion. The first simplification was adopted from the Avrami's theory for kinetics of phase change *[76, 77]*. *Figure 1.12* represents the circular patches on the working electrode originating from the projection of the diffusion zone columns on the electrode surface. The growth of the 3D nucleus with time increases the radius of its diffusion zone column. Thus, the radius of its patch on the electrode surface also increases with time. Under this condition, the growth current is expressed in terms of linear diffusion to the fraction of the electrode area contained within the circular perimeter of the growing diffusion zone.

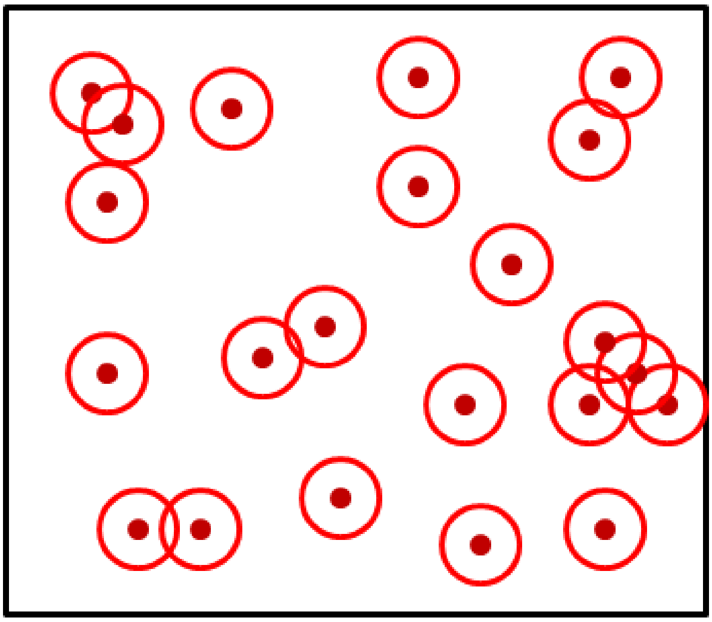

Figure 1.12 *The schematic representation of the distribution of the circular patches of the diffusion zone columns of each nucleus.*

The radial velocity (δ_t) of the circular patch along the electrode is expressed by *Eq. 1.55*.

$$\delta_t = \sqrt{kDt} \qquad (1.55)$$

Where, k is a material constant determined by the conditions of the experiment. The planar area (A_t) of a single diffusion zone at time t is expressed by *Eq. 1.56*.

$$A_t = \pi\delta_t^2 = \pi kDt \qquad (1.56)$$

If immediately following time t = 0, the nuclei number density becomes N (cm^{-2}), then at time t, assuming no overlap, the fraction of the area covered by diffusion zones is θ_{ex}.

$$\theta_{ex} = N\pi kDt \qquad (1.57)$$

Since, the nuclei are randomly distributed on the electrode (*Figure 1.12*), thus there will be overlap and the actual fraction of area (θ) covered by diffusion zone is adopted from the Avrami's theorem.

$$\theta = 1 - exp(-\theta_{ex}) \qquad (1.58)$$

Therefore, the radial flux density of metal ions through the boundaries of the diffusion zones will be given by the equivalent planar diffusion of metal ions to θ. Therefore,

$$i = \frac{nFC^*D^{\frac{1}{2}}\theta}{\pi^{\frac{1}{2}}t^{\frac{1}{2}}} = \frac{nFC^*D^{\frac{1}{2}}}{\pi^{\frac{1}{2}}t^{\frac{1}{2}}}[1 - exp(-N\pi kDt)] \qquad (1.59)$$

Where, C^* is the bulk concentration of the metal ions. For shorter scale of time,

$$[1 - \exp(- N\pi kDt)] \approx N\pi kDt; \quad (\text{for } t \rightarrow 0) \qquad (1.60)$$

For 'instantaneous nucleation', thus $N = N_0$

$$i = nFC^*N_0kD^{\frac{3}{2}}\pi^{\frac{1}{2}}t^{\frac{1}{2}} \qquad (1.61)$$

Comparing *Eqs. 1.53 and 1.61*, we get

$$k = \sqrt{\frac{8\pi C^*M}{\rho}} \qquad (1.62)$$

For 'progressive nucleation', thus $N = aN_0t$

$$i = \frac{2nFC^*D^{\frac{1}{2}}}{\pi^{\frac{1}{2}}t^{\frac{1}{2}}}\left[1 - exp\left(-\frac{aN_0\pi k'Dt^2}{2}\right)\right] \qquad (1.63)$$

Assuming $aN_0t \rightarrow 0$ and comparing *Eqs. 1.54 and 1.63*, we get

$$k' = \frac{4}{3}\sqrt{\frac{8\pi C^* M}{\rho}} \tag{1.64}$$

According to SH model, the *Eqs. 1.59 and 1.63* describe the current transients for the instantaneous and progressive nucleations, respectively *[78, 79]*. The current transients, in practice, are presented by the dimensionless form by plotting $(i/i_m)^2$ vs. t/t_m (*Figure 1.13*). The dimensionless plot of SH model is used for the diagnostic evaluation of potentiostatic current transients for 3D nucleation with diffusion controlled growth.

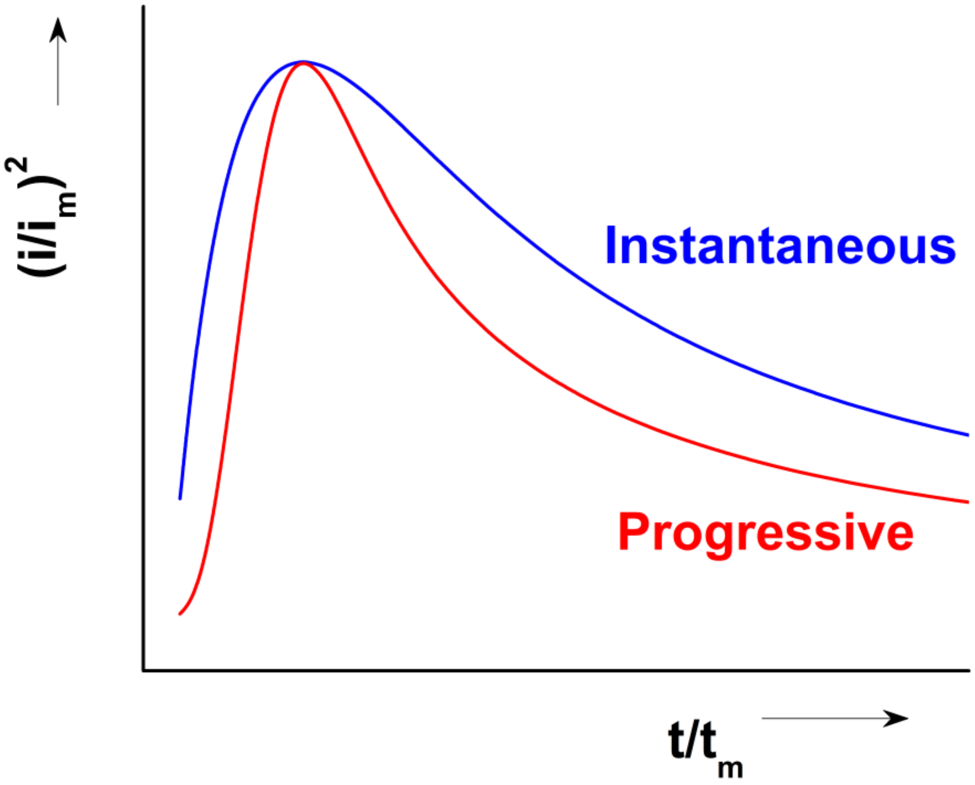

***Figure 1.13** The dimensionless plots of SH-model for the potentiostatic current transients for 3D nucleation with diffusion controlled growth under the instantaneous and progressive nucleations.*

For instantaneous nucleation,

$$\left(\frac{i}{i_m}\right)^2 = \frac{1.9542}{\left(\frac{t}{t_m}\right)}\left\{1 - exp\left[-1.2564\left(\frac{t}{t_m}\right)\right]\right\}^2 \qquad (1.65)$$

For progressive nucleation,

$$\left(\frac{i}{i_m}\right)^2 = \frac{1.2254}{\left(\frac{t}{t_m}\right)}\left\{1 - exp\left[-2.3367\left(\frac{t}{t_m}\right)^2\right]\right\}^2 \qquad (1.66)$$

For progressive nucleation, the fractional area left uncovered continuously decreases with the growth of the diffusion zones. Therefore, an exclusion zone for the further nucleation is always developed around an already nucleated center and new nuclei will only form on parts of the electrode surface uncovered by diffusion zones. The saturation number density (N_s) of nuclei is given by *Eq. 1.67.*

$$N_S = \sqrt{\frac{aN_0}{2k'D}} \qquad (1.67)$$

Several efforts have been made to eliminate the analysis of two separate cases (i.e. instantaneous and progressive nucleation) by establishing a general model of electrochemical nucleation. Three general models namely Scharifker and Mostany (SM) *[80-82]*; Sluyters-Rehbach, Wijenberg, Bosco and Sluyters (SRWBS) *[83]* and Heerman and Tarallo (HT) *[84-87]* have been employed in the literature. They have been established from the same nucleation law and Avrami's theorem used in the SH model, but with different assumptions on the heights of the diffusion zone columns around the nuclei with time. The major assumptions and related equations of these models are given in *Table 1.1.*

Table 1.1 *The prime assumption, equations and limitations of SM, SRWBS and HT models.*

SM	Prime assumption	The height of the diffusion zone column starts to grow from the moment that the nucleus is born.
	Equations	$j = j_0 \exp(-\tau t) + \frac{zFCD^{\frac{1}{2}}}{\sqrt{(\pi t)}}[1 - \exp(-N_0 \pi k' D \theta t)]$ (1.68) $\theta = 1 - \left[\frac{1 - \exp(-at)}{at}\right]$ (1.69)
	Limitations	It does not predict the correct current density at very short time scale.
SRWBS	Prime assumption	The heights of all diffusion zone columns are equal irrespective of the age of the individual nucleus. The time as well as the height I calculated from the birth of the very first nucleus.
	Equations	$j = j_0 \exp(-\tau t) + \frac{zFCD^{\frac{1}{2}}}{\sqrt{(\pi t)}}[1 - \exp(-N_0 \pi k' D \varphi t)]$ (1.70) $\varphi = 1 - \left[\frac{e^{-at}}{\sqrt{(at)}} \int_0^{\sqrt{(at)}} e^{\lambda^2} d\lambda\right]$ (1.71) $\varphi = 1 - \frac{1}{\sqrt{(at)}}\left[\frac{0.051314213 + 0.47910725\sqrt{(at)}}{1 - 1.2068142\sqrt{(at)} + 1.185724(at)}\right]$ (1.72)
	Limitations	It overestimates θ_{ex} with respect to SM model.
HT	Prime assumption	The height of the diffusion zone column should be a function not only of time but also of the nucleation rate constant i.e. the birth rate of the nuclei.
	Equations	$j = j_0 \exp(-\tau t) + \frac{zFCD^{\frac{1}{2}}}{\sqrt{(\pi t)}}\left[\frac{\varphi}{\theta}\right][1 - \exp(-N_0 \pi k' D \theta t)]$ (1.73) $\frac{\varphi}{\theta} = \frac{\left[0.520893(at) - 1.206814(at)^{\frac{3}{4}} + 1.185724(at)^2 - 0.051314\sqrt{(at)}\right]}{\left[\{at - 1 + \exp(-at)\}\left\{1 - 1.206814\sqrt{(at)} + 1.185724(at)\right\}\right]}$ (1.74)
	Limitations	It overestimates the current because of the inaccurate mass balance at individual diffusion zones born at different times.

1.5. Objective of This Thesis

The discussions in the previous section give the fundamentals of the current transient response for the electrochemical phase formation under a constant potential pulse. The different number and sequence of potentiostatic pulses have been employed to electrochemically synthesize metal micro- or nano- particles.

The most common electrochemical route for synthesis of nanoparticles is the single potentiostatic pulse, in which the working electrode is initially kept at the equilibrium with the aqueous solution of the metal salts and then a high cathodic constant overpotential is applied to deposit the nanoparticles. However, this methodology gives least control to the size, shape and morphology of the metal nanoparticles *[75, 88-91]*. Penner and Plieth introduced double potentiostatic pulse strategy to obtain narrow size distribution by uncoupling the nucleation and growth phenomena *[92-97]*. However, the size distribution of the deposited nanoparticles was not much improved. Adzic et al. developed a triple pulse strategy for electrochemically preparing metal nanoparticles. This pulse train consisted of a cathodic pulse to deposit metal nuclei, then an anodic pulse to dissolve them all, but a few, which then serve as sites for growth of metal nanoparticles in the third step *[98]*. However, it showed poor control over the particle size distribution of the metal nanoparticles.

Therefore, the prime objective of this thesis was to develop new pulse strategies for controlling the size, shape, material composition and size distribution of electrochemically synthesized metal nanoparticles without using any templating agent. The pulse strategies were developed after detailed investigation of the mechanism of the electrocrystallization for each electrode-metal-electrolyte system.

CHAPTER 2

Experimental

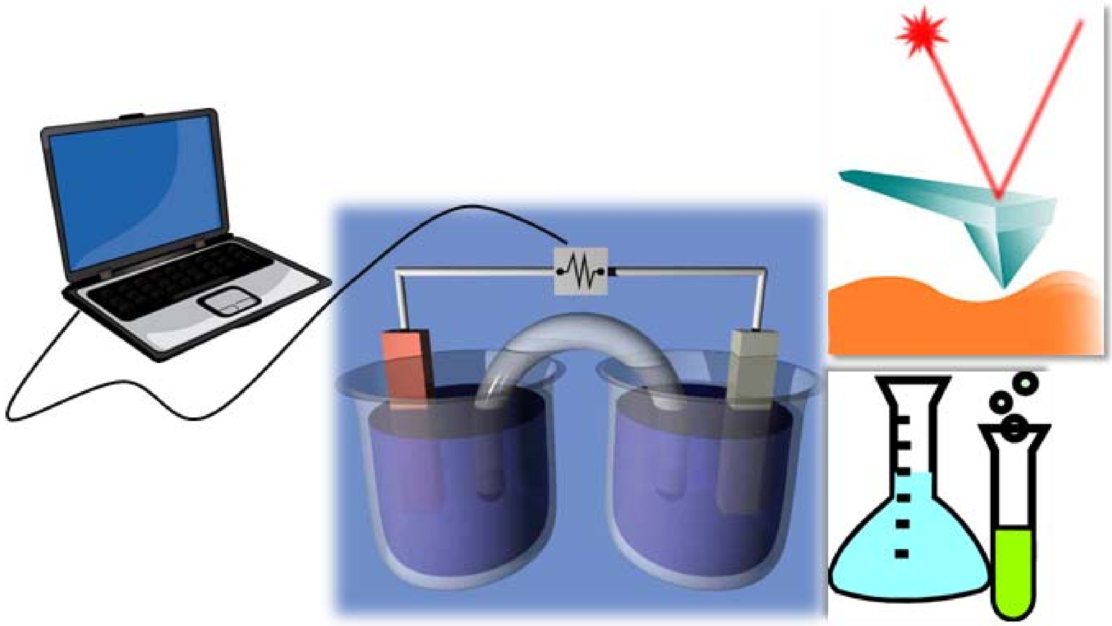

2.1. Electrochemical Instruments and Techniques

2.1.1. Instruments

2.1.1.1. Electrochemical Cell

The electrochemical cell is one in which the faradaic reaction takes place by the imposition of an external voltage. It consists of three electrodes viz. working electrode (WE), reference electrode (RE) and counter electrode (CE) immersed in the working solution. The electrodes are externally connected to an electrochemical workstation (EWS). The electrochemical experiments, unless specified, were performed with CHI-220 cell stand (*Figure 2.1a*). The glass vial was properly clamped and was filled with approximately 5 mL of the working solution. The electrodes were inserted into the glass vial through the channels shown in the top view of the cap. The electrochemical quartz crystal microbalance (EQCM) experiments were performed in a CHI-127 EQCM cell (*Figure 2.1b*) with approximately 2 mL of the working solution. The EQCM crystal was used as the working electrode. The RE and CE were inserted into the cell through the channels shown in the cap.

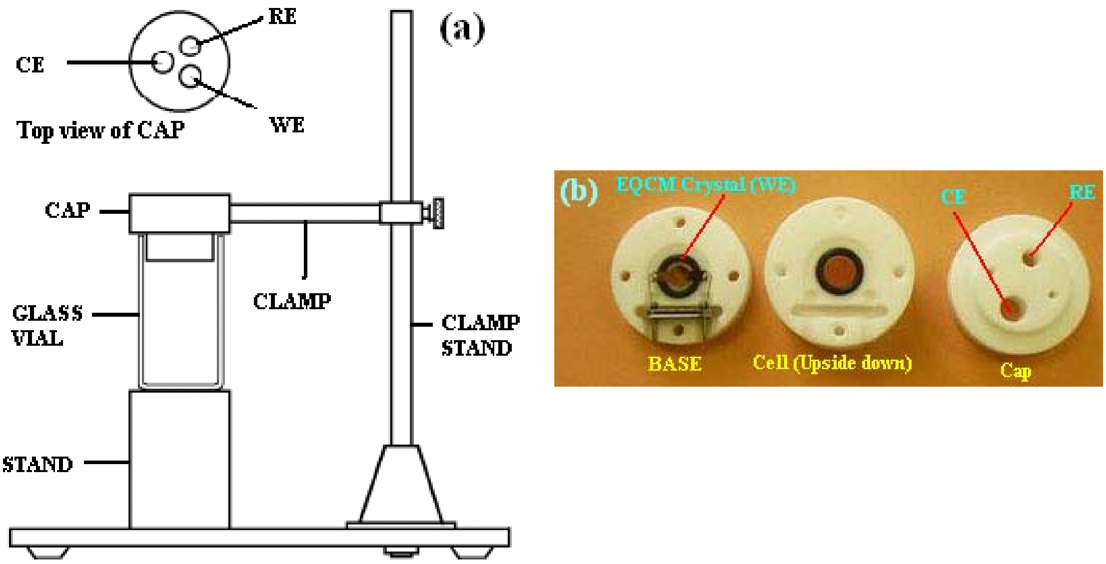

Figure 2.1 *(a) CHI-220 cell stand, (b) CHI-127 EQCM cell.*

2.1.1.2. Working Electrode (WE)

The electrochemical reaction of interest occurs at the WE. Therefore, WE is desired to be electrochemically inert to other reactions over a wide potential range of investigation. Further, the transfer of electrons from the WE to the electrolyte solution (in the absence of the reaction of interest) must be difficult and it needs the WE-electrolyte interface to be polarisable. Hence, the change in potential in the EWS (situated outside of the cell) induces a substantial build-up of excess charge at the WE-electrolyte interface and it indirectly synchronizes the potential of the WE-electrolyte interface to the applied potential from the EWS. Two types of electrode materials viz. gold (Au) and glassy carbon (GC) were used in the work.

Unless specified, three types of commercial working electrodes viz. (1) 2 mm diameter Au-WE (CHI-101); (2) 3 mm diameter GC-WE (CHI-101) and (3) Au crystal EQCM (Au-EQCM) (CHI-125A) were used in the electrochemical experiments.

Glassy carbon or vitreous carbon is prepared from copolymer resin (phenol-formaldehyde or furfuryl alcohol-phenol) via heat treatment (1000-3000° C) under pressure. It has high thermal stability as well as high resistance to chemical attack. The hardness, low density, low electrical resistance, low friction, low thermal resistance and impermeability to gases and liquids are other interesting properties of GC. The GC obtained from commercial suppliers contains conjugated sp^2-carbon with high proportion of fullerene related structures *[99]*.

2.1.1.3. Reference Electrode (RE)

Reference electrode (RE) is used as the reference point to measure the potential of the working electrode in an electrochemical cell. Therefore, the electrodes having well known and stable equilibrium electrode potential are chosen as the RE. The RE needs to provide non-polarisable electrode-electrolyte interface to stabilize the electrode potential at its equilibrium potential. The electron transfer reaction occurs easily across the interface of the RE. Therefore, the external potential source can not build up excess charge at the interface.

The electrochemical experiments were performed with two REs viz. (1) Silver/Silver Chloride [Ag/AgCl(saturated KCl)] (CHI-111) and (2) Mercury/Mercurous Sulfate [Hg/Hg_2SO_4(saturated K_2SO_4)] (CHI-151). The half-cell reactions of these REs and the equilibrium potentials (at 25° C) with respect to the Normal Hydrogen Electrode (NHE) are given in *Eqs. 2.1, 2.2*:*[100]*

$AgCl_{(s)} + e^- = Ag_{(s)} + Cl^-_{aq}$; $E_0 = 0.197$ V (2.1)

$Hg_2SO_{4(s)} + 2e^- = 2Hg_{(s)} + SO_4{}^{2-}{}_{aq}$; $E_0 = 0.640$ V (2.2)

Except chapter 5, all potentials are quoted with respect to Ag/AgCl(saturated KCl) RE. The potentials quoted in the chapter 5 are measured with respect to Mercury/Mercurous Sulfate [Hg/Hg_2SO_4(saturated K_2SO_4)] RE.

2.1.1.4. Counter Electrode (CE)

The electrical current of the electrochemical cell flows through the counter electrode (CE) or auxiliary electrode. CE along with the WE provides the circuit over which the cell current is either applied or measured. The potential of the auxiliary electrode is not measured and is adjusted so as to balance the reaction occurring at the working electrode. This configuration allows the potential of the WE to be measured against a known RE without compromising the stability of that RE by passing current over it. The platinum CE (CHI-115 and CHI-129) was used in the electrochemical experiments.

2.1.1.5. Electrochemical Workstation (EWS)

The electrochemical experiments were performed with the computer controlled electrochemical workstation (EWS) as shown in *Figure 2.2.* The computer controls the microcomputer of the EWS through specially designed software. The microcomputer generates complex digital waveforms depending on the type of experiments and those produce analog voltage and current to the potentiostat and galvanostat by digital-to-analog (DAC) converter. Then the electrochemical responses are recorded at the fixed time intervals by digitizing them by an analog-to-digital (ADC) converter. The microcomputer also controls the operation and signal processing of some additional modules such as EQCM, electrochemical impedance spectroscopy (EIS) etc. The EWS contains fast digital function generator, high speed data acquisition system, filters for the potential and the current signals, multiple secondary gain stages, potentiostat and galvanostat etc. Different EWS models provide different options. The EWSs such as CHI-440A, CHI-450B, CHI-760D and Autolab PGSTAT-30 were used at the various stages of the work.

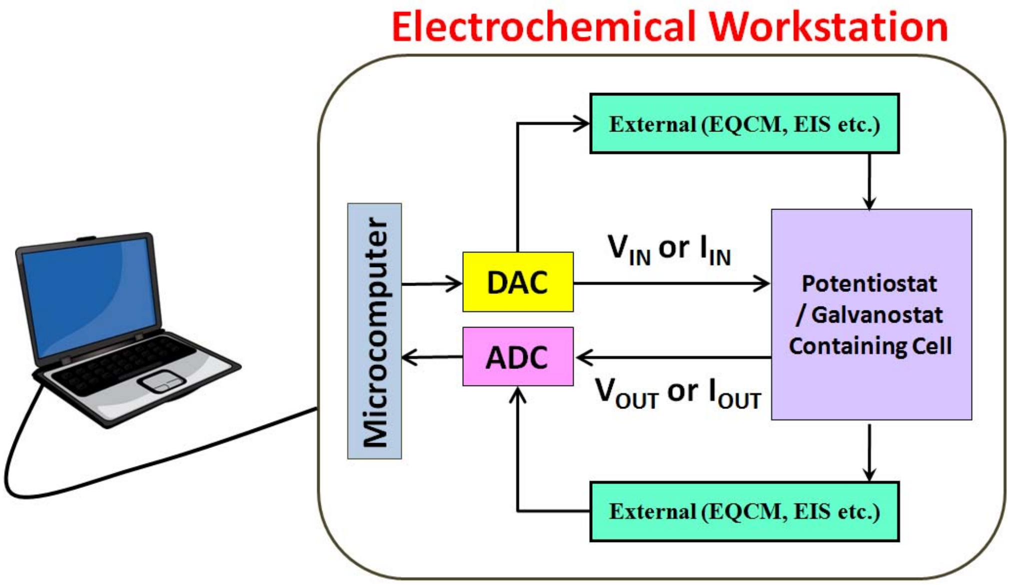

Figure 2.2 *Schematic representation of the EWS attached to a computer.*

Figure 2.3 shows the general configuration of a potentiostat, where A, B, C and D are the operational amplifiers (OPAMPs) with an open loop gain ranging from 10^4-10^8 *[100]*. The adder circuit generates complex voltage waveform (V_{IN}) by flowing current through the resistance (R_1) from the three voltage inputs (V_1, V_2 and V_3). Therefore,

$$V_{IN} = I_{IN}R_1 = R_1(I_1 + I_2 + I_3) = V_1 + V_2 + V_3 \quad (2.3)$$

The RE is connected to the input of a voltage follower, which gives the same output voltage (V_{VF}) as the input. The potential control amplifier amplifies the potential difference between the positive (or non-inverting) input (here it is virtually grounded) and the negative (or inverting) input (here V_{IN}). The "B" OPAMP is the booster. From this,

$$V_{VF} = - V_{IN} \text{ (vs. RE)} \quad (2.4)$$

and $$V_{OUT} = -G_AG_BV_{IN} \text{ (vs. RE)} \quad (2.5)$$

where, G_A and G_B are the gains of the OPAMPS "A" and "B", respectively.

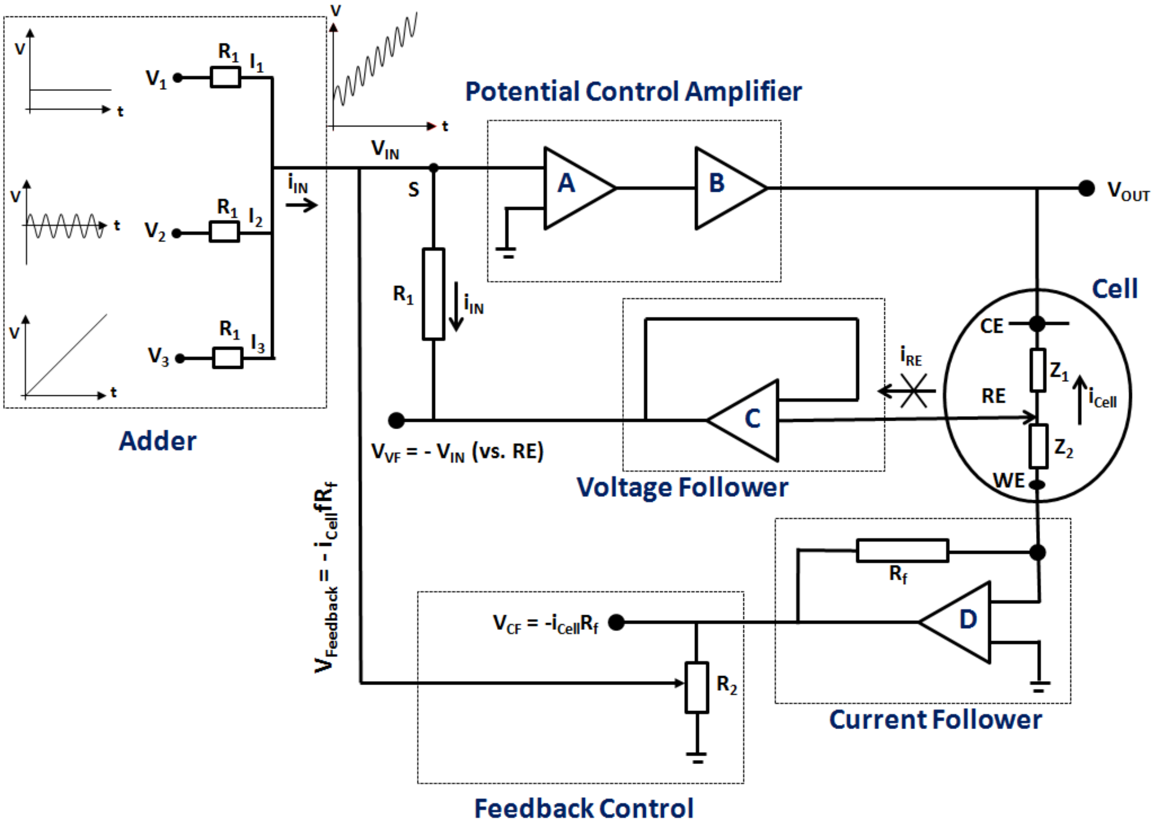

***Figure 2.3** Schematic representation of a potentiostat.*

The cell is composed of CE, RE, WE and two impedances viz. Z_1 and Z_2. No current flows through RE because of the high input impedance of "C" OPAMP. The current (i_{Cell}) flows between the CE and WE. The i_{Cell} flowing through the WE is converted to voltage (V_{CF}) for digitization by a current follower, where R_f is the feedback resistance of the current follower. Therefore,

$$V_{CF} = -i_{Cell}R_f \tag{2.6}$$

The i_{Cell} is a function of total cell impedance (Z) and the electrical equivalent circuit, known as Randle's electrical equivalent circuit, of a faradaic cell is shown in *Figure 2.4.*

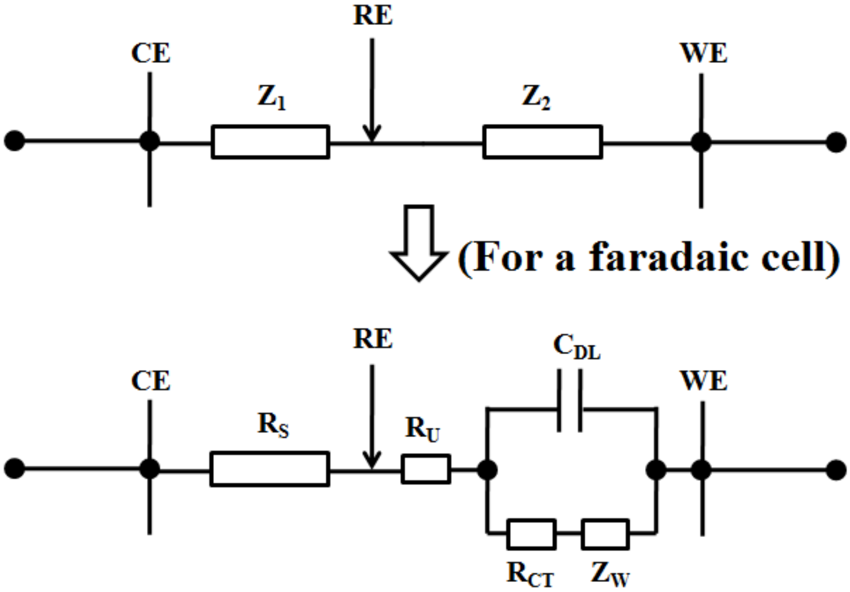

Figure 2.4 *Electrical equivalent circuit of a faradaic cell.*

The general cell components are arranged in series and thus

$$Z = Z_1 + Z_2 \tag{2.7}$$

For a faradaic cell, Z_1 represents the resistance (R_s) of the current flow through the solution (here we are neglecting the interfacial electrical equivalent components (EEC) of the CE).

$$Z_1 = R_s \tag{2.8}$$

The WE is virtually grounded and thus the potential control amplifier tunes the potential of the CE in order to keep the potential difference between the RE and the WE equal to the user-defined value i.e.;

V_{WE} (vs. RE) = $-V_{VF} = V_{IN}$ (2.9)

Further Z_2 has several EEC viz. C_{DL} and R_{CT}, which represent the capacitance and charge transfer resistance of the WE-solution interface, respectively. Z_W represents the impedance corresponding to the diffusion of the analyte from the bulk to the interface and it is commonly known as the Warburg impedance. In a real faradaic cell, the RE is always located at a distance relative to the WE. This means that an additional resistance, the uncompensated resistance, R_u, can never be eliminated completely. The R_u leads to voltage change across the electrochemical interface, called the "iR drop" (V_{iR}), given by:

$V_{iR} = i_{Cell}R_u$ (2.10)

Therefore, whenever i_{Cell} is passed through the Randles equivalent circuit, there is always a potential control error due to V_{iR}. If a cathodic current flows, the true potential difference across the electrochemical interface is less negative than the specified potential and the opposite holds in the case of an anodic current. Therefore,

V_{WE} (vs. RE) = $V_{IN} + i_{Cell}R_u$ (2.11)

In modern potentiostat, an automatic compensation of the iR drop can be attempted by feeding back a correction voltage ($V_{Feedback}$ in *Figure 2.3*) proportional to the current flow to the input of the potentiostat. The variable resistance (R_2) can be trimmed to be set to a fraction "f" of the V_{CF}. Therefore,

$V_{Feedback} = - i_{Cell}fR_f$ (2.12)

and V_{WE} (vs. RE) = $V_{IN} + i_{Cell}(R_u - fR_f)$ (2.13)

The total automatic compensation of the iR drop can be achieved by setting $fR_f = R_u$.

Figure 2.5 shows the general configuration of a galvanostat, which is simpler than a potentiostat, because here the potential of the WE makes no contribution to the control function. The WE is virtually grounded and the i_{Cell} can be controlled by either the variable resistance (R_1) or the input voltage (V_{IN}).

$$i_{Cell} = -i_{IN} = -V_{IN}/R_1 \tag{2.14}$$

For high current experiments, the adder circuits can be used in the input network. The voltage follower gives the potential difference between the RE and WE. However, the V_{WE} (vs. RE) includes the iR drop due to the presence of R_u.

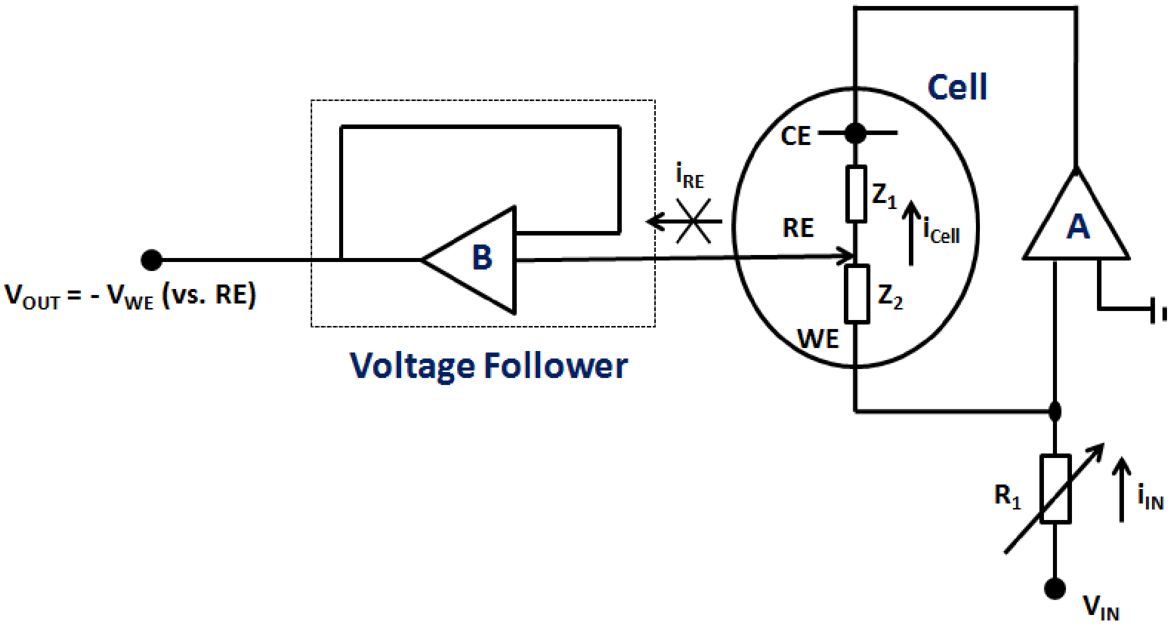

Figure 2.5 *Schematic representation of a galvanostat.*

2.1.2. Techniques

2.1.2.1. Pre-treatment of the WE

The GC-WE and Au-WE were polished smoothly using alumina slurries with powders of size down to 0.05 mm. After each polishing, the electrodes were thoroughly rinsed with water and sonicated in ultrapure water in an ultrasonic bath for 30 min to remove any adsorbed substances from the electrode surface. The Au-EQCM was treated in a mixture of (1:1) concentrated H_2SO_4 and 30% (v/v) H_2O_2 to get dust free fresh surface. After rinsing followed by drying, the potential of the working electrode was cycled between +0.3 and −0.8 V at a scan rate of 10 mV s^{-1} in 0.1 M $HClO_4$ solution until a reproducible background current was obtained.

2.1.2.2. Purging off the Dissolved Oxygen

The solubility of the oxygen gas in water is ~8 mg/L (or 0.26 mM) at 25 °C, though it depends on the temperature, salinity and pH of the solution. The reduction of the dissolved oxygen follows two different paths:

$$O_2 + 2H^+ + 2e^- = H_2O_2 \qquad E_0 = +0.695\ V \qquad (2.15)$$

$$O_2 + 4H^+ + 4e^- = 2H_2O \qquad E_0 = +1.229\ V \qquad (2.16)$$

However, the rate of reduction of oxygen at GC-WE and Au-WE is limited by the electron transfer kinetics and thus the reduction of the dissolved oxygen at these cathodes happens at far negative potentials (about -0.4 V and about -0.8 V vs. Ag/AgCl for reaction 2.15 and 2.16, respectively) than the standard reduction potential. The presence of dissolved oxygen affects the reading of the analytical signal against a large background current. Further, the intermediate product (H_2O_2) interferes in the electrochemistry of the analyte. Therefore, the presence of dissolved oxygen is considered as nuisance in the electrochemistry other than the research related to the oxygen reduction reaction. Prior to performing the electrochemical experiments, the working solution was purged with high purity nitrogen for 15 min to remove the dissolved oxygen from the solution.

2.1.2.3. Voltammetry

Voltammetry is a set of experimental techniques in which the applied potential (E) of the WE is changed with time and current (i) flowing through the WE is recorded as a function of E. The plot of “i” versus E is known as “voltammogram”. In the present work, the IUPAC convention is followed for representing the current, i.e. anodic current is positive and cathodic current is negative. The current depends on three factors i.e., (1) the rate of electron transfers between the electrode and the analyte; (2) the rate of transport of the reactants and products to and from the electrode and (3) the charging current corresponding to the restructuring of the double layer. The first two factors contribute to the faradaic current and the third factor contributes to the non-faradaic current. The potential-time function and the current acquisition define different modes of the voltammetry and among these; the cyclic voltammetry (CV), differential pulse voltammetry (DPV), square wave voltammetry (SWV) and square wave anodic stripping voltammetry (SWASV) were used in this study.

2.1.2.3.1. Cyclic Voltammetry (CV)

The cyclic voltammetry technique is the most widely used voltammetric technique performed to qualitatively diagnose an electrochemical reaction. The potential of the working electrode is varied linearly with time from a start value, say E_1 to a terminal value, say E_2 and then the direction of potential scan is reversed and finally, the WE comes to its initial potential. The E_1 is chosen to correspond to negligible current flow and E_2 is chosen to correspond to the interval (i.e. E_2-E_1) enveloping the oxidation-reduction process of interest. The rate at which the potential of the WE varies with time is known as the scan rate (ν).

Let us suppose, for an arbitrary electrochemical reaction $M^+ + e^- \leftrightarrow M$ (the formal reduction potential of the system ($E_0^{'}$) is expected to be 0 V vs. a selected reference electrode); the CV experiment is performed with $[M^+] = 1\times10^{-3}$ M; [M] = 0 M at 298 K. The potential scan is started at 0.45 V (E_1) at a scan rate of 0.01 V s^{-1} towards the cathodic direction (*Figure 2.6*). The potential scan direction is reversed at -0.45 V (E_2) and the potential is varied with a rate of -0.01 V s^{-1} until 0.45 V. The one cycle takes about 180 s to complete.

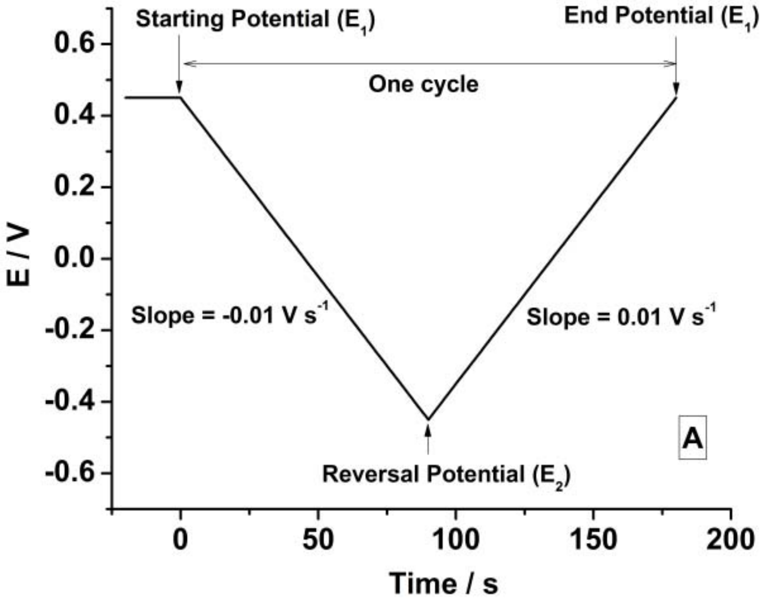

Figure 2.6 *The potential-time function of an electrochemical reaction ($M^+ + e^- \leftrightarrow M$); $E_1 = 0.45$ V, $E_2 = -0.45$ V, $v = 0.01$ V s^{-1}.*

The shape of the CV significantly depends on the value of the standard electrochemical rate constant (k_s, in cm s^{-1}), which is a measure of the kinetics of charge transfer of the redox couple. The higher the value of k_s (1-10 cm s^{-1}), the faster is the attainment of the equilibrium. An infinitesimal reversal in the potential causes the reaction to proportionally reverse in direction. The electrode reaction having higher k_s value is known as "reversible" electron transfer reaction (*Figure 2.7i*). On the contrary, the equilibrium is attained very slowly for lower value of k_s ($< 10^{-5}$ cm s^{-1}). Then, on infinitesimal reversal in the potential, the equilibrium is not reestablished in the reverse direction in a given experimental time scale. The electrode reaction having lower k_s value is known as "irreversible" electron transfer reaction (*Figure 2.7ii*). The electrode reaction, having intermediate value of k_s ($10^{-5}<k_s<10^{-1}$ cm s^{-1}) is known as quasi-reversible electron transfer reaction (*Figure 2.7iii*).

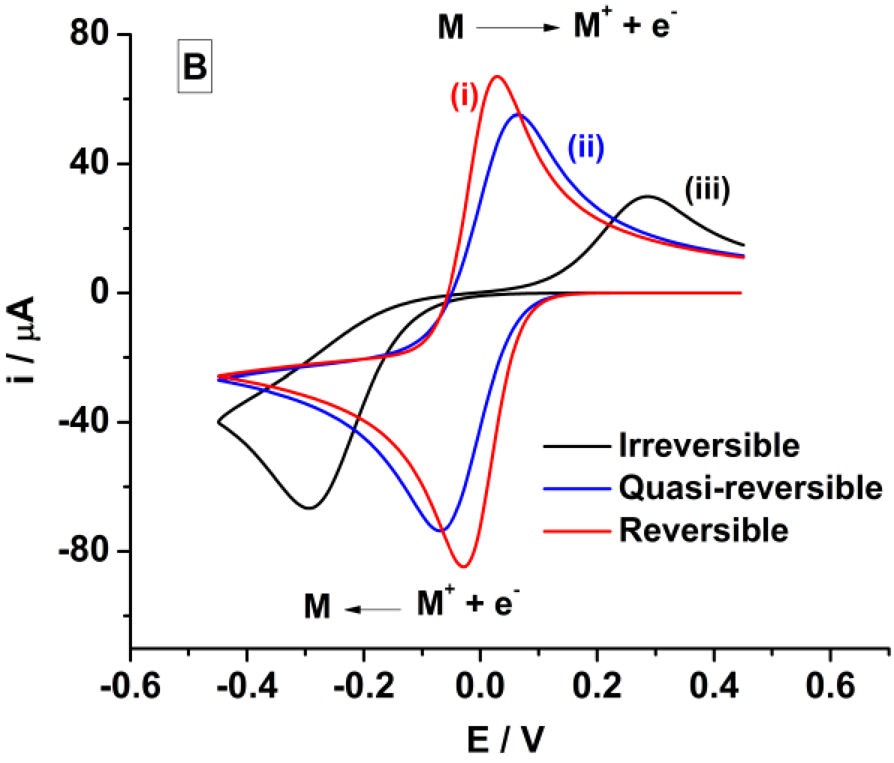

Figure 2.7 *The simulated CVs of the reaction* ($M^+ + e^- \leftrightarrow M$) *for* k_s = *(i) 10, (ii)* 1×10^{-3} *and (iii)* 1×10^{-5} *cm* s^{-1} *for* $[M^+] = 1\times10^{-3}$ *M;* $[M] = 0$ *M;* $E_0{}' = 0$ *V;* $D_{M+} = D_M = 1\times10^{-5}$ cm^2 s^{-1}; $a = 1$ cm^2; $\alpha = 0.5$; $T = 298$ *K;* $E_1 = 0.45$ *V,* $E_2 = -0.45$ *V,* $v = 0.01$ *V* s^{-1}. *The simulation of CV is carried out by DigiSim 3.03b software.*

From the CV, we can get two important parameters viz. peak current (i_p) and peak potential (E_p), which represent current and potential of the cathodic (or anodic) peak, respectively. The expressions of the E_p and i_p for the diffusion controlled reversible and irreversible reactions are shown in *Table 2.1*.

Table 2.1 *The expressions of the E_p and i_p for the diffusion controlled reversible and irreversible reactions.*

Reaction Type	**i_p (A)**	**E_p**
Reversible	$i_p = 2.69 \times 10^5 A n^{\frac{3}{2}} D^{\frac{1}{2}} \nu^{\frac{1}{2}} C^*$ (2.17) (Randle-Sevcik equation)	$\mid E_p - E_{\frac{1}{2}} \mid = 1.109 \frac{RT}{nF}$ (2.18) $E_{\frac{1}{2}} = E_0' - \frac{RT}{2nF} \ln\left(\frac{D_{M+}}{D_M}\right)$ (2.19) $\mid E_p - E_{\frac{p}{2}} \mid = 2.199 \frac{RT}{nF}$ (2.20)
Irreversible	$i_p = 2.99 \times 10^5 A \alpha^{\frac{1}{2}} n^{\frac{3}{2}} D^{\frac{1}{2}} \nu^{\frac{1}{2}} C^*$ (2.21)	$\mid E_p - E_{\frac{p}{2}} \mid = 1.857 \frac{RT}{\alpha nF}$ (2.22)

Where, A is the area of the electrode (in cm^2), n is the number of electron change, D is the diffusion coefficient (in cm^2 s^{-1}), C^* is the bulk concentration in (mol cm^{-3}), R is the universal gas constant (in J mol^{-1} K^{-1}), T is the temperature in absolute scale (in K^{-1}), F is the Faraday constant (C mol^{-1}). RT/F (at 25 °C) = 0.02569 V, α is the charge transfer coefficient.

If both the electroactive analyte and product are adsorbed on the electrode, then the shape of the cathodic part of the voltammogram becomes mirror image of the anodic part of the same (i.e. $E_p^c = E_p^a = E_0'$). Then i_p varies linearly with v as shown in Eq. (23).

$$i_p = \frac{n^2F^2}{4RT} \nu A \Gamma^* \qquad (2.23)$$

where, Γ^* is the total coverage of the analyte and the product.

Therefore, on the basis of *Eqs. 2.17 and 2.23*, one can diagnose whether any particular electrochemical process is controlled by diffusion or adsorption of the analyte. The slopes of the plot of Log (i_p) versus Log (v) should be equal to 0.5 and 1 for the diffusion and adsorption controlled reaction, respectively.

The CV has three limitations, (1) due to i-E asymmetry (for diffusion controlled process) the resolutions between two closely spaced charged transfer reaction becomes very poor, (2) the high capacitive (i.e. the non-faradaic) current distorts the peak shape and sometimes it may hide the peak (for adsorption controlled process) and (3) the concentration of the analyte should be very high (~1 mM) to get reliable mechanistic information.

2.1.2.3.2. Differential Pulse Voltammetry (DPV)

DPV is designed to overcome the capacitive limitations of CV. If a potential pulse of fixed magnitude (E_{Pulse} = 10-100 mV) is applied on a base potential, both the faradaic and non-faradaic currents (i_{NF}) increased simultaneously at the onset of the pulse. The non-faradaic current decays with the time constant ($\tau = R_uC_{DL}$) as given in *Eq. 2.24*.

$$i_{NF} = \frac{AE_{Pulse}}{R_u}\exp\left(-\frac{t}{R_uC_{DL}}\right) \qquad (2.24)$$

The typical value of τ is ~ 20 μs for $R_u = 1\ \Omega$ and $C_{DL} = 20\ \mu F$. After the time τ, the i_{NF} decreases by 63 % and after 3τ by 95 %. On the other hand, the faradaic current (i_F) for a planar electrode decays with $t^{1/2}$.

$$i_F = \frac{nFAD^{\frac{1}{2}}C^*}{\pi^{\frac{1}{2}}t^{\frac{1}{2}}} \qquad (2.25)$$

Therefore, the current for DPV is sampled twice: (1) just before the pulse application and (2) again late in the pulse life, when the charging current has decayed (*Figure 2.8a*). The first current is instrumentally subtracted from the second, and this current difference (Δi) is plotted versus the applied potential (E) (*Figure 2.8b*). The resulting differential pulse voltammogram consists of current peak (Δi_p), with the height directly proportional to the concentration of the corresponding analyte, while peak potential (E_p) can be used to identify the species, as it occurs near the polarographic half-wave potential.

$$\Delta i_p = \frac{nFAD^{1/2}C^*}{\pi^{1/2}t_{Pulse}^{1/2}}\left[\frac{1-\sigma}{1+\sigma}\right] \qquad (2.26)$$

$$\sigma = \exp\left[\frac{nFE_{Pulse}}{2RT}\right] \qquad (2.27)$$

$$E_P = E_{\frac{1}{2}} - \frac{1}{2}E_{Pulse} \qquad (2.28)$$

Therefore, we can say for small E_{Pulse}, $E_p \sim E_{1/2}$ and the analyzable concentration range of the analyte comes down to $\sim 10^{-6}$ M.

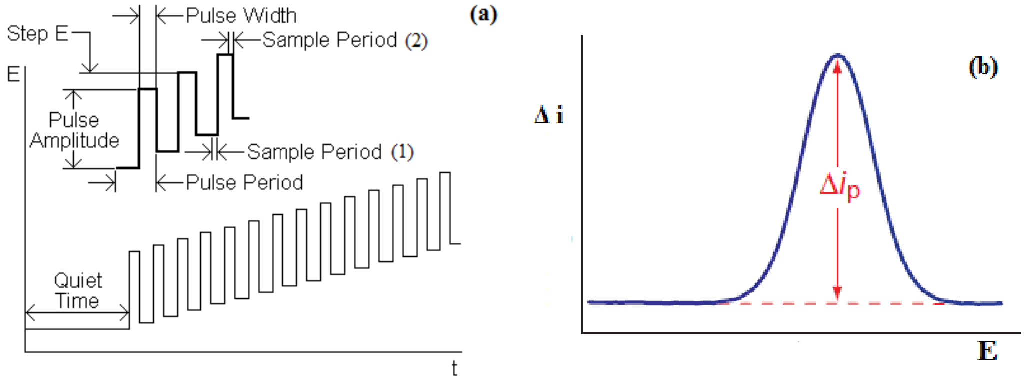

Figure 2.8 *(a) The waveform of the DPV and (b) the differential pulse voltammogram showing Δi versus E.*

2.1.1.1.1. Square Wave Voltammetry (SWV)

SWV is a large-amplitude differential technique in which a waveform composed of a symmetrical square wave (E_{SW}), superimposed on a base staircase potential, and is applied to the working electrode. (*Figure 2.9a*). If the frequency of the SW is f_{SW}, then the time period (T) for one complete cycle is $1/f_{SW}$ and it is equal to twice the pulse width (t_p).

Therefore, $T = 1/f_{SW} = 2t_p$ (2.29)

and the scan rate $(\nu) = f_{SW}\Delta E_s$ (2.30)

where, ΔE_s is the shift in the base potential between two successive cycles.

The current is sampled twice during each square-wave cycle, first at the end of the forward pulse (at t_f) and second at the end of the reverse pulse (at t_r). The difference between the two measurements (Δi) is plotted versus the base applied potential (E) (*Figure 2.9b*).

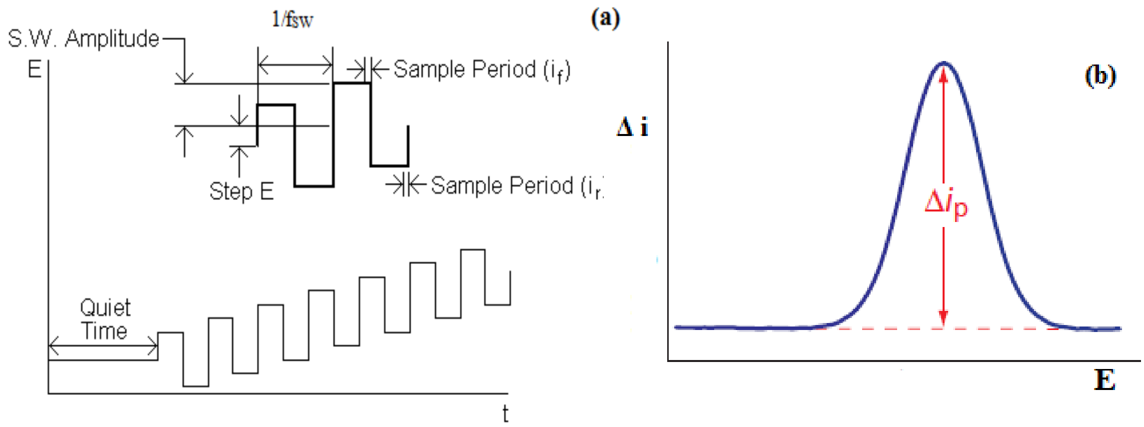

Figure 2.9 *(a) The waveform of the SWV and (b) the differential pulse voltammogram showing Δi versus E.*

$$\Delta i_p = \frac{nFAD^{\frac{1}{2}}C^*}{\pi^{\frac{1}{2}}t_{Pulse}^{\frac{1}{2}}}\Delta\Psi_p \qquad (2.31)$$

$$\Delta\Psi_p = \frac{\Delta i_p}{i_l} \qquad (2.32)$$

where, i_l is the limiting current in the normal pulse voltammetry. The $\Delta\Psi_p$ is equivalent to the factor [(1-σ)(1+ σ)] of Eq. (26) but, for pulse heights 10-50 mV; $\Delta\Psi_p >$ [(1-σ)(1+ σ)] and thus SWV can be performed with the analyte concentration range down to ~10^{-8} M.

2.1.2.3.4. Square Wave Anodic Stripping Voltammetry (SWASV)

It is an extended form of the SWV where the metal ions of interest are preconcentrated on the WE by applying high cathodic potential under stirring condition for an optimized duration. This is followed by a SWV analysis in the unstirred solution from the deposition potential to the anodic direction when the deposited metal ions are stripped out from the WE to the solution at their respective $E_{1/2}$.

2.1.2.4. Chronoamperometry

This is a type of the potential controlled electrochemical technique, where the potential of the WE is stepped from a value at which no faradaic reaction or no redox process occurs to a potential at which the surface concentration of electroactive species is effectively zero or to a value at which the reduction or oxidation is driven. Then the faradaic current (i_F) follows *Eq. 2.25*, which is known as the Cottrell equation. As discussed in chapter 1, chronoamperometry is a powerful technique to study the initial information about nucleation and growth mechanism of electrocrystallization.

2.1.2.5. Chronopotentiometry

This is a controlled current technique, where the i_{Cell} is stepped from zero to a constant cathodic (say, $-i_1$) value at t = 0 (*Figure 2.10A*) and the change in the potential of the WE is monitored as a function of time (*Figure 2.10B*). At the beginning, a sharp decrease in the potential is observed because of the charging of the double layer. Then the potential of reduction of the analyte is reached and the potential of the WE slowly varies following the Nernst equation (*Eq. 2.33*), until the surface concentration of the analyte reaches essentially zero.

$$E = E_0' + \frac{RT}{nF} ln\left[\frac{C_{Ox}}{C_{Red}}\right] \qquad (2.33)$$

where, C_{Ox} and C_{Red} are the concentrations of the oxidized and reduced form, respectively. The flux of the analyte to the surface is then no longer sufficient to maintain the applied current, and the electrode potential again falls more sharply, until a further secondary electrode process occurs. The time interval from the start of the current pulse to the transition of the potential for the secondary electrode process is known as the transition time (τ').

$$\tau'^{\frac{1}{2}} = \frac{nFA\pi^{\frac{1}{2}}D^{\frac{1}{2}}C^*}{2\,|\,i_{Cell}\,|} \qquad (2.34)$$

and $\tau'_{\frac{1}{4}} \cong E_{\frac{1}{2}}$ (2.35)

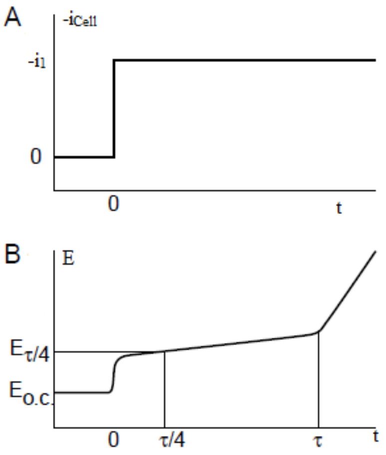

Figure 2.10 *(A) Current function and (B) potential response of chronopotentiometry.*

2.1.2.6. Electrochemical Impedance Spectroscopy (EIS)

The electrochemistry of a faradaic cell involves (i) movement of the ions through solution, (ii) charge transfer resistance across the interface, (iii) double-layer rearrangement at the interface, and (iv) diffusion of the analyte from bulk of the solution to the interface. These four processes are strongly coupled and occur at different time scales. The contribution of the individual process to the overall faradaic cell can not be separated in voltammetry, chronoamperometry and chronopotentiometry experiments where the large potential/current perturbation is applied to drive the WE far from the equilibrium state. On the contrary, the contributions of these four processes to the faradaic cell can be determined separately by perturbing the WE from its equilibrium state by applying a small amplitude alternating signal with different frequencies and monitoring the relaxations of these processes with time to the steady state.

The Randle's electrical equivalent circuit, as shown in *Figure 2.4*, represents the electrical equivalents of solution resistance (R_S), charge transfer resistance across the interface (R_{CT}), double layer capacitance (C_{DL}) and diffusion of analyte from solution (W). When the potential (ΔE) of the WE is varied with an alternating small amplitude (E_0) perturbation around the equilibrium potential (at $E = E_0^{'}$);

$$\Delta E = E_0 \,\mathrm{Sin}\,(2\pi ft) \qquad (2.36)$$

Then the response current (ΔI) of the cell is changed according to *Eq. 2.37*:

$$\Delta I = I_0 \,\mathrm{Sin}\,(2\pi ft + \varphi) \qquad (2.37)$$

where, φ is the phase difference between the applied voltage and the response current. Then the impedance [Z(ω)] of the faradaic cell is defined as:

$$Z(\omega) = Z_0 \frac{\sin(\omega t)}{\sin(\omega t + \varphi)} \qquad (2.38)$$

where, $Z_0 = E_0/I_0$. Now, using Euler's formula, the Z(ω) can be rewritten as

$$Z(\omega) = Z_0 \cos(\omega, \varphi) - jZ_0 \sin(\omega, \varphi) \qquad (2.39)$$

Where j = √(-1) and the *Eq. 2.39* can be rewritten as

$$Z(\omega) = Z_{Re}(\omega, \varphi) - jZ_{Im}(\omega, \varphi) \qquad (2.40)$$

Where, $Z_{Re} = Z_0\mathrm{Cos}(\omega,\varphi)$ and $Z_{Im} = Z_0\mathrm{Sin}(\omega,\varphi)$. The Z_{Re} and Z_{Im} sometimes are represented as $Z^{'}$ and $Z^{''}$, respectively. Therefore, we have

$$\varphi = \tan^{-1}\left[\frac{Z_{Im}}{Z_{Re}}\right] \qquad (2.41)$$

$$Z_0^2 = Z_{Re}^2 + Z_{Im}^2 \qquad (2.42)$$

Figure 2.11 shows the Nyquist plot ($-Z_{Im}$ versus Z_{Re}) of the Randle's electrical equivalent circuit. The difference between the high frequency and low frequency cuts at Z_{Re} gives the R_{CT} value. The linear shape at the lower frequency region is mainly contributed by the Warburg impedance. The EIS experiment was carried out in 5 mM $K_3[Fe(CN)_6]/K_4[Fe(CN)_6]$ in 0.1 M KCl at the open circuit potential with 5 mV E_0 in the frequency range 10^5 – 0.1 Hz.

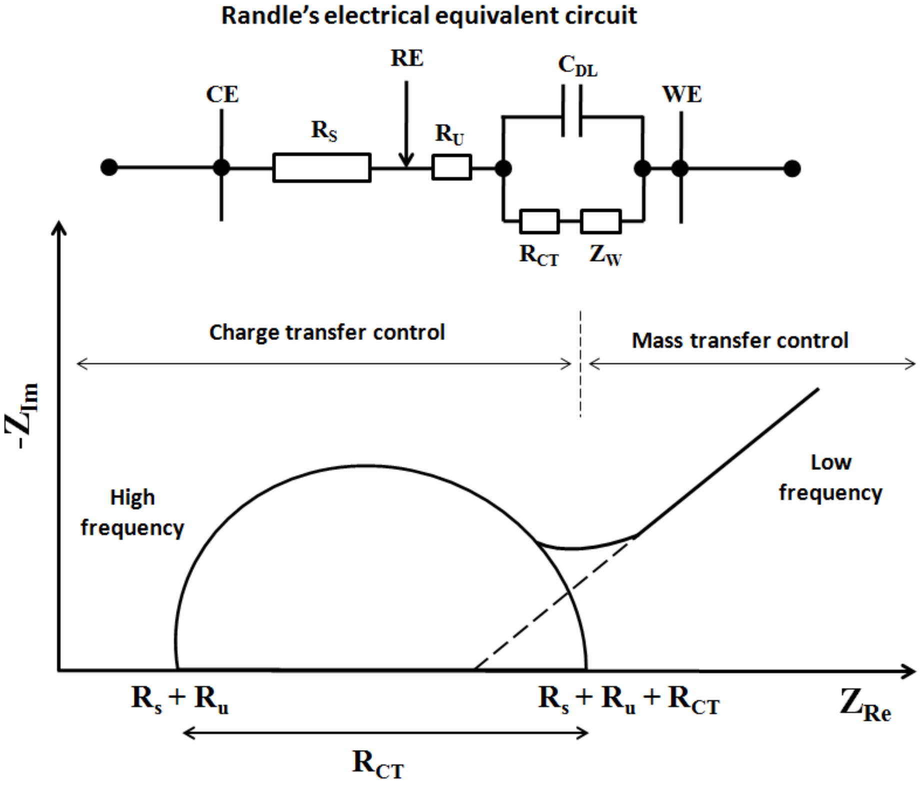

Figure 2.11 *Nyquist plot of the Randle's electrical equivalent circuit of the faradaic cell.*

2.2. Electrochemical Quartz Crystal Microbalance (EQCM)

Electrochemical quartz crystal microbalance (EQCM) is a device which can measure a small change in mass at the electrode surface during an electrochemical experiment. The quartz crystal oscillator consists of a very small and thin piece or wafer of AT-cut quartz of diameter ~13-14 mm sandwiched between two parallel 100 nm thick gold disks. The gold disks are placed perpendicular to the electrical axes of quartz plate. The 10 nm thick titanium layer is placed between the gold and quartz for the mechanical adherence of the disks on the quartz. When the alternating electric field is applied to the gold disks potential, an alternating mechanical expansion-compression takes place along the mechanical axes of the quartz plate and the quartz oscillates at its resonance frequency (f_0, here f_0 =8 MHz). This is known as inverse piezoelectric effect. The gold disk deposited on the top side of the crystal comes in the contact with the electrolyte solution and is used as the working electrode. The 8 MHz Au-QC (CHI-125; electrode area = 0.222 cm^2) was used in the study (*Figure 2.12*).

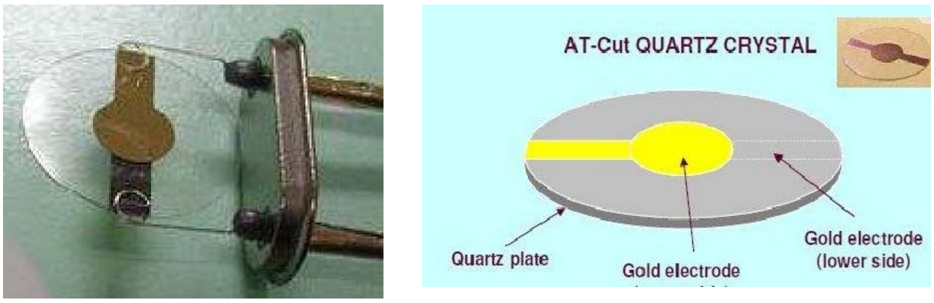

Figure 2.12 *Schematic representation of the CHI-125 quartz crystal resonator.*

During electrochemisty, if some mass (not exceeding 2% mass of the crystal) of the foreign material is loaded on the electrode surface, the resonant frequency of the crystal decreases by following the Sauerbrey equation:

$$\Delta f_0 = -C_f \Delta m_Q \qquad (2.43)$$

where, C_f is known as the sensitivity factor and C_f (Hz cm^2 g^{-1}) is expressed as *[101]*:

$$C_f = \frac{2nf_n^2}{A\sqrt{(\rho_Q \mu_Q)}} \qquad (2.44)$$

For $\mu_Q = 2.947 \times 10^{11}$ g cm^{-1} s^{-2}; $\rho_Q = 2.648$ g cm^{-3}; a = 0.222 cm^2 and n = 1, the C_f can be calculated as 0.71 Hz ng^{-1}.

2.3. *In situ* Spectroelectrochemistry

Spectroelectrochemistry is a hyphenated technique combining the advantages of the electrochemical and spectroscopic measurements to unveil the redox reactions occurring at the electrode surface. In situ UV-visible spectroelectrochemical experiment was performed during the electrosynthesis of gold nanoparticles in a spectroelectrochemical cell by placing a reflection probe (R-200-7-UV/VIS) facing the surface of the GC electrode at a distance of approximately 1.5 mm. The light beam, supplied by a deuterium-halogen light source (DH-2000-BAL), was incident perpendicularly to the electrode surface with a spot size of 1.5 mm diameter and the reflected light was collected by the central read fibre of the reflection probe connected to the spectrometer QE65000 for recording the spectrum every 1 s with a 1044 × 64 element diode array detector.

2.4. *Ex situ* Microscopic Techniques

2.4.1. Scanning Electron Microscope (SEM)

The substrate containing the electrosynthesized metal NPs was rinsed carefully with Milli-Q water followed by drying in cold water. The Ex-situ microscopic analysis was performed to get the real image of the NPs as well as to characterize their size and shape. For imaging purpose, we first think about the optical microscopic camera. The resolution (Re) of the optical microscope is limited by the wavelength (λ) of the illuminating light which is known as the Abbe diffraction limit (*Eq. 2.45*)

$$Re = \frac{0.61\lambda}{2n\sin\theta} \qquad (2.45)$$

where, n is the refractive index of the medium and θ is the solid angle. The term "nSinθ" is known as numerical aperture of the microscope and in air, nSinθ ≈ 1. Therefore, the lowest resolution of an optical microscope is decided by the lowest visible wavelength used for illuminating the NPs and it sets the lowest possible theoretical resolution of an optical microscopic camera to ~200 nm. To overcome the Abbe diffraction limit, the NPs are probed with electron beam rather than visible light. If an electron (of charge e) is accelerated by a voltage V, then its de-Broglie wavelength (λ) is defined by Eq. 2.46:

$$\lambda = \frac{h}{\sqrt{2meV}} \qquad (2.46)$$

where, h is the Planck's constant and m is the relativistic mass of the electron.

$$m = \frac{m_0}{\sqrt{1-\left(\frac{v}{c}\right)^2}} \qquad (2.47)$$

where, m_0 is the rest mass of the electron; v and c are the velocities of the electron and light, respectively. Therefore, an accelerating electron beam of 1 keV can give a theoretical resolution down to 0.04 nm.

In the present study, the electrons emitted from the thermonic tungsten filament are accelerated with a voltage 5-20 kV and followed by collimating and focusing through magnetic lenses to a fine spot on the sample kept at 9-10 mm working distance. Charging of the samples was generally not encountered due to conducting nature of the metal NPs as well as the substrate. A carbon tape was used to hold the sample on the SEM sample stand as well as to pass the excess charge to the ground. The secondary electrons generated from the sample surface are collected by the Everhart-Thornley scintillator-photomultiplier detector, which gives the contrast image of the NPs depending on the variation of the intensity of the secondary electrons from the NPs and the substrate. The linear magnification of the SEM image is defined by *Eq. 2.48*.

$$M\,(in\,X) = \frac{L}{l} \qquad (2.48)$$

where, L and l are the length of the line of the image in the display (usually computer monitor) and the sample space, respectively. Since L is fixed for a particular instrument, thus higher magnification can be achieved by decreasing the scanning size in the sample space. This study reports the SEM images ranging from 5000X-50000X.

2.4.2. Atomic Force Microscope (AFM)

The SEM, as discussed in the previous section, presents a two-dimensional (2D) image of a three-dimensional (3D) sample. Therefore, the 3D information of the NPs was obtained by the AFM. An AFM is composed of six major components; (i) cantilever, (ii) laser, (iii) position sensitive photodetector, (iv) feedback circuit, (v) piezo scanner stage, (vi) computer (*Figure 2.13a*). The sample is placed over the piezo scanner stage and the cantilever moves along the surface of the sample with precise X-Y positioner. The laser light falls on the cantilever and reflects to the photodetector, which gives the Z-position of the tip of the cantilever with respect to the sample surface. Depending on the surface morphology, the feedback circuit adjusts the position of the cantilever with respect to the sample. The computer and software control the entire operation and display the 3D topography of the sample. The Nanosurf Easyscan-2 AFM with the CONTR cantilever (Nano World) having a silicon pyramidal tip of height 10 μm (*Figure 2.13b*) was used in this study. The atoms present at the tip of the cantilever interact with the surface atoms of the sample by atomic force (*Figure 2.13c*). As the tip approaches the sample, initially it experiences attractive force followed by a minimum and then it experiences repulsive force very near to the sample. The AFM images were recorded in the contact mode with a constant repulsive force of 20 nN in air.

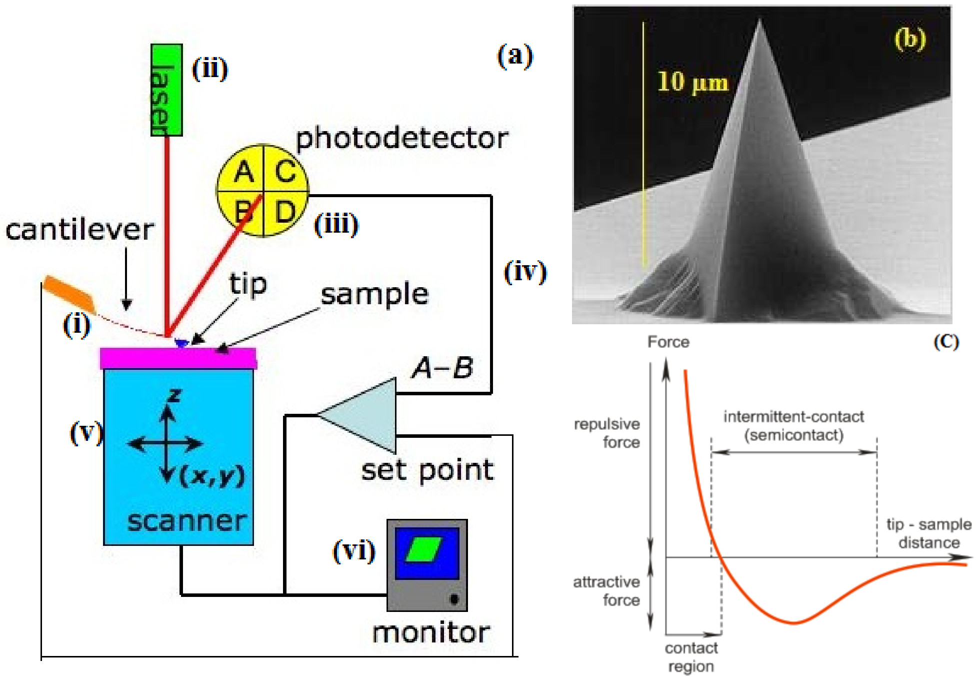

Figure 2.13 *Schematic diagram of a common AFM instrument; (b) the silicon tip of CONTR cantilever; (c) atomic force curve as a function of distance between the tip and the sample surface.*

The characteristics of the recorded AFM images were studied by the inbuilt programs of the Nanosurf Report 4.1 software.

2.5. X-ray Diffraction (XRD)

The XRD is used to characterize the crystallographic property of the NPs. The beam of monochromatic X-ray (of wavelength λ) emitted from the X-ray tube followed by passing through the filter falls on the sample and interacts with the electron density of the atoms positioned in the crystal planes of the sample. The atoms of the crystal planes diffract the X-ray in various directions resulting into constructive-destructive diffraction pattern. The constructive interference and hence a so called Bragg reflection is obtained when the path of the wavelet scattered of the lower of the two planes is longer by an integer number of λ than that of the wavelet scattered off the upper plane. A reflection will thus occur when,

$$n\lambda = 2d \sin\theta \qquad (2.49)$$

where, n is an integer representing the number of planes in the lattice, θ is the angle between the lattice planes and the incident beam and d is the distance of the lattice planes for which the constructive interference occurs. The diffraction pattern (i.e. the intensity versus 2θ) contains many distinct peaks, each corresponding to a different interplanar spacing, d.

The X-ray diffraction patterns were recorded in air atmosphere by STOE-Theta-Theta X-ray diffractometer using graphite monochromatised Cu-K_α radiation (λ= 0.15406 nm). The XRD patterns obtained matched with the standard PCPDF Data Card Files (for Au and Pb: 4-784 and 4-686, respectively).

2.6. X-ray Photoelectron Spectroscopy (XPS)

X-ray Photoelectron Spectroscopy (XPS), also known as Electron Spectroscopy for Chemical Analysis (ESCA) is a widely used technique to investigate the chemical composition of surfaces of the metal NPs. The monochromatic X-ray (of known energy, hν) falls on the surface of the sample and ejects photoelectrons from the atoms of the samples. The photoelectrons are allowed to pass through ultra high vacuum and the kinetic energy (E_K) of the photoelectron is measured by the ΔE/E detector. If the work function (φ) of the spectrometer is known, then the binding energy (E_B) of the emitted photoelectron can be calculated by *Eq. 2.50*.

$$E_B = h\nu - E_K - \varphi \qquad (2.50)$$

The characteristic E_B is used to identify the chemical composition of the sample. The incident X-ray interacts with the bulk of the sample and ejects photoelectrons from the bulk. However, the photoelectrons emitted deeper in the sample lose energy by inelastic collisions with the bulk atoms while traveling towards the surface. Effectively its intensity to reach the detector significantly decreases. Only electrons close to surface (within a distance < 10 nm from the surface) can reach the detector with sufficient intensity. Therefore, XPS is considered as a surface characterization technique.

XPS can identify the chemical oxidation state of an element, because an increase in oxidation state causes E_B to increase (< 5 eV) due to a decrease in the screening of the bound electron from the ion core. The reverse is true for decrease in the oxidation state.

XPS measurements were carried out by Mac-2 analyzer using the Al-Kα line (1486.6 eV) as the incident radiation. The spectrum was recorded by performing 5 scans at step size of 0.0625 eV. The E_B was calibrated considering the Au $4_{f7/2}$ peak at 84.3 eV with respect to the Fermi level. XPS peak positions were taken as the centre of the peak at half height and were corrected by adventitious carbon 1_s (C 1_s) peak at 284.6 eV. The shift of E_B due to the surface charging effect was calibrated by assuming the binding energy peak of C 1_s to be always 284.6 eV.

2.7. Inductively Coupled Plasma Mass Spectrometry (ICPMS)

ICPMS is a highly sensitive mass spectrometric technique which ionizes the atoms by inductively coupled plasma and the ions are analysed by the mass spectrometer on the basis of respective m/z values. An electric spark is applied for a short time to introduce free electrons into the argon gas stream. These electrons are accelerated by the oscillating magnetic field (27.12 of 40.68 MHz), created by an applied high frequency electric field. The accelerated electrons collide with argon atoms and ionize them. The released electrons are in turn accelerated by the oscillating magnetic field. This produces plasma (consisting of electrons and argon ions) with temperature ranging from 6000-10000 K. A significant portion of the atoms of the sample analyte (nebulized into the plasma) is ionized and is passed to the quadrupole analyzer through the sample and skimmer cones. ICPMS can analyze almost 65 elements in the parts per billion concentration range. ICP-oa-TOF-MS (Optimass 8000R, GBC, Australia) was employed to validate the concentrations of lead determined by square wave anodic stripping voltammetry (SWASV).

2.8. Chemicals and Materials

Extrapure ACS grade tetrachloroauric acid trihydrate ($HAuCl_4$, $3H_2O$), uranyl nitrate hexahydrate [$UO_2(NO_3)_2$, $6H_2O$], hydrochloric acid (HCl), potassium chloride (KCl), perchloric acid ($HClO_4$, 60%) were used as received. AR grade potassium ferrocyanide ($K_4[Fe(CN)_6]$), potassium ferricyanide ($K_3[Fe(CN)_6]$), sulphuric acid (H_2SO_4), silver nitrate ($AgNO_3$), potassium nitrate (KNO_3), methanol (MeOH) and tetrabutylammonium tetrafluoroborate ($TBABF_4$, 99%) were used without any further purification. Metrohm standard aqueous lead ion solution ($C_{Pb2+} = 0.1000 \pm 0.0005$ M) and Merck standards (1000 mg L^{-1}) were used for preparing Pb(II) solutions. All the solutions were prepared using ultra pure water (Milli-Q, Millipore, 18.2 MΩ cm). The saturated $TBABF_4$ solution was prepared by Millipore-MilliQ water containing 10% MeOH and the excess solid residue of $TBABF_4$ was filtered out.

2.9. Computer Based Programs

2.9.1. Hybrid Genetic Algorithm (HGA)

The hybrid genetic algorithm was used to evaluate the electrocrystallization parameters viz. initial current density (j_0), decay constant (τ), diffusion coefficient (D) of Ag(I), number of active sites (N_0) and nucleation rate (a) by fitting the experimentally obtained current transient with the current transient calculated from the electrocrystallization model. The home built code was used for genetic algorithm (GA).

The deduced parameters were finally optimized by Origin software using Levenberg-Marquardt algorithms (LMA). The optimised values obtained from GA were taken as the initial guess values in LMA. The brief descriptions of implementation of GA and LMA are given below:

2.9.1.1. Initialization of the Population

The population is made up of individuals or chromosomes by analogy with genetics. Each individual is a code of the parameters (j_0, τ, D, N_0 and a) in a particular model and represents a trial solution to the fitting model. The initial population is randomly generated with distribution over the entire search region and is therefore less likely to become trapped in any local optima. In our studies, we have set the size of population (n) to 100. The search of j_0, τ, D, N_0 and "a" were defined within the physical relevant range of [1×10^{-4}, 5×10^{-2}], [0.1, 400], [1×10^{-6}, 1×10^{-3}], [1×10^{3}, 5×10^{7}], [0.1, 1000], respectively.

2.9.1.2. Evaluation of the Fitness

The fitness of an individual will be determined by the value of the residue (R). The experimental current transient contains m data points denoted as (j_i, t_i) (i = 1 to 2000). The individual population, p_k (k = 1 to n) also contains m data points denoted as (J_i, t_i) (i = 1 to 2000). The residue is calculated by the *Eqs. 2.51 and 2.52* given below:

$$j_{av} = \sum_{i=1}^{m} \frac{j_i}{m} \qquad (2.51)$$

$$R = \frac{\sum_{i=1}^{m} (j_i - J_i)^2}{\sum_{i=1}^{m} (j_i - j_{av})^2} \qquad (2.52)$$

The lower the value of R, better is the individual.

2.9.1.3. Genetic Operation

The genetic operation allows the good fitness of the first generation to survive in the next generation. Two operators viz. Crossover and Mutation are used for the genetic operation. Crossover operator combines the parameters from two parents to create two children. Mutation operator randomly alters one or more of the parameter(s) of a single individual randomly chosen from the population. Mutation adds random changes in the new generation and removes hereditary faults of the initial population.

2.9.1.4. Sorting and Replacement of Population

The individuals in the old and new populations are sorted according to their fitness values, and better "n" individuals are selected for the population in the next generation. The genetic operations were carried out over 500 generations for arriving at the best individuals.

2.9.1.5. LM Algorithm

The best individuals obtained from GA were used as the initial guess values for LMA and for this purpose; we adopted the standard LMA in built in Origin software for this process.

2.9.2. Principal Component Analysis (PCA)

PCA was performed to statistically evaluate the electrocrystallization parameters of the nucleation and growth of silver on GC calculated from different electrocrystallization models. PCA is a way of reducing the dimensions of a large data matrix without losing the importance of any data. The principle behind the PCA is that the multivariate data can be decomposed by linear projections onto a new co-ordinate system. The new axes, known as principal components (PCs), are orientated so that the first PC (PC1) captures the largest amount of common variance. The next PC (PC2) is orthogonal to the first PC and it captures the second largest amount of common variance in its direction. The PCA was carried out by home built code.

2.9.3. Quantum Mechanical Calculation

Full geometry optimization of $[U^{VI}O_2(SO_4)_2, nH_2O]^{2-}$ (n = 2-3) was carried out by applying a popular nonlocal correlated hybrid density function, namely, B3LYP. Gaussian type atomic basis functions, 6-31+G(d) were adopted for O and S atoms while for U atom, SARC-ZORA basis sets were used for all the calculations *[102]*. SARC-ZORA basis sets are segmented all-electron scalar relativistic basis sets in which the coefficients of contracted GTOs have been optimized for use with the ZORA scalar relativistic Hamiltonian. This particular basis set for U was obtained from Extensible Computational Chemistry Environment Basis Set Database, Pacific Northwest National Laboratory *[103]*. Geometry optimization to locate the minimum energy structure was carried out applying quasi-Newton-Raphson based algorithm. All these calculations are carried out applying GAMESS suit of ab initio program for electronic structure calculation *[104]*. Vibrational analysis of U(VI)-species was performed to ensure the true minima and to assess the effect on the actinyl bond due to changes in the number of equatorial ligands. Changes to the thermal contributions and zero point energies are negligible and, therefore, were not included.

CHAPTER 3

Template-free Electrosynthesis of Lead Nanoparticles (PbNPs) by Potentiostatic Triple Pulse Strategy (PTPS)

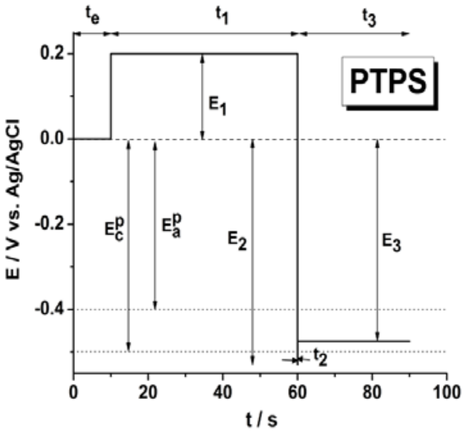

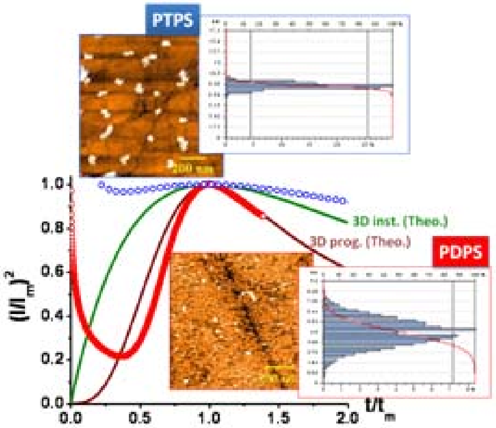

Sections of this chapter have been published in the following peer-reviewed journals:

‘Electrosynthesis of lead nanoparticles on template free gold surface by potentiostatic triple pulse technique’, Saurav K. Guin, H.S. Sharma, Suresh K. Aggarwal, *Electrochimica Acta*, **55** (2010) 1245-1257.

‘Prospective use of the potentiostatic triple pulse strategy for the template-free electrosynthesis of metal nanoparticles’ Saurav K. Guin, Suresh K. Aggarwal, *RSC Advances*, **4** (2014) 55349-55353.

3.1. Research Aim of this Chapter

Lead nanoparticles (PbNPs) have the potential to be used in (i) lithium-ion batteries *[105]*, (ii) wavelength filter with impervious ranges between 270 and 525 nm *[106]*, (iii) super-conductor *[107]*, super-paramagnet *[108-111]*, semiconductor *[112]*, anti-wearing agent *[113]*, X-ray attenuator in the energy range of 14-30 keV *[114]*, catalyst *[115]* etc. The both physical and chemical properties of the materials depend on the size of nanoparticles. Therefore, it is important to achieve good control over the size, shape and crystal structure of the nanoparticles.

The PbNPs can be prepared by physical vapour deposition *[108]*, modified polyol process *[109]*, bioreduction *[116]*, solution based chemical reduction *[114, 117-120]* and gamma radiolytic reduction *[121]*. The presence of any excess amount of chemical agent and radiolytic products (like H_2O_2, etc.) can influence the stability of the PbNPs. From this point of view, electrochemical deposition is advantageous because of the least requirement of the additives and absence of any interfering products generated during the electrodeposition.

It is interesting to note that the deposition of PbNPs on a supported material has not been attempted electrochemically in spite of the reversible electrochemical behaviour of the Pb(II)/Pb couple. To the best of our knowledge, this is the first effort for the electrosynthesis of PbNPs on a template free substrate in the absence of any assisting additives and this necessitated the optimization of different electrochemical parameters to achieve the desired quality of the PbNPs. In this context, the potentiostatic triple pulse strategy (PTPS) was developed for the electrochemical synthesis of PbNPs on a template free substrate without using any additional structure directing agents. The influence of the electrochemical parameters on size and size distribution of PbNPs is also presented in this chapter.

3.2. Results and Discussion

3.2.1. Electrocrystallization of PbNPs on a Gold Electrode

The binding energy for Pb-Au is more negative than that for Pb-Pb. For diatomic molecules, Pb-Au and Pb-Pb, the binding energies are -1.35 and -0.897 eV, respectively *[47]*. Therefore, the electrodeposition of Pb on Au is thermodynamically favourable. However, Pb (atomic radius = 175 pm) is bigger than Au (atomic radius = 144 pm) and the bulk alloy formation is not favoured due to the lattice mismatch. Therefore, the gold substrate (Au-QC) was preferred for the template-free electrosynthesis of PbNPs by PTPS.

3.2.1.1. Cyclic Voltammetry and EQCM Studies of Pb on Au-QC

Cyclic voltammetric (CV) and EQCM experiments were carried out concurrently with 1 mM $Pb(ClO_4)_2$ in 0.1 M $HClO_4$ at Au-QC by scanning the electrode potential between 0.3 V and -0.8 V at a scan rate of 10 mV s^{-1}. The superimposed CV and EQCM profiles are shown in *Figure 3.1*.

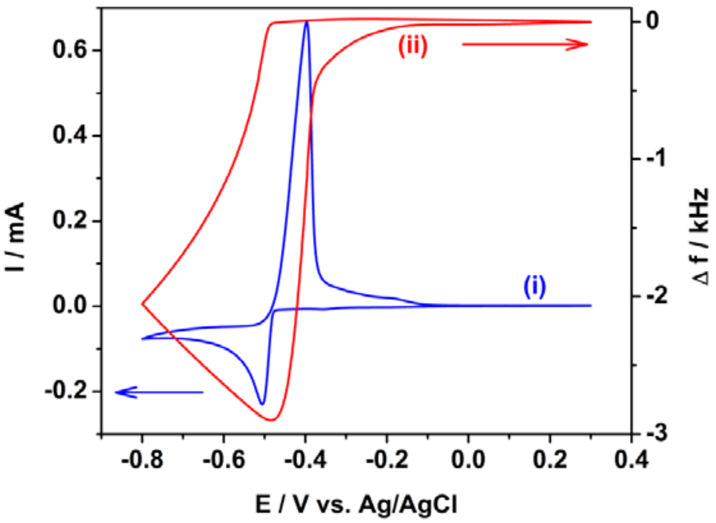

Figure 3.1 *(i) CV and (ii) the frequency shifts (Δf) of 1 mM* $Pb(ClO_4)_2$ *in 0.1 M* $HClO_4$ *at Au-QC with a scan rate of 10 mV* s^{-1}*.*

In the scan direction from 0.3 V to -0.8 V, a surge of reduction current and concurrently a rapid decrease in the resonance frequency of the Au-QC was observed at about -0.476 V, with a reduction peak at -0.505 V. During the reverse scan, a surge of oxidation current and concurrently a rapid increase in the resonance frequency of the Au-QC was observed at about -0.478 V, with an oxidation peak at -0.397 V. These observations suggest that the bulk deposition of Pb and bulk dissolution of the deposited Pb started at potentials more negative than -0.476 V and more positive than -0.476 V, respectively.

In order to check the proportionality of the rate of the mass deposition on Au-QC with that of the rate of the charge transfer and also to understand the coulombic efficiency of Pb nano-deposition under the experimental conditions, the change in mass (Δm) corresponding to observed change in frequency (Δf) was calculated by employing the Sauerbrey equation (*Eqs. 2.43, 2.44*), i.e. by dividing the observed frequency change (Δf) in the EQCM experiment with the calculated value of the sensitivity factor (C_f in Hz cm^2 g^{-1}). Further, the time intervals were obtained from the potential and scan rate (ν) data of the corresponding CV plot. The massogram *[122-125]*, thus obtained by differentiating the Δm with respect to the time (t) and superimposed on the CV is shown in *Figure 3.2.*

It can be understood that the rate of change of mass due to the deposition or dissolution of lead on the Au-QC surface is directly proportional to the rate of charge transfer across the electrode-electrolyte interface and this illustrates ~100% coulombic efficiency of the electrodeposition and electrodissolution of Pb under the experimental conditions.

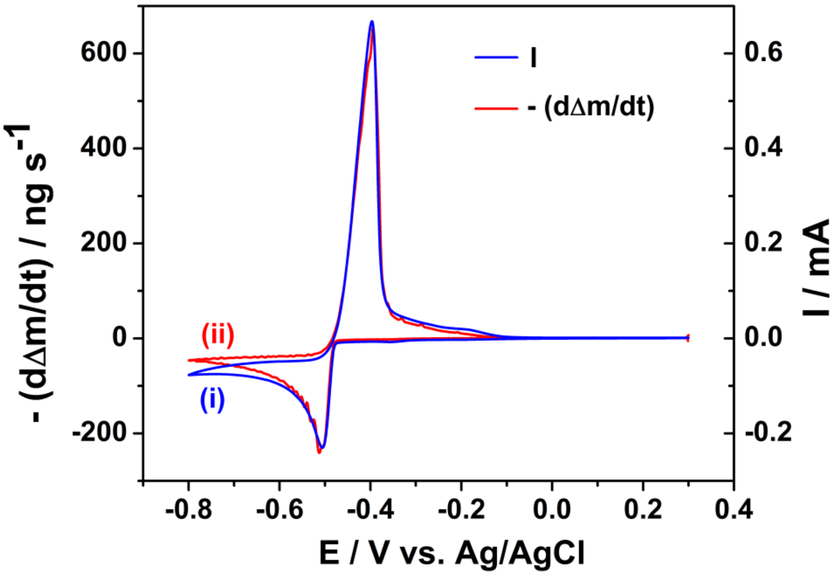

Figure 3.2 *(i) CV and (ii) massogram calculated from the Δf values shown in Figure 3.1.*

3.2.1.2. Designing the PTPS for the Electrosynthesis of PbNPs

The PTPS is designed to synthesize monodispersed PbNPs on Au-QC. The basic design of the PTPS is shown in *Figure 3.3*. The potentials of the first, second and third pulses are represented by E_1, E_2 and E_3, respectively. The corresponding time of the first, second and third pulses are t_1, t_2 and t_3, respectively. The equilibration time duration is denoted as t_e. The second pulse is zoomed from *Figure 3.3a* and is represented in *Figure 3.3b*. The first pulse is the perturbation pulse and it is responsible for the removal of the adsorbed Pb^{2+} ions from the gold surface and helps in fresh nucleation at the free latent active sites present on the gold surface. The second pulse is applied for instantaneous nucleation on the gold surface. Controlled growth of the nuclei is achieved by the third pulse.

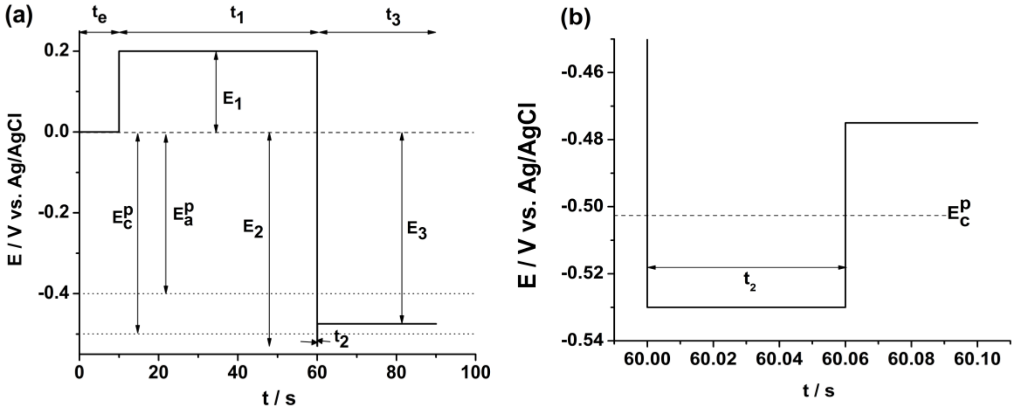

Figure 3.3 *(a) The schematic diagram of PTPS employed for the electrosynthesis of PbNPs. E_1, E_2 and E_3 are the potentials of perturbation, nucleation and growth pulses, respectively. t_1, t_2 and t_3 are the durations of perturbation, nucleation and growth pulse, respectively. t_e is the equilibration duration. (b) Zoomed image of the nucleation pulse region of (a).*

The strategy for controlling the electrodeposition of PbNPs via controlling the Au-electrolyte interface is shown schematically in *Figure 3.4*, where the red circles, blue circles and yellow bar represent the Pb_{aq}^{2+}, $ClO_{4(aq)}^{-}$ and Au-QC electrode, respectively. During the rest period (i.e., equilibration time, t_e) all the ions are homogeneously distributed throughout the entire solution. During this period, some of the Pb_{aq}^{2+} ions may get adsorbed on the electrode surface itself (*Figure 3.4A*). Application of the perturbation pulse potential E_1 for a duration t_1 (about 1 min) would remove all the adsorbed Pb_{aq}^{2+} ions from the interface and lead to a depletion region of Pb_{aq}^{2+} ions near the electrode surface (*Figure 3.4B*). Then the application of nucleation pulse potential E_2 for duration t_2 (about a few milliseconds) would seed the Pb nuclei on the Au surface via diffusion of Pb_{aq}^{2+} ions from the bulk of the solution (*Figure 3.4C*). Finally, the growth pulse potential E_3 for duration t_3 (about a few seconds to a few minutes) would cause the growth of the Pb nuclei through diffusion of Pb_{aq}^{2+} ions from the bulk of the solution towards the nuclei. During this growth process, a few of the PbNPs might overlap among themselves (*Figure 3.4D*).

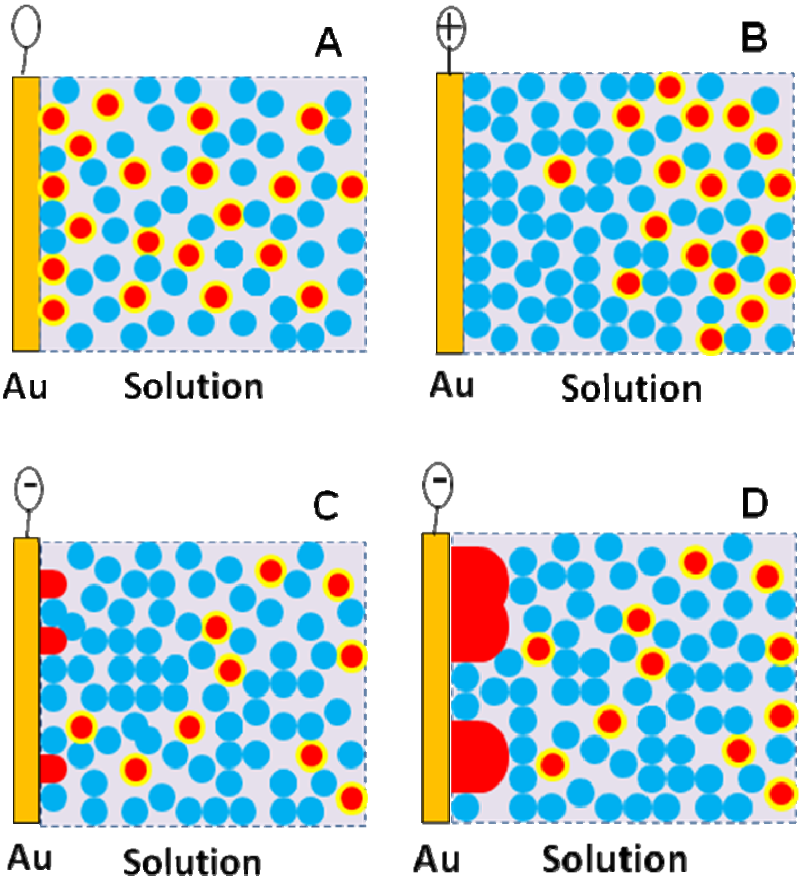

Figure 3.4 *The schematic diagram of the strategy obtained for the electrodeposition of PbNPs by controlling the Au-electrolyte interface. The red circles, blue circles and yellow bar are representing the* Pb_{aq}^{2+}, $ClO_{4(aq)}^{-}$ *and Au-QC electrode, respectively, during (A) equilibration period, (B) application of the perturbation pulse, (C) operation of the nucleation pulse and (D) application of the growth pulse.*

3.2.1.2.1. Choice of First Potential Pulse Parameters

According to PTPS, the first potential pulse is responsible for desorption of the adsorbed Pb_{aq}^{2+} ions from the latent active sites on the gold surface, but at the same time it should not cause any surface oxidation of the electrode. It is understood that $ClO_{4(aq)}^{-}$ ions would experience coulombic attraction and Pb_{aq}^{2+} ions and H_{aq}^{+} ions would experience coulombic repulsion from the positively polarized electrode surface. In order to understand the adsorption-desorption behavior of Pb_{aq}^{2+}, H_{aq}^{+} and $ClO_{4(aq)}^{-}$ ions at the gold surface, the Δf vs. E plot was critically analysed in the potential range 0.3 V to -0.45 V as shown in *Figure 3.5*. It can be seen that during the potential scan from 0.3 V to the negative direction, the Δf increased steadily up to ~20 Hz showing the maximum at about -0.244 V and then steeply decreased.

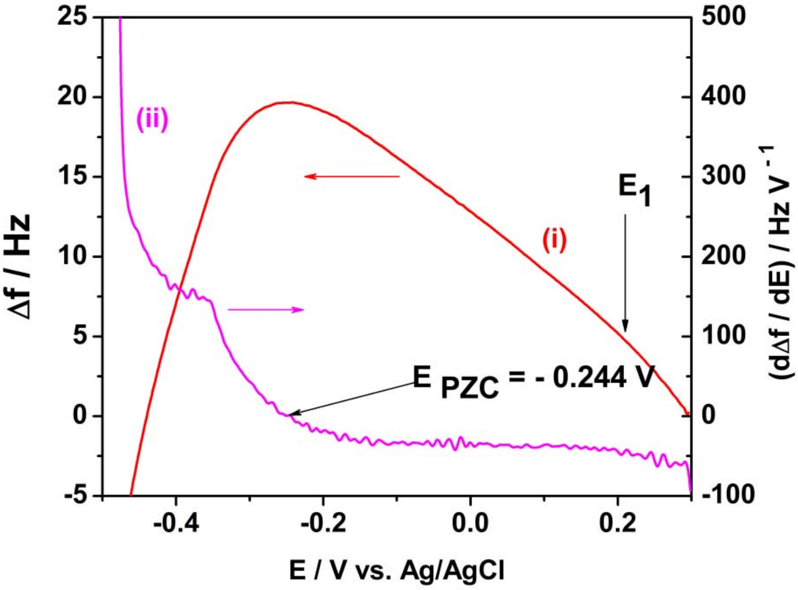

Figure 3.5 *(i) Δf vs. E and (ii)* dΔf/dE *vs. E of 1 mM* $Pb(ClO_4)_2$ *in 0.1 M* $HClO_4$ *at Au-QC with a scan rate of 10 mV* s^{-1}.

The observed steady increase in the frequency shift of Au-QC is attributed to the desorption of the adsorbed $ClO_{4(aq)}^{-}$ from the electrode surface, whereas the steep decrease in Δf is attributed to the adsorption followed by reduction of Pb_{aq}^{2+} ions on the negatively polarized electrode surface. The observed difference in the slopes at the two sides of the maxima is due to the significant difference in the atomic masses of the adsorbing ions (Pb^{2+}: 207.19, ClO_4^-: 99.5). The potential of zero charge (PZC) was evaluated from the maxima of the Δf vs. E plot by following the procedure as reported in literature *[126]*. In order to locate accurate value of PZC, (dΔf/dE) vs. E plot was superimposed on Δf vs. E plot in *Figure 3.5*. A closer look of the differential plot showed that the change in slope was not appreciable in the potential region from 0.3 V to about -0.2 V. However, at potential more negative than -0.2 V, the slope change is appreciable and steeper in magnitude at potential more negative to -0.4 V. The exact PZC value of -0.244 V was also evaluated from the differential curve. We understand that in the potential region 0.3 V to about -0.2 V, $ClO_{4(aq)}^-$ ions are desorbed from the electrode surface and at potentials more negative to -0.244 V, Pb_{aq}^{2+} ions are adsorbed followed by the UPD of the adsorbed Pb_{aq}^{2+} at -0.3 V. In *Figure 3.5*, the slightly steeper slope of the differential curve at about -0.3 V is due to the UPD of Pb on the gold surface. The evidence of the UPD of Pb on the gold surface at potential -0.3 V is also reported in the literature *[127]*. This UPD of Pb on the Au would not only affect the fresh nucleation process, but also would direct the electrodeposition towards the film formation *[Note: This film formation should be avoided in the synthesis of discrete nanoparticles]*. Based on these studies, 0.2 V was selected as the potential of first pulse which is sufficiently positive to remove the adsorbed Pb_{aq}^{2+} ions from the electrode surface as well as unable to oxidize the gold surface. We have maintained the first pulse potential (E_1) at 0.2 V and duration (t_1) of 60 s in the present studies.

3.2.1.2.2. Choice of Second Potential Pulse Parameters

The second pulse is responsible for fast seeding of nuclei on the gold surface. The potential of the nucleation pulse of -0.530 V (E_2) was chosen from the limiting diffusion current region of the CV as shown in *Figure 3.6*, in order to achieve the high rate of nucleation. This potential value is sufficiently higher as compared to the threshold potential value for initiating deposition on Au-QC. In our studies, the duration (t_2) of the nucleation pulse was varied from 60-100 ms.

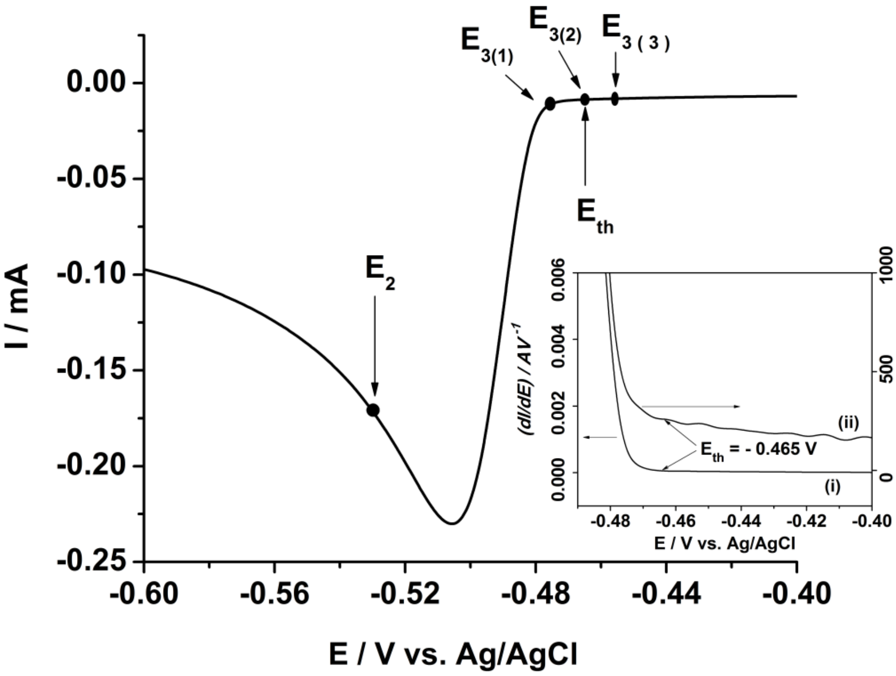

Figure 3.6 *The selection of nucleation pulse potential (E_2) and growth pulse potential (E_3). Here i =1, 2, 3 represent three different indexes of growth potential. Inset shows the plot of (i) (dI/dE) vs. E and (ii) dΔf/dt vs. E of 1 mM $Pb(ClO_4)_2$ in 0.1 M $HClO_4$ at Au-QC with a scan rate of 10 mV s^{-1}.*

3.2.1.2.3. Choice of Third Potential Pulse Parameters

Objective of the application of the third potential pulse is to maintain a steady growth of Pb nuclei and simultaneously arrest the progressive nucleation at the gold surface. Steady growth of the nuclei can be achieved by maintaining the slow rate of growth and this can be achieved by choosing a growth pulse potential near to the threshold value of nucleation potential, at about -0.475 V, apparently evaluated from CV shown in *Figure 3.1*. In the present studies, growth pulse potential of -0.475 V was applied for the durations of 30 s, 60 s and 90 s. However, as discussed earlier in *Section*

3.2.1.2.1, adsorption of Pb_{aq}^{2+} ions on the gold surface followed by reduction may even start at marginally more positive potentials than -0.475 V. In view of this, an attempt was made to find the exact value of threshold nucleation potential for preventing the progressive nucleation during the growth of the deposited Pb nuclei. It can be seen in the derivative plots, ($d\Delta f/dE$) and (dI/dE), shown in the *inset* of *Figure 3.6*, that significant change in frequency and current is observed at about -0.465 V. Hence, -0.465V should be more realistic value of the threshold potential (E_{th}) required for the nucleation of Pb under the conditions of present studies. In view of this, the growth pulse potential of -0.475 V ($E_{3(1)}$), -0.465 V ($E_{3(2)}$) and -0.455 V ($E_{3(3)}$) were applied for a period of 60 s to study the impact of progressive nucleation on the deposited PbNPs (*Figure 3.6*).

3.2.1.3. Characterization of PbNPs

3.2.1.3.1. Anodic Stripping Voltammetry (ASV) Study

The chemical state of the PbNPs deposited on Au-QC was first investigated electrochemically. The PbNPs were synthesized by employing the pulse parameters: E_1 = 0.2 V, t_1 = 60 s; E_2 = -0.530 V, t_2 = 100 ms; E_3 = -0.475 V, t_3 = 90 s. The PbNPs obtained on the Au-QC were rinsed with Milli-Q water followed by drying in cold air and kept in air for ~1.5 h. The electrochemical setup (electrochemical cell, reference electrode and counter electrode) was washed thoroughly with Milli-Q water and 0.1 M $HClO_4$ (supporting electrolyte) was taken into the cell followed by purging of high purity nitrogen for about 15 min. The anodic stripping voltammetry was carried out by scanning potential of the Au-QC (with deposited PbNPs) from -0.6 V to 0.2 V with the amplitude and pulse width of 0.05 V and 0.06 s, respectively. The stripping voltammogram obtained is shown in *Figure 3.7*. The anodic peak observed at -0.399 V is responsible for the stripping of Pb^{2+} from metallic PbNPs. However, Au has high affinity for Pb, thus the last traces of Pb of the PbNPs directly in contact with Au are stripped off at a little more positive potential (at -0.234 V) than the main anodic peak at -0.399 V. It is understood that, if the deposited PbNPs were oxidized within the experimental time frame, then the anodic stripping peak would have been absent in the above mentioned study. The result obtained suggests that PbNPs appeared to be in the metallic state.

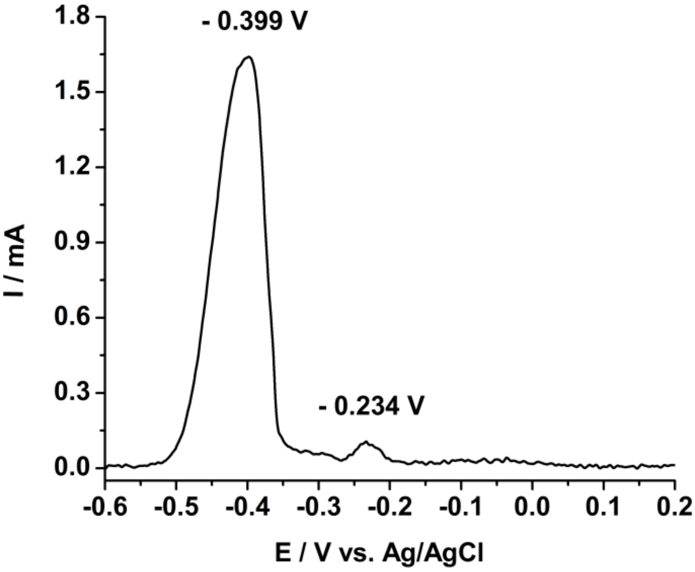

Figure 3.7 *The anodic stripping voltammogram of the PbNPs in blank 0.1 M* $HClO_4$ *solution. The PbNPs were deposited by applying the triple potentiostatic pulse (*E_1 *= 0.2 V,* t_1 *= 60 s;* E_2 *= -0.53 V,* t_2 *= 100 ms;* E_3 *= -0.475 V,* t_3 *= 90 s).*

3.2.1.3.2. X-ray Diffraction (XRD) Studies

X-ray diffraction studies were carried out to characterize the PbNPs deposited under the conditions mentioned above in *Section 3.2.1.3.1.* The deposit was exposed to atmospheric air for ~1 h prior to carrying out the XRD experiment. For reference, XRD pattern of the blank Au-QC (i.e. without any deposit) was also recorded. The XRD patterns of both the blank Au-QC (A) and the deposited PbNPs on Au-QC (B) are shown in *Figure 3.8*. The XRD patterns obtained matched with the standard PCPDF Data Card Files (for Au 4-784 and for Pb 4-686). It was observed that the Au-QCs used in this work are mono-crystalline Au(111) and the deposits are metallic Pb. Since the amount of Pb of the deposited PbNPs is insignificant compared to Au electrode, the most intense Pb(111) peak could only be observed over the background. Peaks corresponding to the most intense lines of α-PbO(111) and α-PbO_2(111) expected at 2θ values of 28.74 (PCPDF: 35-1482) and 28.47 (PCPDF: 37-517), respectively, were totally absent. The above observation suggests that the PbNPs were in the metallic state and it remained same for at least ~1.5 h in air atmosphere under the conditions of the experiment.

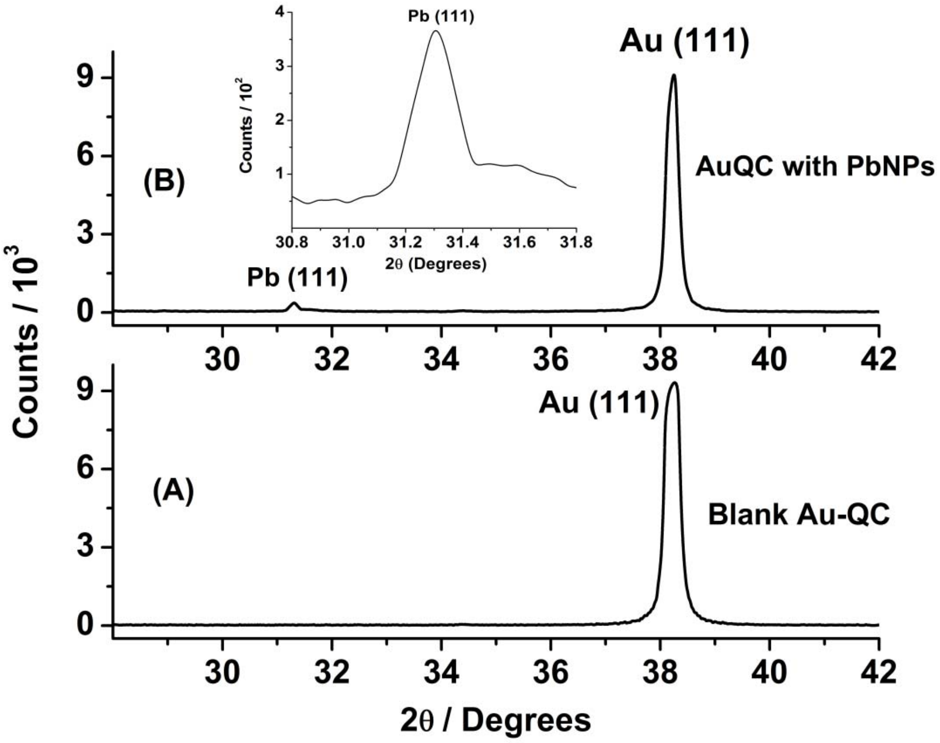

Figure 3.8 *The XRD patterns recorded for the (A) blank Au-QC and (B) the PbNPs deposited on Au-QC under the same conditions as for Figure 3.7. The inset shows the observed profile (zoomed) of Pb (111).*

In the earlier report on the XRD characterization of PbNPs, it was noticed that the peaks due to the formation of oxides of Pb were not observed for PbNPs of particle size of ~9 nm after ~2.8 h exposure in air *[108]*. It should be noted that XRD has the limitation for identifying the amorphous and low crystalline oxides; especially at the surface of the PbNPs. In view of this, the surface of the PbNPs further studied by XPS.

3.2.1.3.3. X-ray Photoelectron Spectroscopy (XPS) Studies

The XPS measurements were carried out for the PbNPs deposited under the experimental conditions mentioned in *Section 3.2.1.3.1.* The initial survey of the binding energy spectrum is shown in *Figure 3.9A* and it shows the presence of gold (4f and 4p peaks), adventitious carbon (1s peak), Pb-species (4f and 4d peaks) and O-species (1s peak). The narrow scan spectra in the C_{1s}, O_{1s} and Pb_{4f} regions for the PbNPs are presented in *Figures 3.9B-D,* respectively. The C_{1s} spectrum (*Figure 3.9B*) of adventitious carbon shows the binding energy peak at 284.6 eV and thus all the given binding energies are believed to be free from the charging effect. The peaks of the O_{1s} and $Pb_{4f7/2}$ were observed at 530.3 eV (*Figure 3.9C*) and 137.5 eV (*Figure 3.9D*), respectively. In earlier reports *[128, 129]*, a similar combination of binding energy peaks of O_{1s} and $Pb_{4f7/2}$ (O_{1s} and $Pb_{4f7/2}$ at 530.7 eV and 137.6 eV, respectively) was observed for the chemisorbed oxygen over lead metal. It was observed from the same reports *[128, 129]* that after the oxide layer formation (predominantly PbO) by aerial oxidation, the $Pb_{4f7/2}$ binding energy peak shifted to higher energy i.e. 137.9 eV (for both rhombic and tetragonal), whereas the O_{1s} binding energy peak shifted to lesser energy i.e. 529.7 eV (for rhombic) and 527.8 eV (for tetragonal). Although our route for the synthesis of PbNPs was quite different from the route followed for the synthesis of Pb film reported *[128, 129]*, but the matching of both the O_{1s} and $Pb_{4f7/2}$ binding energy peaks suggests the presence of chemisorbed oxygen over the deposited PbNPs.

The above mentioned characterizations of PbNPs suggest that the PbNPs synthesized by the triple potentiostatic pulse strategy were in metallic form with the presence of chemisorbed oxygen on its surface.

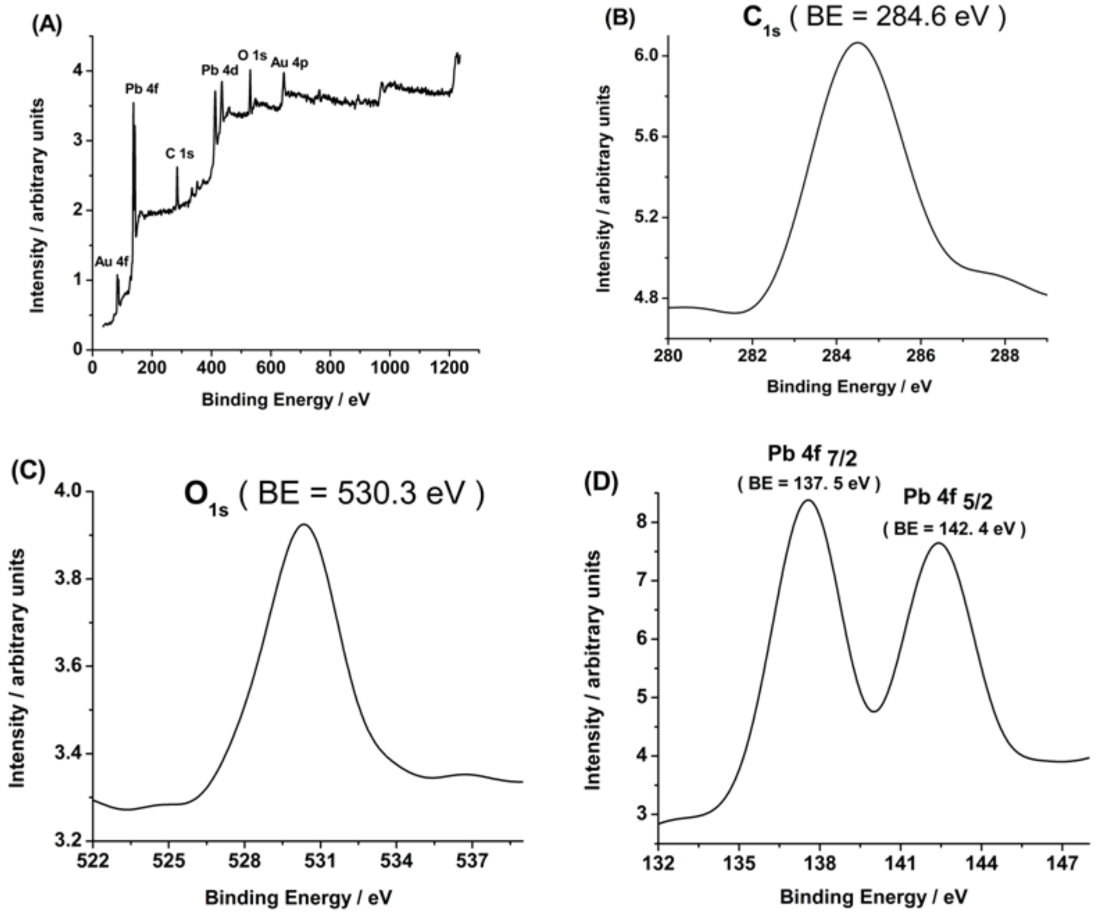

Figure 3.9 *The XPS spectra of PbNPs deposited under the same conditions as for Figure 3.7. The binding energy peaks of (A) Survey scan, (B)* C_{1s}*, (C)* O_{1s} *and (D)* $Pb_{4f7/2}$ *and* $Pb_{4f5/2}$*.*

3.2.1.4. Characterization of the Deposited PbNPs by AFM

The PbNPs deposited on Au-QC surface were characterized by AFM. The surface topographies of PbNPs were compared with the bare Au-QC. Surface characteristics such as monodispersity, particle density and size distributions of the deposited PbNPs were evaluated from the recorded 2D(XY)-AFM topographies as shown in *Figure 3.10.*

The numbers at the colour bar placed adjacent to each 2D(XY) topography independently represent the heights of PbNPs along the Z direction. In most of the topographies, two prominent contrast colours are used in the vertical colour bar, where the lower contrast colour represents the bare surface and the upper contrast colour represents the deposited PbNPs. The extent of spreading of the upper contrast colour in the topography indicates the overlapping of the deposited PbNPs as well as increase in the particle density of PbNPs on the surface.

The area roughness average (S_a) and the root mean square roughness average (S_q) can be represented by *Eqs. 3.1 and 3.2*:

$$S_a = \frac{\sum_{k=0}^{M-1}\sum_{l=0}^{N-1} \mid z(x_k,y_l) \mid}{MN} \qquad (3.1)$$

$$S_q = \frac{\sum_{k=0}^{M-1}\sum_{l=0}^{N-1}[z(x_k,y_l)]^2}{MN} \qquad (3.2)$$

where $z(x_k,y_l)$ is the height in Z direction at the point (x_k,y_l) in the area M×N. In *Eqs. 3.1 and 3.2*, the summation term in the numerator represents the sum of heights in the Z direction for a surface area of M×N. The values of S_a and S_q were evaluated for the AFM images with the Nanosurf Easyscan-2 software. By virtue of the mathematical formulation, the variation of S_a and S_q can indirectly represent the variation of the particle density on the surface for a constant area. The blank surface of the Au-QC, which seemed to be very fine polished surface in bare eyes, showed S_a and S_q values of 0.62 and 0.77 nm, respectively, for a scan area of ~(5 μm × 5 μm). These inherent random surface defects in a few nanometer dimensions on Au-QC are merely the indices of the latent active sites for the occurrence of nucleation during the electrodeposition of PbNPs. The AFM characterizations were carried out by scanning different order of areas as (5 μm × 5 μm), (1 μm × 1 μm) and (0.5 μm × 0.5 μm) for each sample (all figures have not been shown in the present discussion). The size distribution of PbNPs was studied by the particle size histograms calculated by Nanosurf Report 4.1 software from the scanned AFM topographies. The shape of the PbNPs formed by PTPS was found to be capped hemispherical. The heights of the capped hemispherical PbNPs varied in the nm range, while lateral size (i.e. chord of NPs) varied in the sub-micron ranges. Henceforth, we would express the average height of NPs and the variation (i.e. range) of the heights of NPs by the terms “size” and “size dispersion”, respectively. The wider size dispersion is termed as “polydispersion” while the narrower size dispersion tends to be called as “monodispersion”.

3.2.1.4.1. Effect of Nucleation Pulse Duration upon the Deposited PbNPs

The ex situ 2D-AFM topographies of PbNPs deposited on Au-QCs at E_2 = -0.530 V as a function of nucleation pulse duration (t_2) of 60, 80 and 100 ms are shown in *Figure 3.10A-C*. In this context, it should be mentioned that E_1, E_3, t_1 and t_3 were kept constant at the values of 0.2 V, -0.475 V, 60 s and 30 s, respectively. It can be seen from the figure that, as t_2 increases, the fraction of the upper contrast colour (at greater than about 12 nm in the vertical colour bar) appears to increase in the topographies along with the appearance of a few prominent overlaps. The particle size histograms show the average particle size and the size distribution of PbNPs as a function of the nucleation pulse duration (*Figure 3.10D*). The band of the histogram shifted toward the lower size on increasing t_2. *Table 3.1* shows other characteristics of the deposited PbNPs as a function of t_2. *Figure 3.10* and *Table 3.1* reveal that the particle size initially decreased with the increase of t_2 to 80 ms and remained almost constant on further increasing t_2 to 100 s. Further, the maximum observed value in each histogram also decreased with the increase of t_2. On the other hand, the increase of S_a and S_q values with increasing t_2 illustrates that the surface roughness after electrodeposition increased significantly as compared to the bare surface. The roughness values increased more upon increasing t_2

up to 80 ms and remained almost constant for further longer duration. The observed increase in roughness despite the decrease in the particle height indirectly indicates the increase in density of PbNPs and it is supported by the topographies.

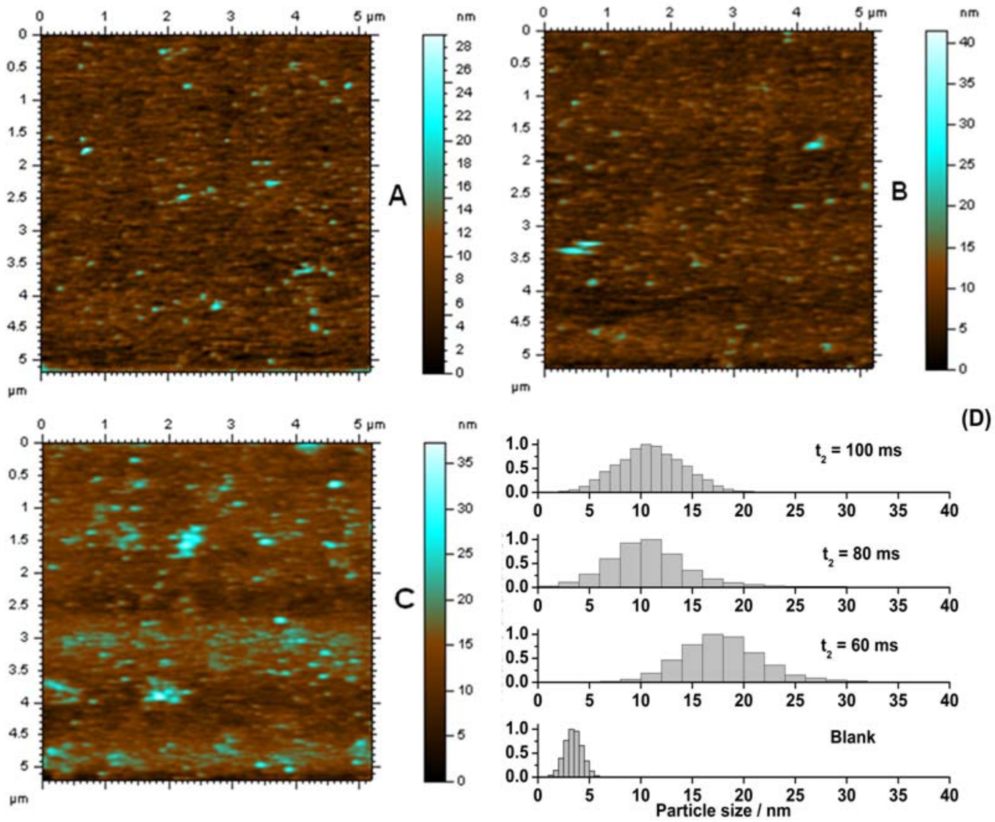

Figure 3.10 *2D(XY)-AFM topographies (5 μm × 5 μm) of PbNPs on Au-QC deposited at E_2 = -0.53 V for t_2 = (A) 60 ms, (B) 80 ms and (C) 100 ms. E_1, E_3, t_1 and t_3 were kept constant at 0.2 V, -0.475 V, 60 s and 30 s, respectively; (D) Particle size histogram of PbNPs as a function of t_2.*

Table 3.1 *Some characteristics of the deposited PbNPs as a function of t_2.*

Parameters	**t_2 /s**			**Blank**
	0.060	**0.080**	**0.100**	
S_a (nm)	2.26	2.47	2.52	0.62
S_q (nm)	3.03	3.28	3.31	0.77
Mean size ± σ (nm)	18 ± 4	11 ± 4	11 ± 3	3.5 ± 1
Maximum size from the histogram (nm)	40	35	27	8

The effect of t_2 on the size and size distribution of PbNPs deposited on Au-QC surface was also studied for the smaller (0.5 µm × 0.5 µm) area scans and the corresponding 2D(XY)-AFM topographies under the same experimental conditions as mentioned in *Figure 3.10* and the topographies are shown in *Figure 3.11A-C*. The distribution of colours in these topographies reveals that the size of PbNPs observed in *Figure 3.11A* was 15-25 nm and it decreased to 9-17 nm and 7-14 nm in *Figure 3.11B & C*, respectively, with the increase of nucleation pulse duration. Further, on increasing t_2, the fraction of the upper contrast colour (at greater than about 12 nm in the vertical colour bar) appears to increase along with the appearance of a few prominent overlaps. These show similar trends as observed in the large area scans. The mean size of the particles (17 ± 3 nm) observed in the small area scan (i.e. 0.5 µm × 0.5 µm) is closer to the mean size (18 ± 4 nm) of the particles observed in the large area scans (i.e. 5 µm × 5 µm) t_2 = 60 ms (*Figure 3.11D*). Since there were no significant differences in the characteristics of PbNPs with the scan areas; the bigger scan images are presented throughout the discussion for showing a wider view of the particle positions and overlaps.

Therefore, the particle density of PbNPs increases and the size of PbNPs decreases with the increase of t_2. However, the overlaps among the neighbouring particles increase in longer pulse duration. Due to the progressive nucleation, nuclei appear randomly on the electrode surface with time and as a result, the particle density of the PbNPs increases. The densely nucleated areas are expected to grow slower than the areas with smaller number of nuclei. Thus the competition in growth between the neighbouring nuclei and the coupling of their diffusion zones diminish the overall particle size as well as increase the overlaps among the nuclei in a densely nucleated area. The density of the PbNPs increases rapidly in the early stage of nucleation and as the time progresses, overlaps become prominent in a highly populated surface. These observations are in agreement with the reported simulation studies *[93]* and studies on the nucleation and growth of silver nanoparticles on ITO surface *[97,130]*.

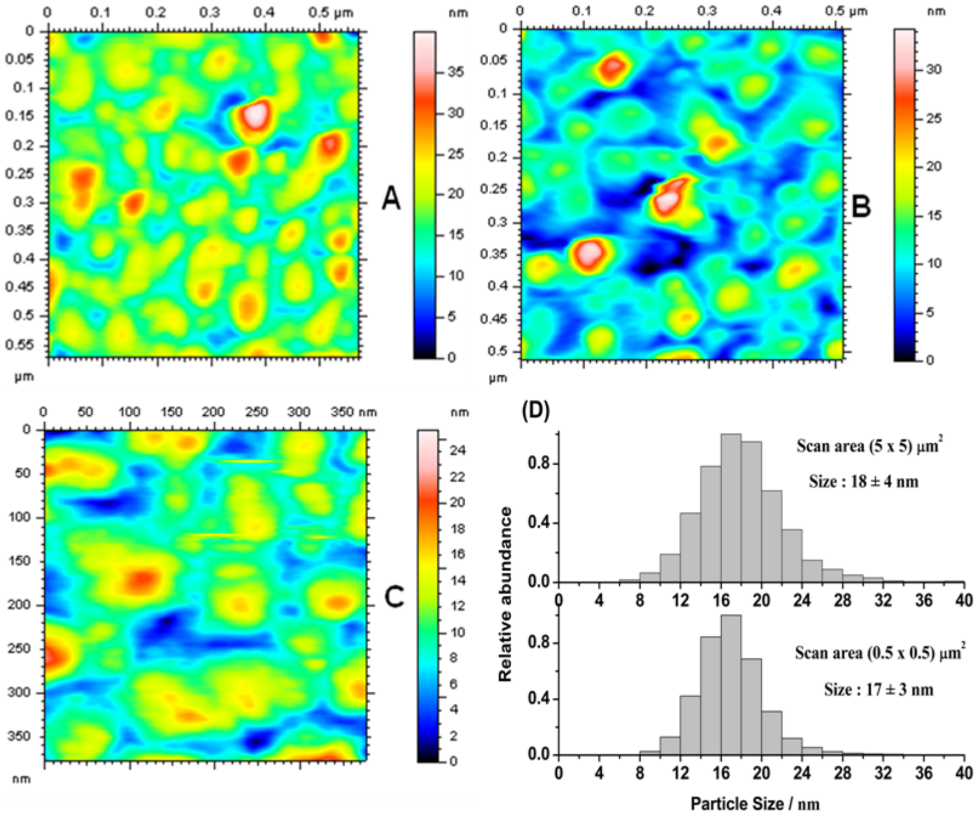

Figure 3.11 2D(XY)-AFM topographies (0.5 µm × 0.5 µm) of PbNPs on Au-QC deposited at $E_2 = -0.53$ V for t_2 = (A) 60 ms, (B) 80 ms and (C) 100 ms. E_1, E_3, t_1 and t_3 were kept constant at 0.2 V, -0.475 V, 60 s and 30 s, respectively; (D) Comparison of particle size histogram of PbNPs for t_2 = 60 ms obtained from the scan area (5 µm × 5 µm) and (0.5 µm × 0.5 µm).

3.2.1.4.2. Effect of the Growth Pulse Duration upon the Deposited PbNPs

The 2D(XY)-AFM topographies of PbNPs deposited on Au-QC at E_3 of -0.475 V as a function of growth pulse duration (t_3) of 30, 60 and 90 s are shown in *Figure 3.12A-C*. In this context, it should be mentioned that E_1, E_2, t_1 and t_2 were kept constant at the values of 0.2 V, -0.530 V, 60 s and 60 ms, respectively. With increasing t_3, the fraction of the upper contrast colour (at greater than about 12 nm in the vertical colour bar) in the topographies increased as well as the extent of overlaps among the neighbouring particles increased. The band of the particle size histogram shifted toward the higher size on increasing t_3 (*Figure 3.12D*). *Table 3.2* shows some more characteristics of the deposited PbNPs as a function of t_3. *Figure 3.12* and *Table 3.2* reveal that the particle size of PbNPs increases consistently upon increasing t_3. Besides, the maximum observed value in each histogram also increases significantly for increasing t_3. On the other hand, the S_a and S_q values increased consistently upon increasing t_3. Since the growth pulse potential was kept constant at -0.475 V, which is more negative than E_{th}, thus the significant and systematic increase in S_a and S_q was attributed to a combined effect of increase in the particle density as well as the particle size.

***Table 3.2** Some characteristics of the deposited PbNPs as a function of t_3.*

Parameters	**t_3 /s**			**Blank**
	30	**60**	**90**	
S_a (nm)	2.26	2.71	3.72	0.62
S_q (nm)	3.03	4.06	5.06	0.77
Mean size ± σ (nm)	12 ± 3	13 ± 4	15 ± 5	3.5 ± 1
Maximum size from the histogram (nm)	30	44	54	8

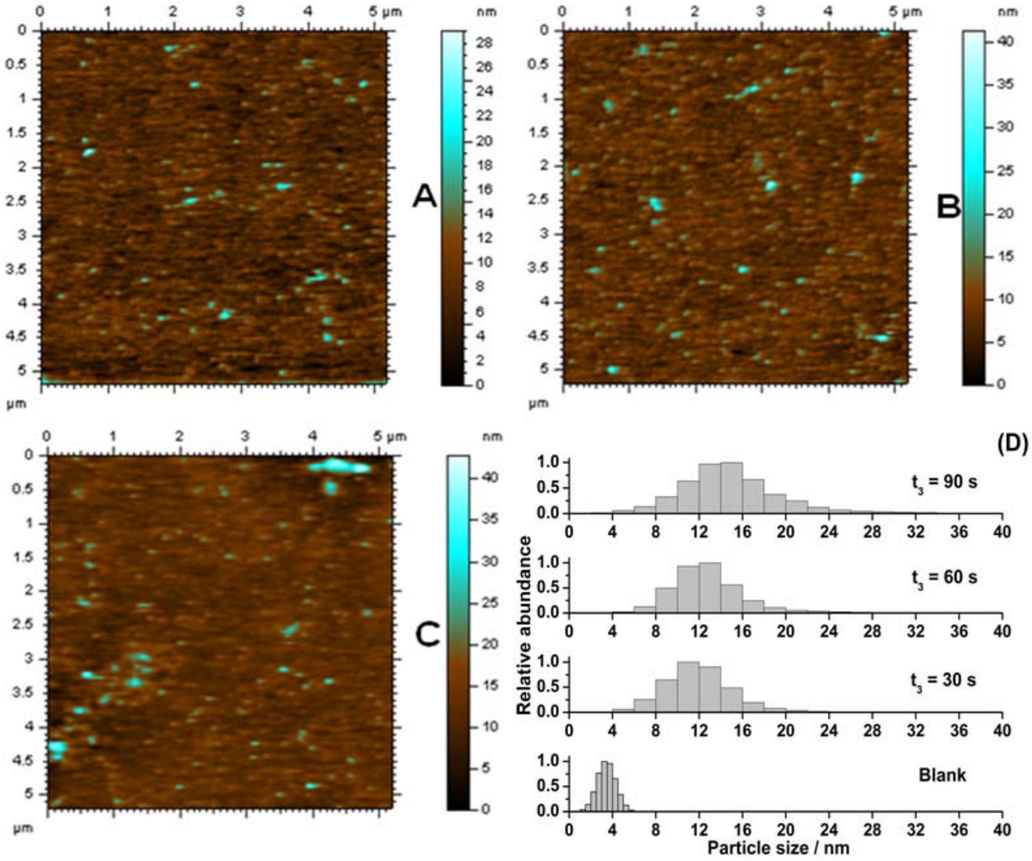

Figure 3.12 *2D(XY)-AFM topographies (5 µm × 5 µm) of PbNPs on Au-QC deposited at* E_3 *= -0.475 V for* t_3 *= (A) 30 s, (B) 60 s and (C) 90 s.* E_1, E_2, t_1 *and* t_2 *were kept constant at 0.2 V, -0.530 V, 60 s and 60 ms, respectively; (D) Particle size histogram of PbNPs as a function of* t_3.

The results show that both the size and polydispersity of PbNPs increase on increasing t_3. The diffusion zones of larger PbNPs overlap with diffusion zones of smaller PbNPs for longer growth pulse duration. This allows larger PbNPs to draw an increased disproportionate fraction of the Pb_{aq}^{2+} ions at the expense of the growth of smaller particles. Thus, due to the lack of Pb_{aq}^{2+} ions in the solution around the smaller PbNPs, they become unstable and start dissolving leading to polydispersity in particle size and shape. These observations are also in agreement with the reported studies on the nucleation and growth of silver nanoparticles on ITO surface *[97,130]*.

3.2.1.4.3. Effect of the Growth Pulse Potential upon the Deposited PbNPs

The 2D(XY)-AFM topographies of PbNPs deposited on Au-QCs for a constant duration (t_3) of 60 s as a function of growth pulse potential (E_3) of -0.475 V, -0.465 V and -0.455 V are shown in *Figure 3.13A-C.* In this context, it should be recalled that E_1, E_2, t_1 and t_2 were kept constant at the values of 0.2 V, -0.530 V, 60 s and 60 ms, respectively. As E_3 decreases, the fraction of the upper contrast colour (at greater than about 12 nm in the vertical colour bar) as well as the extent of overlaps decrease in the topographies. The band of the particle size histogram is shifted toward the lower size upon decreasing E_3 (*Figure 3.13D*). *Table 3.3* shows some more characteristics of the deposited PbNPs as a function of E_3. *Figure 3.13* and *Table 3.2* reveal that the particle size decreases consistently upon decreasing E_3 from -0.475 V to -0.455 V. Further, the maximum particle size observed in each histogram also decreases significantly with decreasing E_3. The S_a and S_q values also decrease with the decreasing E_3. The roughness values rarely decrease upon decreasing E_3 from -0.475 V to -0.465 V; but the same significantly decreases for further decreasing E_3 to -0.455 V. This significant decrease of roughness at -0.455 V (a potential lesser than -0.465 V (E_{th})) occurs not only due to the fall of growth rate of the existing Pb nuclei, but also for the ceasing of the further birth of any fresh nuclei during the growth of the existing nuclei. The results obtained show that, the size as well as the polydispersity of PbNPs decrease with the decreasing E_3 to lesser negative potentials. At a potential earlier to E_{th}, the growth rate becomes slow and progressive nucleation ceases as the potential becomes insufficient to cause any fresh nucleation on a bare surface, but becomes sufficient to grow the nucleated centers only.

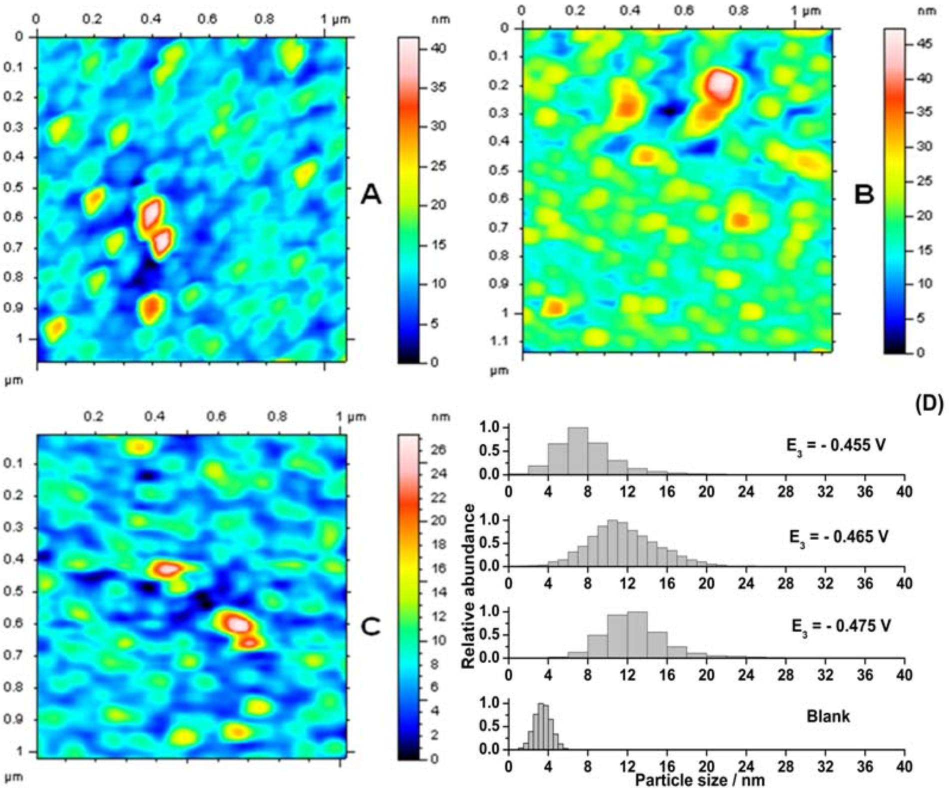

Figure 3.13 *2D(XY)-AFM topographies (1 μm × 1 μm) of PbNPs on Au-QC deposited for t_3 = 60 s for E_3 = (A) -0.475 V, (B) -0.465V and (C) -0.455 V. E_1, E_2, t_1 and t_2 were kept constant at 0.2 V, -0.530 V, 60 s and 60 ms, respectively. (D) Particle size histogram of PbNPs as a function of E_3.*

Table 3.3 *Some characteristics of the deposited PbNPs as a function of E_3.*

Parameters	***E*$_3$ / V**			**Blank**
	-0.475	**-0.465**	**-0.455**	
S_a (nm)	2.71	2.67	2.36	0.62
S_q (nm)	4.06	3.48	3.40	0.77
Mean size ± *σ* (nm)	13 ± 4	11 ± 4	8 ± 5	3.5 ± 1
Maximum size from the histogram (nm)	44	47	36	8

The studies revealed that the synthesis of PbNPs, without a Pb adlayer, can be achieved by restricting the under potential deposition (UPD) and simultaneously facilitating the nucleation and growth of 3D islands on the substrate. It is understood that, the first positive longer pulse removes the pre-adsorbed Pb^{2+} ions from the substrate. During the application of a short and high cathodic pulse (second pulse) in the overpotential deposition (OPD) range, instantaneously the electrode-electrolyte interface becomes devoid of the Pb^{2+} ions and then the diffusion of ions from the bulk of the solution to the interface controls the overall electrodeposition process. In view of this, the potentiostatic short pulses of high overpotential in the OPD range, just after the first positive pulse, can serve the purpose of restricting UPD of Pb and subsequently promoting the formation of 3D islands of Pb.

3.2.1.5. Exploring the Electrocrystallization Mechanism of Pb on Au

The average size and the size dispersity of the PbNPs could be controlled by tuning the pulse parameters of the “potentiostatic triple pulse strategy (PTPS)”. It should be noted that the ‘triple pulse’ was first termed by Adzic et al. *[98]*; in which the sequence of the pulses started with a negative pulse to deposit silver crystallites, then a positive pulse to dissolve them all, but a few, which then serve as sites for growth in the third negative pulse. It is important to remember that the discussed PTPS is strategically much different than the ‘triple pulse’ of Adzic et al. The mechanism of nucleation and growth of Pb on Au by PTPS is qualitatively discussed in this section.

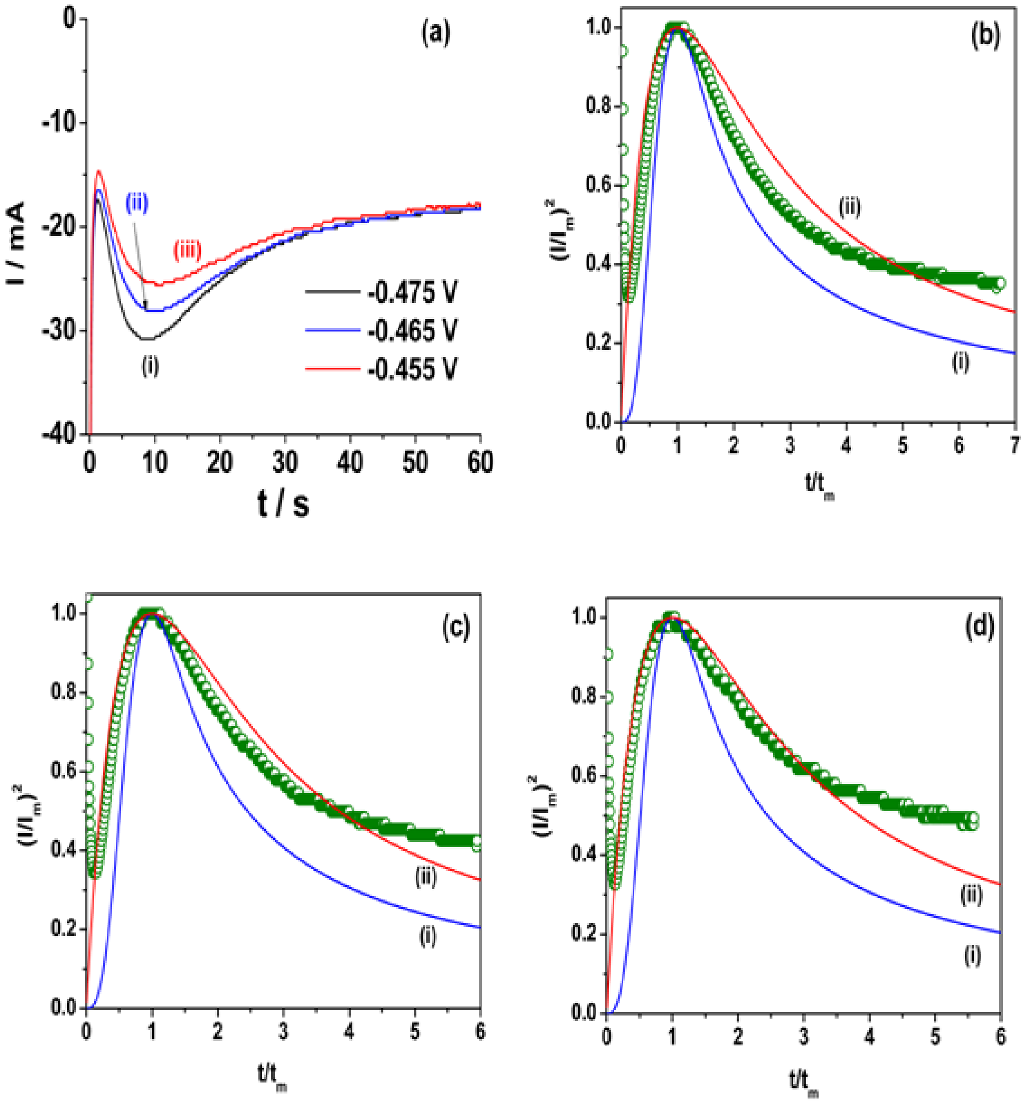

Figure 3.14 *(a) Chronoamperograms of 1 mM* $Pb(ClO_4)_2$ *in 0.1 M* $HClO_4$ *on Au-QC recorded at* E_3 *= (i) -0.475, (ii) -0.465, (iii) -0.465 V for 60 s (*t_3*); Preceded pulses:* E_1 *= 0.2 V,* t_1 *= 60 s,* E_2 *= -0.530 V,* t_2 *= 60 ms. The dimensionless plot of* $(I/I_m)^2$ *vs.* t/t_m *for the chronoamperogram of* E_3 *= (b) -0.475, (c) -0.465 V and (d) -0.455 V along with the theoretical curves for progressive (i) and instantaneous (ii) nucleation according to the SH model.*

Figure 3.14a shows the current transients of 1 mM $Pb(ClO_4)_2$ recorded in 0.1 M $HClO_4$ on Au-QC during the growth step (third pulse) of PbNPs under the experimental conditions described in *Figure 3.13*. The current maxima (I_m) of the transient as well as the time (t_m) corresponding to the current maxima change appreciably with E_3. This type of three dimensional multiple nucleation and diffusion controlled growth was qualitatively studied by the dimensionless plot of $(I/I_m)^2$ vs. t/t_m for two limiting cases (i.e. progressive and instantaneous nucleation) using the Scharifker-Hills (SH) model (*Eqs. 1.65, 1.66*). It is important to mention that the quantitative evaluation of the electrocrystallization parameters from the SH model is undisputedly sensitive and controversial *[131-133]*. However, it is still used by the electrodeposition community for a qualitative understanding of the early stage of nucleation and growth *[134-136]*.

Figures 3.14b-d show the dimensionless plots of $(I/I_m)^2$ vs. t/t_m at E_3 = (b) -0.475, (c) -0.465 and -0.455 V, respectively. The nucleation and growth of Pb nuclei become more instantaneous as the overpotential decreases. This may help in the tuning the average size and the size monodisperdity of the PbNPs in PTPS.

3.2.2 Electrocrystallization of PbNPs on Glassy Carbon Electrode

It can be understood from the discussion of *Section 3.2.1.5* that PTPS influences the mechanism of the nucleation and growth of PbNPs on gold and finally produces monodispersed PbNPs on gold. However, the reason behind the considerable improvement in the average particle size as well as size dispersion in PTPS is not well understood. There are two possibilities: (1) the substrate Au leads to a better electrocrystallization of Pb due to the thermodynamic favourable interaction between Au-Pb upto the first monolayer and (2) the sequence, potential, duration of the PTPS leads to better control on the electrocrystallization of Pb. Therefore, the assisting substrate (i.e. the first possibility) should be eliminated first to understand the importance of the PTPS. From this aspect, glassy carbon (GC) provides a low surface energy conductive substrate and exhibits weak metal-substrate interaction.

The nucleation of lead on GC has been investigated for decades by single potentiostatic pulse *[137]*. Further, 'potentiostatic double pulse strategy (PDPS)' consisting of a short highly cathodic pulse from the open circuit potential followed by a longer cathodic pulse at low overvoltage is very popular for the electrosynthesis of the metal nanoparticles *[97, 130]*. Here, on the basis of the electrocrystallization of PbNPs on GC, we report that the number of potentiostatic pulse and its potentials and sequences have great influence on the mechanism of electrocrystallization as well as in the particle size and size dispersion. We note that, the polishing of GC electrode in between the experiments was carried out by following standard protocol (*Section 2.1.2.1*). The polishing of GC electrode in between the experiments did not alter the overall activation and quality of the GC surface (*Figure 3.15*).

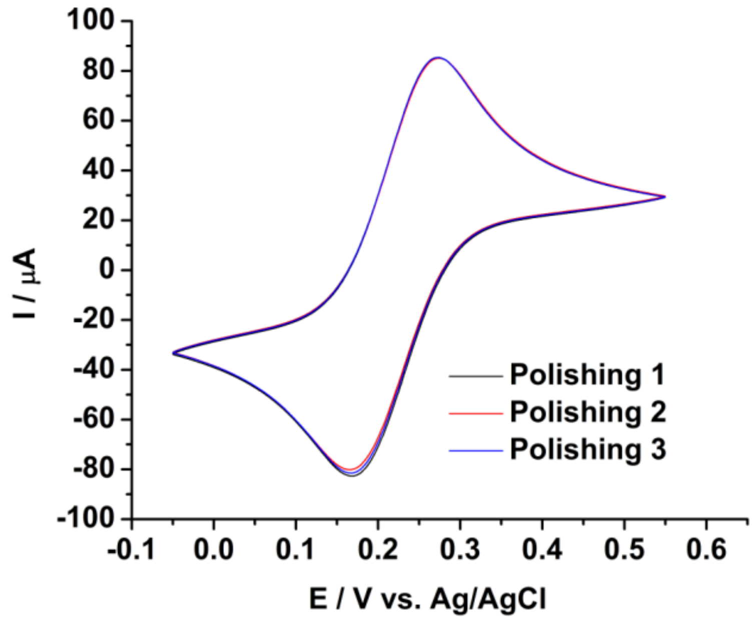

Figure 3.15 *Cyclic voltammograms of 5 mM* $K_3[Fe(CN)_6]/K_4[Fe(CN)_6]$ *in 0.1 M KCl at GC electrode polished in between the experiments. Polishing -1, -2 and -3 represent the polished electrodes between the 1st and 2nd, 2nd and 3rd, and 3rd and 4th experiments, respectively.*

Figure 3.16A shows the cyclic voltammogram of 1 mM $Pb(ClO_4)_2$ in 0.1 M $HClO_4$ on GC electrode at a scan rate of 10 mV s^{-1}. The potential scan starts from 0.4 V towards the cathodic direction. A surge of cathodic current starts from -0.49 V for the reduction of Pb(II)/Pb resulting in a cathodic peak at -0.58 V. In the reverse scan direction, two crossovers were observed at -0.55 V and -0.47 V between the forward and the reverse scans. This characteristic nucleation loop suggests that the deposition of Pb(II) on GC has a nucleation overpotential, which is eventually the extra potential applied for nucleation over the thermodynamic equilibrium potential of Pb(II)/Pb(0) *[138]*. Since, the activity of Pb(0) and GC in solid states are unity; thus the nucleation overpotential is an indirect measure of the kinetic hindrance of nucleation of Pb on GC than the nucleation of Pb on Pb. Therefore, GC does not provide any favorable interaction on Pb deposition i.e. Pb adatoms-adatoms interaction is stronger than the interaction of Pd adatoms with the GC surface. Thus, nuclei of Pb are expected to be formed on GC followed by the three dimensional diffusion controlled growth *[139]*. At more positive potential, the anodic current increased due to the oxidation of the deposited Pb. A sharp anodic peak was observed with a peak potential at -0.41 V. It indicates that the anodic dissolution of the lead deposits is quite labile under the present experimental conditions. The open circuit potential (OCP, E_{OCP}) of the system was measured as -0.41 V, which is in agreement with the expected value (-0.40 V) calculated from the Nernst equation *[140]*. The open circuit potential or equilibrium potential, for the overall reaction at room temperature is given by Nernst equation: OCP $= E_0^{'} + 0.0295 \log[Pb(II)]$; where; $E_0^{'} = -0.312$ V (vs. Ag/AgCl(saturated)), and [Pb(II)] is 0.001 M.

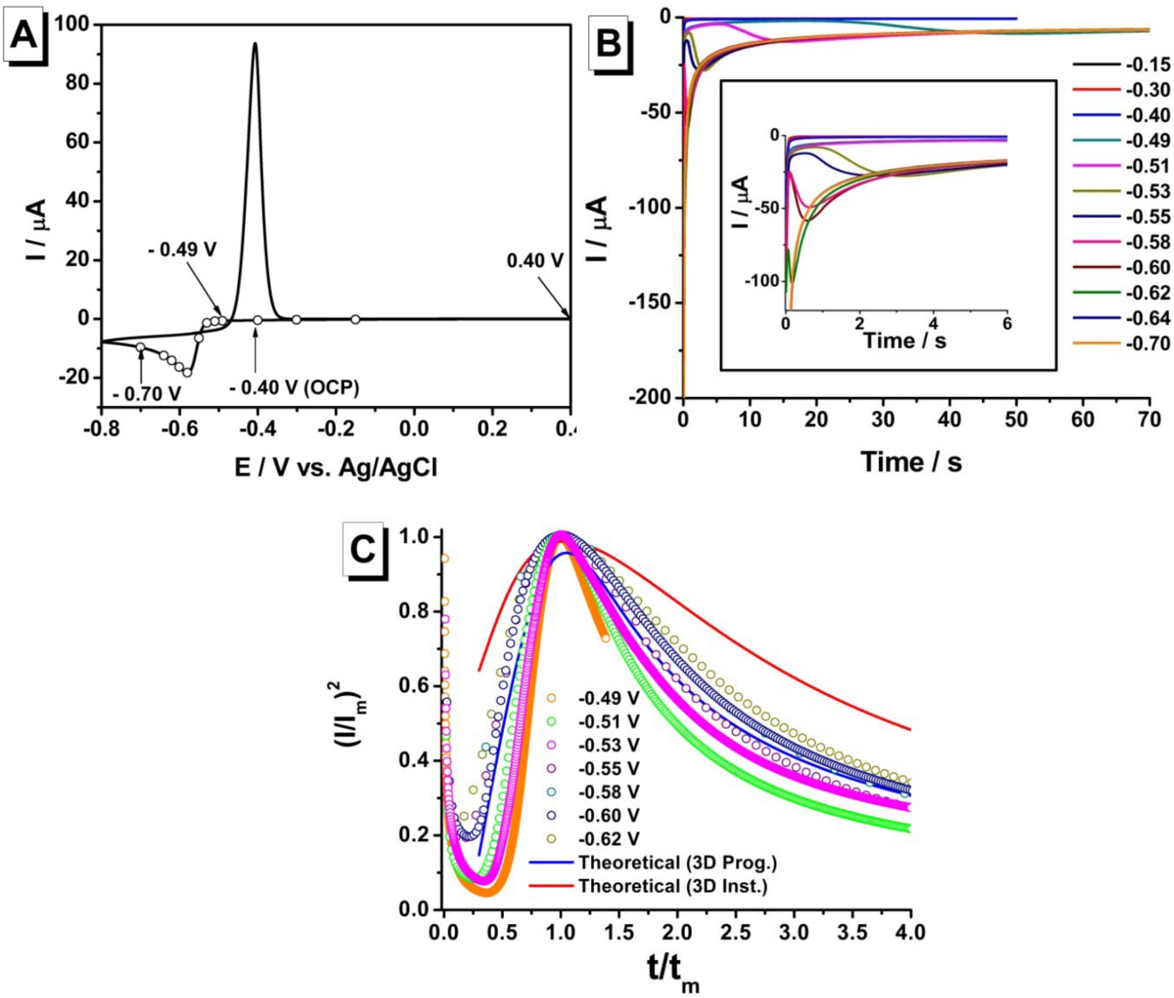

Figure 3.16 *(A) Cyclic voltammogram of 1 mM* $Pb(ClO_4)_2$ *in 0.1 M* $HClO_4$ *on GC electrode at a scan rate of 10 mV* s^{-1}*. (B) Chronoamperograms recorded at -0.15, -0.30, -0.40, -0.49, -0.51, -0.53, -0.55, -0.58, -0.60, -0.62, -0.64 and -0.70 V; Preceded pulse:* E_1 *= 0.4 V,* t_1 *= 60 s. (C) The dimensionless plot of* $(I/I_m)^2$ *vs.* t/t_m *along with the theoretical curves for instantaneous and progressive nucleation according to SH model.*

The mechanism of nucleation and growth of lead on GC by PDPS was studied by holding the potential of the electrode initially at +0.40 V (E_1) for 60 s (t_1) followed by a sharp change to a different potential (E_2) as indicated by the circles in *Figure 3.16A*. The current transients were recorded at E_2 for a duration ranging between 10-70 s and are shown in *Figure 3.16B*. No characteristic nucleation and growth features were observed, except that the discharge current originated from the double layer molecular rearrangements within a few ms, for the current transients recorded up to 70 s at -0.15, -0.3, -0.4 V. The cathodic current sharply decreased at very short time scale also at -0.49 V due to the rearrangement of electrolyte species at the electrode-electrolyte interface, but it slowly increased after a delay time for ~22 s. This is attributed to an increase in the overall electroactive area due to increase in the number of Pb nuclei and/or growth of Pb nuclei. The spherical diffusion zone around each nucleus grew with time and at time (t_m) 50.44 s corresponding to the current maximum (I_m; -8.4 μA), these spherical diffusion zones overlapped and mass transfer became linear to GC surface. The change in diffusion regime led to a decrease in the current with time following Cottrell equation. The value of t_m decreased, but the value of I_m increased as E_2 became more cathodic. At E_2 = -0.62 V, the values of t_m and I_m were observed as 0.64 s and 49.2 μA, respectively. It indicates that the rate of reduction of Pb(II) on GC increased with increasing the cathodic overpotential. For E_2 = -0.64 and -0.70 V, no current maxima could be resolved in the experimental time frame due to the fast nucleation and fast change of diffusion regime to Cottrell behavior. No characteristics of 2D or 2D-2D type transients were observed in any case. This type of three dimensional multiple nucleation and diffusion controlled growth was qualitatively studied by the dimensionless plot of $(I/I_m)^2$ vs. t/t_m for two limiting cases viz. instantaneous and progressive nucleations by following Scharifker-Hills(SH) model (*Eqs. 1.65, 1.66*) and are shown in *Figure 3.16C*. It could be inferred from *Figure 3.16C* that at E_2 = -0.49 V, the nucleation and growth was progressive i.e. new nuclei being continuously formed at low nucleation rate during the whole process of deposition. As the cathodic overpotential increased to -0.62 V, the nucleation and growth tended towards the instantaneous i.e. all the nuclei being immediately created at high nucleation rate and the number of nuclei remained constant during the growth process. From our present understanding, we anticipated that the nucleation and growth of Pb nuclei would be instantaneous at E_2 = -0.7 V. Here, we have not put any effort to extract the nucleation parameters from the current transients by Scharifker–Mostany (SM); Sluyters–Rehbach, Wijenberg, Bosco, Sluyters (SRWBS) and Heerman-Tarallo (HT) models; because our recent study revealed that no correlation exists in the nucleation parameters obtained from SH, SM, SRWBS, and HT models *[131]*.

Based on the above mentioned analysis as well as with the experience gained from earlier discussions, we designed a similar PTPS strategy, where the first pulse (E_1) was fixed at 0.4 V for 60 s (t_1), followed by a short second pulse (E_2) at -0.7 V for 0.1 ms (t_2) and then a third pulse (E_3) at -0.49 V for 70 s (t_3). The current transient was recorded during the third pulse and is shown in *Figure 3.17A(i)*. The current transient recorded during PDPS (ii) at -0.49 V (where E_2 for time t_2 was skipped) was also overlaid in *Figure 3.17A*. The time for current maximum significantly decreased to 0.94 s in PTPS from 50.44 s in PDPS, though the maximum current did not change much (PTPS: -7.6 µA; PDPS: -8.4 µA). In PTPS, as t_2 increased from 0.1 ms to 1 ms, the t_m increased from 0.94 s to 34.1 s, though i_m did not change much (*Figure 3.17A(iii)). When* E_1 was changed to the OCP value (-0.4 V) keeping all other parameters constant, the t_m increased from 0.94 s to 42.1 s, though i_m did not change much *(Figure 3.17A(iv))*. The dimensionless plots of $(I/I_m)^2$ vs. t/t_m (*Figure 3.17 B*) showed a crucial change in mechanism of nucleation and growth. The nucleation and growth of Pb nuclei at -0.49 V became instantaneous in PTPS (i), while it was predominantly progressive in PDPS (ii). Moreover, the domination of the instantaneous type of nucleation and growth decreased as t_2 became longer (iii). Similar behaviour was also observed while E_1 was changed to the OCP value (-0.4 V) (iv).

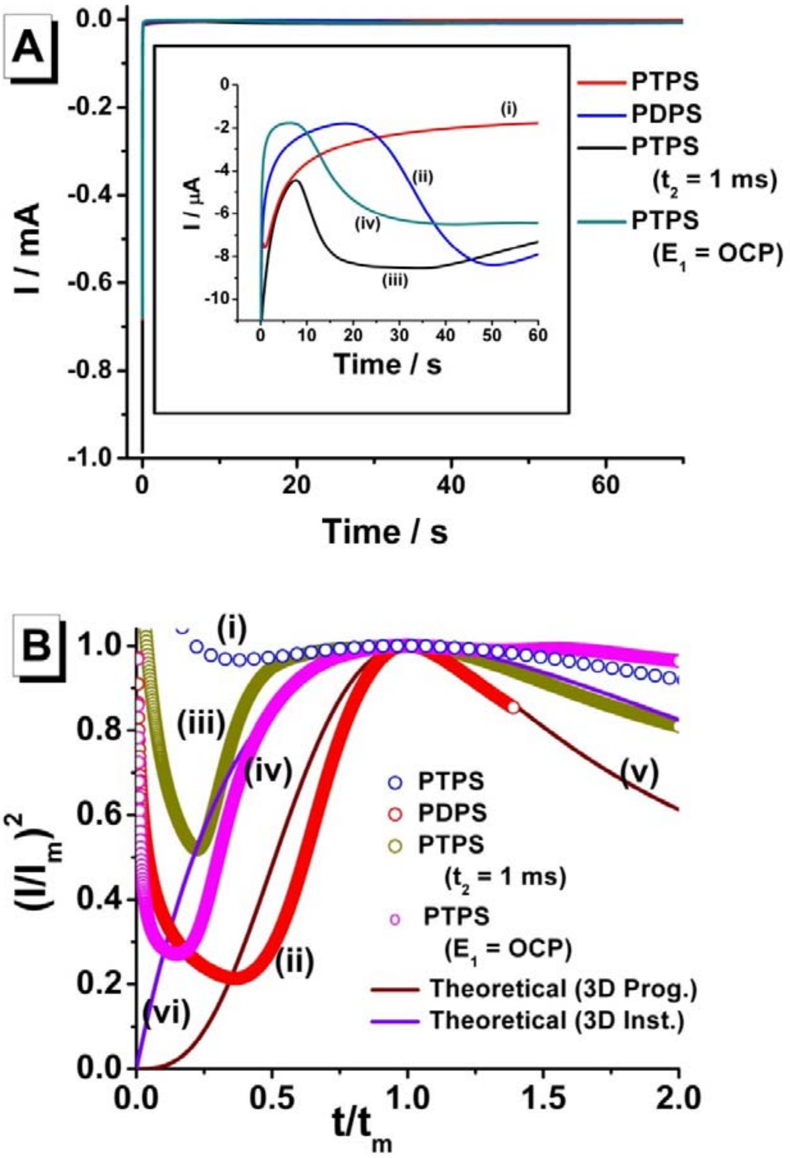

Figure 3.17 *(A) Chronoamperograms recorded at -0.49 V for 70 s for (i) PTPS (Preceded pulses:* $E_1 = 0.4$ *V,* $t_1 = 60$ *s,* $E_2 = -0.7$ *V,* $t_2 = 0.1$ *ms), (ii) PDPS (Preceded pulse:* $E_1 = 0.4$ *V,* $t_1 = 60$ *s), (iii) PTPS (Preceded pulses:* $E_1 = 0.4$ *V,* $t_1 = 60$ *s,* $E_2 = -0.7$ *V,* $t_2 = 1$ *ms); (iv) PTPS (Preceded pulses:* $E_1 = -0.4$ *V,* $t_1 = 60$ *s,* $E_2 = -0.7$ *V,* $t_2 = 0.1$ *ms). (B) The dimensionless plot of* $(I/I_m)^2$ *vs.* t/t_m *along with the theoretical curves for instantaneous and progressive nucleation according to SH model.*

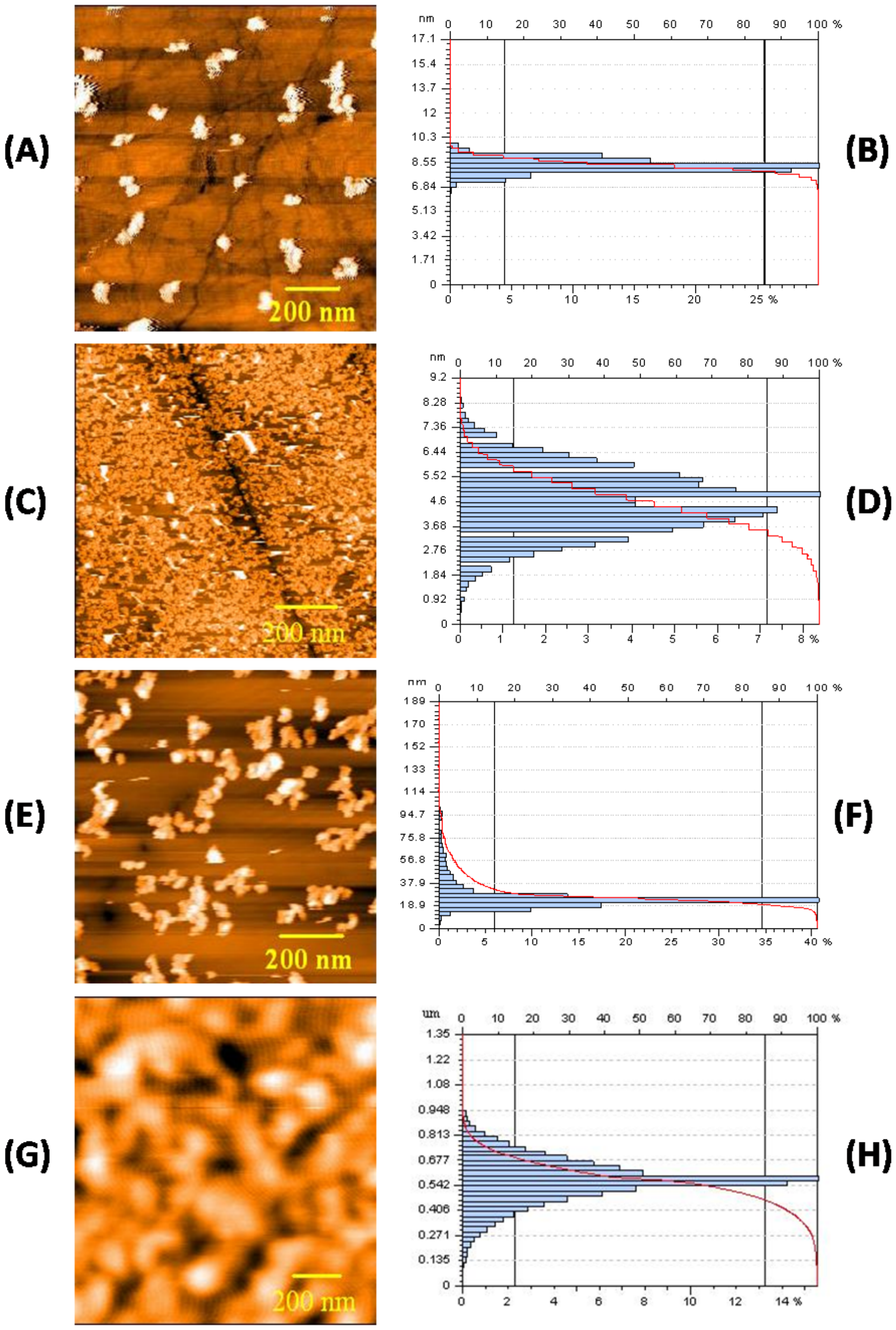

Figure 3.18 *The surface topographies (A,C,E,G) and particle size distributions (B,D,F,H) of PbNPs after (A,B) PTPS (E_1 = 0.4 V, t_1 = 60 s, E_2 = -0.7 V, t_2 = 0.1 ms, E_3 = -0.49 V, t_3 = 70 s), (C,D) PDPS (E_1 = 0.4 V, t_1 = 60 s, E_2 = -0.49 V, t_2 = 70 s), (E,F) PTPS (E_1 = 0.4 V, t_1 = 60 s, E_2 = -0.7 V, t_2 = 1 ms, E_3 = -0.49 V, t_3 = 70 s); (G,H) PTPS (E_1 = -0.4 V, t_1 = 60 s, E_2 = -0.7 V, t_2 = 0.1 ms, E_3 = -0.49 V, t_3 = 70 s).*

The final surface topographies of the PbNPs/GC at the end of 70 s of the current transients (i-iv) are shown in *Figure 3.18*. The instantaneous nucleation and growth of PTPS resulted into discrete and monodispersed (average size 8 ± 2 nm) tapped hemispherical PbNPs (*Figure 3.18*A,B). However, the progressive nucleation and growth and prolonged induction time resulted in small, overlapped and polydispersed (average size 5 ± 5 nm) PbNPs (*Figure 3.18C,D*). Moreover, in PTPS, on increasing the second pulse duration, the dispersity of the size of PbNPs increased (*Figure 3.18E,F*). It is interesting to note that both the size and dispersity in size of the PbNPs increased when the PTPS experiment was started from OCP (*Figure 3.18G,H*).

The difference between PTPS and PDPS in the mechanism of nucleation and growth as well as in the dispersion in particle size of PbNPs arose because of the presence of a very short nucleation pulse of high cathodic overpotential in between the start and growth pulses. In case of PDPS, when the potential is switched from 0.4 V to -0.49 V, the surface sites on GC got slowly activated during the prolonged induction period of ~22 s. Then nucleation and growth of PbNPs passed through slow progressive type of nucleation depending on the dynamics of activation-deactivation of surface sites. In PTPS, an enormous number of surface sites activated in very short time scale, when the potential is switched from 0.4 V to -0.7 V. However, due to very short imposition time (0.1 ms) of this pulse, a large number of active sites remained unoccupied as well as the electrode-electrolyte interface remains in a non-steady state and thus while the potential was switched back to -0.49 V, instantaneous nucleation happened to these unoccupied active sites (the dissolution of the subcritical nuclei upon the potential transition replenishes the Pb(II) ions in the double layer). This mechanism is believed to squeeze the size dispersion of PbNPs. Again, the majority of the active sites became occupied on increasing the duration of the second pulse as well as the electrode-electrolyte interface attains a steady state; thus its influence on nucleation and growth became inferior at the third pulse. That is why the dispersion in the particle size comparatively increased on increasing the duration of the second pulse. The start potential is crucial to restrict the irregular nucleation and growth of the pre-adsorbed Pb(II) on the GC surface. At OCP, a sufficient amount of Pb(II) ions got adsorbed at the oxygenated functionalities on GC surface and its irregular nucleation and growth throughout three pulses resulted into the large particle size distribution and overlapped particles.

Therefore, the better monodispersity in the particle size could be achieved by the PTPS because of the controlled nucleation and growth at the final (the third) pulse step. The history of the GC surface, just before the final pulse, was created by the controlled activation and nucleation during the first and second pulses, respectively. However, *Figure 3.18* shows some aggregates of the PbNPs. It is important to note that the active sites are randomly distributed on the electrode in the absence of any physical or chemical templates. Therefore, it is still challenging to avoid particle coalescence by the potentiostatic pulse strategies on a template-free substrate. However, the discrete particles could be formed by the multiple galvanostatic pulse strategy on a template-free electrode and it will be discussed in the next chapter.

3.3. Conclusions

The work presented in this chapter demonstrates that electrosynthesis of PbNPs of controlled size and size distribution on a template free gold surface by PTPS. The CV and EQCM studies have been utilized to locate the threshold potential for nucleation (E_{th}) and the potential of zero charge (PZC). Further studies have shown that the electrodeposition of PbNPs occurred with quantitative coulombic efficiency. The choice of the first pulse potential at positive to the PZC basically reduces the effective particle size by restricting deposition of any pre-adsorbed Pb_{aq}^{2+} ions at the latent active sites on the Au surface. ASV and XRD studies suggested the metallic form of electrosynthesized PbNPs; whereas XPS studies suggested that PbNPs are not in virgin metallic state and are covered with the chemisorbed oxygen.

The second part of this chapter reveals, for the first time, the cause of improvement in the particle size and size dispersion in PTPS compared to PDPS. It also shows a prospective of PTPS for template-free electrosynthesis of metal nanoparticles. The potential of the start (first) pulse is important to restrict the irregular nucleation and growth of the pre-adsorbed ions on the electrode surface and OCP is not ideal selection for the start potential. The potential and duration of the seed (second) pulse are the most important features of the PTPS as it implements the number of unoccupied active sites to the following growth pulse. The better monodispersity in the particle size could be achieved by the controlled nucleation and growth in the final (third) pulse with the pre-history effects of the first and second pulses on the GC surface. It can be noted that both thermodynamics and surface kinetics parameters (of both substrate and the deposited metals) play a key role in the electrochemical nucleation and growth of metal nanoparticles on the substrate. Therefore, the present work is expected to motivate detailed investigations of the thermodynamics and surface kinetics of PTPS for the electrosynthesis of metal nanoparticles. After detailed investigation of the metal(deposited)-substrate pair, the PTPS could also be applicable to metals other than Pb. Further, the critically designed PTPS can electrochemically produce discrete and monodispersed capped hemispherical metal nanoparticles on a low surface energy conductive substrate. This study would be useful for designing systems of controlled size for fundamental studies and practical purposes in the field of material sciences and condensed-matter physics.

CHAPTER 4

Template-free Electrosynthesis of Gold Nanoparticles (AuNPs)

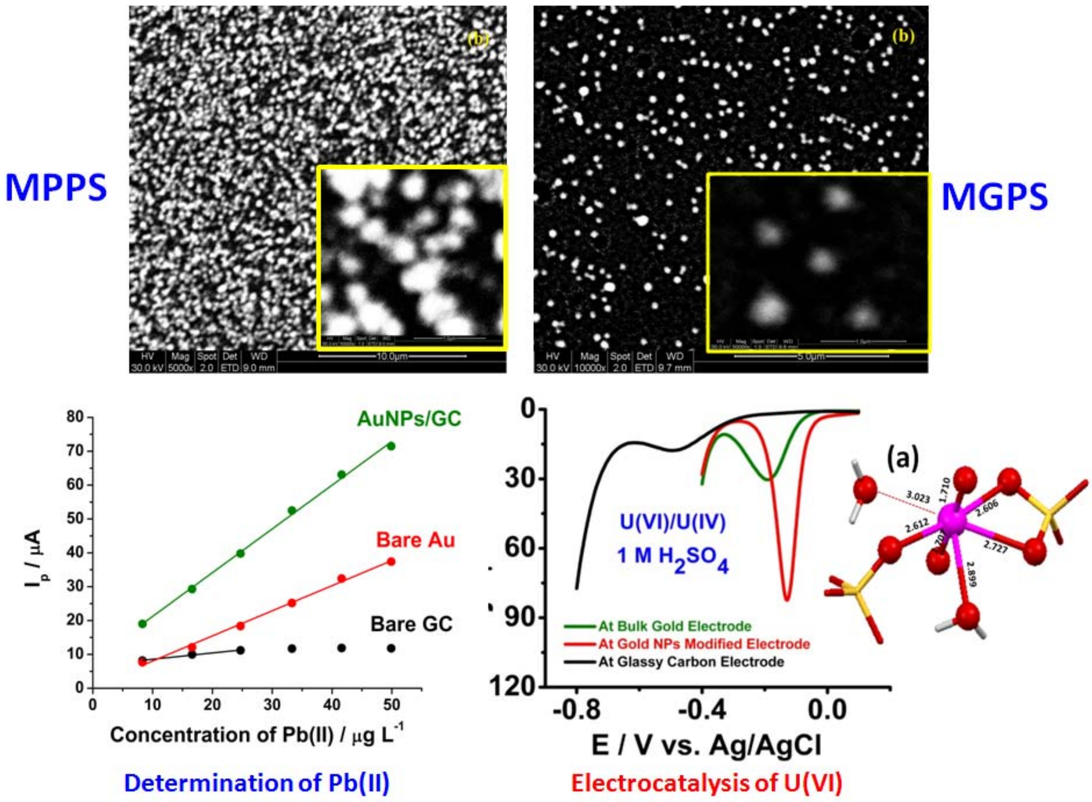

Sections of this chapter have been published in the following peer-reviewed journals:

‘Template-free electrosynthesis of gold nanoparticles of controlled size dispersion for the determination of lead at ultratrace levels’, Saurav K. Guin, Jisha S. Pillai, Arvind S. Ambolikar, Abhijit Saha, Suresh K. Aggarwal, *RSC Advances*, **3** (2013) 17977-17988.

‘An insight into the electrocatalysis of uranyl sulphate on gold nanoparticles modified glassy carbon electrode’ Saurav K. Guin, Parvathi K., Arvind S. Ambolikar, Jisha S. Pillai, Dilip K. Maity, S. Kannan, Suresh K. Aggarwal, 2014 (*Submitted to Electrochim. Acta).*

4.1. Research Aim of this Chapter

Gold metal behaves as an inert material, with high stability in corrosive environments and low catalytic activity for most of the reactions. Therefore, bulk gold metal has not received much attention in chemistry. On the other hand, gold nanoparticles (AuNPs) have received great interests in the development of sensors due to their attractive electronic, optical, thermal as well as catalytic properties and potential applications in the fields of physics, chemistry, biology, medicine, material science and their different interdisciplinary fields *[18, 141-157]*. Therefore, the controlled synthesis of AuNPs, including the chemically template assisted synthesis, attracts considerable attention from a fundamental and practical point of view *[18, 39, 141, 143-145, 158-161]*.

This chapter discusses two electrochemical strategies viz. (1) Multiple Potentiostatic Pulse Strategy (MPPS) and (2) Multiple Galvanostatic Pulse Strategy (MGPS) for the template free electrosynthesis of AuNPs on glassy carbon (GC) electrode. The first part of this chapter deals with the investigations of the electrodeposition of gold on GC for developing the strategies for the electrosynthesis of AuNPs.

As discussed in *Section 3.2.1*, Pb has a favourable tendency to atomically deposit on a gold surface. Therefore, the second part of this chapter describes the use of AuNPs for the determination of lead (Pb) at ultratrace levels. Further, the oxygen reduction on AuNPs occurs in the potential range -0.5 to -0.15 V vs. Ag/AgCl (saturated KCl) reference electrode *[156]*, which is in similar range of reduction potential of the uranyl (UO_2^{2+}) complexes on mercury pool electrode *[162]*. Therefore, the possibility for catalytic reduction of $U^{VI}O_2^{2+}$ in 1 M H_2SO_4 at AuNPs supported on glassy carbon electrode (AuNPs/GC) was explored in the third part of this chapter.

4.2. Results and Discussion

4.2.1. Synthesis of AuNPs

4.2.1.1. Cyclic Voltammetry of $H[AuCl_4]$ on a GC Electrode in 0.1 M HCl

Figure 4.1 shows the cyclic voltammograms of 1 mM $H[AuCl_4]$ in 0.1 M HCl on a GC electrode at a scan rate of 100 mV s^{-1} for (1) first, (2) second, (3) third and (4) fourth cycles. A single reduction peak was observed at 0.314 V during the forward scan (starting from 1.5 V) in the first cycle. This is attributed to the reduction of Au(III) to Au(0) on the bare GC electrode obeying the following *Eq. 4.1*:

$$H[AuCl_4] + 3\,H^+ + 3\,e^- = Au + 4\,HCl \qquad (4.1)$$

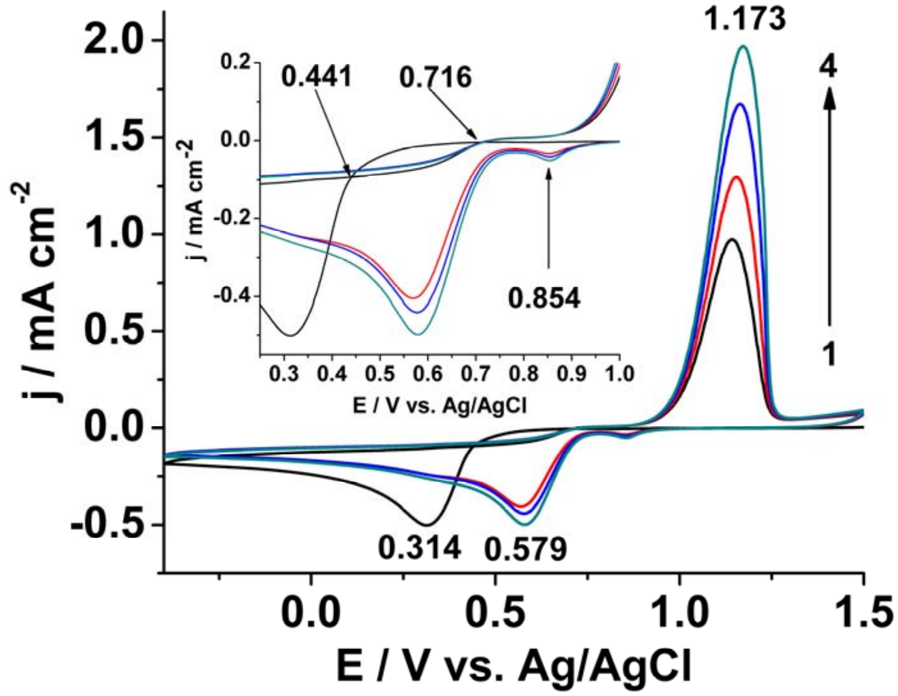

Figure 4.1 *Cyclic voltammograms of 1 mM $HAuCl_4$ in 0.1 M HCl on GC at a scan rate of 100 mV s^{-1} for (1) 1st, (2) 2nd, (3) 3rd and (4) 4th cycles. Starting potential is 1.50 V. Inset shows the magnified image in the potential range 0.25-1.00 V.*

In the backward scan (starting from -0.4 V), a very small current crossover was observed at about 0.441 V and the backward cathodic current became higher than the forward one in the potential range 0.441-0.716 V. This is consistent with thermodynamics which predicts that the deposition of Au(III) on Au is easier than the nucleation of gold on the GC electrode. A sharp anodic peak at 1.173 V represents the stripping of Au(0) to $[AuCl_4]^-$ by obeying the following *Eq. 4.2:*

$$Au + 4\ Cl^- = [AuCl_4]^- + 3\ e^- \qquad (4.2)$$

The gold deposited on the GC electrode during forward scan in the first cycle was not completely stripped out from the GC electrode surface during the backward scan. Therefore, Au deposition during the second cycle preferentially occurred on the gold active sites created during the first cycle. From the second cycle onwards, two reduction peaks were observed at 0.854 V and 0.579 V during the forward scan. The reduction peak at 0.579 V is attributed to the reduction of Au(III) to Au(0) on the trace amount of gold remaining on the GC electrode after the first cycle. The open circuit potential (OCP, $E_0^{'}$) of 1 mM $H[AuCl_4]$ in 0.1 M HCl was measured as 0.820 V. It was in agreement with the expected value (0.824 V) calculated from the Nernst equation. The standard redox potential of $[AuCl_4]^-/Au(0)$ reaction was 0.804 V vs. Ag/AgCl (saturated) reference electrode *[163]*. Therefore, the cathodic peak of $[AuCl_4]^-/Au(0)$ appeared at an overpotential ($\eta = E - E_0^{'}$) of -0.506 V on the GC electrode and -0.241 V on deposited Au active sites remaining on the GC electrode. This is consistent with the thermodynamics which predicts that the deposition of gold requires less energy on gold than on GC.

From the second cycle onwards, the small cathodic peak at 0.854 V corresponds to the reduction of $[AuCl_4]^-$ to $[AuCl_2]^-$ *[163]*. However, the electro-generated $[AuCl_2]^-$ is unstable in solution and disproportionates to Au(0) and $[AuCl_4]^-$.

$[AuCl_4]^- + 2\ e^- = [AuCl_2]^- + 2\ Cl^-$ (4.3)

$3\ [AuCl_2]^- = 2\ Au + [AuCl_4]^- + 2\ Cl^-$ (4.4)

$[AuCl_2]^-$ is adequately stable in moderately concentrated chloride medium and leads to trace amounts of Au on the GC electrode by the disproportionation reaction of $[AuCl_2]^-$ as shown in *Eq. 4.4*. The Au(I) species are present around 0.80-0.95 V in 0.1 M HCl *[163]*.

4.2.1.2. Chronoamperometry of H[AuCl₄] on a GC Electrode in 0.1 M HCl

The interesting features of the cyclic voltammograms, as discussed above, opened up the possibility of template free electrochemical synthesis of AuNPs on a GC electrode by using judiciously chosen potentiostatic pulses. The key parameters in this technique were the sequence, potential and duration of the potentiostatic pulses. Therefore, an extensive set of preliminary chronoamperometric experiments were carried out by varying the potential and duration of the potentiostatic pulses. The significant observations, which helped us to develop the synthesis strategy, are discussed in the following paragraphs.

Figure 4.2a shows the chronoamperogram of 1 mM $H[AuCl_4]$ in 0.1 M HCl on the GC electrode for three consecutive cycles with a cathodic pulse of -0.13 V and an anodic pulse of 0.92 V for 10 ms each. A small hump at 3 μs was observed in the cathodic transient during the first cycle and this hump slowly decreased and almost vanished in the cathodic transients during the second and third cycles. The anodic transient reached a plateau at ~12 ms after the commencement of the anodic pulse. *Figure 4.2b* shows the chronoamperogram of 1 mM $H[AuCl_4]$ in 0.1 M HCl on the GC and Au electrodes for three consecutive cycles with a cathodic pulse of 0.55 V and an anodic pulse of 0.92 V of 2 s each. Except for the first cathodic transients, both the electrodes showed almost similar shapes of amperograms. The magnified image of the first cathodic transient of *Figure 4.2b* is shown in *Figure 4.2c*. It is noteworthy that an induction period of nucleation on the GC electrode was observed up to ~0.7 s. Then the cathodic current increased because of the nucleation of gold on the GC electrode as well as the higher rate of mass transfer around the hemispherical nuclei. As the time progressed, the nuclei grew further and the hemispherical diffusion zones merged into a linear diffusion zone and the cathodic current reached a maximum at ~1.59 s. Then the current decreased by following the usual Cottrell behaviour. In contrast, the nucleation maximum was not observed at all in the case of the Au electrode under the same experimental conditions. The cathodic transient showed the usual Cottrell behaviour on the Au electrode from the very beginning. Therefore, it can be concluded that the deposition of gold nuclei on the GC electrode surface is not only energetically challenging as compared to that on the Au electrode surface, but the kinetics of the formation of gold nuclei is also slow on the GC electrode surface as compared to that on the Au electrode surface.

The electrocrystallization mechanism of gold on the GC electrode was investigated at -0.13 V and 0.55 V. According to the model including diffusion-controlled growth of hemispherical particles proposed by Scharifker and Hills, the deposition transients for progressive and instantaneous nucleations can be described by *Eq. 1.65 and 1.66*. Non-dimensional $(j/j_m)^2$ vs. t/t_m plots of the experimentally obtained current transients for electrocrystallization of gold on the GC electrode at (a) -0.13 V and (b) 0.55 V are shown in *Figure 4.3* and they were compared with the theoretically calculated curves for instantaneous and progressive nucleations given by *Eq. 1.65 and 1.66*. It is clearly seen that the experimental current transient at 0.55 V corresponds to the model involving progressive nucleation. However, the transient at -0.13 V fits relatively well with the theoretical curve for the instantaneous nucleation.

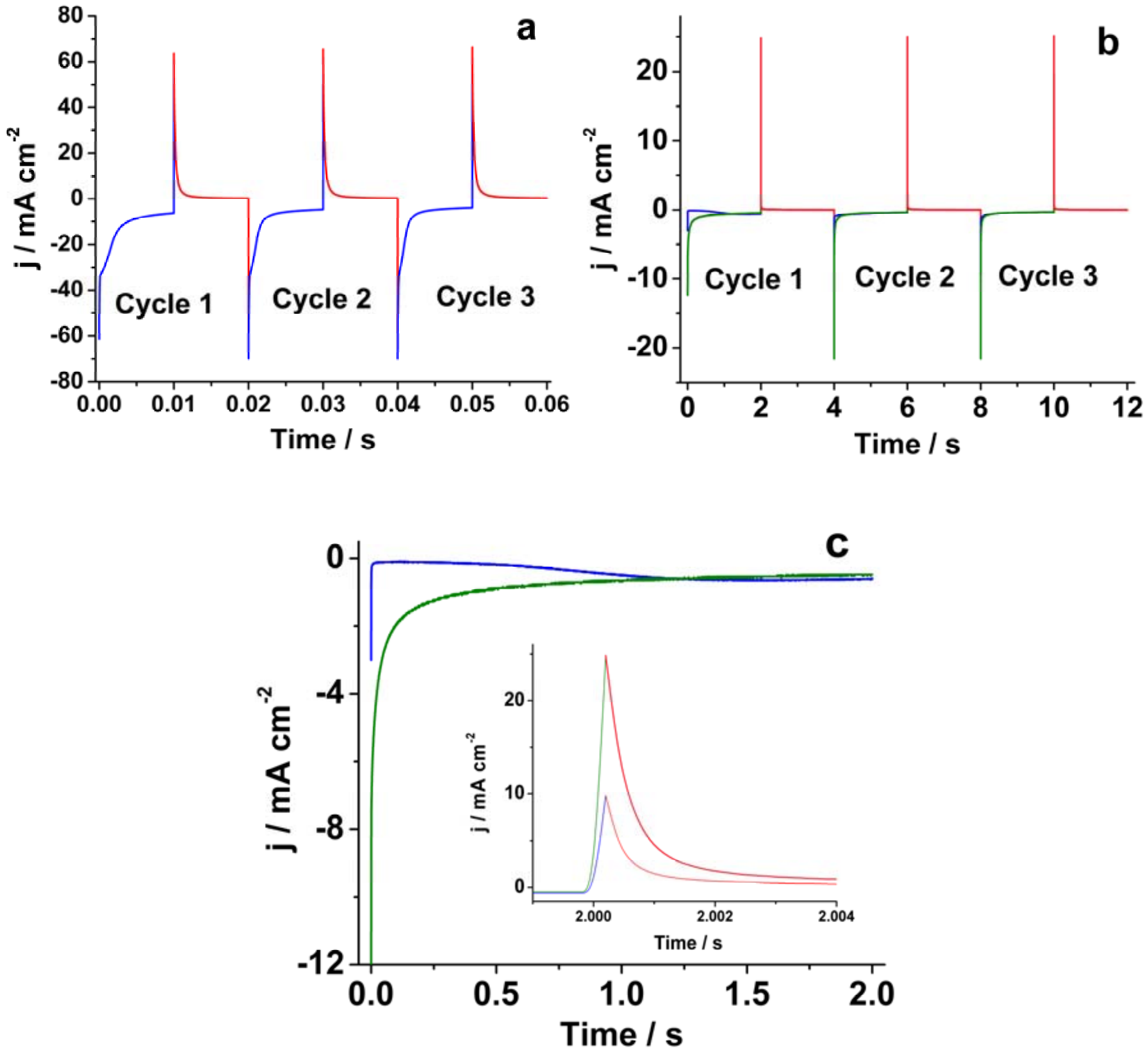

Figure 4.2 *(a) Chronoamperograms of 1 mM* $HAuCl_4$ *in 0.1 M HCl on GC for three consecutive cycles.* $E_i = 0.8$ *V,* $E_a = 0.92$ *V,* $E_c = -0.13$ *V,* $t_c = t_a = 0.01$ *s. Blue and red lines represent the cathodic and anodic transients, respectively. (b) Chronoamperograms of 1 mM* $HAuCl_4$ *in 0.1 M HCl on GC and Au for three consecutive cycles.* $E_i = 0.8$ *V,* $E_a = 0.92$ *V,* $E_c = 0.55$ *V,* $t_c = t_a = 2$ *s. Blue and red lines represent the cathodic and anodic transients on GC, respectively. Green and pink lines represent the cathodic and anodic transients on Au, respectively. (c) The magnified image of the first cathodic transients of (b) and inset shows the magnified view of the first anodic transient of (b).*

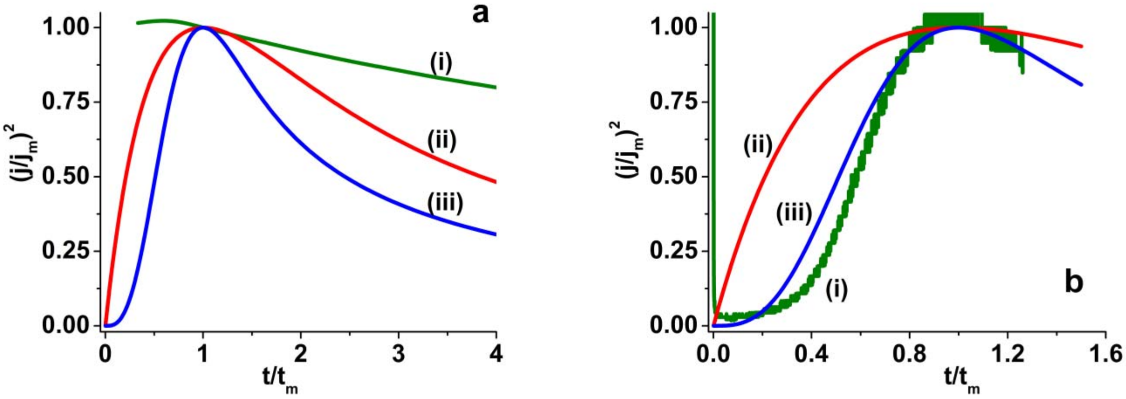

Figure 4.3 *Non-dimensional* $(j/j_m)^2$ *vs.* t/t_m *plots of current transients for electrocrystallization of gold on GC at (a) -0.13 V and (b) 0.55 V. (i) experimentally obtained nucleation curve, (ii) theoretically calculated curve for instantaneous nucleation and (iii) theoretically calculated curve for progressive nucleation according to SH model.*

4.2.1.3. Chronopotentiometry of H[AuCl$_4$] on a GC Electrode in 0.1 M HCl

Figure 4.4 shows that the first cathodic galvanostatic pulse of -0.64 mA cm^{-2} (it is the cathodic peak current of the 1st cycle in *Figure 4.1*) was applied for 60 ms, the potential of the interface sharply dropped from 0.67 V to 0.46 V within 5 ms and attained a steady value till 60 ms (inset of *Figure 4.4*). This is attributed to the formation of the gold nuclei on the GC electrode surface and their subsequent growth under a steady state condition. The potential was then steadily raised to 0.93 V after applying the first anodic galvanostatic pulse of 1.26 mA cm^{-2} (it is the anodic peak current of the 2nd cycle in *Figure 4.1*) for 5 ms. A sufficient amount of subcritical nuclei are believed to be dissolved in the solution during this step (inset of *Figure 4.4*).

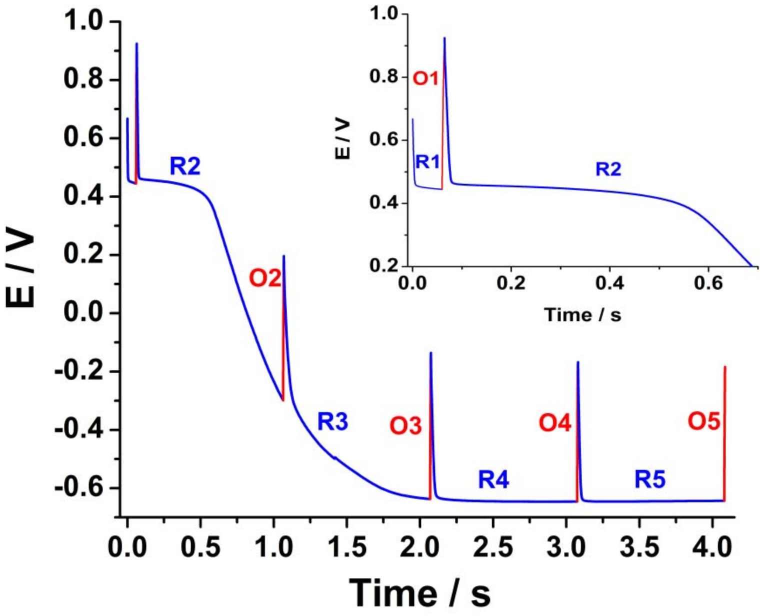

Figure 4.4 *Chronopotentiogram of 1 mM H[AuCl$_4$] in 0.1 M HCl on GC for five consecutive cycles.* j_i *= 0 A cm*$^{-2}$*,* j_c *(R1) = -0.64 mA cm*$^{-2}$*,* t_c *(R1) = 6 ms,* j_c *(R2-R5) = -0. 46 mA cm*$^{-2}$*,* t_c *(R2-R5) = 1 s,* j_a *(O1-O5) = 1.26 mA cm*$^{-2}$*,* t_c *(O1-O5) = 5 ms. Blue and red lines represent the cathodic and anodic potential transients, respectively. Inset shows the magnified image of the R1 and O1.*

When the second cathodic galvanostatic pulse of -0.46 mA cm^{-2} (it is the cathodic peak current of the 2nd cycle in *Figure 4.1*) was applied for 1 s, then the potential of the interface dropped to 0.46 V within 100 ms and again attained a steady value till 500 ms and after this, a steady transition of potential was observed at the rate of about -1.5 V s^{-1} till 1 s. This transition is believed to be caused by the diffusion polarisation of the [AuCl$_4$]$^-$ ions at the interface. In brief, the [AuCl$_4$]$^-$ ions were depleted at the electrode-electrolyte interface because of the formation of sufficient nuclei on the GC electrode surface. Then the potential shifted towards more negative potential (in the diffusion polarization regime) where secondary reactions such as surface diffusion, sacrificial dissolution–redeposition etc. could be initiated. The anodic dissolution and cathodic deposition under diffusion–polarization continued till the third cycle. From the fourth cycle onwards, both the cathodic and the anodic potential characteristics attained a steady state behavior.

4.2.1.4. Template-free Electrosynthesis of AuNPs on the GC Electrode by the Multiple Potentiostatic Pulse Strategy (MPPS)

The MPPS for the template-free electrosynthesis of AuNPs on a GC electrode was developed based on the initial investigations as discussed in the *Section 4.2.1.2*. The AuNPs deposited on the GC by MPPS will be designated as AuNPs(P)/GC. A sequence of 1500 potentiostatic pulses was designed in such a way that the seed (or nucleation) pulse was applied only once at -0.13 V for 60 ms followed by a short anodic pulse of 0.92 V for 5 ms to dissolve the subcritical nuclei. Then a pair of growth pulses at 0.55 V for 1 s and an anodic pulse at 0.92 V for 5 ms was applied for 749 times. The total number of pulses was optimized by monitoring the analytical signal (anodic stripping peak current) of Pb(II)/Pb on the AuNPs(P)/GC electrode. The stripping peak current increased up to 1500 pulses and thereafter, a saturation of the signal followed by a decrease in the peak current was observed. Therefore, the total number of pulses was optimized to 1500. The potentiostatic pulse sequence is summarized below:

Seed (or Nucleation) pulse (P_1) : $E_1 = -0.13$ V; $t_1 = 0.06$ s
Anodic pulse (P_2) : $E_2 = 0.92$ V; $t_2 = 0.005$ s
Growth pulse (P_m) : $E_m = 0.55$ V; $t_m = 1$ s ($m = 3, 5, 7, \ldots, 1499$)
Anodic pulse (P_n) : $E_n = 0.92$ V; $t_n = 0.005$ s ($n = 4, 6, 8, \ldots, 1500$)
Total number of pulses : 1500 (optimized).

4.2.1.5. Characterization of AuNPs(P)/GC

In situ UV-visible spectra were recorded during the electrosynthesis of AuNPs after each growth pulse and these are shown in *Figure 4.5a*. The UV-visible reflection spectrum of the AuNPs(P)/GC electrode synthesized after 119 growth pulses (including the seed pulse) shows a major scattering peak at 460 nm and the characteristic surface plasmon peak of AuNPs at 518 nm *[165,166]*. The surface plasmon peak progressively shifted to higher wavelengths with increasing in the number of growth pulses (*inset of Figure 4.5a*). This is attributed to the increase in the size of the deposited AuNPs with time.

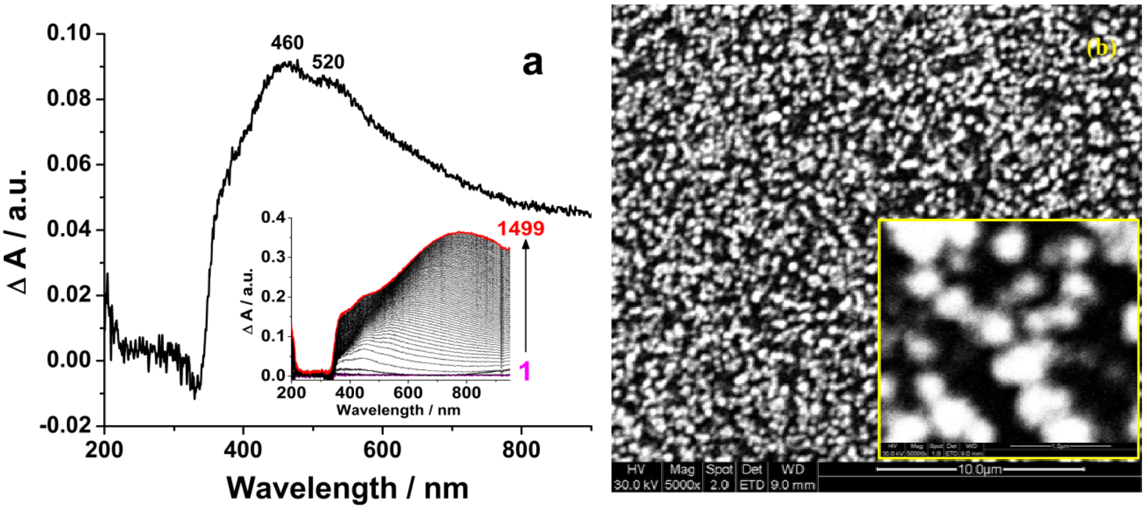

Figure 4.5 *(a) In-situ UV-visible reflection spectra of AuNPs(P)/GC synthesized just after 119 growth pulses (including the seed pulse). Inset shows the progress of the spectra of AuNPs(P)/GC from the first to 1499th growth pulse. (b) SEM image (5000X) of AuNPs(P)/GC. Inset shows the magnified image at 50000X (the scale shows 1 µm length).*

The SEM image of the AuNPs(P)/GC electrode is shown in *Figure 4.5b*. It can be seen that the AuNPs of size 250-300 nm are deposited on the GC electrode with a high particle population. A few particles overlap with each other because of the higher density of the nanoparticles on the GC electrode.

AFM topography (in the XY-plane) of the AuNPs(P)/GC electrode is shown in *Figure 4.6a* and it shows similar diameters of the AuNPs as observed in the SEM image. However, the features at the ZX-plane (*Figure 4.6b*) along the long yellow line drawn in the XY topography revealed that the average height of the AuNPs varied between 10-15 nm. Therefore, the deposited AuNPs were of tapped hemispherical shape. The height distribution of the particles was quite wide (*Figure 4.6c*) because of the interparticle overlaps. Smaller resolution images were recorded but they were almost featureless and not presentable because of the high extent of inter-particle overlaps.

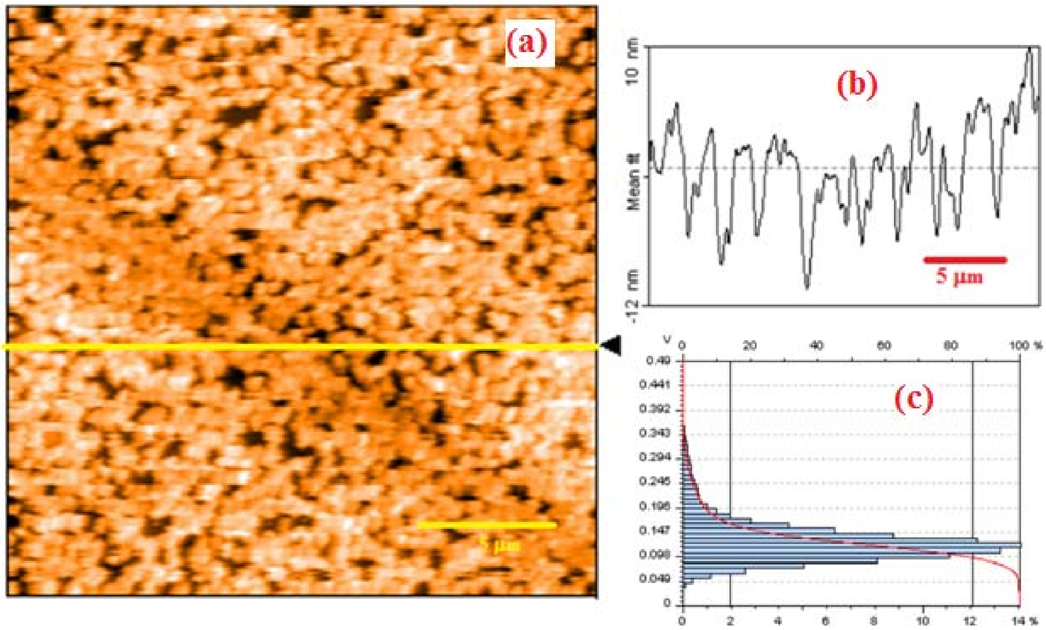

Figure 4.6 *(a) The AFM topography (XY-plane) of the AuNPs(P)/GC. The small yellow line shows a length scale of 5 µm. (b) Particle features at the ZX-plane along the long yellow line drawn in the XY topography. (c) Histogram of the particle height distribution (in terms of the tip deflection voltage) in the entire scan area.*

The electrochemically active area (A_e) of the working electrode was measured by using the Randles-Sevcik equation (*Eq. 2.17*) from the slopes of the cathodic peak current versus the square root of the scan rate (ranging from 10-500 mV s^{-1}) plots obtained in the cyclic voltammetry experiments with 5 mM potassium ferricyanide in 0.1 M KCl. The number of electrons transferred and the diffusion coefficient of ferricyanide in 0.1 M KCl were taken as 1 and 6.73×10^{-6} cm^2 s^{-1}, respectively, for the calculation of A_e *[167]*. The electrochemically active areas of the commercial GC and bare Au electrodes were calculated as 0.121 and 0.053 cm^2, respectively. Unless specified, the current density (j) was calculated by using these values. The roughness factor ($\rho = A_e/A_g$) were calculated as 1.7 for both the electrodes.

The electrochemically active area (A_e) and the roughness factor of the AuNPs(P)/GC electrode were calculated as 0.142 cm^2 and 2.0, respectively. The roughness of the AuNPs(P)/GC electrode increased compared to bare GC electrode because of the higher particle density of AuNPs on the GC surface (as observed from *Figures 4.5b and 4.6*). A cyclic voltammetric experiment was performed with the AuNPs(P)/GC electrode in 1 M H_2SO_4 solution in the potential range -0.6 V to 1.5 V at a scan rate of 100 mV s^{-1}. The gold oxide (AuO) formation peak was observed at 1.248 V and the gold oxide reduction peak was observed at 0.937 V (*Figure 4.7*). The cathodic charge corresponding to the AuO/Au reaction was found to be -33.85 μC. The effective surface area of Au (A_{Au}) was calculated as 0.0868 cm^2 for the AuNPs(P)/GC electrode assuming the charge density of the reduction of AuO to be -390 μC cm^{-2} *[168]*. The particle coverage [$\theta_p = (100\times A_{Au})/A_e$] was calculated as ~61% for the AuNPs(P)/GC electrode.

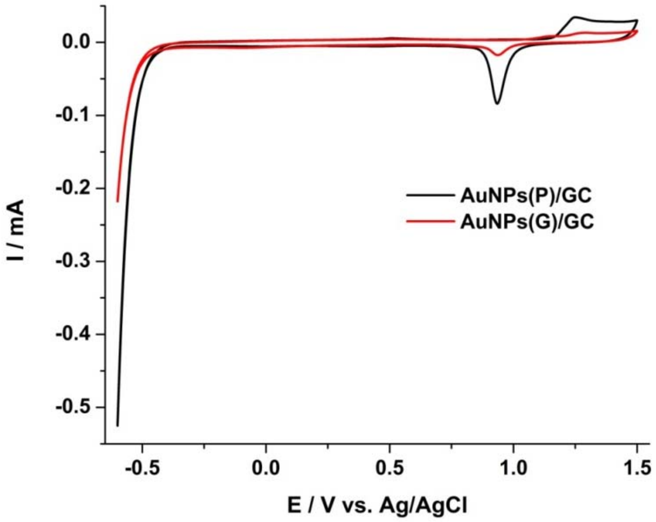

Figure 4.7 *Cyclic voltammograms of AuNPs(P)/GC (black line) and AuNPs(G)/GC (red line) in 1 M* H_2SO_4 *in the potential range -0.6 V to 1.5 V at a scan rate of 100 mV* s^{-1}.

4.2.1.6. Template-free Electrosynthesis of AuNPs on the GC Electrode by the Multiple Galvanostatic Pule Strategy (MGPS)

The MGPS for the template-free electrosynthesis of AuNPs on a GC electrode was developed based on the initial investigations as discussed in the *Section 4.2.1.3*. The galvanostatic pulse strategy was employed to reduce the number density of the AuNPs as well as to control the dispersion in the particle size. The AuNPs deposited on the GC by MGPS will be designated as AuNPs(G)/GC. After carrying out an extensive set of experiments, high cathodic and anodic current densities were selected to decrease the particle size dispersion. A sequence of 1500 galvanostatic pulses (for comparing the result with the MPPS) was designed in such a way that the seed (or nucleation) pulse was applied only once at -0.64 mA cm^{-2} for 60 ms followed by a short anodic pulse of 1.26 mA cm^{-2} for 5 ms to dissolve the subcritical nuclei. Then a pair of growth pulses at -0.46 mA cm^{-2} for 1 s and an anodic pulse at 1.26 mA cm^{-2} for 5 ms was applied 749 times. The galvanostatic pulse sequence is summarized below:

Seed (or Nucleation) pulse (P_1): $j_1 = -0.64$ mA cm^{-2}; $t_1 = 0.06$ s
Anodic pulse (P_2) : $j_2 = 1.26$ mA cm^{-2}; $t_2 = 0.005$ s
Growth pulse (P_m) : $j_m = -0.46$ mA cm^{-2}; $t_m = 1$ s (m = 3, 5, 7,, 1499)
Anodic pulse (P_n) : $j_n = 1.26$ mA cm^{-2}; $t_n = 0.005$ s (n = 4, 6, 8,…, 1500)
Total number of pulses : 1500 (optimized).

4.2.1.7. Characterization of AuNPs(G)/GC

In situ UV-visible spectra were recorded during the electrosynthesis of AuNPs after each growth pulse and these are shown in *Figure 4.8a*. The UV-visible reflection spectrum of the AuNPs(G)/GC electrode synthesized after 119 growth pulses (including the seed pulse) shows a major scattering peak at 460 nm and the characteristic surface plasmon peak of the AuNPs at 560 nm *[169]*. The surface plasmon peak progressively shifted to higher wavelengths with an increase in the number of growth pulses (*inset of Figure 4.8a*). This is attributed to the increase in the size of the deposited AuNPs with time. The wavelength of the plasmon band shifted towards the higher wavelength for galvanostatic pulse strategy as compared to the potentiostatic pulse strategy (*Figures 4.5a and 4.8a*). This indicates the possibility of synthesizing bigger sized nanoparticles in the galvanostatic pulse strategy. The SEM image of the AuNPs(G)/GC electrode is shown in *Figure 4.8b*. It shows that AuNPs of size 350-400 nm are deposited on the GC electrode with a lower particle population. The synthesized particles had a very narrow dispersion of particle size.

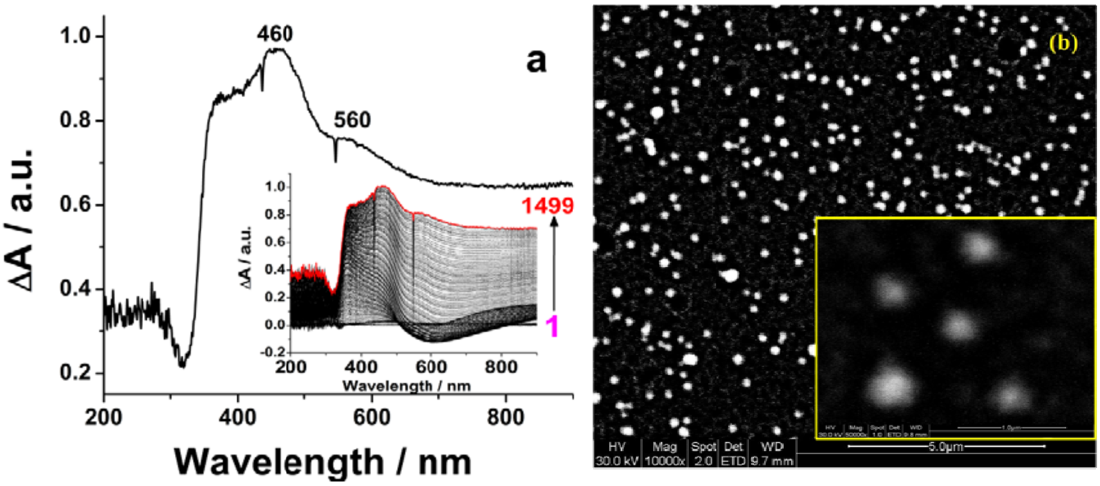

Figure 4.8 *(a) In-situ UV-visible reflection spectrum of AuNPs(G)/GC synthesized just after 119 growth pulses (including the seed pulse). Inset shows the progress of the spectra of AuNPs(G)/GC from the first to 1499th growth pulse. (b) SEM image (10000X) of AuNPs(G)/GC. Inset shows the magnified image at 50000X (the scale shows 1 µm length).*

AFM topography (in the XY-plane) of the AuNPs(G)/GC electrode is shown in *Figure 4.9a* and it shows the similar diameter of the AuNPs. However, the features at the ZX-plane (*Figure 4.9b*) along the long yellow line drawn in the XY topography revealed that the average height of the AuNPs varied between 25-30 nm. Therefore, the deposited AuNPs were of tapped hemispherical shape, but were bigger in size as compared to the AuNPs(P)/GC electrode. The height distribution of the particles is narrower (*Figure 4.9c*) because of the lower extent of inter-particle overlaps.

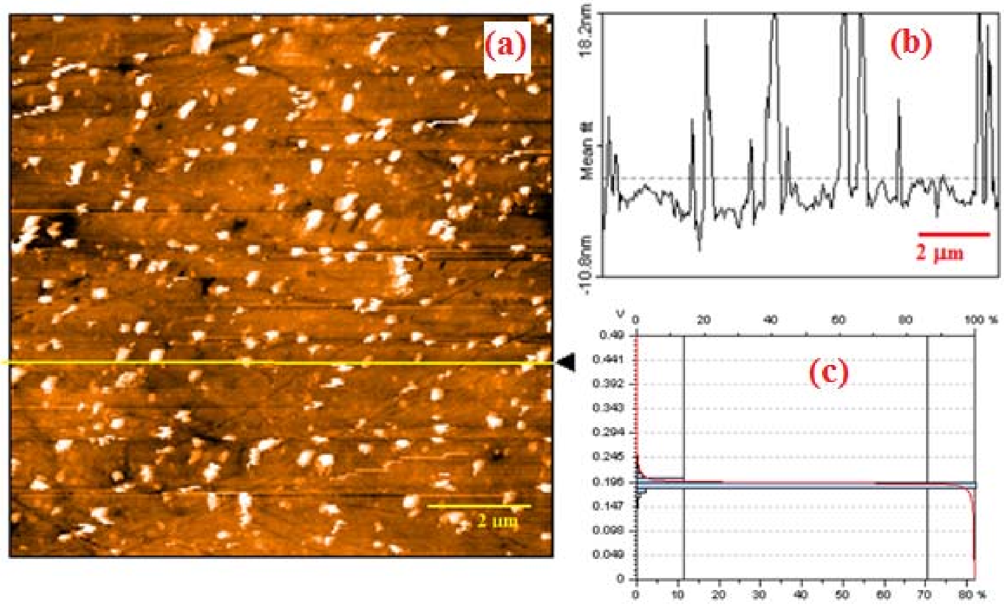

Figure 4.9 *(a) The AFM topography (XY-plane) of the AuNPs(G)/GC. The small yellow line shows a length scale of 2 µm. (b) Particle features at the ZX-plane along the long yellow line drawn in the XY topography. (c) Histogram of the particle height distribution (in terms of the tip deflection voltage) in the entire scan area.*

The electrochemically active area (A_e) and the roughness factor of the AuNPs(G)/GC electrode were calculated as 0.107 cm^2 and 1.5, respectively. The roughness of the AuNP(G)/GC electrode was found to be less compared to that of the bare GC electrode, though sufficient AuNPs were deposited on the GC electrode surface. This is attributed to the suppression of the active kink sites of the GC electrode by the smoother AuNPs at low particle population (as observed from *Figures 4.8b and 4.9*). A cyclic voltammetric experiment was performed with the AuNPs(G)/GC electrode in 1 M H_2SO_4 solution in the potential range -0.6 V to 1.5 V at a scan rate of 100 mV s^{-1} (*Figure 4.7*). The cathodic charge corresponding to the AuO/Au reaction was found to be -7.39 µC. The effective surface area of Au (A_{Au}) and θ_p were calculated as 0.0189 cm^2 and ~18%, respectively, for the AuNPs(G)/GC electrode.

The low particle number density and better monodispersed AuNPs were obtained in PGPS, which is attributed to the steady dissolution-redeposition of the gold nanoparticles as shown in *Figure 4.10*. When a sufficient amount of gold was deposited on the GC electrode surface in the form of particles and the $[AuCl_4]^-$ ions were depleted from the electrode-electrolyte interface, then a constant current was maintained by the sacrificial dissolution of smaller nuclei (from the electrode surface) to $[AuCl_4]^-$ and $[AuCl_2]^-$ and growth of the adjacent supercritical nuclei by the re-deposition of those ions. The number density of the particles decreased due to the dissolution of adjacent smaller nuclei and finally, the relatively bigger sized AuNPs were retained because of the steady growth of the super-critical nuclei at the cost of the sub-critical nuclei.

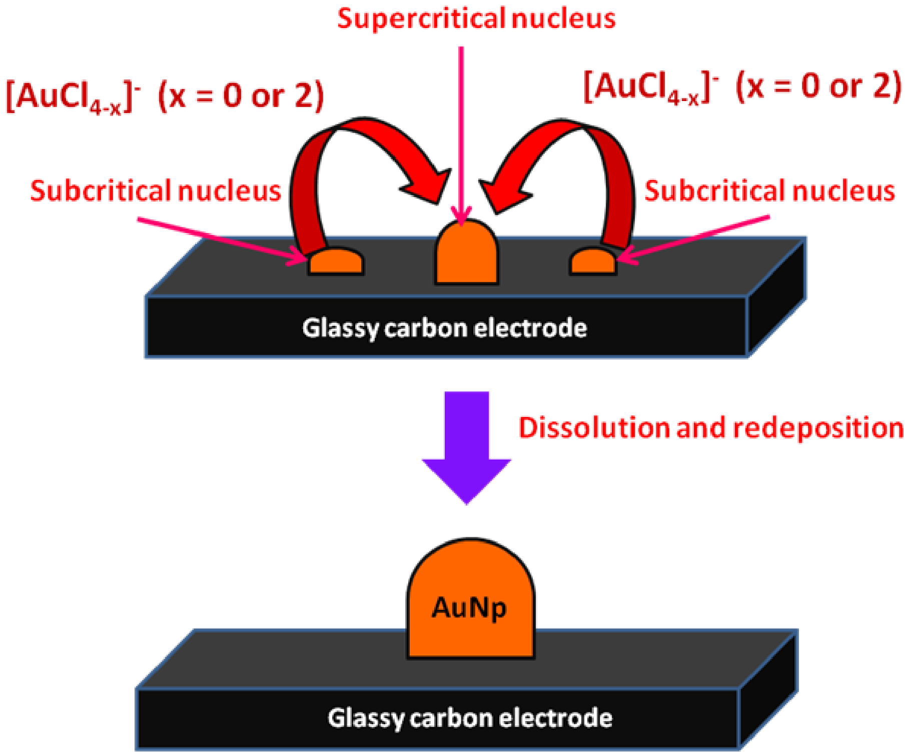

Figure 4.10 *The schematic representation of the dissolution of the subcritical nuclei and the growth of the supercritical nucleus under the galvanostatic steady state condition.*

4.2.2. Determination of Pb(II) at AuNPs in 0.1 M KCl by SWASV

The natural occurrence of lead (Pb) in soils is a consequence of local geological conditions as Pb is the end product of natural radioactive decay chains. Moreover, Pb is common in the environment due to its widespread historic use in petrol, paint, lead-acid batteries, water pipes etc. Pb has been found to be toxic to a wide variety of organs in both humans and animals. The low-level exposure of Pb changes the neurotransmitter levels in the nervous system, harms the vitamin-D metabolism, decreases the sexual hormone levels, and prevents lymphocyte function in living beings. Pb is present in the drinking water primarily because of the corrosion of household plumbing systems containing lead in pipes, solder, fittings or the service connections to homes. The amount of Pb dissolved from the plumbing system depends on several factors, including pH, temperature, water hardness and standing time of the water inside the pipelines. Though there is no evidence of threshold or safe exposure of Pb, the World Health Organization (WHO) has set a provisional guideline value of Pb in drinking water as 10 $\mu g\ L^{-1}$ *[170]*. As per the survey report of the Quality Council of India in 2010, the water samples collected from bore well, well water and municipal water from the top cities of India viz. Kolkata, Kochi, Mumbai, Pune, Nagpur, Nasik, Guwahati tested positive for harmful content of Pb *[171]*. Further, the binding energy of Pb on Au is greater than the binding energies of Pb in a Pb metal lattice and Au in a Au metal lattice. Therefore, an atomic monolayer or submonolayer of Pb electrochemically deposits on Au at electrode potentials which are more positive than the Nernstian potential required for the deposition of the corresponding bulk Pb phase. This phenomenon is known as the underpotential deposition (UPD) of Pb on Au and, by the virtue of this, the AuNPs/GC was utilized to determine lead(II), i.e. Pb(II) at ultra-trace levels in the drinking water collected from three different locations in India.

4.2.2.1. Understanding the UPD of Pb on Au in 0.1 M KCl

The UPD of Pb on Au is a consequent effect of the adsorption of Pb(II) on Au surface. The chloride ions (Cl^-) also adsorb on the Au surface and they induce the adsorption of Pb(II) on Au through a ligand (Cl^-) bridge *[46, 48]*. Therefore, 0.1 M KCl was chosen as the supporting electrolyte for ultratrace determination of Pb(II). The cyclic voltammogram of 10 μM $Pb(ClO_4)_2$ in 0.1 M KCl on the AuNPs(P)/GC electrode is shown in *Figure 4.11*.

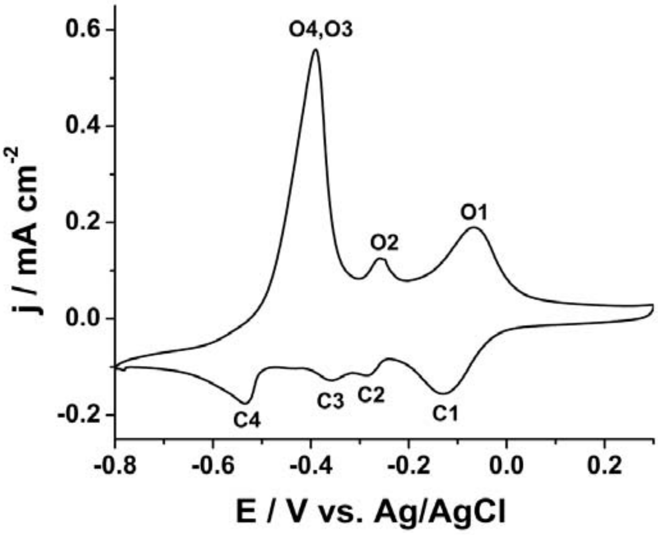

Figure 4.11 *Cyclic voltammogram of 10 μM Pb(II) in 0.1 M KCl at a scan rate of 10 mV* s^{-1}.

It shows four reduction peaks at -0.131 V (C1), -0.285 V (C2), -0.357 V (C3) and -0.534 V (C4) and three oxidation peaks at -0.066 V (O1), -0.258 V (O2) and -0.391 V (O3,O4). The two oxidation peaks overlap in the peak at -0.391 V. The pair of broad peaks C1 (-0.131 V) and O1 (-0.066 V) corresponds to the underpotential deposition and dissolution of Pb on the low index Au(110) facet *[172, 173]*. The (110) plane has the lowest atom density and it is the most reactive plane in the polycrystalline gold. In the potential range -0.131 V and -0.066 V, sufficient Cl^- remained adsorbed on the

Au(110) plane and a sluggish electron transfer between Pb(II) and Au(110) through the Cl^- ligands broadened the UPD peaks. The atom density of the low index planes increased in the order (111)>(100)>(110) and it is the same order for the stability of the planes. The pairs of peaks (C2,O2) and (C3,O3) are attributed to the UPD of Pb(II) on Au(100) and Au(111), respectively. The pair of peaks (C4,O4) is attributed to the overpotential deposition (OPD) of Pb(II) on the Pb monolayer. The polycrystallinity of AuNPs was evidenced from the characteristic UPD peaks of Pb on Au *[172, 173]*.

4.2.2.2. Square Wave Anodic Stripping Voltammetry (SWASV) of Pb(II) in 0.1 M KCl

The optimized SWASV experimental parameters were the condition potential: 0.5 V, duration of conditioning: 120 s, deposition potential: -1.0 V, deposition time: 120 s, equilibration time: 30 s, frequency: 50 Hz, step potential: 0.001 V, pulse amplitude: 40 mV, potential scan range: -0.1 V to 0.5 V. *Figure 4.12* shows the calibration plots of Pb(II) in 0.1 M KCl on (a) bare GC electrode, (b) bare Au electrode, (c) AuNPs(G)/GC electrode and (d) AuNPs(P)/GC electrode.

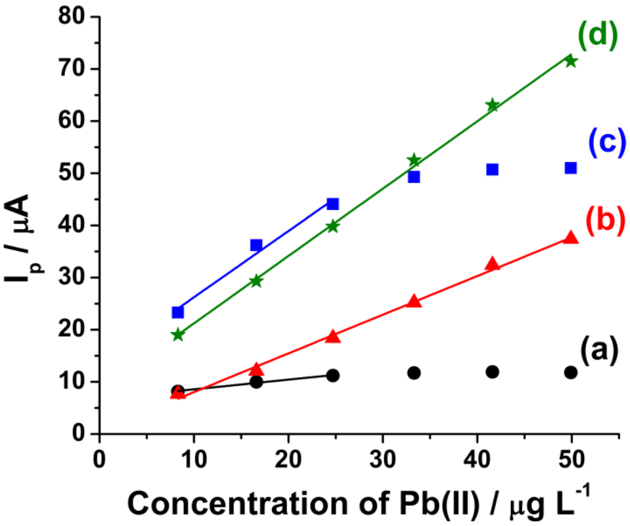

Figure 4.12 *Calibration plots of Pb(II) in 0.1 M KCl on (a) bare GC, (b) bare Au, (c) AuNPs(G)/GC and (d) AuNPs(P)/GC. The straight lines show the corresponding linear ranges.*

The linear dynamic ranges at the bare GC electrode and AuNPs(G)/GC electrode were up to ~30 μg L^{-1}, whereas the linear dynamic range at the bare Au electrode and AuNPs(P)/GC electrode were up to 50 μg L^{-1} and above 50 μg L^{-1}, respectively. The linear equations of the calibration plots are given below (*Eqs. 4.5-4.8*):

Bare GC : I_p (μA) = 6.74 μA + 0.1843 μA / (μg L^{-1}); ($R^2 = 0.9755$) (4.5)

Bare Au : I_p (μA) = 0.64 μA + 0.7417 μA / (μg L^{-1}); ($R^2 = 0.9949$) (4.6)

AuNPs(G)/GC: I_p (μA) = 13.55 μA + 1.2695 μA / (μg L^{-1}); ($R^2 = 0.9659$) (4.7)

AuNPs(P)/GC: I_p (μA) = 8.32 μA + 1.2916 μA / (μg L^{-1}); ($R^2 = 0.9972$) (4.8)

The limits of detection (LODs) of Pb(II) for the bare GC, bare Au, AuNPs(G)/GC and AuNPs(P)/GC electrodes were calculated as 1.22 μg L^{-1} (5.86 nM), 122 ng L^{-1} (587 pM), 86.4 ng L^{-1} (416 pM) and 57 ng L^{-1} (274 pM), respectively, at S/N = 3. It can be seen that the analytical merit of the AuNPs(P)/GC electrode was the best among the four electrodes. This is attributed to the higher surface coverage of AuNPs on the GC in the case of the AuNPs(P)/GC electrode. Therefore, further studies were carried out with only the AuNPs(P)/GC electrode.

4.2.2.3. Studies on the Repeatability and Reproducibility of the Analytical Signal and the Stability of the AuNPs(P)/GC Electrode

The repeatability of the electrochemical signal of the AuNPs(P)/GC electrode was checked by carrying out a series of repetitive experiments (n = 10) for a fixed concentration of Pb(II) of 8.3 μg L^{-1}. Precise peak currents were obtained with a relative standard deviation (RSD) of 5.4% (n = 10). The same electrode was used for the determination of 8.3 μg L^{-1} of Pb(II) for five consecutive days (five signals were recorded on each day) and repeatable peak currents were obtained with RSD of 8.2% (n = 25). Five AuNPs(P)/GC electrodes were prepared by following the same procedure and were used to determine 8.3 μg L^{-1} of Pb(II) by recording 3 signals from each electrode. Reproducible peak currents were obtained with RSD of 4.8% (n = 15). Therefore, the AuNPs(P)/GC electrode exhibited a highly sensitive, precise, reproducible and stable response for the ultratrace determination of Pb(II).

4.2.2.4. Recovery Test and Interference Study

Five recovery tests were performed with 8.3 μg L^{-1} of Pb(II) in 0.1 M KCl and the results are given in *Table 4.1*. The recovery results obtained were within ±10% of the expected values.

Table 4.1 *The % recovery test of 8.3 μg L^{-1} Pb(II) in 0.1 M KCl.*

Test No.	**Added Concentration of Pb(II) in 0.1 M KCl (μg L^{-1}) [P]**	**Mean peak current (n=3) (%RSD) (μA)**	**Measured Concentration of Pb(II) in 0.1 M KCl by *Eq. 4.8* (μg L^{-1}) [Q]**	**% Recovery [100×(Q/P)]**
1.	8.3	18.3 (±0.8)	7.7	93
2.	8.3	18.0 (±1.0)	7.5	91
3.	8.3	19.9 (±1.3)	8.9	107
4.	8.3	18.6 (±0.9)	7.9	95
5.	8.3	20.0 (±0.7)	9.0	108

Bismuth (Bi(III)), Cadmium (Cd(II)) and Thallium (Tl(I)) were found to be interfering during the determination of Pb(II) on the AuNPs(P)/GC electrode. Bi(III) deposits at more positive potential (at about -0.13 V) than Pb(II). Therefore, it destroyed the underpotential deposition of Pb on Au. In the presence of an equal amount (i.e. 8.3 μg L^{-1}) of Cd(II), the peak current of Pb(II) decreased by 5.3%. Further, about 13.3% decrease in the stripping peak of Pb(II) was observed in the presence of ten times higher concentration of Cd(II) than that of Pb(II). The stripping peak of Cd(II) was prominent at -0.73 V at 100 times higher concentration of Cd(II) than that of Pb(II) and suppression and splitting of the stripping peak of Pb(II) were observed. In the presence of an equal amount (i.e. 8.3 μg L^{-1}) of Tl(I), the peak current of Pb(II) decreased by ~45%. About 47% decrease in the stripping peak of Pb(II) was observed in the presence of a three times higher concentration of Tl(I) than that of Pb(II). The peaks of Tl(I) and Pb(II) merged together in a solution of 8.3 μg L^{-1} of Pb(II) in the presence of ~25 μg L^{-1} of Tl(I).

4.2.2.5. Determination of Pb(II) in Real Samples

The developed methodology was utilized for the determination of Pb(II) in the water samples collected from the lake of Raja Ramanna Centre for Advanced Technology (RRCAT) in Indore, laboratory tap at BARC and near the Aassi ghat of the Ganges River in Varanasi, India. A precise measured quantity of KCl was added to each sample of known volume to give a 0.1 M concentration of the supporting electrolyte in the samples. Nanopure water containing 0.1 M KCl was taken as the blank which was subtracted from the sample data (*Figure 4.13(i)*). SWASV of each sample was recorded by using the developed methodology and then a standard addition protocol was followed with four consecutive standard additions of 8.3 μg L^{-1} Pb(II). Each experiment was repeated thrice and the corresponding concentrations of Pb(II) were evaluated by extrapolation of the straight line to the negative x-axis intercept (i.e. considering the y-axis value as 0). *Figure 4.13* shows the SWASVs of the (i) baseline (blank is subtracted from itself), (ii) sample lake water (blank subtracted), four (iii – vi) consecutive standard additions (blank subtracted) of 8.3 μg L^{-1} Pb(II) to the lake water. The inset shows the intercept at negative x-axis for the standard addition shown in *Figure 4.13*. The calculated concentrations of Pb(II) in the water samples obtained by the present methodology are listed in *Table 4.2*. It can be seen that the concentrations of

Pb(II) obtained from the present methodology are in good agreement with the concentrations of Pb in the same samples measured by ICP-MS (*Table 4.2*). The concentrations of Pb(II) in all the samples are below the warning value limit of 10 µg L^{-1} as per the provisional guidelines set by WHO in 2011.

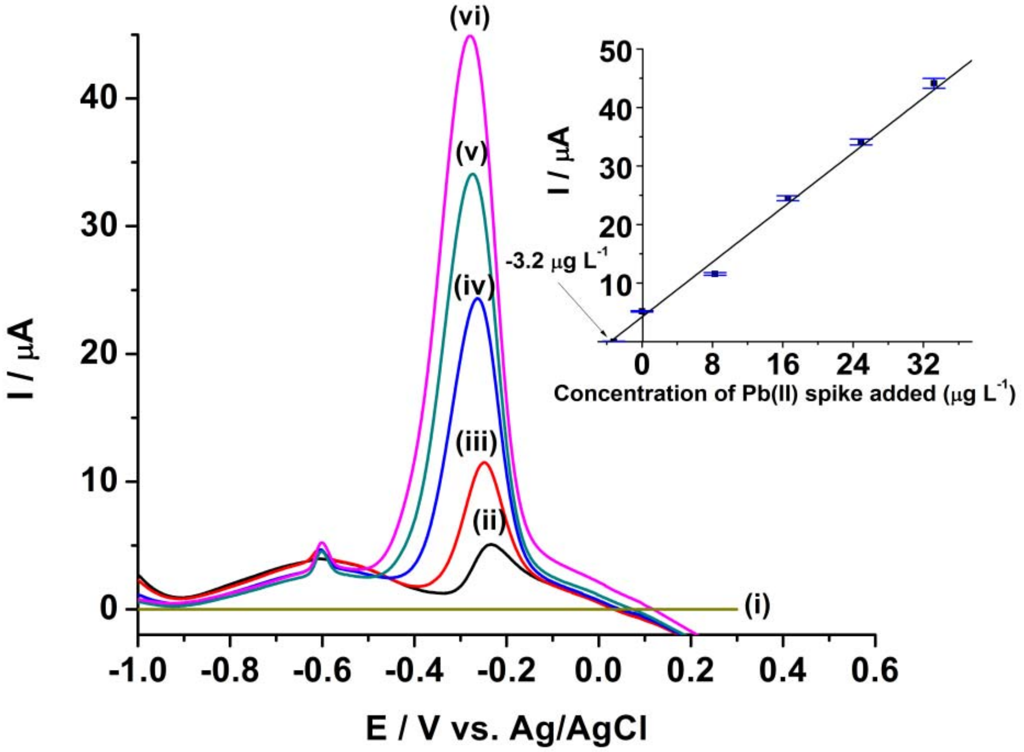

Figure 4.13 *The SWASV of (i) Baseline (the current signal of 0.1 M KCl in nanopure water, termed as blank, was subtracted from itself at each potential); (ii) lake water sample (after blank subtraction). The standard addition SWASVs (after blank subtraction) by adding (iii) 8.3 (iv) 16.6 (v) 24.9 and (vi) 33.2 µg* L^{-1} *standard Pb(II) into the lake water sample. The inset shows the standard addition plot taking the current of lake water sample at x=0.*

Table 4.2 *The measured concentration of Pb(II) in the water samples.*

Sample	**Concentration of Pb(II) in µg L^{-1} measured by**	
	SWASV (n=3)	**ICP-MS (n=10)**
Lake water from RRCAT	3.2 (±1.1%)	3.0 (±2.6%)
Laboratory tap water	1.7 (±2.3%)	2.3 (±10.7%)
Ganges river water	8.4 (±3.9%)	9.4 (±3.5%)

4.2.3. Electrocatalysis of Uranyl Sulphate in 1 M H_2SO_4 at AuNP(G)/GC

The resurgence of research in actinide chemistry has been fuelled not only by their important technological and scientific attributes in nuclear power production, but also by the complexity in the actinyl redox chemistry from the industrial and environmental point of view. Of all the actinide ions, uranyl ion ($U^{VI}O_2^{2+}$) has been studied most thoroughly, as it has the most stable oxidation state (VI) of uranium and, therefore, is the prevalent form of natural uranium in the environment. $U^{VI}O_2^{2+}$ is chemically robust due to the presence of trans-dioxo bonds around uranium and is highly oxidative in acidic solutions, exhibiting interesting and useful oxidation-reduction chemistry. The oxygen reduction on AuNPs occurs in the potential range -0.5 to -0.15 V vs. Ag/AgCl (saturated KCl) reference electrode *[156],* which is in similar range of reduction potential of the uranyl (UO_2^{2+}) complexes on mercury pool electrode *[162]*. Therefore catalytic reduction of $U^{VI}O_2^{2+}$ might be possible on AuNPs. This is the first report on the electrocatalysis of $U^{VI}O_2^{2+}$ in 1 M H_2SO_4 at AuNPs supported on glassy carbon electrode (AuNP(G)/GC) evidenced from cyclic voltammetry (CV), differential pulse voltammetry (DPV) and electrochemical impedance spectroscopy (EIS) experiments. The molecular understanding of the electrocatalytic mechanism was investigated by the relative stability of molecular orbitals of the most abundant U(VI) complex in sulphuric acid solution by quantum chemical calculations.

4.2.3.1. Differential Pulse Voltammetry (DPV) of 5 mM U(VI) in 1 M H_2SO_4

Figure 4.14 shows the DPV of 5 mM U(VI) in 1 M H_2SO_4 on (i) GC, (ii) Au and (iii) AuNP(G)/GC at 10 mV pulse amplitude. The cathodic peak of U(VI) on GC was observed at -0.494 V with a peak current density of -17.8 μA cm^{-2}. The cathodic peak potential was shifted to -0.191 V and -0.129 V on Au and AuNP(G)/GC, respectively. The peak current density increased to -30.4 and -82.4 μA cm^{-2} on Au and AuNP(G)/GC, respectively. *Figure 4.14* indicates that the energy barrier of the electron transfer reaction from the electrode to U(VI) centre is significantly minimized at AuNP(G)/GC. Therefore, AuNP(G)/GC acts as a catalyst for the electrochemical reduction of U(VI) in 1 M H_2SO_4. Further, the significant enhancement of the cathodic peak current of U(VI) at AuNP(G)/GC draws analytical importance for the quantitative measurement of U(VI).

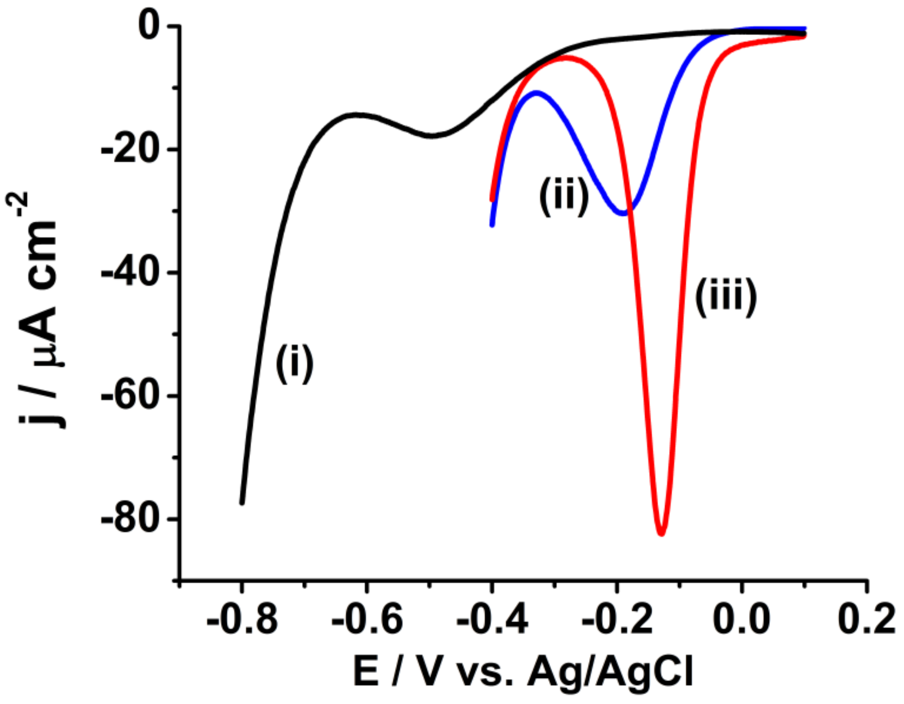

Figure 4.14 *The DPV of 5 mM U(VI) in 1 M H_2SO_4 on (i) GC, (ii) Au and (iii) AuNP(G)/GC at 10 mV pulse amplitude.*

4.2.3.2. Cyclic Voltammetry of 5 mM U(VI) in 1 M H_2SO_4

The electrocatalytic reduction of U(VI) was also supported by the cyclic voltammograms (*Figure 4.15*). The cathodic peak of U(VI) was observed at -0.560 V, -0.202 V and -0.110 V at GC, Au and AuNP(G)/GC, respectively. The cathodic peak current densities (j_p) were -193.9, -201.2 and -315.7 μA cm^{-2} on GC, Au and AuNP(G)/GC, respectively. For the same electrode, the cathodic peak potential as well as peak current density has different values in CV and DPV. This is attributed to the differences in the potential function and current sampling of CV and DPV as reported elsewhere *[174]*.

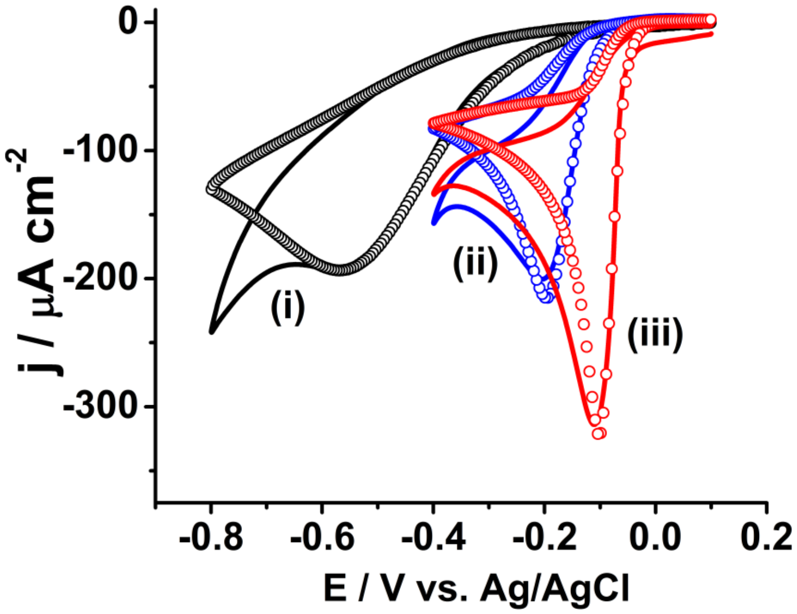

Figure 4.15 *CV of 5 mM U(VI) in 1 M H_2SO_4 on (i) GC, (ii) Au and (iii) AuNP(G)/GC at a scan rate (v) of 10 mV s^{-1}. The solid lines and circles represent the experimental data and fitted curves, respectively.*

The j_p of U(VI) reduction showed linear dependencies on the scan rates (ν) at Au and AuNP(G)/GC; but this exercise could not be done for the GC electrodes as the peak shapes were lost at scan rate higher than 40 mV s^{-1} (*Figures 4.16 – 4.18*). Further, the slopes of the plots of Log(-j_p) vs. Log(ν) for Au (*Figure 4.17B*) and AuNP(G)/GC (*Figure 4.18B*) were calculated as 0.6 and 0.9, respectively. It indicates that the reduction of U(VI) in 1 M H_2SO_4 happens at Au and AuNP(G)/GC electrodes through a mixed adsorption-diffusion mechanism and the contribution of adorption increased in AuNP(G)/GC *[175]*. The cathodic peak current function ($j_p/\nu^{0.5}$) of the U(VI) reduction at Au and AuNP(G)/GC increased to higher cathodic values at higher scan rates (*Figures 4.17C, 4.18C*). This is an indication of involvement of the electrochemical-chemical (EC) mechanism for the reduction of U(VI) in 1 M H_2SO_4 *[175]*.

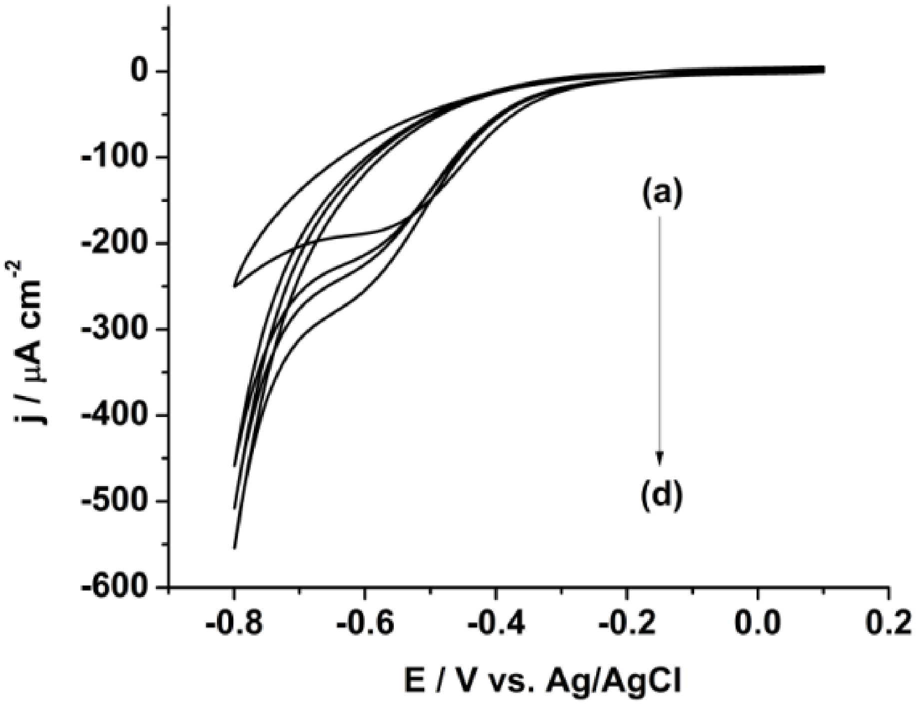

Figure 4.16 *Cyclic voltammograms (CVs) of 5 mM U(VI) in 1 M H_2SO_4 at GC with the scan rate (a) 10 (b) 20 (c) 30 (d) 40 mV s^{-1}.The peak shape was lost at CVs with higher scan rates.*

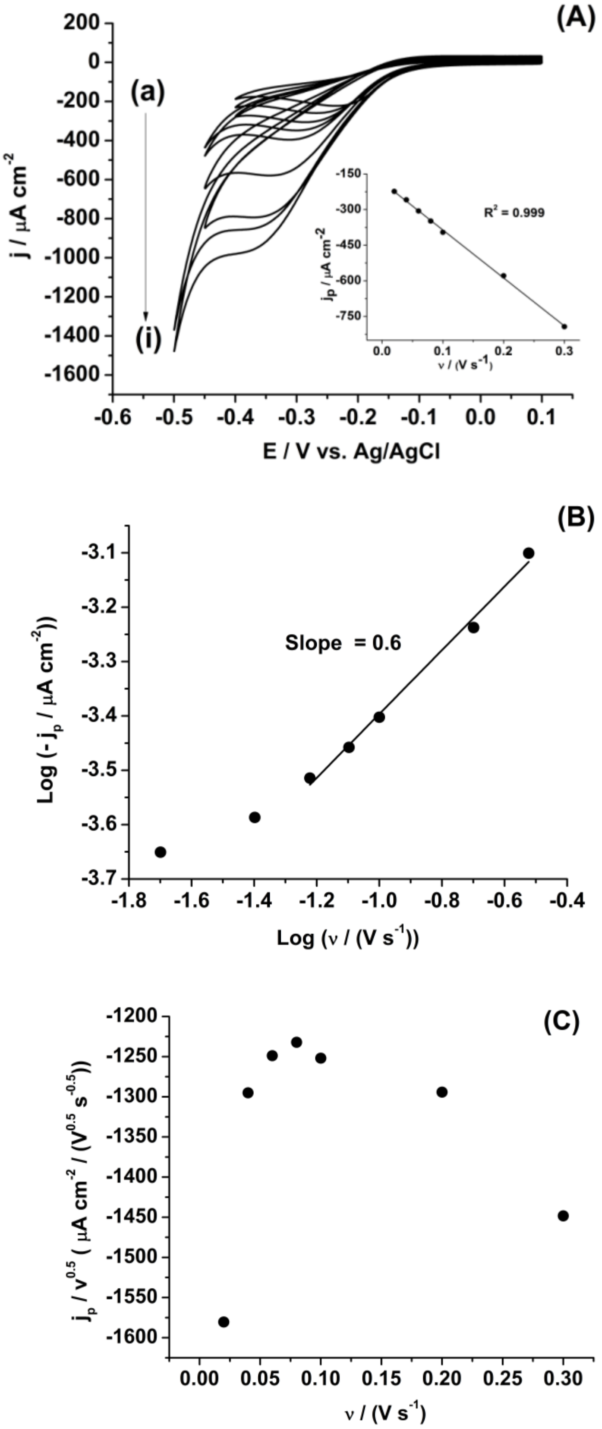

Figure 4.17 *(A) Cyclic voltammograms (CVs) of 5 mM U(VI) in 1 M* H_2SO_4 *at Au with the scan rate (a) 20 (b) 40 (c) 60 (d) 80 (e) 100 (f) 200 (g) 300 (f) 400 (i) 500 mV* s^{-1}*. Inset: The linear dependency of cathodic peak current* (j_p) *on the scan rate (v). (B) The Log(*$-j_p$*) vs. Log(v) plot of (A). (C) The plot of current function* ($j_p/v^{0.5}$) *vs. v.*

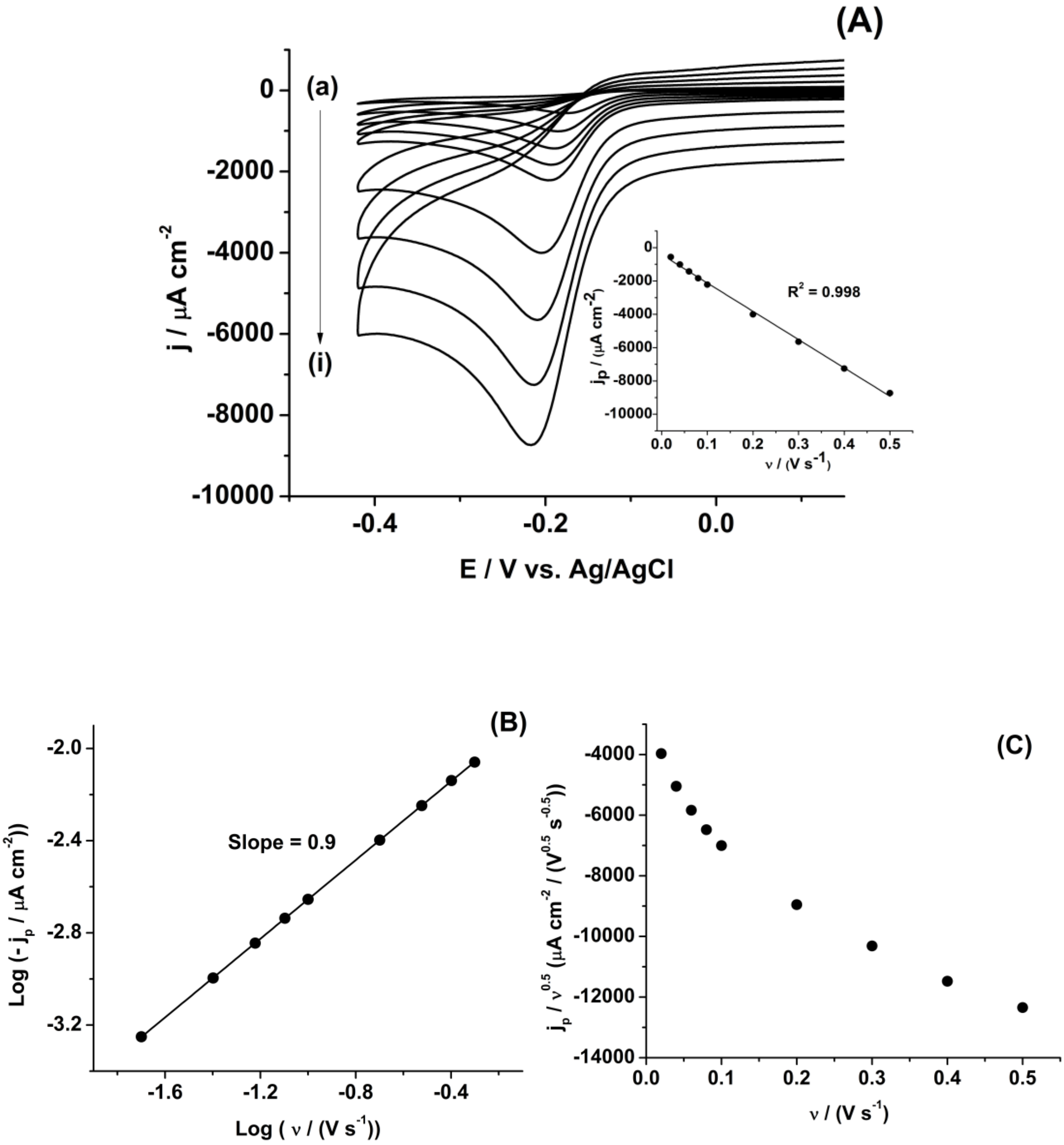

Figure 4.18 *(A) Cyclic voltammograms (CVs) of 5 mM U(VI) in 1 M* H_2SO_4 *at AuNP(G)/GC with the scan rate (a) 20 (b) 40 (c) 60 (d) 80 (e) 100 (f) 200 (g) 300 (f) 400 (i) 500 mV* s^{-1}. *Inset: The linear dependency of cathodic peak current* (j_p) *on the scan rate (v). (B) The Log(*$-j_p$*) vs. Log(v) plot of (A). (C) The plot of current function* ($j_p/v^{0.5}$) *vs. v.*

U(VI) generally reduces to U(V) at approximately -0.2 V vs. Ag/AgCl on mercury pool electrode (*Eq. 4.9*) *[162, 176-180]*.

$$2\ \mathrm{U(VI)} + 2\ e^- = 2\ \mathrm{U(V)} \qquad (4.9)$$

In acidic solution, U(V) disproportionates into U(VI) and U(IV) (*Eq. 4.10*) *[162, 176-180]*.

$$2\ \mathrm{U(V)} = \mathrm{U(VI)} + \mathrm{U(IV)} \qquad (4.10)$$

From the shapes of the CVs, it could be speculated that under strongly acidic conditions (i.e. 1 M H_2SO_4), reaction *4.10* occurs so fast that at the potential corresponding to reaction *4.9*, the U(VI) ions are reduced completely to U(IV) according to *Eq. 4.11 [162, 176-180].*

$$\mathrm{U(VI)} + 2\ e^- = \mathrm{U(IV)} \qquad (4.11)$$

U(IV) is stable in 1 M H_2SO_4 and the oxidation of U(IV) involves the formation of two U=O bonds, which occurs much slowly compared to the recommended time frame of the electrochemical potential sweep at the electrode. Therefore, U(IV)/U(VI) showed irreversible redox behaviour and no oxidation peak of uranium (IV) was observed in anodic scan direction irrespective of the scan rate (*Figure 4.19*).

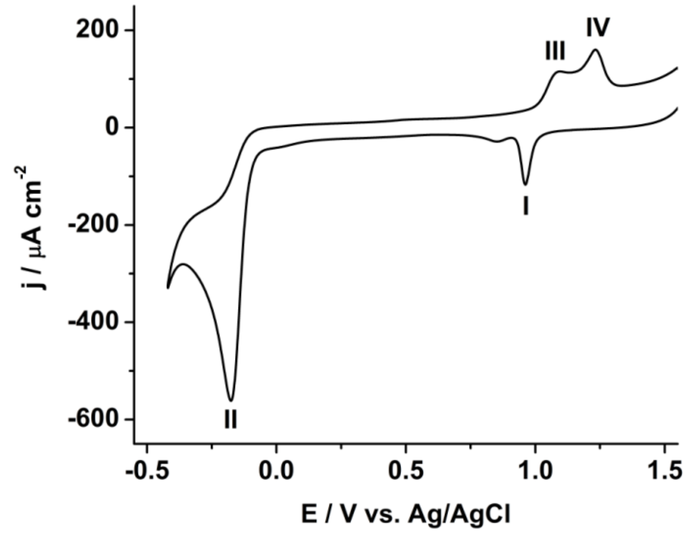

Figure 4.19 *Cyclic voltammogram of 5 mM U(VI) in 1 M H_2SO_4 at AuNP(G)/GC with the scan rate of 20 mV s^{-1}. The peaks (I, III and IV) correspond to the reduction and oxidation of gold and the peak II corresponds to the reduction of U(VI).*

The onset of the reduction of U(VI) to U(V) appeared at -0.278, -0.108 and -0.101 V at GC, Au and AuNP(G)/GC, respectively. The cathodic onset potential (E_c) is an important parameter to understand the energy level of the virtual state, where electron transfer takes place from the electrode to the analyte molecule/ion. The energy of the virtual state ($E_{VS\text{-}LUMO}$) is given by *Eq. 4.12 [181].*

$$E_{VS\text{-}LUMO} = -e[E_c + 4.65] \text{ eV vs. vacuum} \qquad (4.12)$$

when, the onset potential is measured with respect to Ag/AgCl reference electrode. The systematic decrease in the value of E_c from GC to AuNP(G)/GC suggests that the energy of the virtual state of the electron transfer of the electrode to U(VI) systematically decreases from GC to AuNP(G)/GC. The $E_{VS\text{-}LUMO}$ was calculated as -4.372, -4.549 and -4.542 eV vs. vacuum for GC, Au and AuNP(G)/GC, respectively.

To get more insight into the electrocatalytic action of AuNP(G)/GC, the kinetic parameters of reduction of U(VI) were evaluated by fitting the cyclic voltammograms with reactions *4.9* and *4.10* by *DigiSim 3.03b*. The fitted curves are shown in *Figure 4.15* by circles. It should be noted that the deviation of the fitted circles from the experimental lines is attributed to the background contribution which was not subtracted from the experimental curves *[182-185]*. The optimized values of formal reduction potential ($E^{'}_{0}$) for these three electrodes were found in the range between -0.2 to -0.15 V, which is in agreement with the literature value *[162, 176-180]*. The average equilibrium constant of the coupled chemical step was calculated as ~ 1.9×10^{3} M^{-1} s^{-1}. Further, the rate of electron transfer reaction from the electrode to U(VI) was calculated as 3.5×10^{-5}, 5.0×10^{-5} and 5.4×10^{-3} cm s^{-1} at GC, Au and AuNP(G)/GC, respectively. This shows that the heterogeneous charge transfer rate of AuNP(G)/GC is much faster compared to those of Au and GC. Interestingly, the charge transfer coefficient (α; symmetry factor of the transition state) improves from 0.13 at GC to 0.50 at Au and 0.90 at AuNP(G)/GC. The values of α at GC and AuNP(G)/GC seemed to be quite spurious (i.e. beyond 0.3 to 0.7). Therefore, α was again analytically calculated from Tafel's slope (*Eq. 4.13*).

$$\text{Tafel slope} = -\ 2.303RT/(\alpha nF) \qquad (4.13)$$

Here, we considered n=2 for the overall reaction *4.11* as the analytical signal was the sum of the reactions *4.9* and *4.10*; but it showed similar results (0.11 at GC, 0.49 at Au and 0.87 at AuNP(G)/GC). The values of α were again analytically calculated for the irreversible cyclic voltammetric waves (n=2) by *Eq. 4.14 [162, 176-180].*

$$E_p - E_{p/2} = 1.857\ RT\ /\ (\alpha nF) \qquad (4.14)$$

It also showed similar values of α (0.18 at GC, 0.41 at Au and 0.71 at AuNP(G)/GC). Therefore, it can be speculated that the rate as well as the symmetry of the potential energy barrier of the heterogeneous electron transfer reaction from metal to U(VI) follows the order GC < Au < AuNP(G)/GC.

There are two common possibilities to get enhanced current of the electrochemical reaction at the modified electrodes with nanoparticles: (1) enhancement in the overall surface area of the electrode because of the higher surface-to-volume ratio of the nanoparticles; and (2) presence of higher number of synthetic defects or active sites on the nanoparticles. In these cases, the nanoparticles modified electrode is expected to show electrocatalytic action irrespective of the redox system. Therefore, the cyclic voltammetry and electrochemical impedance spectroscopy experiments were performed at GC, Au and AuNP(G)/GC electrodes with an electrochemically reversible probe, i.e. $K_3[Fe(CN)_6]/K_4[Fe(CN)_6]$ redox couple. *Figure 4.20(i)* shows the CV of 5 mM $K_3[Fe(CN)_6]/K_4[Fe(CN)_6]$ in 0.1 M KCl at GC, Au and AuNP(G)/GC electrodes. No appreciable change in the peak current densities and peak potentials was observed for these electrodes. It may rule out the first possibility. Further, the Nyquist plot (*Figure 4.20(ii)*) showed that the charge transfer resistance (R_{CT}) significantly decreased from GC (361 Ω) to Au (41.3 Ω) and AuNP(G)/GC (38.5 Ω). Therefore, no appreciable change in R_{CT} was observed between Au and AuNP(G)/GC for $K_3[Fe(CN)_6]/K_4[Fe(CN)_6]$. The fitted values of the individual component of the Randle's electrical equivalent circuit for three electrodes are given in *Table 4.3*. It may rule out the second possibility.

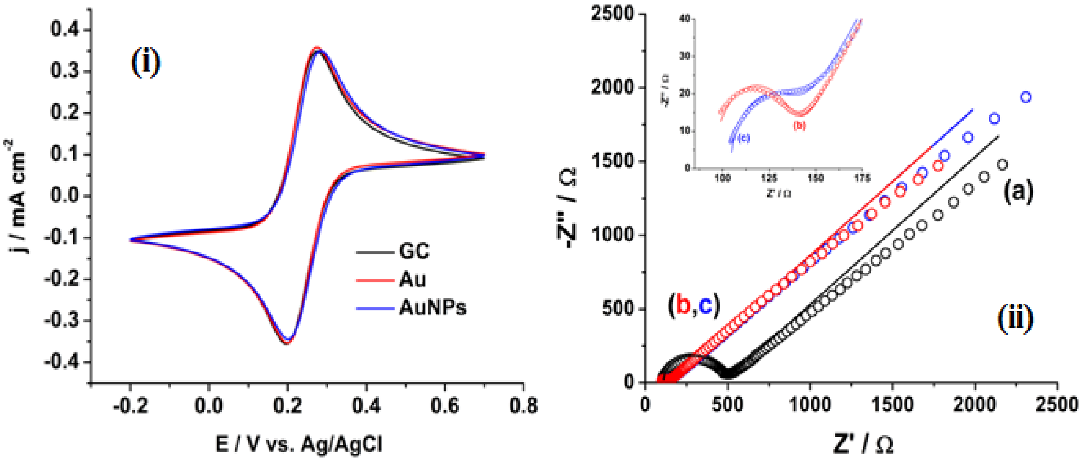

Figure 4.19 *The cyclic voltammograms of 5 mM* $K_3[Fe(CN)_6]/K_4[Fe(CN)_6]$ *in 0.1 M KCl at Au, GC and AuNP(G)/GC at a scan rate of 10 mV* s^{-1}*. (ii) The Nyquist plot of the same at (a) GC, (b) Au and (c) AuNP(G)/GC for the frequency range* 10^5 *– 0.1 Hz at amplitude of 5 mV. The circular points represent the experimental data and solid line is the fitted data by FRA 2 with the Randle's electrical equivalent circuit. Inset shows the zoomed image of the semicircular portions of (b) and (c).*

Table 4.3 *The fitted values of the components of Randle's electrical equivalent circuit from Figure 4.19(ii). The errors of the fitted parameters are within 5% of the reported value.*

Electrode	$(R_s + R_u) / \Omega$	R_{CT} / Ω	C_{DL} / µF	$W / (\Omega^{-1} s^{1/2})$	**Reduced** χ^2
GC	108	361	0.766	0.0017	0.022
Au	95	41.3	1.13	0.0018	0.003
AuNP(G)/GC	104	38.5	3.69	0.0015	0.009

The electrocatalysis can also be defined by the decrease in the height of the activation barrier of the electron transfer reaction. We already showed appreciable change in the cathodic peak potential for U(VI) at GC, Au and AuNP(G)/GC (*Figures 4.14 & 4.15*), while no change in peak potential was observed for $K_3[Fe(CN)_6]$ at these electrodes (*Figure 20(i)*). Further, a change in the energy of the virtual states as well as the contribution of adsorption of U(VI) at the electrodes was discussed earlier. Therefore, quantum mechanical calculations were performed for understanding the electrocatalysis of U(VI) by AuNP(G)/GC at molecular levels.

The most probable species of uranyl sulfate in moderate sulfate concentration (i.e. 1 M H_2SO_4) is $[U^{VI}O_2(SO_4)_2, n\ H_2O]^{2-}$, where n = 2-3 *[185-188]*. However, several controversies exist in the isomers of the species *[185,189]*. In order to understand the above mentioned electrocatalytic reduction of U(VI) on AuNPs, we optimized the geometries of $[U^{VI}O_2(SO_4)_2, nH_2O]^{2-}$ (n = 2-3) in gas phase and then re-optimized them in the presence of solvent water medium applying the polarizable continuum model (PCM). The optimized structures are shown in *Figure 4.21* and it shows the presence of one monodentate (η^1), one bidentate (η^2) sulfates and two water molecules at the equatorial plane perpendicular to two axial oxygen atoms.

For four isomers, the bond distances of U-O_{Axial}, U-$O_{Chelating}$, U-$O_{Monodentate}$, U-O_{Water}, U-$S_{Chelating}$ and U-$S_{Monodentate}$ are approximately 1.7, 2.5, 2.4, 2.8, 3.2 and 3.6 Å, respectively. These computed bond distances are in good agreement with the reported values of the similar complexes *[49, 53]*. In gas phase, the free energy of formation of $[U^{VI}O_2(\eta^1\text{-}OSO_3)(\eta^2\text{-}O_2SO_2), 2H_2O]^{2-}$ (*Figure 4.21a*) and $[U^{VI}O_2(\eta^1\text{-}OSO_3)(\eta^2\text{-}O_2SO_2), 3\ H_2O]^{2-}$ (*Figure 4.21c*) are -2693.3 and -2699.2 kJ mol^{-1}, respectively. It means that $[U^{VI}O_2(\eta^1\text{-}OSO_3)(\eta^2\text{-}O_2SO_2), 3H_2O]^{2-}$ is more stable in gas phase by -5.8 kJ mol^{-1}. However, the relative stability is reversed upon solvation. In solution phase, the free energy of formation of $[U^{VI}O_2(\eta^1\text{-}OSO_3)(\eta^2\text{-}O_2SO_2), 2H_2O]^{2-}$ (*Figure 4.21b*) and $[U^{VI}O_2(\eta^1\text{-}OSO_3)(\eta^2\text{-}O_2SO_2), 3H_2O]^{2-}$ (*Figure 4.21d*) are -3580.2 and -3502.3 kJ mol^{-1}, respectively. Therefore, $[U^{VI}O_2(\eta^1\text{-}OSO_3)(\eta^2\text{-}O_2SO_2), 2\ H_2O]^{2-}$ becomes more stable by ~78 kJ mol^{-1} in solvated state. Since the difference in free energy between these two isomers is greater than the thermal energy (2.5 kJ mol^{-1}) at room temperature, $[U^{VI}O_2(\eta^1\text{-}OSO_3)(\eta^2\text{-}O_2SO_2),\ 2H_2O]^{2-}$ (*Figure 4.21b*) could be considered as the predominant species under studies.

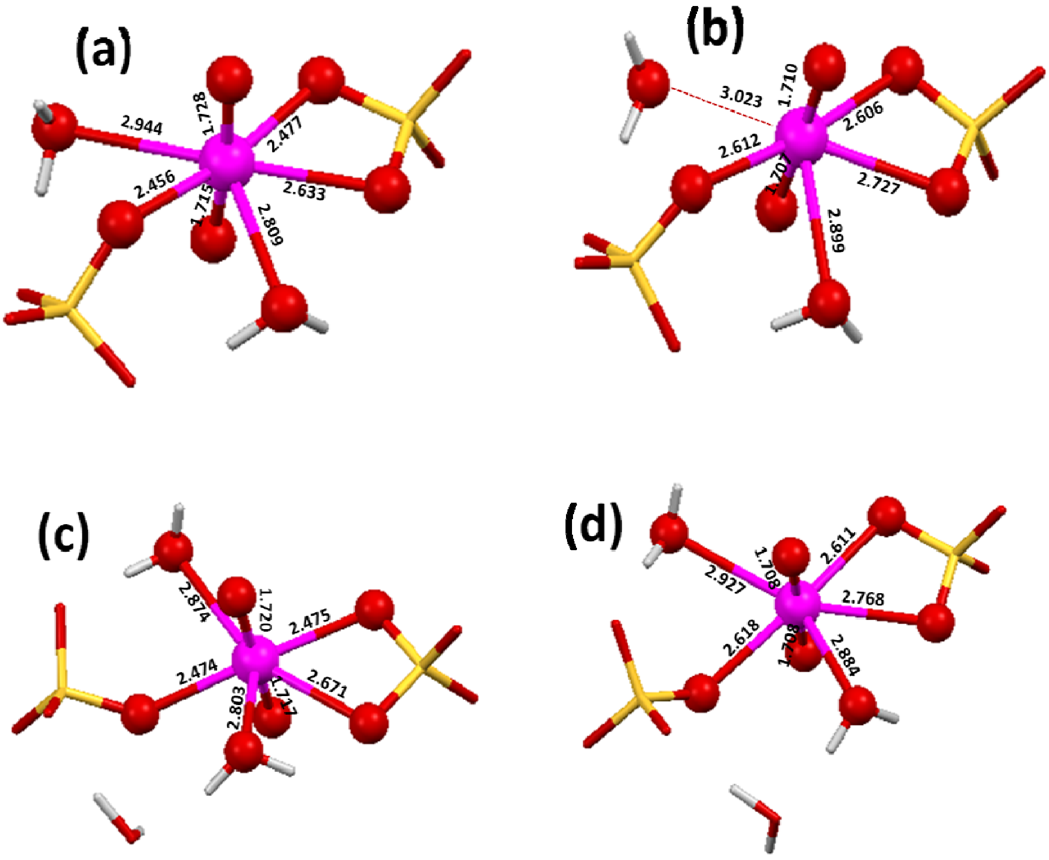

Figure 4.21 *The optimized structures of (a)* $[U^{VI}O_2(SO_4)_2,\ 2H_2O]^{2-}$ *(vacuum), (b)* $[U^{VI}O_2(SO_4)_2,\ 2\ H_2O]^{2-}$ *(hydrated), (c)* $[U^{VI}O_2(SO_4)_2,\ 3H_2O]^{2-}$ *(vacuum) and (d)* $[U^{VI}O_2(SO_4)_2,\ 3H_2O]^{2-}$ *(hydrated). The bond distances given are in Å.*

The accurate theoretical calculation of redox potentials of actinide systems remains one of the most important technical challenges due to the presence of large number of electrons, complexity of the electrochemical process and necessity of thermodynamic accuracy. The nonadiabatic electron affinity of $[U^{VI}O_2(\eta^1\text{-}OSO_3)(\eta^2\text{-}O_2SO_2),\ 2H_2O]^{2-}$ was calculated as -6.57 eV vs. vacuum in the aqueous phase without structural optimization of the reduced state using the optimised structure of the oxidised form for the starting point of the electron transfer. It should be noted that the solvation energy of the reduced species is calculated at the geometry of the oxidised complex. The energies of the highest occupied molecular orbital (HOMO) and lowest unoccupied molecular orbital (LUMO) were calculated as -7.01 eV and -5.84 eV vs. vacuum, respectively. The (a) HOMO and (b) LUMO of $[U^{VI}O_2(\eta^1\text{-}OSO_3)(\eta^2\text{-}O_2SO_2), 2H_2O]^{2-}$ are shown in *Figure 4.22*. More interestingly HOMO is comprised mostly of O(p) orbitals of monodentate sulfate; whereas LUMO is comprised of U[5f $_{z(x2-y2)}$] orbital. It shows that an interaction between filled p-orbital of oxygen atom of sulphate with that of vacant f-orbital of U(VI) ion, indicating the f-orbital participation in bonding *[190, 191]*.

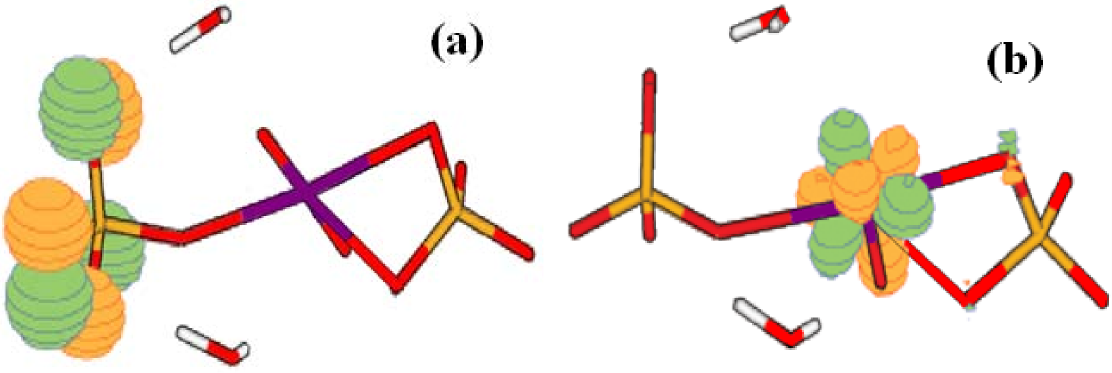

Figure 4.22 *(a) HOMO and (b) LUMO of hydrated $[U^{VI}O_2(\eta^1\text{-}OSO_3)(\eta^2\text{-}O_2SO_2), 2H_2O]^{2-}$. HOMO is comprised of lone pair from oxygen atoms of SO_4^{2-} group which acts as monodentate ligand whereas LUMO is made of 5f $_{z(x2-y2)}$ orbital of U.*

The density of states (DOS) of the sp-band of GC depends on the energy range and it is very low (~2.2×10^{-3} states/eV) i.e. below -0.1 V vs. Ag/AgCl *[192, 193]*. As it is known that the heterogeneous electron transfer rates are dependent on the DOS of the electrode material i.e. higher DOS means a higher probability of electrons of correct energy available for an electron transfer to a redox system. Therefore, the heterogeneous rate of electron transfer to U(VI) was found to be the lowest at GC. Further, the weak interaction of LUMO (consisting of U-5f orbital) of $[U^{VI}O_2(\eta^1\text{-}OSO_3)(\eta^2\text{-}O_2SO_2), 2H_2O]^{2-}$ with carbon sp-band creates a virtual energy state at -4.372 eV vs. vacuum, as discussed earlier, for the heterogeneous electron transfer reaction to take place (*Figure 4.23a*). The weak absorption of $[U^{VI}O_2(\eta^1\text{-}OSO_3)(\eta^2\text{-}O_2SO_2), 2H_2O]^{2-}$ on GC surface results into the lowest charge transfer coefficient of the reaction as evidenced from the electrochemical experiments.

On the other hand, gold has a DOS of 0.28 states/eV and this value is relatively constant with energy *[194]*. Therefore, the heterogeneous rate of electron transfer to U(VI) increased at Au. The Fermi energy of Au is -5.31 eV vs. vacuum and the centre of 5d band of Au is situated at -9.01 eV vs. vacuum. The metal 5d band interacts comparatively strongly with the LUMO (U-5f orbital) of $[U^{VI}O_2(\eta^1\text{-}OSO_3)(\eta^2\text{-}O_2SO_2), 2H_2O]^{2-}$ creating VS-LUMO at -4.549 eV vs. vacuum (*Figure 4.23b*). Moreover, the better adsorption of $[U^{VI}O_2(\eta^1\text{-}OSO_3)(\eta^2\text{-}O_2SO_2), 2H_2O]^{2-}$ on Au improves the charge transfer coefficient of the cathodic reaction.

We have proved that the defects, kinks and surface sites of the AuNP(G)/GC are not contributing in the electrocatalytic reduction of U(VI). Further, it was evidenced in the literature that work function of the AuNPs (size 5-40 nm) decorated graphene oxide is quite different compared to that of bulk gold *[195]*. Therefore, in AuNP(G)/GC, the DOS is not only expected to be increased, but the energy level of the 5d band is also expected to change. At this primitive stage, it is very difficult to prove the above mentioned speculation because lots of systematic multidisciplinary research are required to define the energy levels of the electronic bands in multiple spherical cap AuNPs decorated GC electrode.

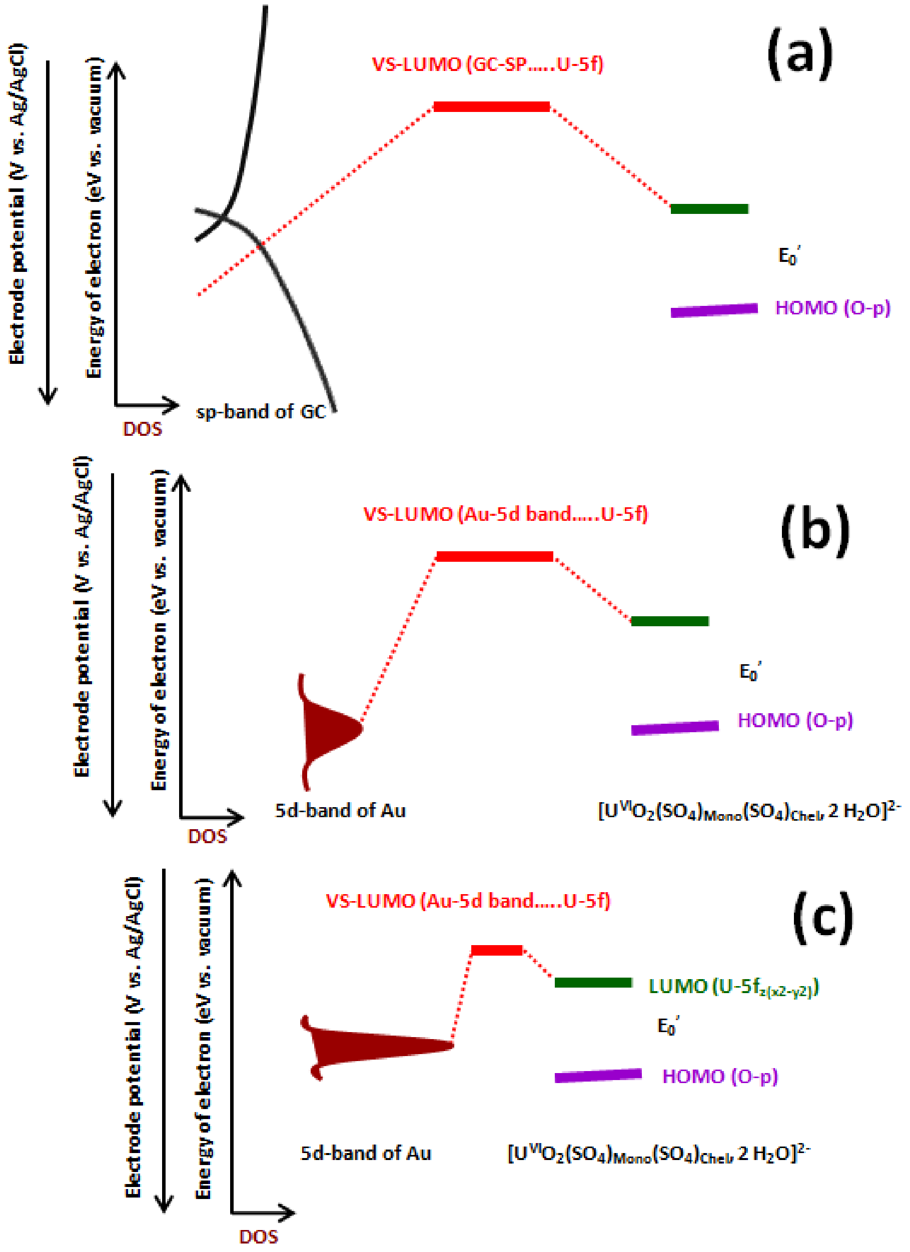

Figure 4.23 *The representation (not in absolute scale) of the interaction of LUMO with the electronic bands of* ***(a)*** *GC,* ***(b)*** *Au and* ***(c)*** *AuNP(G)/GC. VS-LUMO represents the virtual state of LUMO after interacting with the electronic bands of electrode.*

Based on the above discussions of electrochemical results and quantum mechanical calculations, it is speculated at present that the contribution of adsorption of $[U^{VI}O_2(\eta^1\text{-}OSO_3)(\eta^2\text{-}O_2SO_2), 2H_2O]^{2-}$ on AuNP(G)/GC is increased due to the increase of the DOS at AuNPs and more interaction of the U(VI)-LUMO with the Au-5d band of AuNPs. This phenomenon was indirectly supported by the energy of the VS-LUMO (at -4.542 eV vs. vacuum) and the highest observed value of the charge transfer coefficient at AuNP(G)/GC (*Figure 4.23c*).

4.3. Conclusions

The chemically pure AuNPs were electrochemically synthesized by MPPS and MGPS from a solution of H[AuCl$_4$] in 0.1 M HCl without adding any additional chemicals from any external source. Excellent control in the particle size dispersion was achieved for both the strategies and the AuNPs, as synthesized, showed excellent electrocatalytic activity in spite of using no surface stabilizing agents.

The synthesized AuNPs were polycrystalline in nature and showed excellent sensitivity for the determination of Pb(II) by square wave anodic stripping voltammetry by virtue of the atomically underpotential deposition of lead on the gold surface. The AuNPs(P)/GC electrode showed the best analytical response due to higher surface coverage of AuNPs on the GC. The linear dynamic range, sensitivity, stability, repeatability, reproducibility, accuracy and LOD of the AuNPs(P)/GC electrode were found to be quite satisfactory for the electrochemical determination of Pb(II) in drinking water.

The present study, for the first time, unravels the electrocatalytic action of AuNPs for the reduction of actinyl complexes (more precisely uranyl complexes). For this purpose, we selected the monodispersed and lesser number density AuNPs i.e. AuNP(G)/GC. The CV, DPV and EIS revealed that AuNP(G)/GC is a superior electrocatalyst compared to Au or GC for reduction of $U^{VI}O_2^{2+}$ in 1 M H_2SO_4. The highest observed value of the charge transfer coefficient and rate of electron transfer at

AuNPs are proposed because of the highest density of states of 5d band of AuNPs and its better interaction with the LUMO contributed by U-$5f_{z(x2-y2)}$ orbital of $[U^{VI}O_2(\eta^1\text{-}OSO_3)(\eta^2\text{-}O_2SO_2),2H_2O]^{2-}$, predominant stable species of $U^{VI}O_2^{2+}$ in 1 M H_2SO_4. This is the first report on the participation of the 5f-orbital of actinyl ion in the electrocatalysis at AuNPs and we can expect many new developments in this area in the near future.

These overall synthesis strategies of AuNPs may open up a few possibilities for the electrochemical preparation of electroactive pure metal nanoparticles without adding any template, directing or stabilizing agent.

CHAPTER 5

The Effect of Surface Protecting Agent on Electrocrystallization of Silver Nanoparticles (AgNPs)

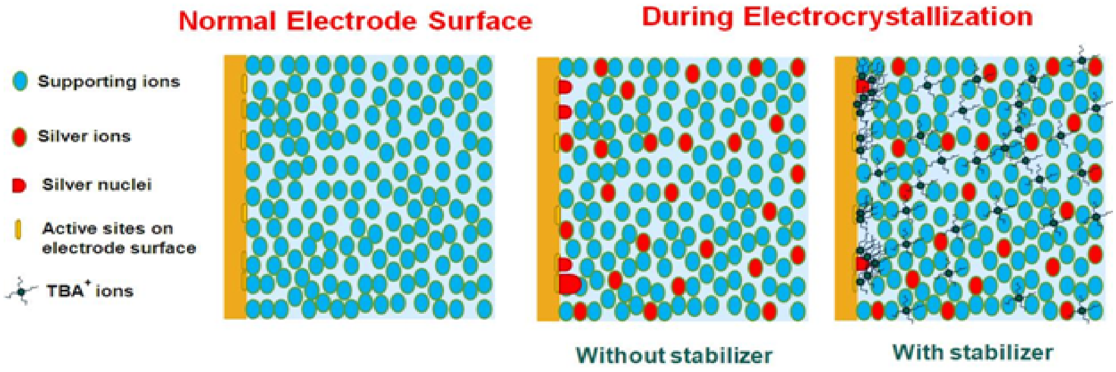

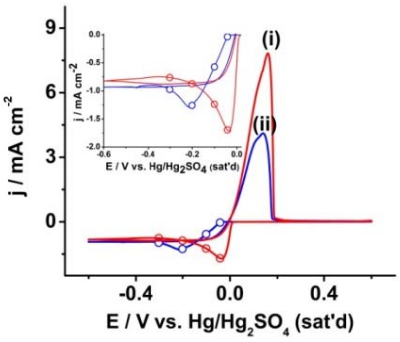

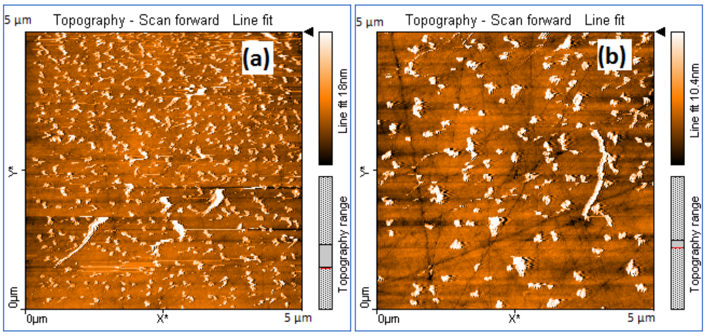

Sections of this chapter have been published in the following peer-reviewed journal:

'A Mechanistic Study on the Effect of Surface Protecting Agent on Electrocrystallization of Silver Nanoparticles', Saurav K. Guin, Rohan Phatak, Jisha S. Pillai, Arnab Sarkar and Suresh K. Aggarwal, *RSC Advances*, 2014, DOI: 10.1039/C4RA12877J.

5.1. Research Aim of this Chapter

Silver nanoparticles (AgNPs) have received considerable attention in the field of catalysis, biological and chemical sensors, degradation of pollutants and Surface-Enhanced Raman Spectroscopy (SERS) *[196-214]*. The plasmonic resonance and other properties of AgNPs strongly depend on their size, shape and composition *[203, 215-216]*. However, synthesizing nanoparticles of uniform shapes and monodispersity is still a challenging task, which attracts several researchers worldwide. Further, the surface oxide formation of the highly reactive nanoparticles alters the property of the AgNPs *[217]*. In this context, the surface protecting agents play an important role in controlling the shape and size of NPs as well as to prevent chemisorptions of oxygen on the reactive surfaces of the AgNPs. The cationic surfactant, cetyltrimethylammonium bromide (CTAB), is most extensively used as a surface stabilizer to fabricate positively charged bi-layer shell on AgNPs, where CTA^+ ions present in the first layer cap the Ag clusters via their head groups. Methylene chains of the two layers form a bi-layer shell and the head groups of the CTA^+ ions, present in the second layer, are exposed to the solution *[218]*.

In this chapter, the mechanism of electrocrystallization of AgNPs from its aqueous solution at selected potentials both in the presence and absence of surface protecting agent tetrabutylammonium tetrafluoroborate ($TBABF_4$) is discussed. The cyclic voltammetry and chronoamperometry were used to understand the influence of $TBABF_4$ on the formation and growth of silver nuclei on glassy carbon electrode. The other possible counter anions of TBA^+ viz. Br^-, ClO_4^-, PF_6^- etc. were avoided to eliminate any precipitation and decomposition.

5.2. Results and Discussion

Figure 5.1 shows cyclic voltammograms of 10 mM $AgNO_3$ + 0.1 M KNO_3 on GC in (i) absence and (ii) presence of $TBABF_4$ at a scan rate of 10 mV s^{-1}. In the absence of $TBABF_4$, the cathodic and anodic peaks of silver were observed at -0.043 V and 0.159 V, respectively. However, the cathodic peak shifted to more negative potential (-0.2 V) in the presence of $TBABF_4$ and anodic peak potential did not change much. Both the cathodic and the anodic peak currents decreased significantly. The reduction of silver in the presence of $TBABF_4$ initiated at higher overpotential of about -0.043 V and this suggests that the cathodic reaction of Ag(I) in presence of TBA^+ ions might be governed by the charge transfer polarization.

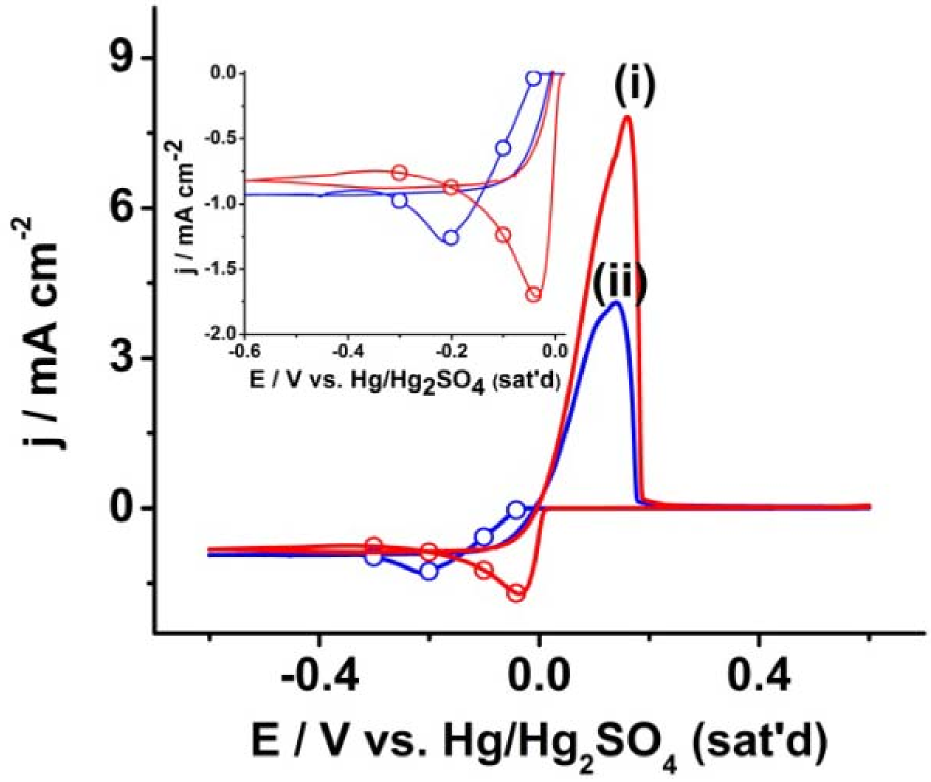

Figure 5.1 *Cyclic voltammograms of 10 mM* $AgNO_3$ *+ 0.1 M* KNO_3 *in (i) absence and (ii) presence of* $TBABF_4$ *on GC at a scan rate of 10 mV* s^{-1}*. Inset shows the zoomed image of the cathodic peaks.*

The electrocrystallization mechanism of metals can be studied by various approaches e.g. potentiostatic current transient analysis, computer simulation and scanning probe microscopic observations of electrode surface *[219]*. The first approach is simple and used more frequently in electrochemistry and was, therefore, also selected for the present study. As discussed in chapter 1, the electrocrystallization of metal involves nucleation of metal adatoms on the active sites of the electrodes followed by three dimensional diffusion controlled growth of the nuclei. The electrocrystallization and more precisely, the nucleation and growth of silver were investigated by chronoamperometry in the (a) absence and the (b) presence of $TBABF_4$ at selective constant potentials of (i) -0.300 (ii) -0.200 (iii) -0.100 and (iv) -0.043 V (*Figure 5.2*). These potentials were selected to represent the domain of concentration polarization for the cathodic reduction of Ag(I) in the absence of $TBABF_4$; and at the same time, they would represent the domains of nucleation, charge transfer polarization and concentration polarization in the presence of $TBABF_4$.

Each of the chronoamperomertic current transients (*Figure 5.2*) typically represents the three dimensional multiple nucleation and diffusion controlled growth of metal on GC. The initial current decreased significantly at time scales 5-300 ms. In the succeeding part of the transient, the current increased with time and passed through a maximum value followed by a steady decrease. The time constant ($1/\tau$) for the rearrangement of electrolyte species (ions/molecules) at the electrode-electrolyte interface would be observed within 1 ms. In present experiment, the current transients exhibit the time constants in the range 5-300 ms, which are relatively longer and this may be attributed to the parallel formation of adions or adatoms in addition to the nucleation and growth by direct attachment *[220]*.

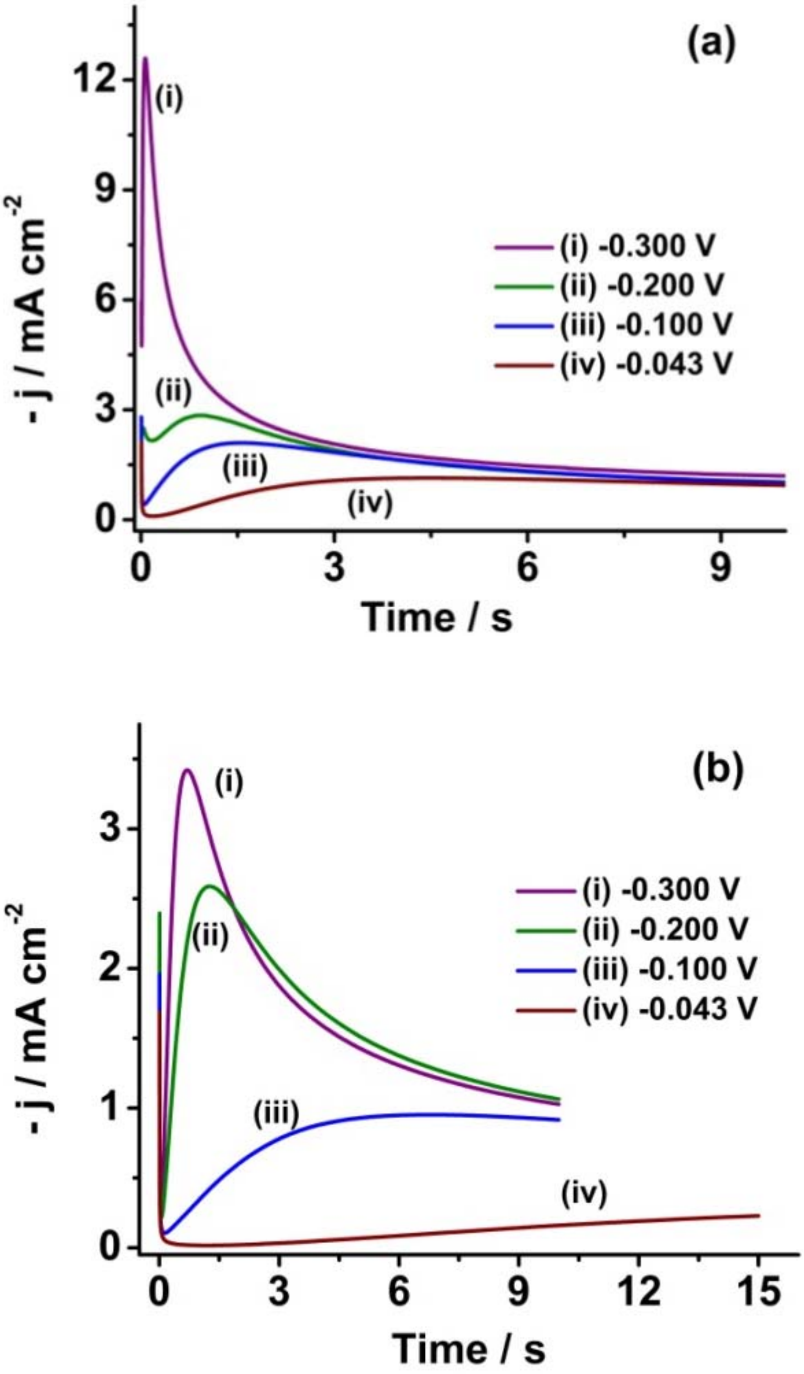

Figure 5.2 *The chronoamperometric current transients of 10 mM* $AgNO_3$ *+ 0.1 M* KNO_3 *at (i) -0.300, (ii) -0.200, (iii) -0.100 and (iv) -0.043 V in (a) absence and (b) presence of* $TBABF_4$*.*

The subsequent rise in current corresponds to increase in the overall electroactive area due to increase(s) in the number and/or size of nuclei. The spherical diffusion zone around each nucleus grows with time. At the time corresponding to the current maxima, the spherical diffusion zones overlap and mass transfer becomes linear. The change in diffusion regime leads to a decrease in the current with increasing time obeying Cottrell equation. At -0.300 V, the j_m at time t_m was 12.6 mA cm^{-2} at 67.3 ms (*Figure 5.2a(i)*) and 3.4 mA cm^{-2} at 692.0 ms (*Figure 5.2b(i)*) in the absence and the presence of $TBABF_4$, respectively. It suggests that the increase in the electroactive area was suppressed as well as overlaps of the spherical diffusion zones became sluggish in the presence of $TBABF_4$. It should be noted that no current maximum was observed for sufficient time (15 s) in the potentiostatic current transient at -0.043 V in the presence of $TBABF_4$ (*Figure 5.2b(iv)*); whereas j_m of 2.1 mA cm^{-2} was observed at t_m 1.55 s at the same potential in the absence of $TBABF_4$ (*Figure 5.2a(iv)*). It indicates that the time period for the introduction of nucleation on GC was prolonged in presence of $TBABF_4$.

To identify the nucleation mechanism, the experimental current transients were compared with those obtained through Scharifker and Hills (SH) model (*Section 1.4*) for two limiting cases viz. instantaneous and progressive nucleations *[134-136, 221]*. The dimensionless variables, $(j/j_m)^2$ vs. t/t_m obtained from the experimental current transients were plotted along with the theoretical curves for instantaneous and progressive nucleations (*Eqs. 1.65, 1.66*) (*Figure 5.3*). In the absence of $TBABF_4$, the experimental curves for all applied potentials were observed in between the two limiting cases of SH-model (*Figure 5.3a*). In the presence of $TBABF_4$, these curves became closer to the progressive type of nucleation (*Figure 5.3b*). The nucleation parameters viz. diffusion coefficient of Ag^+ ions (D), effective nucleation rate (aN_0, cm^-

^{2} s^{-1}) [where, “a” is the nucleation rate constant (s^{-1}) and N_0 is the number of active sites (cm^{-2})] and saturation nucleus density (N_S, cm^{-2}) were calculated for progressive type of nucleation (*Eqs. 1.67, 5.1, 5.2*) (*Table 5.1*).

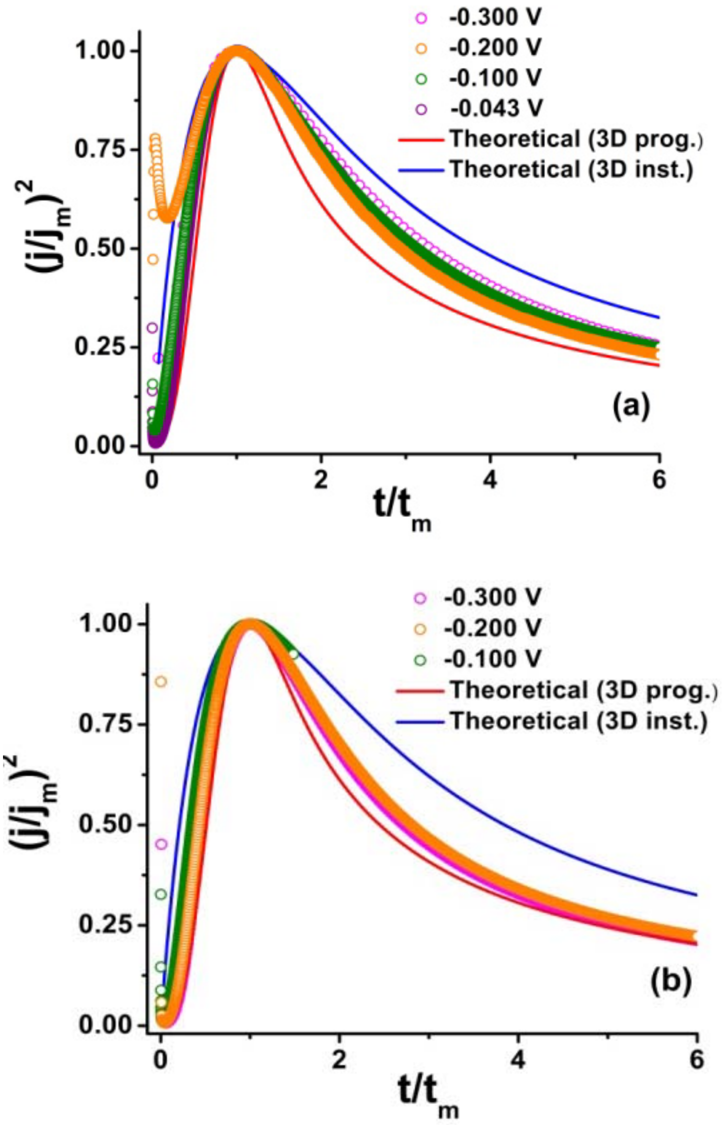

Figure 5.3 *The plot of dimensionless variables,* $(j/j_m)^2$ *vs.* t/t_m *obtained from the experimental current transients in the (a) absence and (b) presence of* $TBABF_4$*. The dimensionless variables of the calculated (theoretical) current transients for instantaneous and progressive nucleation according to the SH model are also overlaid in each graph.*

$$j_m^2 t_m = 0.2598D(zFC)^2 \quad (5.1)$$

$$|j_m| = 0.4615zFCD^{\frac{3}{4}}(k'aN_0)^{\frac{1}{4}} \quad (5.2)$$

Table 5.1 *Derived values of D, aN_0 and N_S from the current transients at different potentials by following SH Model.*

Potential (V)	**In absence of TBABF$_4$**			**In presence of TBABF$_4$**		
	D ($cm^2\ s^{-1}$)	**aN_0 ($cm^{-2}\ s^{-1}$)**	**N_S (cm^{-2})**	**D ($cm^2\ s^{-1}$)**	**aN_0 ($cm^{-2}\ s^{-1}$)**	**N_S (cm^{-2})**
-0.300	4.4×10^{-5}	1.3×10^{8}	4.7×10^{6}	3.5×10^{-5}	1.6×10^{6}	5.8×10^{5}
-0.200	3.1×10^{-5}	9.6×10^{5}	4.8×10^{5}	3.4×10^{-5}	4.6×10^{5}	3.2×10^{5}
-0.100	2.8×10^{-5}	3.7×10^{5}	3.1×10^{5}	2.5×10^{-5}	2.2×10^{4}	8.1×10^{4}
-0.043	2.4×10^{-5}	5.4×10^{4}	1.3×10^{5}	Could not be calculated because of absence of prominent current maximum		

The average values of D in the absence and presence of TBABF$_4$ are 3.2×10^{-5} and 3.1×10^{-5} cm^2 s^{-1}, respectively. Therefore, the presence of TBABF$_4$ did not affect the diffusion controlled growth of the silver nuclei. However, the aN_0 and N_S significantly decreased with decrease in the applied overpotential. It suggests that the electrocrystallization of silver nuclei was governed by the activation overpotential. As the overpotential increases, more and more substrate sites become active at the electrode-electrolyte interface for transferring electrons to Ag^+ ions. It is interesting to note that the number of active substrate sites as well as aN_0 decreased drastically in the presence of TBABF$_4$ at the same overpotential. This is attributed to increase in the activation overpotential for electrocrystallization of silver in the presence of TBABF$_4$. The activation polarization could be evaluated in terms of two parameters viz. “a” and N_0. However, evaluation of these two parameters separately for each transient was not possible by SH model. Further, the accuracy of the values of D, aN_0 and N_S can not be ascertained because of a single point (t_m, j_m) measurement. It also should be emphasized that the actual nucleation and growth, as evidenced in *Figure 5.3*, did not belong to two extreme cases. Therefore, SH model does not represent the actual electrocrystallization mechanism.

As was mentioned in chapter 1, Scharifker and Mostany (SM) *[80]*, Sluyters-Rehbach, Wijenberg, Bosco and Sluyters (SRWBS) *[83]*, Heerman and Tarallo (HT) *[84, 85, 87]* models have been made to eliminate the analysis of two separate cases by establishing a general model of electrochemical nucleation. For the convenience of reading, it should be mentioned here that all these models viz. SH, SM, SRWBS and HT have been established from the same nucleation law and Avrami's theorem, but with different assumptions on the thickness of the diffusion layer around the nuclei (*Section 1.4 and Table 1.1*).

The genetic algorithm, a useful stochastic approach, has been earlier used to get the values of D, N_0 and "a" by fitting a portion of the experimental current transient with SM model *[222]*. In this chapter, the mechanism of electrocrystalization is discussed through the evaluation of the initial current density (j_0 in A cm^{-2}), decay constant (τ in s^{-1}), D, N_0 and "a" by fitting the entire experimental current transients (for the first time, the double layer discharge region was also considered in the fitting of electrocrystallization model) with the calculated current transients (from the SM, SRWBS and HT models) using hybrid genetic algorithm (HGA). The design intention of the hybrid algorithm is to exert fully the random search ability of the genetic algorithm (GA) to provide good initial estimates of parameters for the nonlinear regression by Levenberg-Marquardt algorithms (LMA) (*Figure 5.4*).

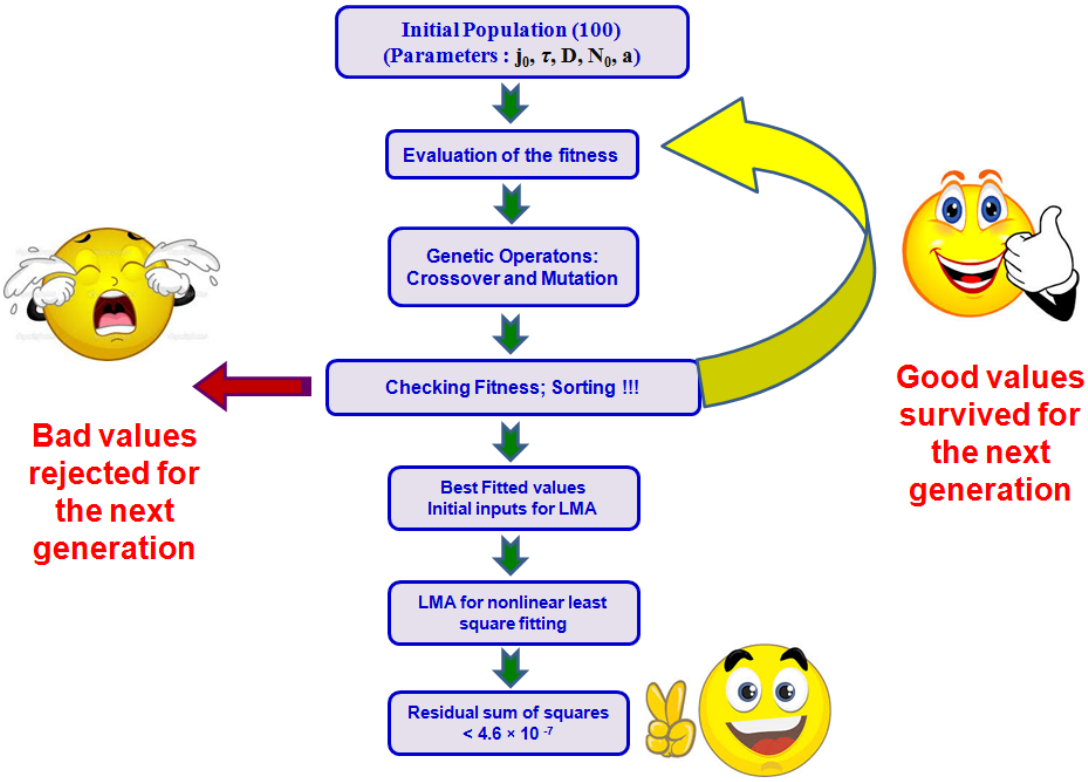

Figure 5.4 *Schematic representation of HGA. The detailed procedure is discussed in Section 2.9.1.*

It is important to mention that the potentiostatic current transients fitted well by HGA with all the three models with residual sum of squares ($\sim 10^{-7}$) and reduced χ^2($\sim 10^{-10}$) (*Figure 5.5*). The values of five parameters obtained from three models for all the potentiostatic current transients are shown in *Figure 5.6*. It can be seen that the values of j_0 and τ increased while N_0 and “a” decreased significantly at all potentiostatic transients in presence of $TBABF_4$. The values of D remained unaffected by the presence of $TBABF_4$. It was earlier reported that SM and SRWBS theories accurately fitted and yielded nearly equal values for N_0 *[81]*. However, the initial fall of current was ignored in those calculations. In contrast, we considered the complete experimental current transient for the fitting purpose. Therefore, the parallel formation of adions or adatoms during the initial fall of current was considered in our calculations. Hence, diverse values of N_0 and "a" were calculated by different models for the same current transient.

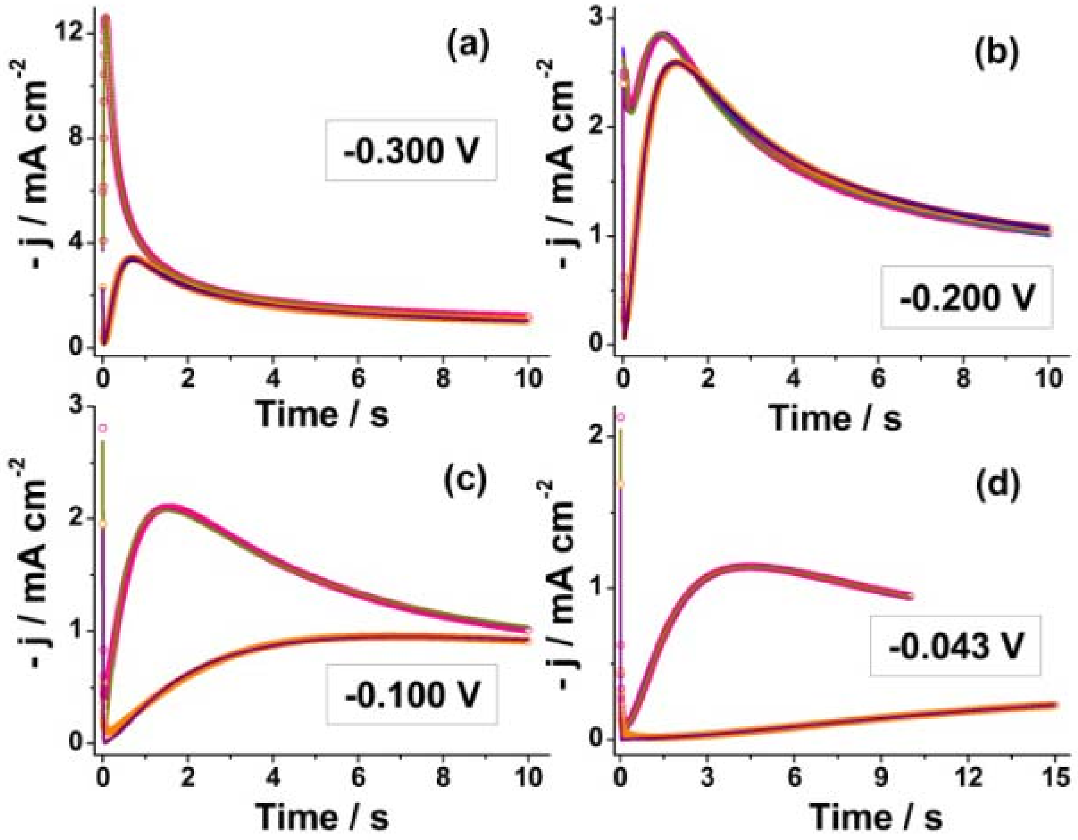

Figure 5.5 *The potentiostatic current transients at (a) -0.300 (b) -0.200 (c) -0.100 and (d) -0.043 V in the (i) absence (pink circles) and (ii) presence (saffron circles) of TBABF$_4$. The solid lines (colour of each line is not visible indistinguishably because of overlapping among them) are the fitted lines according to SM, SRWBS and HT models.*

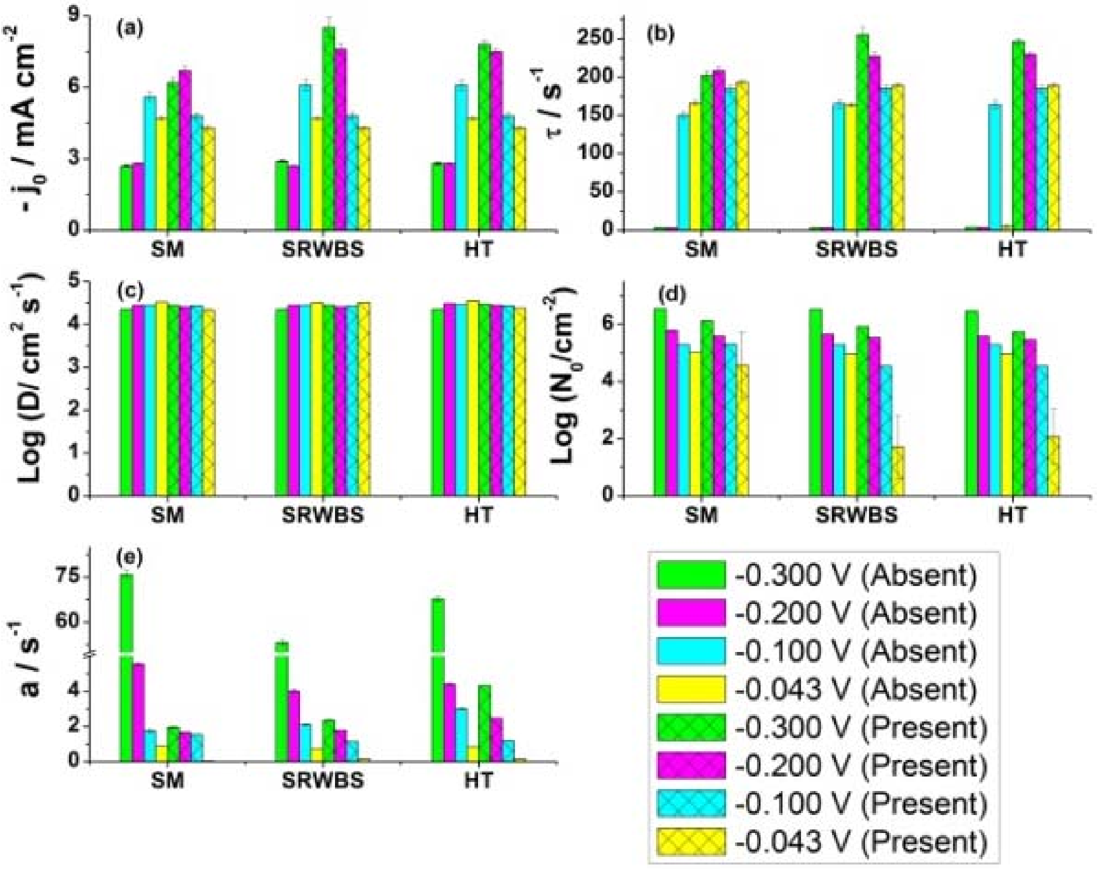

Figure 5.6 *The optimized fitted parameters viz.* j_0, τ, *Log D, Log N and "a" obtained by fitting through SM, SRWBS and HT models for each potentiostatic transient. Here (Absent) and (Present) represent the absence and presence of* $TBABF_4$, *respectively.*

It is known that j_0 and τ are inversely proportional to the resistance of the electrolyte solution, thus they increased upon addition of $TBABF_4$ in the electrolyte. The TBA^+ ions in the bulk electrolyte do not affect the diffusion of Ag_{aq}^+ ions in the solution. However, TBA^+ ions compete with Ag_{aq}^+ ions to occupy the active sites on the electrode at negative potentials. Moreover, the adsorption of TBA^+ ions onto the electrode surface blocks the active sites as well as introduces their electrostatic interaction with the Ag_{aq}^+ ions. Therefore, the kinetics of electrocrystallization and subsequently the number of nuclei decrease in presence of TBA^+ ions. The schematic representations of the difference of electrocrystallization in the absence and presence of TBA$^+$ ions are shown in *Figure 5.7*.

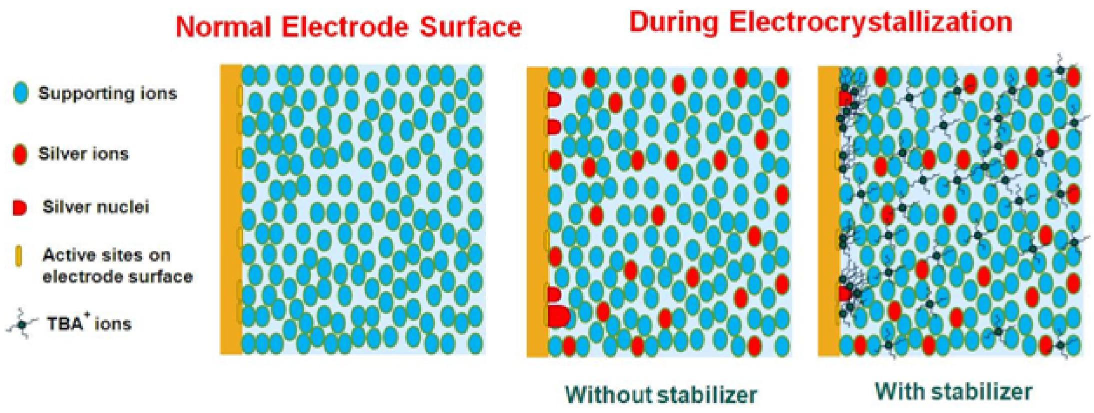

Figure 5.7 *Schematic representation of the difference of electrocrystallization in the absence and presence of TBA$^+$ ions.*

As was discussed earlier, the accurate fits for each current transient were obtained for SM, SRWBS and HT models. However, for same current transient, the values of j_0, τ, N_0 and “a” differed from model to model. The variations in the values of N_0 and “a” are quite significant. Similar observations were also reported elsewhere *[81, 88]*. We considered it worthwhile to perform a statistical analysis using PCA for SH, SM, SRWBS and HT models with the values given in *Table 5.2*.

Figure 5.8 shows the distribution of SH, SM, SRWBS and HT models on PC1 vs. PC2 in the (a) absence and (b) presence of TBABF$_4$. It can clearly be seen that the four models are devoid of any correlation due to dispersion in the values of the important parameters such as N_0 and “a”.

Table 5.2 *The values of the fitted parameters used for PCA.*

Model		**D / (10^{-5} cm^2 s^{-1})**			**N_S / (10^6 cm^{-2})**			**aN_0 / (10^6 cm^{-2} s^{-1})**		
		Potential (V)								
		-0.3	**-0.2**	**-0.1**	**-0.3**	**-0.2**	**-0.1**	**-0.3**	**-0.2**	**-0.1**
In presence of TBABF$_4$	**SM**	4.40	3.60	3.60	3.60	0.610	0.190	273	3.37	0.331
	SRWBS	4.40	3.60	3.60	3.40	0.450	0.190	181	1.80	0.397
	HT	4.40	3.30	3.50	3.00	0.390	0.190	203	1.72	0.57
	SH	4.40	3.10	2.80	4.70	0.480	0.310	130	0.96	0.37
In absence of TBABF$_4$	**SM**	3.60	3.90	3.70	1.30	0.390	0.200	2.54	0.644	0.306
	SRWBS	3.60	3.90	3.80	0.810	0.340	0.034	1.90	0.602	0.039
	HT	3.40	3.60	3.70	0.540	0.290	0.035	2.33	0.716	0.042
	SH	3.50	3.40	2.50	0.580	0.320	0.081	1.60	0.46	0.022

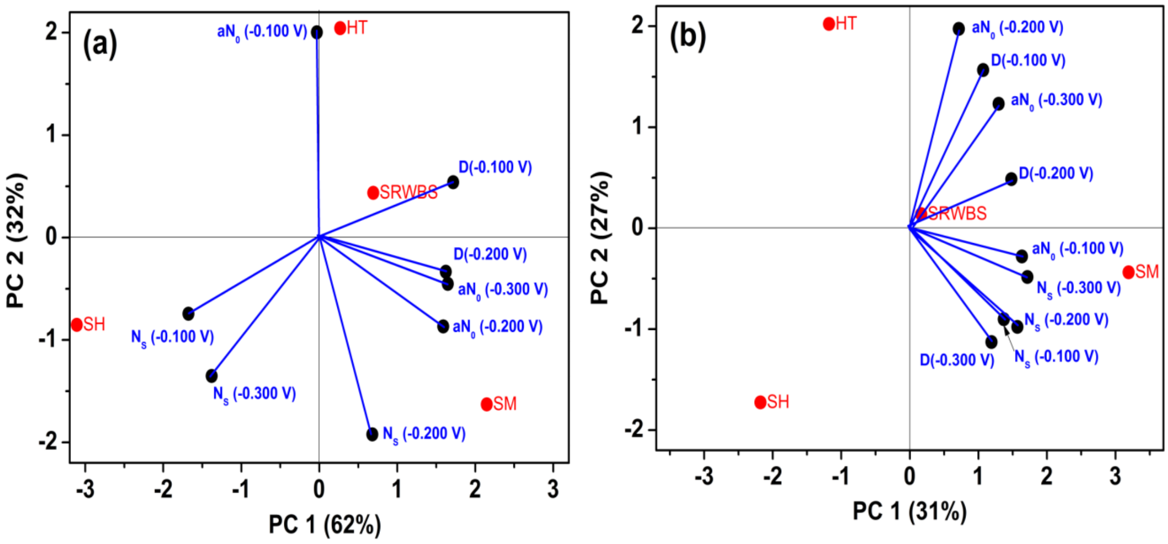

Figure 5.8 *The distribution of SH, SM, SRWBS and HT models on PC2 vs. PC1 in the (a) absence and (b) the presence of TBABF$_4$. The loadings of each parameter are shown by the distance of the black points from the origin. In (a) D (-0.300 V) is not shown in the calculation because it had same values for the four models.*

Further, *Figure 5.9a* shows the AFM topography (5 µm × 5 µm) of the AgNPs deposited at -0.300 V for 10 s in the absence of $TBABF_4$. The approximate density of nuclei (N_0) was found to be 2.8×10^9 cm^{-2}, which is much underestimated by SM (~3.0×10^6 cm^{-2}), SRWBS (~3.6×10^6 cm^{-2}) and HT (~3.4×10^6 cm^{-2}) models. Similar result was observed for the AFM topography (5 µm × 5 µm) of the AgNPs deposited at -0.300 V for 10 s in the presence of $TBABF_4$ (*Figure 5.8b*). The approximate density of nuclei was found to be 5.1×10^8 cm^{-2}, which is much underestimated by SM (~1.3×10^6 cm^{-2}), SRWBS (~8.1×10^5 cm^{-2}) and HT (~5.4×10^5 cm^{-2}) models. Although the calculated values are far from the reality, a significant decrease in the number of nuclei was also observed in the presence of $TBABF_4$ and it supports the former discussions.

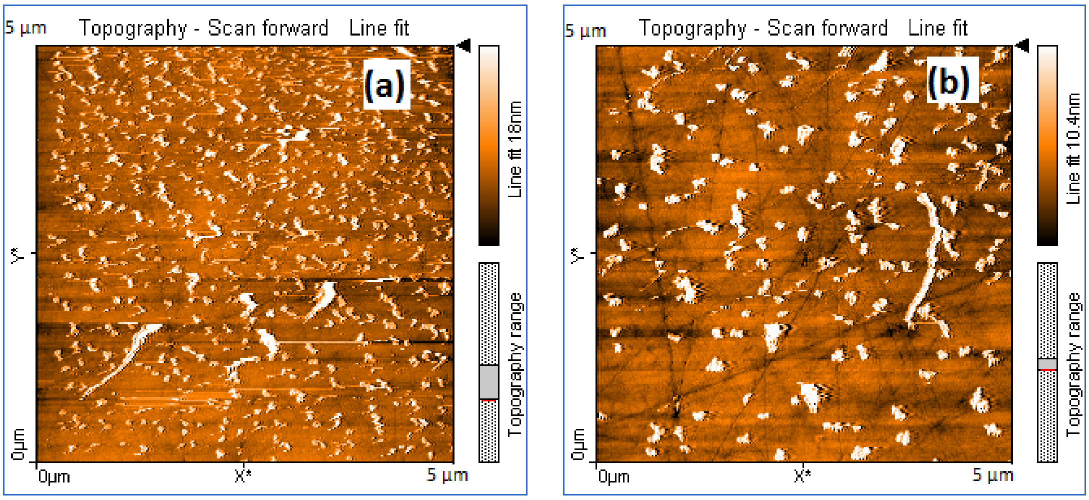

Figure 5.9 *The AFM topography (XY) of the AgNPs deposited on GC at -0.300 V for 10 s in (a) the absence and (b) the presence of* $TBABF_4$. *The vertical bar at the top right of each image represents the z-profile of the XY image.*

There are a few reports which similarly observed higher nuclei density by scanning electron microscope than those calculated from the models *[90, 223-225]* and no attempt was made to evaluate the value of N_0 for other cases. We note that, in the presence of $TBABF_4$, the particle size (in XY-direction) increases while it decreases along the Z-direction. The exact reason of this is not known at present and it will be explored in more details in the future. Further, the GC electrode, polished to mirror finish, inherently contains scratches of a few nano- to micro-meter widths. The interfacial Gibbs energy of these scratches would be much more than the planes of GC. Therefore, more number of nuclei is located around the scratches (*Figure 5.9*). It also supports that the assumption of constant nucleation rate is not valid in the reality of electrochemical nucleation *[226-229]*. Thus the higher rate of nucleation at the scratches can lead to higher number of nuclei around them. However, we note that the microscopic picture of the small segment of the electrode may not give the true quantitative nuclei density of the entire GC surface because of (1) dispersion in the particle size, (2) overlaps between the neighbouring nuclei and (3) cluster formation around the scratches.

Based on the above statistical analysis of data and the absence of any correlation among the different models, the following observations can be made. (1) The researchers should be careful in attaching any extra significance to the numerical values of j_0, τ, D, N_0, “a” of any system only based on the quality of fitting. (2) The true density of nuclei significantly differs from the calculated values from the models. (3) The compatibility of the realistic nucleation and growth mechanism with the (a) nucleation rate law (*Eq. 1.27*) along with the assumption of the constant nucleation rate, (b) assumptions of the diffusion zones *[230-232]* and (c) the compatibility of the Avrami’s theory should be revaluated. The present study, therefore, corroborates the need to revise electrochemical nucleation and growth *[221, 233]*.

5.3. Conclusion

The above study shows that the electrocrystallization of silver nuclei in presence of TBA^+ ions is governed by the activation overpotential. The TBA^+ ions in the bulk electrolyte do not affect the diffusion of Ag_{aq}^+ ions in the solution. However, TBA^+ ions compete with Ag_{aq}^+ ions to occupy the active sites on the electrode at negative potentials. Moreover, the adsorption of TBA^+ ions onto the electrode surface blocked the active sites as well as introduced, to some extent, an electrostatic interaction with the Ag_{aq}^+ ions. Therefore, the kinetics of electrocrystallization and subsequently the number of nuclei decreased in presence of TBA^+ ions. The PCA showed that the SH, SM, SRWBS and HT models do not correlate among themselves; though these four models were originated from the same nucleation law of electrocrystallization and Avrami's theorem with different arguments, which make physical sense.


SUMMARY

Summary of Key Findings

This dissertation presents different strategies for the template-free electrosynthesis of lead, gold and silver nanoparticles. The discrete and monodispersed capped hemispherical metal nanoparticles can be produced on a low surface energy conductive substrate by following these strategies. Though detailed investigation of the metal(deposited)-substrate pair has to be performed to design the efficient strategy, because the thermodynamics and surface kinetics parameters play key roles in the electrochemical nucleation and growth of metal nanoparticles on the substrate. Hence, this study would be useful for designing systems of controlled size for fundamental studies and practical purposes in the field of material sciences and condensed-matter physics.

The novel potentiostatic triple pulse strategy (PTPS) was developed for room temperature template-free electrosynthesis of lead nanoparticles (PbNPs) from aqueous solution of Pb(II). The chemisorbed oxygen covers the surface of PbNP. This is the first effort for the electrosynthesis of PbNPs (without any adlayer of Pb) on a template free substrate. The cause of improvement in the particle size and size dispersion in PTPS compared to conventional potentiostatic double pulse strategy (PDPS) was also revealed.

Novel multiple potentiostatic pulse strategy (MPPS) and multiple galvanostatic pulse strategy (MGPS) were developed for the template free electrosynthesis of gold nanoparticles (AuNPs) on a GC electrode. Excellent control of the particle size dispersion was achieved in both the routes of synthesis. The AuNPs showed excellent sensitivity and lowest limit of detection (57 ng L^{-1} or 274 pM) for the determination of Pb(II) at ultratrace levels by square wave anodic stripping voltammetry (SWASV). The stability, repeatability, reproducibility and accuracy of the analytical response were found to be satisfactory for the analytical purposes. The AuNPs also showed excellent electrocatalytic reduction of U(VI) in 1 M H_2SO_4. This is the first report on the electrocatalysis of $U^{VI}O_2^{2+}$ in 1 M H_2SO_4 at AuNPs supported on glassy carbon electrode. The quantum chemical calculations were performed to understand the mechanism of electrocatalysis at molecular levels. The highest observed values of the charge transfer coefficient as well as the rate of electron transfer at AuNPs are attributed to the highest density of states of 5d-band of gold and its strong interaction with the LUMO contributed by U-$5f_{z(x2-y2)}$ orbital of $[U^{VI}O_2(\eta^1\text{-}OSO_3)(\eta^2\text{-}O_2SO_2), 2H_2O]^{2-}$, predominant stable species of $U^{VI}O_2^{2+}$ in 1 M H_2SO_4.

The surface protecting agent, viz. tetrabutylammonium tetrafluoroborate ($TBABF_4$) can be used for avoiding chemisorptions of oxygen on the surface of nanoparticles. However, the presence of surface protecting agent slowed down the kinetics of electrocrystallization of AgNPs because of the induction of activation overpotential at the electrode-electrolyte interface and subsequently the number of nuclei on the electrode surface decreased in presence of TBA^+ ions. Therefore, the electrochemical strategy for the synthesis of metal nanoparticles in the presence of any surface protecting agent is expected to be vastly different compared to the strategy designed for synthesizing metal nanoparticles in the absence of this agent. This study also revealed that enough artifacts exist in the optimized values of the number of nuclei; nucleation rate etc. following SH, SM, SRWBS, and HT models (i.e. models of the electrochemical 3D multiple nucleation and growth) and these models deviate far off from the reality. Therefore, enough need exists to develop new electrocrystallization model or to modify the existing models of electrocrystallization.

BIBLIOGRAPHY

References

1. B.N. Taylor, A. Thompson (Editors); *The international system of units (SI)*, NIST Special Publication 330, 2008, 29.
2. N. Xia, L. Zhang, Nanomaterials-based sensing strategies for electrochemical detection of microRNAs, *Materials, 7* (2014) 5366-5384.
3. C. Burda, X. Chen, R. Narayanan, M.A. El-Sayed, Chemistry and properties of nanocrystals of different shapes, *Chem. Rev.*, **105** (2005) 1025-1102.
4. K. Elouarzaki, A.L. Goff, M. Holzinger, C. Agnes, F. Duclairoir, J.-L. Putaux, S. Cosnier, From gold porphyrins to gold nanoparticles: catalytic nanomaterials for glucose oxidation, *Nanoscale*, **6** (2014) 8556-8560.
5. G. Baffou, R. Quidant, Nanoplasmonics for chemistry, *Chem. Soc. Rev.*, **43** (2014) 3898-3907.
6. Q. Zhang, E. Uchaker, S.L. Candelaria, G. Cao, Nanomaterials for energy conversion and storage, *Chem. Soc. Rev.*, **42** (2013) 3127-3171.
7. H.-J. Freund, N. Nilius, T. Risse, S. Schauermann, A fresh look at an old nano-technology: Catalysis, *Phys. Chem. Chem. Phys.*, **16** (2014) 8148-8167.
8. J. Solla-Gullon, F.J. Vidal-Iglesias, J.M. Feliu, Shape dependent electrocatalysis, *Annu. Rep. Prog. Chem., Sect. C*, **107** (2011) 263-297.
9. C.M. Welch, R.G. Compton, The use of nanoparticles in electroanalysis: a review, *Anal. Bioanal. Chem.*, **384** (2006) 601-619.
10. S.E.F. Kleijn, S.C.S. Lai, M.T.M. Koper, P.R. Unwin, Electrochemistry of nanoparticles, *Angew. Chem. Int. Ed.*, **53** (2014) 3558-3586.
11. A. Merkoci, Nanoparticles based electroanalysis in diagnostics applications, *Electroanalysis*, **25** (2013) 15-27.

12. L. Rassaei, M. Amiri, C.M. Cirtiu, M. Sillanpaa, F. Marken, M. Sillanpaa, Nanoparticles in electrochemical sensors for environmental monitoring, *Trend. Anal. Chem.*, **30** (2011) 1704-1715.

13. T.K. Sau, A.L. Rogach, Nonspherical noble metal nanoparticles: Colloid-chemical synthesis and morphology control, *Adv. Mater.*, **22** (2010) 1781-1804.

14. T.K. Sau, A.L. Rogach, F. Jackel, T.A. Klar, J. Feldmann, Properties and applications of colloidal nonspherical noble metal nanoparticles, *Adv. Mater.*, **22** (2010) 1805-1825.

15. A.J. Arvia, R.C. Salvarezza, W.E. Triaca, Noble metal surfaces and electrocatalysis: Review and perspectives, *J. New Mat. Electr. Sys.*, **7** (2004) 133-143.

16. D. Astruc (Editor), Nanoparticles and catalysis, Wiley-VCH Verlag GmbH & Co. KGaA, Weinheim, 2008.

17. J. Jayabalan, M.P. Singh, A. Banerjee, K.C. Rustagi, Linear and nonlinear second-order polarizabilities of hemispherical and sector-shaped metal nanoparticles, *Phys. Rev. B*, **77** (2008) 045421(10 pages).

18. S. Guo, E. Wang, Noble metal nanomaterials: Controllable synthesis and application in fuel cells and analytical sensors, *Nano Today*, **6** (2011) 240-264.

19. L. Zhang, E. Wang, Metal nanoclusters: New fluorescent probes for sensors and bioimaging, *Nano Today*, **9** (2014) 132-157.

20. J.A. Blackman (Editor), *Metallic nanoparticles*, Elsevier, 1st Edition, 2009.

21. Y. Tan, Y. Li, D. Zhu, *Noble metal nanoparticles*, Encyclopedia of Nanoscience and Nanotechnology, **8** (2004) 9-40.

22. D.L. Feldheim, Jr. C.A. Foss (Editors), *Metal nanoparticles: Synthesis, characterization and applications*, Marcel Dekker, 2002.

23. J. Behari, Principles of nanoscience: An overview, *Indian J. Exp. Biol.,* **48** (2010) 1008-1019.

24. R.P. Feynman, *Miniaturization*, Reinhold, New York, 1961.

25. J.M. Lehn, *Supramolecular chemistry*, VCH, Weinheim, 1995.

26. Y. Wang, Y. Xia, Bottom-up and top-down approaches to the synthesis of monodispersed spherical colloids of low melting-point metals, *Nano Lett.*, **4** (2004) 2047-2050.

27. Y. Ju-Nam, J.R. Lead, Manufactured nanoparticles: An overview of their chemistry, interactions and potential environmental implications, *Sci. Total Environ.*, **400** (2008) 396-414.

28. L.P. Bicelli, B. Bozzini, C. Mele, L. Durzo, A review of nanostructural aspects of metal electrodeposition, *Int. J. Electrochem. Sci.*, **3** (2008) 356-408.

29. M.V. Mandke, H.M. Pathan, Electrochemical growth of copper nanoparticles: Structural and optical properties, *J. Electroanal. Chem.*, **686** (2012) 19-24.

30. M. Rajkumar, C.P. Hong, S.-M. Chen, Electrochemical synthesis of palladium nano urchins decorated multi walled carbon nanotubes for electrocatalytic oxidation of hydrazine and reduction of hydrogen peroxide, *Int. J. Electrochem. Sci.*, **8** (2013) 5262-5274.

31. Z.-L. Xiao, C.Y. Han, W.-K. Kwok, H.-H. Wang, U. Welp, J. Wang, G.W. Crabtree, Tuning the architecture of mesostructures by electrodeposition, *J. Am. Chem. Soc.*, **126** (2004) 2316-2317.

32. C.A.C. Sequeira, D.M.F. Santos, Electrochemical routes for industrial synthesis, *J. Braz. Chem. Soc.*, **20** (2009) 387-406.

33. J.V. Zoval, P.R. Biernacki, R.M. Penner, Implementation of electrochemically synthesized silver nanocrystallites for the preferential SERS enhancement of defect modes on thermally etched graphite surfaces, *Anal. Chem.*, **68** (1996) 1585-1592.

34. B.J. Plowman, S.K. Bhargava, A.P. O'Mullane, Electrochemical fabrication of metallic nanostructured electrodes for electroanalytical applications, *Analyst*, **136** (2011) 5107-5119.

35. K.-S. Choi, Shape control of inorganic materials via electrodeposition, *Dalton Trans.*, (2008) 5432-5438.

36. C.T.J. Low, R.G.A. Wills, F.C. Walsh, Electrodeposition of composite coatings containing nanoparticles in a metal deposit, *Surf. Coat. Technol.*, **201** (2006) 371-383.

37. Y. Liu, J. Goebl, Y. Yin, Templated synthesis of nanostructured materials, *Chem. Soc. Rev.* **42** (2013) 2610-2653.

38. A. Walcarius, Mesoporous materials and electrochemistry, *Chem. Soc. Rev.*, **42** (2013) 4098-4140.

39. B. Plowman, S.J. Ippolito, V. Bansal, Y.M. Sabri, A.P. O'Mullane, S.K. Bhargava, Gold nanospikes formed through a simple electrochemical route with high electrocatalytic and surface enhanced Raman scattering activity, *Chem. Commun.*, (2009) 5039-5041.

40. L. Guo, P.C. Searson, Influence of anion on the kinetics of copper island growth, *Nanoscale*, **2** (2010) 2431-2435.

41. S.E. Lohse, N.D. Burrows, L. Scarabelli, L.M. Liz-Marzán, Anisotropic noble metal nanocrystal growth: The role of halides, *Chem. Mater.*, **26** (2014) 34-43.

42. T. Hirsch, M. Zharnikov, A. Shaporenko, J. Stahl, D. Weiss, O.S. Wolfbeis, V.M. Mirsky, Size-controlled electrochemical synthesis of metal nanoparticles on monomolecular templates, *Angew. Chem. Int. Ed.,* **44** (2005) 6775-6778.
43. S. Liu, Z. Xu, T. Sun, W. Zhao, X. Wu, Z. Ma, X. Zhang, J. He, C. Chen, Polymer-templated electrodeposition of Ag nanosheets assemblies array as reproducible surface-enhanced Raman scattering substrate, *J. Nanosci. Nanotechnol.*, **14** (2014) 4608-4614.
44. M.J. Kofke, E. Wierzbinski, D.H. Waldeck, Seedless CTAB mediated growth of anisotropic nanoparticles and nanoparticle clusters on nanostructured plasmonic templates, *J. Mater. Chem. C*, **1** (2013) 6774-6781.
45. N.I. Kovtyukhova, B.R. Martin, J.K.N. Mbindyo, T.E. Mallouk, M. Cabassi, T.S. Mayer, Layer-by-layer self-assembly strategy for template synthesis of nanoscale devices, *Mater. Sci. Eng.* C **19** (2002) 255-262.
46. X. Zeng, S. Bruckenstein, Underpotential deposition and adsorption of lead on gold polycrystalline electrodes: II. EQCM investigation in acidic 0.1 M $NaClO_4$ and 0.1 M NaCl electrolytes, *J. Electrochem. Soc.*, **146** (1999) 2555-2561.
47. M. Mariscal, W. Schmickler, On the surface properties of lead structures on Au(111), an atom dynamic approach, *J. Electroanal. Chem.*, **582** (2005) 64-68.
48. M.O. Salles, V.L. Martins, R.M. Torresi, M. Bertotti, An EQCM-D study of the influence of chloride on the lead anodic oxidation, *Electrochim. Acta*, **78** (2012) 347-352.
49. S. Szabo, Underpotential deposition of metals on foreign metal substrates, *Int. Rev. Phys. Chem.*, **10** (1991) 2017-248.

50. J. Nutariya, J. Velleuer, W. Schwarzacher, N. Vasiljevic, Surface alloying/dealloying in Pb/Au(111) system, *ECS Trans.*, **28** (2010) 15-25.

51. M.R. Deakin, O. Melroy, Underpotential metal deposition on gold, monitored in situ with a quartz microbalance, *J. Electroanal. Chem.*, **239** (1988) 321-331.

52. K. Engelsmann, W.J. Lorenz, E. Schmidt, Underpotential deposition of lead on polycrystalline and single-crystal gold surfaces. Part I: Thermodynamics, *J. Electroanal. Chem.*, **114** (1980) 1-10.

53. K. Engelsmann, W.J. Lorenz, E. Schmidt, Underpotential deposition of lead on polycrystalline and single-crystal gold surfaces. Part II: Kinetics, *J. Electroanal. Chem.*, **114** (1980) 11-24.

54. A. Hamelin, Lead adsorption on gold single crystal stepped surfaces, *J. Electroanal. Chem.*, **101** (1979) 285-290.

55. A. Hamelin, A. Katayama, G. Picq, P. Vennereau, Surface characterization by underpotential deposition: Lead on gold surfaces, *J. Electroanal. Chem.*, **113** (1980) 293-300.

56. A. Hamelin, Underpotential deposition of lead on single crystal faces of gold: Part 1. The influence of crystallographic orientation of the substrate, *J. Electroanal. Chem.*, **165** (1984) 167-180.

57. A. Hamelin, J. Lipkowski, Underpotential deposition of lead on gold single crystal faces, Part II. General Discussion, *J. Electroanal. Chem.*, **171** (1984) 317-330.

58. J.W. Shin, U. Bertocci, G.R. Stafford, Stress response to surface alloying and dealloying during underpotential deposition of Pb on (111)-textured Au, *J. Phys. Chem. C*, **114** (2010) 7926-7932.

59. G.R. Stafford, U. Bertocci, In situ stress and nanogravimetric measurements during underpotential deposition of Pb on (111)-textured Au, *J. Phys. Chem. C*, **111** (2007) 17580-17586.

60. M.J. Henderson, E. Bitziou, A.R. Hillman, E. Vieil, Lead underpotential deposition on polycrystalline gold electrode in perchloric acid solution: A combined electrochemical quartz crystal microbalance and probe beam deflection study, *J. Electrochem. Soc.*, **148** (2001) E105-E111.

61. D.M. Kolb, J. Schneider, Surface reconstruction in electrochemistry: Au(100)-(5×20), Au(111)-(1×23) and Au(110)-(1×2), *Electrochim. Acta,* **31** (1986) 929-936.

62. J.J. Calvante, N.S. Marinkovic, Z. Kováčová, W.R. Fawcett, SNIFTIRS studies of the double layer at the metal/solution interface. Part 1. Single crystal gold electrodes in aqueous perchloric, *J. Electroanal. Chem.,* **421** (1997) 49-57.

63. N. Pangarov, Thermodynamics of electrochemical phase formation and underpotential metal deposition, *Electrochim. Acta,* **28** (1983) 763-775.

64. G. Staikov, *Electrocrystallization in nanotechnology*, Wiley-VCH, 2007.

65. A. Milchev, *Electrocrystallization: Fundamentals of nucleation and growth*, Kluwer Academic Publishers, 2002.

66. A. Milchev, Electrochemical phase formation: some fundamental concepts, *J. Solid State Electrochem.*, **15** (2011) 1401-1415.

67. E. Budevski, G. Staikov, W.J. Lorenz, Electrocrystallization: Nucleation and growth phenomena, *Electrochim. Acta*, **45** (2000) 2559-2574.

68. L. Guo, G. Oskam, A. Radisic, P.M. Hoffmann, P.C. Searson, Island growth in electrodeposition, *J. Phys. D: Appl. Phys.*, **44** (2011) 443001 (12 pages).

69. W. Plieth, Electrocrystallization – factors influencing structure, *J. Solid State Electrochem.*, **15** (2011) 1417-1423.

70. F.C. Walsh, M.E. Herron, Electrocrystallization and electrochemical control of crystal growth: Fundamental considerations and electrodeposition of metals, *J. Phys. D: Appl. Phys.,* **24** (1991) 217-225.

71. M. Fleischmann, H.R. Thirsk, *Metal Deposition and Electrocrystallization*, in Advances in Electrochemistry and Electrochemical Engineering, Paul Delahay (Editor), Vol. **3**, (1963) 123.

72. D.J. Astley, J.A. Harrison, H.R. Thirsk, Electrocrystallization of mercury, silver and palladium, *Trans. Faraday Soc.*, **64** (1968) 192-201.

73. G.J. Hills, D.J. Schiffrin, J. Thompson, Electrochemical nucleation from molten salt – I. Diffusion controlled electrodeposition of silver from alkali molten nitrates, *Electrochim. Acta*, **19** (1974) 657-670.

74. G.A. Gunawardena, G.J. Hills, I. Montenegro, Potentiostatic studies of electrochemical nucleation, *Electrochim. Acta*, **23** (1978) 693-697.

75. J.W.M. Jacobs, Note on a theory of three-dimensional electrochemical nucleation with diffusion-controlled growth, *J. Electroanal. Chem.*, **247** (1988) 135-144.

76. M. Avrami, Kinetics of phase change. I: General theory, *J. Chem. Phys.*, **7** (1939) 1103-1112.

77. W.H. Mulder, J.H.O.J. Wijenberg, M. Sluyters-Rehbach, J.H. Sluyters, On the validity of the Avrami theorem in the case of decelerating growth, *J. Electroanal. Chem.*, **270** (1989) 7-19.

78. G. Gunawardena, G. Hills, I. Montenegro, B. Scharifker, Electrochemical nucleation, Part I. General considerations, *J. Electroanal. Chem.*, **138** (1982) 225-239.

79. B. Scharifker, G. Hills, Theoretical and experimental studies of multiple nucleations, *Electrochim. Acta*, **28** (1983) 879-889.

80. B. Scharifker, J. Mostany, Three-dimensional nucleation with diffusion controlled growth: Part I. Number density of active sites and nucleation rates per site, *J. Electroanal. Chem.*, **177** (1984) 13-23.

81. B.R. Scharifker, J. Mostany, M. Palomar-Pardave, I. Gonzalez, On the theory of the potentiostatic current transient for diffusion-controlled three-dimensional electrocrystallization processes, *J. Electrochem. Soc.*, **146** (1999) 1005-1012.

82. D. Mazaira, C. Borras, J. Mostany, B.R. Scharifker, Three-dimensional nucleation with diffusion controlled growth : imulation of hierarchical diffusion zones overlap, *J. Electroanal. Chem.*, **631** (2009) 22-28.

83. M. Sluyters-Rehbach, J.H.O.J. Wijenberg, E. Bosco, J.H. Sluyters, The theory of chronoamperometry for the investigation of electrocrystallization: Mathematical description and analysis in the case of diffusion-controlled growth, *J. Electroanal. Chem.*, **236** (1987) 1-20.

84. L. Heerman, A. Tarallo, Theory of the chronoamperometric transient for electrochemical nucleation with diffusion-controlled growth, *J. Electroanal. Chem.*, **470** (1999) 70-76.

85. L. Heerman, A. Tarallo, Electrochemical nucleation on microelectrodes. Theory and experiment for diffusion-controlled growth, *J. Electroanal. Chem.*, **451** (1998) 101-109.

86. L. Heerman, A. Tarallo, Electrochemical nucleation with diffusion-limited growth, Properties and analysis of transients, *Electrochem. Commun.*, **2** (2000) 85-89.

87. M. Arbib, B. Zhang, V. Lazarov, D. Stoychev, A. Milchev, C. Buess-Herman, Electrochemical nucleation and growth of rhodium on gold substrates, *J. Electroanal. Chem.*, **510** (2001) 67-77.

88. O. Brylev, L. Roue, D. Belanger, Rhodium electrodeposition on pyrolytic graphite electrode: Analysis of chronoamperometric curves, *J. Electroanal. Chem.,* **581** (2005) 22-30.

89. A. Milchev, Role of the substrate state in electrochemical nucleation, *Electrochim. Acta,* **28** (1983) 947-953.

90. A.O. Simm, X. Ji, C.E. Banks, M.E. Hyde, R.G. Compton, AFM studies of metal deposition: Instantaneous nucleation and the growth of cobalt nanoparticles on boron-doped diamond electrodes, *Chem. Phys. Chem.*, **7** (2006) 704-709.

91. M.E. Hyde, R. Jacobs, R.G. Compton, In situ AFM studies of metal deposition, *J. Phys. Chem. B*, **106** (2002) 11075-11080.

92. H. Liu, R.M. Penner, Size-selective electrodeposition of mesoscale metal particles in the uncoupled limit, *J. Phys. Chem. B*, **104** (2000) 9131-9139.

93. J.L. Fransaer, R.M. Penner, Brownian dynamics simulations of the growth of metal nanocrystal ensembles on electrode surfaces from solution: 1. Instantaneous nucleation and diffusion controlled growth, *J. Phys. Chem. B*, **103** (1999) 7643-7653.

94. R.M. Penner, Brownian dynamics simulations of the growth of metal nanocrystal ensembles on electrode surface in solution: 2. The effect of

deposition rate on particles size dispersion, *J. Phys. Chem. B*, **105** (2001) 8672-8678.

95. J.V. Zoval, R.M. Stiger, P.R. Biernacki, R.M. Penner, Electrochemical deposition of silver nanocrystallites on the atomically graphite basal plane, *J. Phys. Chem.,* **100** (1996) 837-844.
96. J.V. Zoval, J. Lee, S. Gorer, R.M. Penner, Electrochemical preparation of silver nanocrystallites with size selectivity on basal plane oriented graphite surfaces, *J. Phys. Chem.,* **100** (1996) 837-844.
97. M. Ueda, H. Dietz, A. Anders, H. Kneppe, A. Meixner, W. Plieth, Double-pulse technique as an electrochemical tool for controlling the preparation of metallic nanoparticles, *Electrochim. Acta*, **48** (2002) 377-386.
98. G.D. Adzic, D.M. Drazic, A.R. Despic, A method of obtaining a small number of nucleation sites and growing large crystal grains, *J. Electroanal. Chem.*, **239** (1988) 107-111.
99. P.J.F. Harris, Fullerene-related structure of commercial glassy carbons, *Philosophical Magazine*, **84** (2004) 3159-3167.
100. A.J. Bard, Larry R. Faulkner, *Electrochemical methods: Fundamentals and applications,* 2nd Edition, 2006, Wiley India.
101. S.K. Guin, S.K. Aggarwal, *Understanding electrochemical quartz crystal microbalance*, Highlights in Electro-Analytical Techniques (HEAT); ISEAC Publications, **2** (2013) 76-81.
102. D.A. Pantazis and F. Neese, All-electron scalar relativistic basis sets for the actinides, *J. Chem. Theory Comput.*, **7** (2011) 677-684.

103. K.L. Schuchardt, B.T. Didier, T. Elsethagen, L. Sun, V. Gurumoorthi, J. Chase, J. Li, T.L. Windus, Basis Set Exchange: A community database for computational sciences, *J. Chem. Inf. Model.,* **47** (2007) 1045-1052.

104. W. Schmidt, K.K. Baldridge, J.A. Boatz, S.T. Elbert, M.S. Gordon, J.H. Jensen, S. Koseki, N. Matsunaga, K.A. Nguyen, S.J. Su, T.L. Windus, M. Dupuis, J.A. Montgomery, General atomic and molecular electronic structure system, *J. Comput. Chem.,* **14** (1993) 1347-1363.

105. M. Martos, J. Morales, L. Sanchez, Lead-based systems as suitable anode materials for Li-ion batteries, *Electrochim. Acta*, **48** (2003) 615-621.

106. M. Veith, J. Frères, P. König, O. Schütt, V. Huch, J. Blin, Nanoscaled Sn and Pb particles aligned in Al_2O_3 tubes obtained from molecular precursors, *Eur. J. Inorg. Chem.,* (2005) 3699-3710.

107. A. Lungu, M. Bleiweiss, J. Amirzadeh, S. Saygi, A. Dimofte, M. Yin, Z. Iqbal, T. Datta, Superconductivity in nanostructured lead, *Physica C,* **349** (2001) 1-7.

108. W.-H. Li, C.C. Yang, F.C. Tsao, K.C. Lee, Quantum size effects on the superconducting parameters of zero-dimensional Pb nanoparticles, *Phys. Rev. B*, **68** (2003) 184507 (6 pages).

109. E. Bernardi, A. Lascialfari, A. Rigamonti, Zero-dimensional superconducting fluctuations and fluctuating diamagnetism in lead nanoparticles, *Phys. Rev. B*, **74** (2006) 134509 (8 pages).

110. T. Schneider, S. Weyeneth, Diamagnetism, Nernst signal, and finite-size effects in superconductors above the transition temperature T_c, *Phys. Rev. B*, **83** (2011) 144527 (11 pages).

111. T. Theivasanthi, M. Alagar, Innovation of superparamagnetism in lead nanoparticles, *Physics and Technical Sciences* (2013) 39-45.

112. T. Theivasanthi, M. Alagar, Lead nanopowder as advanced semi-conductor-an insight, *Research and Application of Material* (2013) 36-43.

113. Y. Zhao, Z. Zhang, H. Dang, Fabrication and tribological properties of Pb nanoparticles, *J. Nanopart. Res.* **6** (2004) 47-51.

114. S.H. Hosseini, M. Askari, S.N. Ezzati, X-ray attenuating nanocomposite based on polyaniline using Pb nanoparticles, *Synth. Met.*, **196** (2014) 68-75.

115. J. Kano, T. Kizuka, F. Shikanai, S. Kojima, Structural dynamics of lead nanoparticles with stable metallic surfaces on $Pb_xSr_{1-x}TiO_3$ prepared by co-Precipitation, Proceedings of *9th IEEE Conference on Nanotechnology, IEEE NANO,* 2009, ISBN. 978-981-08-3694-8 (RPS), 287-290.

116. E. Castro-Longoria, K. Trejo-Guillén, A.R. Vilchis-Nestor, M. Avalos-Borjad, S.B. Andrade-Canto, D.A. Leal-Alvarado, J.M. Santamaría, Biosynthesis of lead nanoparticles by the aquatic water fern, Salvinia minima Baker, when exposed to high lead concentration, *Colloids Surf. B*, **114** (2014) 277-283.

117. S. Reich, G. Leitus, R.P. Biro, M. Schechter, Magnetization of small lead particles, *Phys. Rev. Lett.*, **91** (2003) 147001.

118. C. Nabais, R. Schneider, C. Bellouard, J. Lambert, P. Willmann, D. Billaud, A new method for the size- and shape-controlled synthesis of lead nanostructures, *Mater. Chem. Phys.*, **117** (2009) 268-275.

119. M. Veith, S. Mathur, P. König, C. Cavelius, J. Biegler, A. Rammo,V. Huch, H. Shen, G. Schmid, Template-assisted ordering of Pb nanoparticles prepared from molecular-level colloidal processing, *C.R. Chimie*, **7** (2004) 509-519.

120. J. Kano, T. Kizuka, F. Shikanai, S. Kojima, Pure lead nanoparticles with stable metallic surfaces, on perovskite lead strontium titanate particles, *Nanotechnology*, **20** (2009) 295704 (4 pages).

121. A. Sarkar, R. Chadha, T. Mukherjee, S. Kapoor, Oxidation and magnetic properties of lead nanoparticles in different matrices, *Chem. Phys. Lett.*, **473** (2009) 111-115.

122. P. Diaz-Arista, R. Antano-Lopez, Y. Meas, R. Ortega, E. Chainet, P. Ozil, G. Trejo, EQCM study of the electrodeposition of manganese in the presence of ammonium thiocyanate in chloride-based acidic solutions, *Electrochim. Acta*, **51** (2006) 4393-4404.

123. A. Méndez, P. Díaz-Arista, L. Salgado, Y. Meas, G. Trejo, EQCM study of the adsorption/desorption processes of polyethyleneglycol with molecular weight 20,000 on Pt in perchloric acid solution, *Int. J. Electrochem. Sci.*, **3** (2008) 918-934.

124. G.A. Snook, A.M. Bond, S. Fletcher, The use of massograms and voltammograms for distinguishing five basic combinations of charge transfer and mass transfer at electrode surfaces, *J. Electroanal. Chem.*, **526** (2002) 1-9.

125. E. Bahena, P.F. Mendez, Y. Meas, R. Ortega, L. Salgado, G. Trejo, An EQCM study of polyethyleneglycol 8000 adsorption and its coadsorption with Cl^- ions on Pt in perchloric acid solutions, *Electrochim. Acta*, **49** (2004) 989-997.

126. J.-H. Chen, L.-H. Nie, S.-Z. Yao, A new method for rapid determination of the potential of zero charge for gold, *J. Electroanal. Chem.*, **414** (1996) 53-59.

127. A.S. Bondarenko, G.A. Ragoisha, N.P. Osipovich, E.A. Streltsov, Potentiodynamic electrochemical impedance spectroscopy of lead UPD on

polycrystalline gold and on selenium atomic underlayer, *Electrochem. Commun.*, **7** (2005) 631-636.

128. K.S. Kim, T.J. O'Leary, N. Winograd, X-ray photoelectron spectra of lead oxides, *Anal. Chem.*, **45** (1973) 2214-2218.

129. K.S. Kim, N. Winograd, Observation of polymorphic lead monoxide surfaces using X-ray photoelectron spectroscopy, *Chem. Phys. Lett.*, **19** (1973) 209-212.

130. G. Sandmann, H. Dietz, W. Plieth, Preparation of silver nanoparticles on ITO surfaces by a double-pulse method, *J. Electroanal. Chem.*, **491** (2000) 78-86.

131. S.K. Guin, R. Phatak, J.S. Pillai, A. Sarkar, S.K. Aggarwal; *RSC Advances*, 2014, DOI: 10.1039/C4RA12877J.

132. A. Milchev, L. Heerman, Electrochemical nucleation and growth of nano- and microparticles: some theoretical and experimental aspects, *Electrochim. Acta*, **48** (2003) 2903-2913.

133. L. Komsiyska, G. Staikov, Electrocrystallization of Au nanoparticles on glassy carbon from $HClO_4$ solution containing $[AuCl_4]^-$, *Electrochim. Acta*, **54** (2008) 168-172.

134. R.-W. Tsai, Y.-T. Hsieh, P.-Y. Chen, I.-W. Sun, Voltammetric study and electrodeposition of tellurium, lead, and lead telluride in room-temperature ionic liquid 1-ethyl-3-methylimidazolium tetrafluoroborate, *Electrochim. Acta*, **137** (2014) 49-56.

135. J. Xu, G. Yua, B. Hub, J. Zhang, Q. Dong, X.Y. Zhang, Preparation of copper coated tungsten powders by intermittent electrodeposition, *Powder Technol.*, **264** (2014) 561-569.

136. A.G. Oshchepkov, A.N. Simonov, P.A. Simonov, A.N. Shmakov, N.A. Rudina, A.V. Ishchenko, O.V. Cherstiouk, V.N. Parmon, Interrelation between catalytic activity for oxygen electroreduction and structure of supported platinum, *J. Electroanal. Chem.*, **729** (2014) 34-42.

137. F. Palmisano, E. Desimoni, L. Sabbatini, G. Torsi, Nucleation phenomena in the electrodeposition of lead onto glassy carbon electrodes, *J. Appl. Electrochem.*, **9** (1979) 517-525.

138. I. Danaee, 2D-3D nucleation and growth of palladium on graphite electrode, *J. Ind. Eng. Chem.,* **19** (2013) 1008-1013.

139. X. Huang, Y. Chen, J. Zhou, Z. Zhang, J. Zhang, Electrochemical nucleation and growth of Sn onto double reduction steel substrate from a stannous fluoborate acid bath, *J. Electroanal. Chem.*, **709** (2013) 83-92.

140. Y. Zhao, F.-X. Deng, L.-F. Hua, Y.-Q. Liua, G.-B. Pana, Electrochemical deposition of copper on single-crystal gallium nitride(0001) electrode: nucleation and growth mechanism, *Electrochim. Acta,* **130** (2014) 537-542.

141. S. Guo, E. Wang, Synthesis and electrochemical applications of gold nanoparticles, *Anal. Chim. Acta,* **598** (2007) 181-192.

142. K. Saha, S.S. Agasti, C. Kim, X. Li, V.M. Rotello, Gold nanoparticles in chemical and biological sensing, *Chem. Rev.*, **112** (2012) 2739-2779.

143. H. Zhang, J.-J. Xu, H.-Y. Chen, Shape-controlled gold nanoarchitectures: Synthesis, superhydrophobicity, and electrocatalytic properties, *J. Phys. Chem. C,* **112** (2008) 13886-13892.

144. E. Boisselier, D. Astruc, Gold nanoparticles in nanomedicine: preparations, imaging, diagnostics, therapies and toxicity, *Chem. Soc. Rev.*, **38** (2009) 1759-1782.

145. M.-C. Daniel, D. Astruc, Gold nanoparticles: Assembly, supramolecular chemistry, quantum-size-related properties, and applications toward biology, catalysis, and nanotechnology, *Chem. Rev.*, **104** (2004) 293-346.

146. H. Haick, Chemical sensors based on molecularly modified metallic nanoparticles, *J. Phys. D: Appl. Phys.,* **40** (2007) 7173-7186.

147. M. Zayats, R. Baron, I. Popov, I. Willner, Biocatalytic growth of Au nanoparticles: From mechanistic aspects to biosensors design, *Nano Lett.*, **5** (2005) 21-25.

148. W. Zhao, M.A. Brook, Y. Li, Design of gold nanoparticle-based colorimetric biosensing assays, *Chem. Bio. Chem.*, **9** (2008) 2363-2371.

149. U.H.F. Bunz, V.M. Rotello, Gold nanoparticles-fluorophore complexes: Sensitive and discerning "noses" for biosystems sensing, *Angew. Chem., Int. Ed.*, **49** (2010) 3268-3279.

150. R.A. Sperling, P.R. Gil, F. Zhang, M. Zanella, W.J. Parak, Biological applications of gold nanoparticles, *Chem. Soc. Rev.,* **37** (2008) 1896-1908.

151. S.H. Radwan, H.M.E. Azzazy, Gold nanoparticles for molecular diagnostics, *Expert Review of Molecular Diagnostics*, **9** (2009) 511-524.

152. S. Zeng, K.-T. Yong, I. Roy, X.-Q. Dinh, X. Yu, F. Luan, A review on functionalized gold nanoparticles for biosensing applications, *Plasmonics*, **6** (2011) 491-506.

153. R. Wilson, The use of gold nanoparticles in diagnostics and detection, *Chem. Soc. Rev.*, **37** (2008) 2028-2045.

154. M.H. Rashid, R.R. Bhattacharjee, A. Kotal, T.K. Mandal, Synthesis of spongy gold nanocrystals with pronounced catalytic activities, *Langmuir*, **22** (2006) 7141-7143.

155. A.A. Herzing, C.J. Kiely, A.F. Carley, P. Landon, G J. Hutchings, Identification of active gold nanoclusters on iron oxide supports for CO oxidation, *Science*, **321** (2008) 1331-1335.
156. W. Chen, S. Chen, Oxygen electroreduction catalyzed by gold nanoclusters: Strong core size effects, *Angew. Chem. Int. Ed.*, **48** (2009) 4386-4389.
157. B. Hvolbaek, T.V.W. Janssens, B.S. Clausen, H. Falsig, C.H. Christensen, J.K. Norskov, Catalytic activity of Au nanoparticles, *Nanotoday*, **2** (2007) 14-18.
158. G. Frens, Controlled nucleation for the regulation of the particle size in monodisperse gold suspensions, *Nature*, **241** (1973) 20-22.
159. M. Brust, J. Fink, D. Bethell, D.J. Schiffrin, C. Kiely, Synthesis and reactions of functionalised gold nanoparticles, *J. Chem. Soc., Chem. Commun.*, (1995) 1655-1656.
160. M. Brust, M. Walker, D. Bethell, D.J. Schiffrin, R. Whyman, Synthesis of thiol-derivatised gold nanoparticles in a two-phase liquid-liquid system, *J. Chem. Soc., Chem. Commun.*, (1994) 801-802.
161. B.J. Plowman, M. Mahajan, A.P. O'Mullane, S.K. Bhargava, Electrochemical detection of dopamine and cytochrome c at a nanostructured gold electrode, *Electrochim. Acta*, **55** (2010) 8953-8959.
162. K.-U. Din, J. Kuta, L. Pospisil, Polarographic and voltammetric measurements of disproportionation of uranium(V) in sulphate and other complexing media on mercury electrodes, *Electrochim. Acta*, **22** (1977) 1109-1112.
163. U. Schmidt, M. Donten, J.G. Osteryoung, Gold electrocrystallization on carbon and highly oriented pyrolytic graphite from concentrated solutions of LiCl, *J. Electrochem. Soc.*, **144** (1997) 2013-2021.

164. T. Oyama, S. Yamaguchi, T. Okajima, T. Ohsaka, N. Oyama, Time-differential frequency response of electrochemical quartz crystal electrode during the dissolution and deposition processes of Au in H_2SO_4 solution containing chloride ion, *J. Electroanal. Chem.*, **659** (2011) 36-42.

165. Z.-L. Jiang, S.-J. Sunb, A.-H. Liang, C.-J. Liu, A new immune resonance scattering spectral assay for trace fibrinogen with gold nanoparticle label, *Anal. Chim. Acta*, **571** (2006) 200-205.

166. Z.-L. Jiang, M.-J. Zou, A.-H. Liang, An immunonanogold resonance scattering spectral probe for rapid assay of human chorionic gonadotrophin, *Clin. Chim. Acta*, **387** (2008) 24-30.

167. O. Chailapakul, E. Popa, H. Tai, B. V. Sarada, D. A. Tryk, A. Fujishima, The electrooxidation of organic acids at boron-doped diamond electrodes, *Electrochem. Commun.*, **2** (2000) 422-426.

168. S. Trasatti, O.A. Petri, Real surface area measurements in electrochemistry, *Pure Appl. Chem.*, **63** (1991) 711-734.

169. G. Gupta, D. Tanaka, Y. Ito, D. Shibata, M. Shimojo, K. Furuya, K. Mitsui, K. Kajikawa, Absorption spectroscopy of gold nanoisland films: optical and structural characterization, *Nanotechnology*, **20** (2009) 025703 (9 pages).

170. World Health Organization, Background document for development of WHO guidelines for drinking-water quality: Lead in drinking water, WHO/SDE/WSH/03.04/09/Rev/1, WHO Press, Switzerland, 2011.

171. M. Maharjan and A. Roberts (ed.), in *Food, Water and Lead Contamination*, LEAD Action News, vol. 10, issue 1, June 2010, ISSN 1324-6011.

172. A.J. Wain, Imaging size effects on the electrocatalytic activity of gold nanoparticles using scanning electrochemical microscopy, *Electrochim. Acta*, **92** (2013) 383-391.

173. J. Hernandez, J. Solla-Gullon, E. Herrero, J.M. Feliu, A. Aldaz, In situ surface characterization and oxygen reduction reaction on shape-controlled gold nanoparticles, *J. Nanosci. Nanotechnol.*, **9** (2009) 2256-2273.

174. A.J. Saleh Ahammad, M.M. Rahman, G.-R. Xu, S. Kim, J.-J. Lee, Highly sensitive and simultaneous determination of hydroquinone and catechol at poly(thionine) modified glassy carbon, *Electrochim. Acta*, **56** (2011) 5266-5271.

175. R. Gupta, S.K. Guin, S.K. Aggarwal, A mechanistic study on the electrocatalysis of the Pu(IV)/Pu(III) redox reaction at a platinum electrode modified with single-walled carbon nanotubes (SWCNTs) and polyaniline (PANI), *RSC Adv.*, **2** (2012) 1810-1819.

176. I.M. Issa, M. Tharwat, Kinetics of reduction of hexavalent uranium in sulphuric acid solutions. A simplified method for determining the parameters of irreversible waves, *Electrochim. Acta*, **17** (1972) 343-349.

177. I.M. Issa, R.M. Issa, L.A. Shalaby, Polarographic analysis. II. Polarography of uranium in sulphate solutions, *Z. Anal. Chem.*, **176** (1960) 250-256.

178. J.I. Watters, U.S.A.E.C. Report CC-2771 (1945).

179. P.J. Elvlng, A.F. Krivls, Polarographic reduction of uranium(vi) under complexing and noncomplexing conditions nature of the uranium(v) sulphate complex, *J. Inorg. Nucl. Chem.*, **11** (1959) 234-241.

180. E.A. Kanevskii, G.R. Pavlovskya, *Zh. Neorg. Khim.*, **5** (1960) 1738.

181. C. Ye, M. Li, J. Luo, L. Chen, Z. Tang, J. Pei, L. Jiang, Y. Song, D. Zhu, Photo-induced amplification of readout contrast in nanoscale data storage, *J. Mater. Chem.*, **22** (2012) 4299-4305.

182. A.S. Jeevarajan, M. Khaled, L.D. Kispert, Simultaneous electrochemical and electron paramagnetic resonance studies of keto and hydroxy carotenoids, *Chem. Phys. Letters*, **225** (1994) 340-345.

183. P. Cekirdek, A.O. Solak, M. Karakus, A. Aydin, H. Yılmaz, Investigation of electrochemical behavior of some dithiophosphonates in acetonitrile on the platinum and gold electrodes, *Electroanalysis,* **18** (2006) 2314-2323.

184. F. Fungo, L. Otero, E. Durantini, W.J. Thompson, J.J. Silber, T.A. Moore, A.L. Moore, D. Gust, L. Sereno, Correlation of fluorescence quenching in carotenoporphyrin dyads with the energy of intramolecular charge transfer states. Effect of the number of conjugated double bonds of the carotenoid moiety, *Phys. Chem. Chem. Phys.,* **5** (2003) 469-475.

185. P. Kalimuthu, S. Leimkühler, P.V. Bernhardt, Catalytic electrochemistry of xanthine dehydrogenase, *J. Phys. Chem. B*, **116** (2012) 11600-11607.

186. V. Vallet, I. Grenthe, On the structure and relative stability of uranyl(VI) sulfate complexes in solution, *C.R. Chimie,* **10** (2007) 905-915.

187. D. Vopalka, K. Stamberg, A. Motl, B. Drtinova, The study of the speciation of uranyl–sulphate complexes by UV–Vis absorption spectra decomposition, *J. Radioanal. Nucl. Chem.*, **286** (2010) 681-686.

188. T. Vercouter, P. Vitorge, B. Amekraz, C. Moulin, Stoichiometries and thermodynamic stabilities for aqueous sulfate complexes of U(VI), *Inorg. Chem.*, **47** (2008) 2180-2189.

189. C. Hennig, A. Ikeda, K. Schmeide, V. Brendler, H. Moll, S. Tsushima, A.C. Scheinost, S. Skanthakumar, R. Wilson, L. Soderholm, K. Servaes, C. Görrler-Walrand, R. Van Deun, The relationship of monodentate and bidentate coordinated uranium(VI) sulfate in aqueous solution, *Radiochim. Acta*, **96** (2008) 607-611.

190. S. Kannan, A.E. Vaughn, E.M. Weis, C.L. Barnes, P.B. Duval, Anhydrous photochemical uranyl(VI) reduction: Unprecedented retention of equatorial coordination accompanying reversible axial oxo/alkoxide exchange, *J. Am. Chem. Soc.*, **128** (2006) 14024-14025.

191. S. Tsushima, On the "yl" bond weakening in uranyl(VI) coordination complexes, *Dalton Trans.*, **40** (2011) 6732-6737.

192. R.C. Tatar, S. Rabii, Electronic properties of graphite: A unified theoretical study, *Phys. Rev. B*, **25** (1982) 4126-4141.

193. A.D. Boardman, M.I. Darby, E.T. Micah, Density of states in perturbed graphite lattice, *Carbon*, **11** (1973) 207-216.

194. R.L. McCreery, Advanced carbon electrode materials for molecular electrochemistry, *Chem. Rev.*, **108** (2008) 2646-2687.

195. N.T. Khoa, S.W. Kim, D.-H. Yoo, E. J. Kim, S.H. Hahn, Size-dependent work function and catalytic performance of gold nanoparticles decorated graphene oxide sheets, *Appl. Catal. A: Gen.*, **469** (2014) 159-164.

196. S. T. Zhang, Y.-J. Song, X.-Y. Zhang, J.-Y. Wu, Synthesis of silver nanostructures by multistep methods, *Sensors*, **14** (2014) 5860-5889.

197. M. Meena-Kumari, D. Philip, Degradation of environment pollutant dyes using phytosynthesized metal nanocatalysts, *Spectrochim. Acta A*, **135** (2015) 632-638.

198. M.R. Bindhu, M. Umadevi, Antibacterial and catalytic activities of green synthesized silver nanoparticles, *Spectrochim. Acta A*, **135** (2015) 373-378.

199. B.A. Makwana, D.J. Vyas, K.D. Bhatt, V.K. Jain, Y.K. Agrawal, Highly stable antibacterial silver nanoparticles as selective fluorescent sensor for Fe^{3+} ions, *Spectrochim. Acta A*, **134** (2015) 73-80.

200. M.A. Herrera, G.P. Jara, R. Villarroel, A.E. Aliaga, J.S. Gómez-Jeria, E. Clavijo, C. Garrido, T. Aguayo, M.M. Campos-Vallette, Surface enhanced Raman scattering study of the antioxidant alkaloid boldine using prismatic silver nanoparticles, *Spectrochim. Acta A*, **133** (2014) 591-596.

201. Q. Wang, X. Cui, W. Guan, L. Zhang, X. Fan, Z. Shi, W. Zheng, Shape-dependent catalytic activity of oxygen reduction reaction (ORR) on silver nanodecahedra and nanocubes, *J. Power Sources*, **269** (2014) 152-157.

202. R. Botta, G. Upender, R. Sathyavathi, D. Narayana Rao, C. Bansal, Silver nanoclusters films for single molecule detection using Surface Enhanced Raman Scattering (SERS), *Mater. Chem. Phys.*, **137** (2013) 699-703.

203. C.M. Cobley, S.E. Skrabalak, D.J. Campbell, Y. Xia, Shape-controlled synthesis of silver nanoparticles for plasmonic and sensing applications, *Plasmonics,* **4** (2009) 171-179.

204. X.-Y. Zhang, A. Hu, T. Zhang, W. Lei, X.-J. Xue, Y. Zhou, W. W. Duley, Self-assembly of large-scale and ultrathin silver nanoplate films with tunable plasmon resonance properties, *ACS Nano,* **5** (2011) 9082-9092.

205. A.C. Power, A.J. Betts, J.F. Cassidy, Silver nanoparticle polymer composite based humidity sensor, *Analyst*, **135** (2010) 1645-1652.

206. A.A. Abdelwahab, Y.-B. Shim, Nonenzymatic H_2O_2 sensing based on silver nanoparticles capped polyterthiophene/MWCNT nanocomposite, *Sens. Actuators B: Chem.*, **201** (2014) 51-58.

207. J. Yin, X. Qi, L. Yang, G. Hao, J. Li, J. Zhong, A hydrogen peroxide electrochemical sensor based on silver nanoparticles decorated silicon nanowire arrays, *Electrochim. Acta*, **56** (2011) 3884-3889.

208. C. Cannilla, G. Bonura, F. Frusteri, D. Spadaro, S. Trocino, G. Neri, Development of an ammonia sensor based on silver nanoparticles in a poly-methacrylic acid matrix, *J. Mater. Chem. C*, **2** (2014) 5778-5786.

209. S.T. Dubas, V. Pimpan, Green synthesis of silver nanoparticles for ammonia sensing, *Talanta*, **76** (2008) 29-33.

210. C.C. Wang, M.O. Luconi, A.N. Masi, L.P. Fernández, Derivatized silver nanoparticles as sensor for ultra-trace nitrate determination based on light scattering phenomenon, *Talanta*, **77** (2009) 1238-1243.

211. K. Fajerwerg, V. Ynam, B. Chaudret, V. Garçon, D. Thouron, M. Comtat, An original nitrate sensor based on silver nanoparticles electrodeposited on a gold electrode, *Electrochem. Commun.*, **12** (2010) 1439-1441.

212. P. Rameshkumar, P. Viswanathan, R. Ramaraj, Silicate sol–gel stabilized silver nanoparticles for sensor applications toward mercuric ions, hydrogen peroxide and nitrobenzene, *Sens. Actuators B: Chem.*, **202** (2014) 1070-1077.

213. Y. Lin, L. Li, L. Hu, K. Liu, Y. Xu, Multifunctional poly(dopamine)-assisted synthesis of silver nano particles/carbon nanotubes nanocomposite: Toward

electrochemical sensing of hydrogen peroxide with enhanced sensitivity, *Sens. Actuators B: Chem.*, **202** (2014) 527-535.

214. C.K. Tagad, H.U. Kim, R.C. Aiyer, P. More, T. Kim, S.H. Moh, A. Kulkarni, S.G. Sabharwal, A sensitive hydrogen peroxide optical sensor based on polysaccharide stabilized silver nanoparticles, *RSC Adv.*, **3** (2013) 22940-22943.
215. P.C. Ray, Size and shape dependent second order nonlinear optical properties of nanomaterials and their application in biological and chemical sensing, *Chem. Rev.*, **110** (2010) 5332-5365.
216. B. Pietrobon, V. Kitaev, Photochemical synthesis of monodisperse size-controlled silver decahedral nanoparticles and their remarkable optical properties, *Chem. Mater.*, **20** (2008) 5186-5190.
217. S. Zhang, Q. Wang, C. Deng, W. Ma, J.-L. Sun, Influence of natural oxidation on the surface enhancement effect of silver nanoparticle films, *J. Nanopart. Res.*, **16** (2014) 2634 (10 pages).
218. Z.M. Sui, X. Chen, L.Y. Wang, L.M. Xu, W.C. Zhuang, Y.C. Chai, C.J. Yang, Capping effect of CTAB on positively charged Ag nanoparticles, *Physica E*, **33** (2006) 308-314.
219. M.E. Hyde, R.G. Compton, A review of the analysis of multiple nucleation with diffusion controlled growth, *J. Electroanal. Chem.*, **549** (2003) 1-12.
220. A. Radisic, F.M. Ross, P.C. Searson, In situ study of the growth kinetics of individual island electrodeposition of copper, *J. Phys. Chem. B,* **110** (2006) 7862-7868.

221. M. Rezaei, S.H. Tabaian, D.F. Haghshenas, Electrochemical nucleation of palladium on graphene: A kinetic study with an emphasis on hydrogen co-reduction, *Electrochim. Acta*, **87** (2013) 381-387.

222. J. Yu, H. Cao, Y. Chen, L. Kang, H. Yang, A new approach to the estimation of electrocrystallization parameters, *J. Electroanal. Chem.*, **474** (1999) 69-73.

223. S. Salomé, N.M. Pereira, E.S. Ferreira, C.M. Pereira, A.F. Silva, Tin electrodeposition from choline chloride based solvent: Influence of the hydrogen bond donors, *J. Electroanal. Chem.*, **703** (2013) 80-87.

224. S. Langerock, L. Heerman, Study of the electrodeposition of rhodium on polycrystalline gold electrodes by quartz microbalance and voltammetric techniques, *J. Electrochem. Soc.*, **151** (2004) C155-C160.

225. F. Gloaguen, J.M. Leger, C. Lamy, A. Marmann, U. Stimming, R. Vogel, Platinum electrodeposition on graphite: electrochemical study and STM imaging, *Electrochim. Acta*, **44** (1999) 1805-1816.

226. S. Fletcher, Extracting nucleation rates from current–time transients. Comments on three papers by Abyaneh and Fleischmann published in this issue, *J. Electroanal. Chem.*, **530** (2002) 105-107.

227. S. Fletcher, Extracting nucleation rates from current–time transients. Concluding remark, *J. Electroanal. Chem.*, **530** (2002) 119-122.

228. R.L. Deutscher, S. Fletcher, Nucleation on active sites: Part IV. Invention of an electronic method of counting the number of crystals as a function of time; and the discovery of nucleation rate dispersion, *J. Electroanal. Chem.*, **239**, **(**1988) 17-54.

229. R.L. Deutscher, S. Fletcher, Nucleation on active sites: Part V. The theory of nucleation rate dispersion, *J. Electroanal. Chem.*, **277** (1990) 1-18.

230. A. Milchev, Electrochemical nucleation on active sites—what do we measure in reality? Part I., *J. Electroanal. Chem.*, **457** (1998) 35-46.

231. A. Milchev, W.S. Kruijt, M. Sluyters-Rehbach, J.H. Sluyters, Distribution of the nucleation rate in the vicinity of a growing spherical cluster: Part 1. Theory and simulation results, *J. Electroanal. Chem.*, **362** (1993) 21-31.

232. W.S. Kruijt, M. Sluyters-Rehbach, J.H. Sluyters, A. Milchev, Distribution of the nucleation rate in the vicinity of a growing spherical cluster.: Part 2. Theory of some special cases and experimental results, *J. Electroanal. Chem.*, **371** (1994) 13-26.

233. H.J. Ustarroz, X. Ke, A. Hubin, S. Bals, H. Terryn, New insights into the early stages of nanoparticle electrodeposition, *J. Phys. Chem. C*, **116** (2012) 2322-2329.

……The End